Robust and adaptive control strategies for closed-loop climate engineering

Federica Bonetti

Submitted in fulfilment of the requirements for the

Degree of Doctor of Philosophy

School of Engineering

College of Science and Engineering

University of Glasgow

Abstract

Climate engineering aims to offset human-driven climate change through engineering interventions. This thesis focuses on the deployment of Solar Radiation Management (SRM) methods which aim to counteract radiative forcing generated by the concentration of atmospheric CO_2. The climate system is investigated as a closed-loop control problem with uncertainties in its dynamics mitigated by robust and adaptive control strategies. Indeed, an adaptive controller for climate engineering is presented for the first time in a multi-variable control scheme. A low order three-box energy model is developed for the climate system to investigate such adaptive control strategies. Climate engineering measures are then deployed in 3 boxes, thus representing northern, southern and central (equatorial) bands. It is demonstrated that, through the on-line estimation of the controller parameters, adaptive control can overcome key-issues related to uncertainties of the climate model, external radiative forcing and actuator dynamics. The use of adaptive control provides a robust means of dealing with unforeseeable abrupt perturbations and the parametrisation of the model considered, while still providing bounds on stability and control performance. Importantly, the convergence of the controller is guaranteed through the Lyapunov stability criterion. Moreover, an analytical model describing the main latitudinal dynamics of the Earth's climate with closed-loop control has been developed. This model has analytical solution and allows for quick evaluations of non-uniform climate engineering strategies. Multi-objective analyses are considered and analytical expressions for control laws with latitudinal resolution are obtained in several scenarios. Results are broadly comparable with the literature, demonstrating model's utility in rapidly assessing climate engineering controls laws. Using the PDE model, ice line dynamics are investigated and a Lyapunov stability analysis is employed to estimate the maximum insolation reduction before the current climate falls into an ice-covered state. This provides an extreme operational boundary for future climate engineering ventures. Finally, the PDE model is employed to investigate strategies involving the deployment of space shields. The grade of obscuration provided at each latitude is estimated and an optimization process performed in order to minimize the shield size and to find the ideal orbit to counteract 2xCO_2 concentration.

Acknowledgements

I would like to thank my supervisor, Professor Colin McInnes, for providing guidance and support throughout my PhD, for his patience and immense knowledge. I am also grateful to the School of Engineering of the University of Glasgow without whom I would never had this opportunity and to my fellow doctoral students for their feedback, cooperation and, of course, friendship.

I would like to thank my friends, for their moral and emotional support. Last, but not least, I would like to thank my parents, my brother, my sister and my partner for supporting and encouraging me throughout the process of researching and writing this thesis.

Declaration

I, the undersigned Federica Bonetti hereby declare that I am the sole author of this thesis. To the best of my knowledge this thesis contains no material previously published by any other person except where due acknowledgement has been made. This thesis contains no material which has been accepted as part of the requirements of any other academic degree or non-degree program, in English or in any other language.

Signed:

Date:

Contents

List of Tables

List of Figures

Chapter 1

Introduction

In this thesis, closed-loop control strategies for solar radiation management(SRM) are employed in two climate models to counteract radiative forcing from the excess of carbon dioxide in the atmosphere. Particular attention is given to space-based SRM methods, such as the deployment of large shields in space. This chapter presents the motivation, objectives, and structure of the thesis. In addition, a list of the author's relevant publications is reported.

1.1 Thesis objectives and motivation

One of the criticisms of climate engineering is that regional impacts are not addressed, therefore effort has been put into the development of two energy balance models which, although simple, take the largest latitudinal disparities into account and provide insight into the main climatic processes involved. Progress in computing speed has led to the development of sophisticated models with millions of degrees of freedom which are capable of describing most climatic processes in great detail. However, these models are slow and computationally expensive. In contrast, low order climate models are quick and can be easily employed to promptly investigate radiative scenarios and control strategies, yet capturing major latitudinal disparities caused by SRM. Two climate models with different latitudinal resolution are developed. These models are not substitutes for high fidelity GCMs, but allow a better understanding of the dynamics of the problem and can easily be employed to assess the performance of new control strategies.

As in previous work [1–4], the problem is considered within the frame of a closed-loop control system with the application of techniques from control theory to develop multi-objective climate engineering strategies. In particular, an adaptive control strategy is proposed for the first

time in climate engineering. With respect to the more classical approaches employed in literature, such as PI control in feedback [1, 2], adaptive control is able to manage the large uncertainties in the climate model and provide the estimation of the radiative forcing required to minimize the temperature anomaly in many different scenarios.

The objectives are listed as follows:

- To develop simple energy balance models to quickly assess the effects of new control strategies with latitudinal resolution.
- To introduce an adaptive controller for climate engineering to deal with highly uncertain climate models, therefore de-emphasising the importance of using an accurate model to describe the climate system.
- To develop a quick and effective method to evaluate multi-objective closed-loop control strategies.
- To define constraints on SRM through investigating the dynamics of the ice line in model with continuous latitude resolution.
- To determine a new strategy for the deployment of shields in Earth orbit for SRM that takes latitudinal disparities into account.

1.2 Thesis structure

In Chapter 2, the main concepts which form the foundation of this thesis are described. A technical evaluation of past progress on Energy Balance Models (EBMs) is given (Section 3.1), along with a model for the dynamics of the ice line (Section 3.2) and a description of the radiative scenarios employed throughout the thesis (Section 3.3). Particular attention is given to the Representative Concentration Pathways (RCPs). Moreover, in Section 3.4, the basic concepts required to describe the dynamics of sulphur aerosol injected in the stratosphere are outlined. In Section 3.5, the orbital dynamics of space shields and perturbations in Low Earth Orbit (LEO) are briefly discussed, along with the characterisation of the Sun's apparent motion around Earth. Finally, the last section of Chapter 3 concerns the description of three control strategies employed in the thesis: a PI controller optimized through the Linear Quadratic Regulator (LQR) method (Sec-

tion 3.6.1), a model reference adaptive controller (Section 3.6.2) and an optimal control strategy (Section 3.6.3).

In Chapter 4, a 3-box model for the climate system is developed and validated. In this model, the Earth is divided into three latitudinal bands to account for largest latitudinal disparities, with heat transfer between the boxes to capture the poleward transport of energy from the equator. The 3-box model is then employed to assess an adaptive controller for climate engineering in three different strategies (Section 4.4). Moreover, the simplicity of the model allows for the investigation of controllability and observability of the system for the first time (Section 4.3).

In Chapter 5, the performance of the adaptive controller is investigated in several scenarios and the outcomes compared with a PI controller in feedback and an optimal control strategy. Importantly, the behaviour of these control strategies is investigated through the response of the 3-box model in the case of large uncertainties in the parameters of the climate model (Section 5.2), and for other perturbations, such as actuators failure (Section 5.3) and changes in actuator dynamics (Section 5.4). Moreover, an extended version of the model to 5 boxes is employed in Section 5.6 in order to investigate the reliability of adaptive control in the case of a dramatic change in albedo due to the collapse of the Arctic ice-sheet.

Taking a step forward from the 3-box model, a continuous Partial Derivative Equation (PDE) model for the climate system with latitudinal resolution is developed in Chapter 6, which can be considered as the extension of the 3-box model to an infinite number of boxes. This model provides an analytical solution and is employed to assess multi-objective control strategies. Specifically, it is shown that analytical control laws for SRM can be developed to achieve a specific temperature profile. In Section 6.3, three different control strategies involving the minimisation of the mean global temperature, the temperature gradient and the equator-to-pole temperature gradient, are considered with a PI controller in a closed-loop system. Also, in Section 6.4, an analytical control law to counteract a doubling of CO_2 is developed through the PDE model.

In Chapter 7, the PDE model is employed to analyse the dynamics of the ice line, defined as the lowest latitude at which the surface is assumed to be covered by snow or ice. The investigation of ice line stability in Section 7.2 allows the estimation of an upper bound on SRM given as the largest insolation reduction applicable before the climate system falls into an ice-covered state (Section 7.3). Moreover, the recovery from an ice-covered state is evaluated and discussed in Section 7.4. This analysis provides an absolute boundary for SRM interventions in the climate system, although it is far from planned SRM interventions.

The other SRM strategy considered in this thesis regards the deployment of large shields in Earth orbit to reduce insolation. This method is investigated in Chapter 8 and the grade of obscuration provided by the shield is estimated through geometrical considerations in Section 8.2. Moreover, in Section 8.2, an optimisation process is performed to design an optimal orbit for the shield to counteract a doubling of CO_2, taking into account latitudinal disparities with the PDE model. Results are reported in Sections (8.6.1,8.6.3), where strategies involving a single shield or multiple shields are considered.

Finally, the conclusions of the thesis and recommended future works can be found in Chapter 9.

1.3 Authored papers and posters

The research which forms this thesis has been presented in two conference posters (Climate engineering research Symposium 2015, AGU Fall Meeting 2016,) and submitted to two peer reviewed journals. In particular, the paper "Multiple input control strategies for robust and adaptive climate engineering in a low order 3-box model" was accepted for publication in Proceeding of the Royal Society A. This paper provides details of the research described in Chapter 4 and Chapter 5. Whereas, the paper "A continuous latitudinal energy balance model to explore non-uniform climate engineering strategies" was accepted for publication in the Journal of Climate Dynamics. The research found in this paper has been outlined in Chapter 6 and Chapter 7.

The full list of authored posters and papers is given as follows:

- Bonetti, F & McInnes, C. (2018). *Multiple input control strategies for robust and adaptive climate engineering in a low-order 3-box model*. Proceedings of the Royal Society A: Mathematical, Physical and Engineering Science. 474. 20180447. 10.1098/rspa.2018.0447.

- Bonetti, F & McInnes, C. (2018). *A continuous latitudinal energy balance model to explore non-uniform climate engineering strategies*. Climate Dynamics. 10.1007/s00382-018-4474-y. .

- Bonetti, F. and McInnes, C.R (2015). *Climate engineering as a robust and adaptive closed-loop system*. In: Climate engineering research Symposium, 7-10 July 2015, Berlin, Germany.

- Bonetti, F. and McInnes, C.R. (2016). *A continuous latitudinal energy balance model to explore non-uniform climate engineering strategies*. In: AGU Fall Meeting, 12-16 December 2016, San Francisco (CA), US.

Chapter 2

Literature review

A literature review of the most relevant topics regarding climate engineering and the issues related to the science of climate modelling can be found in this chapter.

2.1 Earth's energy budget and radiative forcing

The Sun provides the Earth with solar radiation, half of which is absorbed by the Earth's surface, 20% is absorbed by the atmosphere and approximately 30% is reflected back into space due to the Earth's albedo generated by atmospheric gases, aerosols, clouds and surface reflectance. The majority of the outgoing energy flux is longwave radiation, i.e. it is in the infra-red part of the spectrum. A fraction of this energy is absorbed by clouds and by several components of the atmosphere, such as water vapour, carbon dioxide, methane (CH_4), nitrous oxide (N_2O) and other greenhouse gases (GHGs). The component of infra-red radiation directed downwards heats the lower atmosphere and the Earth's surface, generating the so-called greenhouse effect.

The Sun does not provide a uniformly-distributed input of energy. Indeed, a larger fraction of the energy is received by tropical and sub-tropical regions rather than the poles. A fraction of this energy received in the tropics is then redistributed to middle and high latitudes by atmospheric and ocean transport processes. Changes in the Earth' global energy budget can be caused either by changes in the net incoming solar radiation, such as changes in the Sun's total energy output, changes in the Earth's albedo, or changes in the outgoing infra-red radiation.

An other important factor which plays a key role in the quantification of the overall energy budget is aerosols. Some aerosols are capable of increasing atmospheric reflectivity, whereas others substantially absorb radiation. Also, since aerosols can generate cloud condensation nuclei

or ice nuclei, they can also affect cloud albedo. Because of these phenomena, aerosol types, distribution and size can cause important changes in cloud albedo and lifetime [5, 6]. The effect of clouds on the climate system is controversial since they can increase albedo and therefore providing cooling, as well as having warming effects through the transfer of infra-red radiation. It is still uncertain whether the overall radiative effect of clouds is cooling or warming [7]. At the present time, confidence in the representation of processes involving clouds and aerosols is low [8, 9].

Human activities have augmented the greenhouse effect. A primary direct effect is the emission of GHGs (CO_2, CH_4, N_2O and chlorofluorocarbons (CFCs)) into the atmosphere. A secondary effect is provided by the emission of other pollutants, such as carbon monoxide, volatile organic compounds, nitrogen oxides and sulphur dioxide, which act as precursors of aerosols [10]. Additionally, anthropogenic climate change involves effects on the water cycle and land surface processes. In particular, land usage changes such as the conversion of forests to agricultural land modifies the reflectivity of the land, rates of evotranspiration and radiation emissions [10, 11].

These modifications perturb the Earth's radiation budget producing a Radiative Forcing (RF) that affects the entire climate system. When a radiative forcing is applied, internal feedbacks determine the overall response of the climate system [12, 13]. Feedback mechanisms in the climate system that can be either positive, thus amplifying the effect of the forcing on the climate, or negative and therefore reducing it [14]. Two of the main feedback effects are given by water vapour feedback and ice-albedo feedback. Water vapour provides a positive feedback for the climate system. An increase in surface temperature enhances the concentration of water vapour found in the atmosphere and a larger greenhouse effect is generated leading to further warming. The second strong feedback mechanism is ice albedo feedback. The melting of highly reflective ice or snow causes a decrease of albedo due to the low reflectivity of the land exposed beneath the ice layer. Thus, more radiation is absorbed by the land surface providing additional warming [15].

One of the biggest difficulties in accounting for feedback mechanisms is the timescale required to assess their full impact. Some feedbacks work quickly, within hours, whereas others need decades or centuries to take effect [14].

2.2 From climate change to Solar Radiation Management

Human activities have had an impact on the Earth's energy budget, resulting from increasing concentrations of greenhouse gases such as carbon dioxide, methane and nitrous oxide. This conclusion is the result of observations of the atmosphere, oceans and ice sheets through past and present records. It is therefore well established that current atmospheric concentrations of greenhouse gases (GHGs) are unprecedented and that CO_2-producing fossil fuels and industrial processes have been detected as the major cause of rising temperatures [16].

Cumulative emissions of CO_2 largely govern global mean surface warming. Considering emission history and observed warming, a strong linear relationship is found between cumulative CO_2 emissions and global temperature changes. Indeed, it is estimated that the global mean surface temperature change per 1000 GtC of CO_2 is in the range of $0.8°C$ to $2.5°C$. Both modelling and observations are in agreement regarding these values [17].

Risk and impacts due to climate change include rising sea levels, inland and coastal flooding, disrupted livelihoods, periods of extreme heat and more frequent extreme weather events. These phenomena will have a significant impact on food and water supplies, particularly in rural areas, and will likely affect worst those population groups which are the least wealthy. Finally, biodiversity and ecosystems will be affected by dramatic climatic changes [7]. Climate change due to emissions of CO_2 is also found to be irreversible for several centuries unless countermeasures are considered for the reduction of CO_2 concentration in the atmosphere [18].

For these reasons, efforts have focused on the long-term reduction of GHGs emissions through mitigation. However, total anthropogenic emissions have continued to increase despite climate change mitigation policies adopted on a global scale. With high confidence, this steady growth is attributed to the global increase in population, economic activities, lifestyle, energy and land use patterns [7, 9]. Thus, since the required decline in emissions rates has never been achieved [19] and further warming is forecast, interest in climate engineering for future risk-mitigation has developed.

Climate engineering [20], also known as geoengineering, aims to offset human-driven climate change through the intentional manipulation of the climate system. It involves techniques developed both to reduce the concentration of carbon dioxide in the atmosphere and to counteract the radiative forcing that it generates. Climate engineering techniques can therefore be categorised into two main groups: Carbon Dioxide Removal (CDR) and Solar Radiation Man-

agement (SRM) methods [21]. A summary of the main techniques employed can be found in Fig. (2.1).

Strong economic, socio-political and ethical concerns are at the centre of an ongoing debate about whether climate engineering techniques should be deployed [22]. The intrinsic complexity of the climate system and its uncertainties generates a high probability of unexpected side effects. Therefore many scientists think that any intentional human intervention on the climate could never be considered safe [20].

Moreover, the possibility of implementing climate engineering would cause significant geo-political tensions about how to define an optimal strategy. Although geoengineering could be deployed unilaterally or by individual countries, the impacts would be global in any case [23]. In fact, it is expected that any climate engineering strategy would generate large benefits for some countries and disadvantages for others. Also, poorer countries are more vulnerable to climate change but they would likely be unable to afford the deployment of geoengineering [24]. Moreover, agreement on the characterisation of the objectives would represent an additional challenge. More specifically, countries may have varying goals for the implementation of climate engineering.

Although these concerns are extremely relevant to any discussion regarding climate engineering, and therefore to this thesis, they are beyond the scope of this research and they will not be investigated in detail. However, a description of the most relevant CDR and SRM techniques follows, along with a list of relevant side-effects and impacts on population and environment.

2.2.1 CDR methods

CDR methods act on the Global Carbon Cycle (GCC) and aim to increase the CO_2-storage capability of natural reservoirs (land (soil and vegetation), ocean) [25]. The carbon cycle can be described as a series of reservoirs which are connected by exchange fluxes. The increased quantity of carbon in the global system due to anthropogenic sources is therefore distributed amongst these reservoirs. Similarly, the fraction of carbon being stored as CO_2 in the atmosphere is related to the efficiency of the redistribution processes of carbon amongst the reservoirs. The removal of anthropogenic CO_2 from the atmosphere by natural processes requires several hundred thousand years under static climatic conditions [26]. For these reasons, techniques based on the intentional manipulation of the carbon cycle have been considered (CDR). A summary of

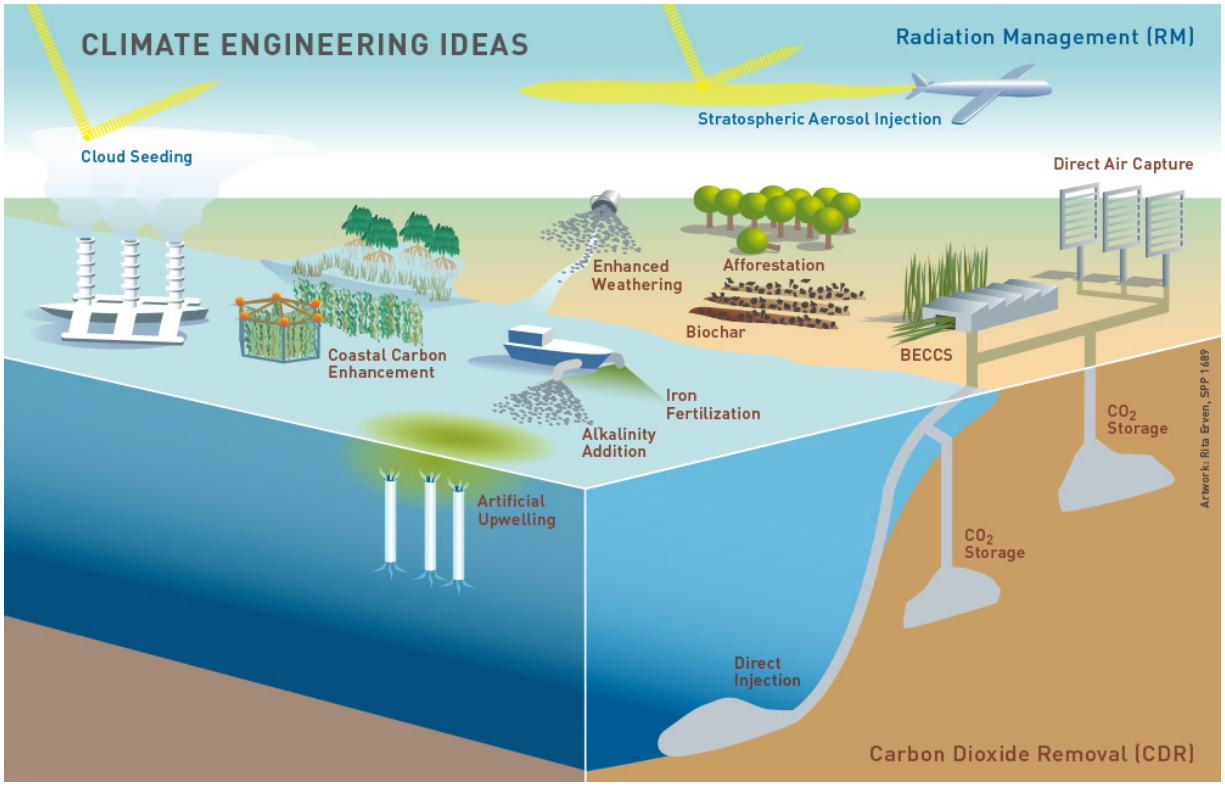

Figure 2.1: Summary of climate engineering strategies. Courtesy of Rita Erven/Kiel-Earth-Institute, licensed under a Creative Commons Attribution-NoDerivatives 4.0 International License, http://www.spp-climate-engineering.de.

the main CDR strategies, aiming to enhance existing ocean or land carbon sinks, or to generate new ones, follows [27].

Initially, the combined use of CDR and SRM techniques was considered for this research, but given that CDR effects are completely irrelevant within the timescales required to observe climate system response to SRM, it was decided to focus the effort on SRM strategies.

The decision to focus the thesis on SRM methods is also related to the initial objective of the research: the investigation of space-based climate engineering strategies such as space mirrors.

Therefore, CDR methods are not further investigated in this thesis but the following description of the main CDR techniques is useful for understanding the key differences between SRM and CDR methods. It is important to emphasise that all of the values reported in the next paragraph regarding radiative forcing achieved through a given technique are subject to uncertainty. In fact, all the specific values reported are the results of one or more simulations which employ models and emissions scenarios subject to uncertainties. Moreover, uncertainties are expected to be larger for those simulations which run over a longer time period as in the case of CDR

techniques.

With regards to the land sink: carbon is currently stored mostly in soil (1500 PgC) and only 550 PgC in vegetation [28]. In general, carbon on land has a shorter lifetime than carbon in the deep ocean and goes from 2 to 500 years. In [29], it was found that land sinks could in principle be increased and an overall radiative forcing of $-0.24\ W/m^2$ could be achieved in the long term. Stronger effects may be obtained, but issues with requirements for food production as well as the increasing global population would follow [30]. The enhancement of land carbon sink can be achieved for example through afforestation (radiative forcing of $-0.49\ W/m^2$ could be achieved by 2050 [29]), biochar ($-0.12\ W/m^2$ by 2050 [21]), bio-energy with carbon capture and storage (BECS) which are similar to air CO_2 capture, but these provide a more economic solution. Optimistic results from [31] provided a possible radiative forcing of $-0.74\ W/m^2$ by 2050. However, the feasibility of many of the proposed solutions is doubtful and subject to uncertainty. Moreoveor, an high demand of land would be required [31]. Concerns are raised upon afforestation (and reforestation) for effects on species diversity due to loss of habitat. Regional impacts would also be observed since terrestrial vegetation is also a source of organic aerosols [32]. Regarding bio-char, long term side effect are expected, such as the final conversion of bio-char in ocean sediments with a small loss of carbon forecast and the darkening of the soil, which would decrease the albedo. Regarding the increase of the ocean carbon sink, the enhancing the solubility pump by increasing dwelling and of the biological pump through the addition of iron are considered. The solubility pump is responsible for the movement of water from low latitudes to high latitudes, providing cooling and absorbing CO_2 before it sinks into the deep ocean. Otherwise the biological pump is driven by the carbon found in biological materials which sinks into the deep ocean [33]. CDR methods aiming to increase ocean reservoirs aim to modify the effects of the pumps and to transport more CO_2 into the deep ocean. Increasing dwelling, according to [34], would be very costly and provide a radiative forcing that could be as low as $-0.0019\ W/m^2$. Otherwise, as shown in [35–37], the addition of iron into areas where it would limit productivity could produce a radiative forcing of $-0.22\ W/m^2$ by 2100. Potential side effects caused by a possible enhancement of the biological pump are the loss of biodiversity and changing emissions of gases and aerosols. Finally, the required ocean acidification is a concern [38]. The return timescale for these type of strategies ranges from weeks to millennia [33]. Finally, the third group of CDR techniques regard the possibility of capturing carbon dioxide from air and storing it in sediments, lithosphere of the deep ocean [39]. Through air capture, it is possible to

create carbon reservoirs of any size [40]. The only limitation of this strategy is represented by the storage capacity of the sink generated. Also, air capture is only in its development phase and materials costs of the infrastructure still need to be addressed [41].

2.2.2 SRM methods

In contrast to CDR techniques, SRM exploits more direct interventions aiming to counter the warming associated with increasing GHG concentrations by reducing the amount of solar energy absorbed. SRM methods include, for example, deploying vast thin-film space mirrors to reduce direct solar insolation and so decrease radiative forcing [42] or injecting scattering aerosols in the stratosphere [43]. These strategies will be discussed in more detail below. Through the description of CDR methods above, it has been pointed out that these methods require long time-scales to deliver a significant reduction in carbon dioxide concentration, while SRM can be considered a relatively fast-acting method, although it does not directly affect the carbon cycle.

However, a general concern with SRM is that its effects will be unevenly distributed across the Earth. Incoming solar radiation is not equally distributed and, since SRM strategies are directly related to the pattern of insolation, when SRM is uniformly applied the poles are left relatively warmer and the tropical regions cooler [44, 45]. This effect would undoubtedly generate adverse impacts of SRM and results suggest a reduction of global precipitation with larger regional variations [45, 46]. More details on regional disparities caused by SRM are given below for each strategy considered.

Moreover, it is worth mentioning that the so-called risk of termination shock is a concern for the deployment of SRM. This effect regards the rapid and harmful rise in temperatures which would be triggered if SRM methods are deployed and then suddenly stopped [47]. Possible events which could cause a sudden interruption of SRM strategies are, for example, wars, political actions, terrorist attacks or natural phenomena. However, as discussed in [47], policies could be considered which make a termination shock less likely.

As discussed in Section 1.1, this thesis focuses on an evaluation of the effects of SRM methods on the climate system using simple climate models and new multi-variable control strategies in order to overcome issues associated with regional disparities.

A summary of the most relevant SRM methods can be found below.

Sun shields in space

The incoming solar radiation can be decreased by deploying large space shields. In [43, 48–50] the possibility of employing space shields for climate engineering near the Sun-Earth L_1 point is explored. In particular, in [50], optimal configurations of orbiting occulting disks were investigated using a globally resolved energy balance model to mitigate regional differences. Moreover, in [43], approximately 10^6 kg small-angle metallic scatterers at L_1 were proposed to scatter rather than directly reflect sunlight.

In a report of the National Academy of Sciences (NAS) [51] the deployment of a space shield in Low-Earth-Orbit (LEO) at an altitude of 200 km was discussed and 55,000 orbiting mirrors of 100 km^2 area each, aligned in random orbits were proposed to counteract climate change from a doubling of atmospheric CO_2.

Moreover, in [52], artificial planetary rings, composed of passive particles or parasols in orbit about Earth were considered to provide shading. Specifically, a one dimensional climate model (10 degrees latitudinal resolution) was employed and it was estimated that a parasol area of 5×10^6 km^2 in an equatorial orbit at 1300-3800 km would be the most useful configuration. According to [53], shields could, in principle, be able to counteract global warming completely within approximately 5 years. However, it is important to remember that these results are affected by uncertainties. Moreover, in reality, because of uncertainties in climate models, in the estimation of radiative forcing and for regional disparities caused by SRM, some excess heat would remain [44]. It is forecast that the deployment of space shields would slow down the hydrological cycle and decrease precipitations of 2% [46, 54]. In particular, in [53] it is found that this effect would be larger over land because elevated CO_2 tends to reduce evapotranspiration. Moreover, regarding regional effects, larger impacts are expected over vegetation. In fact, an over-cooling of the summer and an under-cooling of the winter are foreseen with changes in the plant growing cycle.

This method has been considered in Chapter 8, where strategies for Sun shields deployed in Low Earth Orbit are investigated with latitudinal disparities taken into account.

Stratospheric aerosols

Large volcanic eruptions, such as Mt Pinatubo in June 1991 [55], demonstrated that injecting sulphate aerosols in the lower stratosphere would generate a cooling effect. Analysing the eruptions, it was found that sulphur dioxide in the stratosphere reacts and generates sulphate aerosols which are able to scatter short wave radiation and absorb/emit long wave radiation [56]. Employ-

ing this strategy in simulations, it was estimated that an increase of planetary albedo of 0.012 [21] is required to counteract a doubling of CO_2, although results are affected by uncertainties. The quantity of aerosol required for this task mainly depends on the injection location and size of particles. It was found that the quantity of aerosol required would range between 1.5 Tg S per year and 5 Tg S per year [57, 58]. If smaller particles are employed, a stronger effect could be achieved since these would not affect long wave radiation [56]. However, smaller particles have a shorted lifetime and need to be replaced more often. Lifetime of the particles depends also on the deployment location and lower stratosphere is preferred to the troposphere to have an optimal coverage [57,59]. Also, injection in the troposphere is excluded because of the serious concerns regarding potential impacts on human health [51].

For the injection, artillery guns or balloons have been suggested as a delivery method for SO_2 [55]. Although this strategy show big potential to counteract global warming, it would have significant side effects. It is expected the ozone depletion [55] which would require up to 60 years for the recovery in both hemispheres [60]. Moreover, disruption of monsoons in Asia and Africa is forecast [59] and, also in this case, precipitation over land would decrease. Finally photosynthesis in land and water will be affected.

Further details of the aerosol physics and resulting radiative forcing are reported in Section 3.4.

Enhanced cloud albedo

Another SRM strategy evaluated to counteract radiative forcing regards the increase of reflectivity of marine stratiform clouds through the generation of cloud condensation nuclei (CCN). This strategy would enhance the concentration of cloud droplets and thus of the cloud albedo (Twomey effect) [61, 62]. According to [5], anthropogenic aerosols could currently affect cloud albedo providing a negative radiative forcing of $-0.7\ W/m^2$. However, low confidence is given to this result because of large uncertainties in the aerosol-cloud interaction. In general, cloud albedo can be enhanced mechanically or biologically.

Mechanical processes involve fine sea spray, for example generated by vessels with Flettner rotors which are autonomous and are powered by energy from the wind [63, 64]. A fraction of sea spray would be lifted to provide CCN. The initial concept was discussed in [65] and it was estimated that CCN could be increased by 50-100 % providing a possible increase of cloud albedo of 0.02 and of global albedo of 0.005, which was considered enough to counteract a doubling

of CO_2. However, [21] argued that an increase of 0.074 in the cloud albedo would be required. This argument is due to the large uncertainty in cloud albedo, which ranges between 0.3 and 0.7. Initially, no side effects were found for this strategy [66], but later it has been argued that increasing the reflectivity of clouds would mean that less light reaches the surface and impacts are expected on the ecosystem. Additionally, precipitation could be affected locally.

Cloud albedo can also be increased through biological methods, for example by fertilising areas of the Southern Ocean with iron to stimulate the emission of Dimethylsulphoniopropionate (DMSp) which generates sulphate aerosols [62]. Aerosols deriving from DMSp are in fact the main source of CCN. In [67], it was found that by fertilising the Southern Ocean for 1 month in summer, a regional cooling of 2 degrees could, in principle, be achieved. However, only 50% of the experiments provided good results.

Enhancement of surface albedo

Ideas regarding the increase of surface albedo involve the modification of grassland, croplands, cities and deserts.

Effects of modification of vegetation albedo [68,69] largely depends on the area of the modified surface. In [68], it is estimated that the surface albedo of grasslands can be increased of 25% using bioengineered grasses or variegated plants. This result could provide an annual global average radiative forcing of $-0.56\ W/m^2$. Also, in [69], the TRIFFID vegetation model is employed to find that, increasing the reflectivity of croplands, it could be possible to achieve a radiative forcing of $\approx -0.24\ W/m^2$. Although these methods seem promising, few studies exist thus far and results are considered uncertain and unconvincing [21]. Negative effects of this technique regard the reduction of available light for photosynthesis and thus a reduction of carbon uptake [68].

Moreover, the albedo of human settlement can be increased by the employment of reflective roofs or pavements [68,70]. Again, effects depend on the area where the modification takes place. In particular, in [68] it was found that a globally averaged radiative forcing of $-0.17\ W/m^2$ could, in principle, be achieved providing a worldwide albedo reduction of 0.000875. It is not clear how long the change in albedo would last, but it is expected that this would disappear over time because of the decrease of coating material performance.

Another possibility regards a change of albedo in global desert areas. These regions are of interest because they are uninhabited, flat and in stable conditions [21]. Albedo enhancements

between 0.2 and 0.5 have been forecast and, in [71], a 2% albedo increase (corresponding to a possible radiative forcing of $-2.75\ W/m^2$) was estimated if 4.5 million square miles of desert are covered with reflective surfaces made of white polyethylene on aluminium substrate. However, the authors suggest that both global and regional modelling of the climate should be performed to understand the effects of this technology on temperatures, hydrological cycles and wind patterns. This strong alteration of the surface properties causes the desert to be cooler than before. This effect generates concerns regarding the production of iron from the desert which is of great importance for the ocean. If the productivity of iron decreases then ocean carbon sinks could also be diminished.

2.3 Climate modelling and the role of uncertainties

Climate models were originally employed to reproduce observed surface temperature trends. Afterwards their use has been extended to the forecast of the climate response to changes in the radiative forcing [72].

Many models exist: the simplest energy balance models use only one box to represent the climate system and solve the energy balance problem to obtain the mean global surface temperature. From these simple models, with increased computer speed, complex three-dimensional models with millions of degrees of freedom can provide accurate estimation of the temperature across the Earth's surface, taking into account atmosphere, land, ocean and cryosphere processes, so-called General Circulation Models (GCMs) [26]. Thus, although these models can be physically realistic, they are computationally expensive. In contrast, low order one-dimensional climate models can be found in [73], [74] and [75]. In particular, considering elementary thermodynamics, [73] and [74] proposed low order climate models to investigate the climate state as a function of the solar constant, whereas [75] investigated in detail global energy balance models using a general transport term. Moreover, a Green's function approach is used in [75] to obtain the explicit analytical solution of a diffusive climate model in terms of hyper-geometric functions. Low order energy models are considered in this thesis to take into account the main physical processes that describe the climate system and to efficiently implement closed-loop control strategies.

The components of the climate system present a large range of dynamical timescales, from rapid responses of some radiative feedbacks to millennial scale responses such as those associated with the carbon cycle and ice sheets [76]. Assuming that anthropogenic emissions are suddenly

reduced to zero [77], the climate system would slowly respond until reaching an equilibrium state. However, because of the large timescale of the processes of absorption of CO_2 in the climate system, it could take centuries before reaching a new equilibrium [76]. This behaviour represents an inertia of the climate system to any external change.

Considering a positive change in the radiation budget, while the surface temperature increases, the outgoing radiation increases as well inhibiting the further increase of the temperature [78, 79]. Therefore, a new equilibrium temperature is soon achieved. The most important identifier of climate models is the equilibrium climate sensitivity, which is obtained through an equilibrium climate simulation. Such simulations provide information on the difference between the initial and final states of the model simulated, neglecting the time-dependent response. Assuming a small perturbation of the system, a linear relationship can be considered between the radiative forcing applied and the subsequent temperature change [80].

$$\Delta T = \beta_0^{-1} F \tag{2.1}$$

In general, β_0 in Eq. (2.1) is defined as the climate feedback parameter which depends on the type of forcing applied [81]. The equilibrium climate sensitivity is defined as the equilibrium mean surface air temperature perturbation (ΔT) resulting from a doubling of carbon dioxide radiative forcing above pre-industrial levels [82]. Knowing the equilibrium climate sensitivity is essential for the interpretation of climate models and for future projections in response to a given forcing [78, 80]. However, this quantity is not well known and high uncertainties are carried throughout simulations up to the generation of forecast. Indeed, in [7], several climate models have been compared in order to estimate the correct value for the equilibrium climate sensitivity and it is found that, again, this is an uncertain quantity in the range $1.5°C$ to $4.5°C$.

Managing the uncertainties of the climate system is a significant challenge, specifically because of the multiple spatial and temporal scales involved. Observations may be able to reduce the uncertainties of short timescale processes, but with regards to those processes that occur over longer timescales, the process may require very long observational baselines.

Uncertainty can result from a wide range of sources. Many processes and mechanisms are well understood, but others are not, such as aerosol and clouds effects. The interactions between several climatic and non-climatic influences change with time and lead to high uncertainties [83]. Uncertainties related to climatic influences are, for example, observational uncertainties of an-

thropogenic forcing contributions to temperature increase in Antarctica, or uncertainties due to lack of direct observation of natural phenomena, or large uncertainties in the potential biogeochemical effects and in the evolution of tropical ocean dynamics. Other types of uncertainties are related to the complex interactions between the changing climate and the vulnerability and exposure of people, societies and ecosystems [7].

In the science of climate modelling, uncertainties can be divided into four main categories: uncertainty in radiative forcing, caused by uncertainty on future GHG emissions; uncertainty in the model; climate variability and initial condition uncertainty; and forcing and boundary condition uncertainty [84]. Uncertainty in the climate model is an important contributor to uncertainties in the prediction of the climate response. This is mainly introduced by errors in the representation of the dynamics and physical processes of the climate system and in its response to external forcing. Scenario uncertainties are related to the limited understanding of future emissions, GHG concentration or trends of radiative forcing [85]. Natural variability in the climate does not depend on the presence of radiative forcing [86] and represents the natural variations occurring internal to the climate system. Therefore, it is challenging to quantify and it is affected by high uncertainty.

2.4 Closed-loop climate engineering in MIMO systems

As seen in Section 2.3, uncertainties are a concern in climate modelling. Previous work [1–4, 87] introduced climate engineering strategies in a closed-loop system.

When open-loop strategies are considered, results show significant error in achieving the required climate objectives [1]. Therefore, feedback control strategies are essential to deal with uncertainties and accomplish any SRM strategy [87].

In particular, in [1] an explicit feedback of the observed climate state is implemented in a fully coupled general circulation model of the Earth's climate to manage uncertainty in both the radiative forcing and the climate's dynamic response to this forcing. In [2], a simple PI controller and an H_∞-suboptimal SRM controller are considered in a reduced-complexity climate model MAGICC. Moreover, in [3], a feedback controller is employed to stabilize the global temperature anomaly at $2°C$. Specifically, it is shown that it is possible to achieve a straightforward optimal feedback control design to reflect important aspects of climate mitigation. In particular, in [3], the positioning of closed-loop eigenvalues in the complex plane are considered as a part of the

mitigation debate.

Also, it is important to mention the approach considered in [88], where a model predictive control has been employed. This control method uses a model of the system to predict its future behaviour along a prediction horizon. During every iteration, a finite horizon open-loop optimal control problem is solved using the current state of the plant as the initial state.

In this thesis, closed-loop control strategies are employed to overcome issues related to uncertainties in the climate model employed, the radiative scenarios and the SRM methods considered, such as stratospheric aerosols injection. In particular, effectiveness of an adaptive controller for climate engineering, which involves both feedback and feed forward strategies, is shown for the first time. This is a methodology closely related to the model predictive control employed in [88,89], but as is shown later, adaptive control guarantees convergence through the implementation of the Lyapunov stability criterion. Otherwise, in [88], convergence of the control scheme is not guaranteed when non-stochastic phenomena affect the dynamical system. Further details on the comparison between the adaptive control strategy employed in this thesis and the model predictive control in [88] can be found in Chapters (4,5).

Another issue to deal with regards latitudinal differences due to SRM. In fact, when SRM methods are employed, it is important to assess control strategies taking regional disparities into account. Prior work, where SRM methods are considered using a single control variable, can only influence global dynamics. For this reason other recent work [90–94] has investigated Multi-Input-Multi-Output (MIMO) systems and control strategies to assess latitudinal disparities of SRM. In [95] and [90] an atmosphere-ocean general circulation model (AOGCM) is used to explore the potential of SRM with multiple degrees of freedom. Also, in [91,92,96], injections of sulphate aerosols at multiple locations are considered to reduce incoming solar radiation with a coupled atmosphere-ocean general circulation model. MIMO systems will be considered in this thesis by employing climate models with latitudinal resolution and independent control variables to quickly address regional disparities of SRM.

Thus, closed-loop control strategies for MIMO systems will be developed in this thesis to deal with uncertainties and regional disparities caused by SRM.

Chapter 3

Dynamical models and control techniques

This chapter describes the key technical concepts which are employed in this thesis. These concepts will be adapted later in the thesis to provide the tools necessary to assess climate engineering techniques and, more specifically, issues with regional disparities due to SRM as well as uncertainties in climate modelling.

In this thesis, two different types of energy models are employed to describe the climate system. In Section 3.1, these models are described, forming the baseline for the development of the 3-box model in Chapter 4 and the PDE model in Chapter 6. In Section 3.2, an analytical method for the investigation of the dynamics of the ice line is described. This analysis will be employed in Chapter 7 for the assessment of constraints on SRM used in combination with the PDE model developed in Section 6.2.

Moreover, the concept of radiative forcing due to carbon dioxide and, in particular, the Representative Concentration Pathways (RCPs) are found in Section 3.3. The radiative scenarios described in this section will be employed for the validation of the 3-box model in Section 4.2.1 and to assess the performance of adaptive control in several scenarios in Chapters (4,5).

In this thesis, two particular SRM strategies are investigated: sulphur aerosol injection and the deployment of space shields. In Section 3.4, the dynamics of sulphur aerosols in the stratosphere are described. This allows an estimation of the radiative forcing from aerosol injection, and will be included in the closed-loop control system for the 3-box model in Section 5.4. In Section 3.5, the orbital mechanics required to develop SRM strategies involving space shields are briefly described. In particular, Section 3.5.1 describes the estimation of the position of the shield in space. Also, in Section 3.5.2, orbital perturbations for a high area-to-mass ratio object in Low Earth Orbit (LEO) are investigated and in Section 3.5.3 the Sun's apparent motion around the

Earth is described, which is required to determine the geometry between Sun and shield. These concepts will be later employed in Chapter 8.

Finally, the control strategies employed in this thesis are described in Section 3.6, where the dynamics of PI control (Section 3.6.1), adaptive control (Section 3.6.2) and optimal control (Section 3.6.3) are reported. In particular, optimal control and PI control are considered in Chapter 5 for comparison with adaptive control. Furthermore, in Chapter 6, PI control is considered for estimation of the required insolation reduction in several multi-objective control strategies.

3.1 Energy Models for the climate system

This section describes the dynamics of the energy balance model which is employed to develop the climate model in Chapter 4 for the 3-box model and in Chapter 6 for the PDE model.

The Earth's climate is governed by its energy budget, which is the energy balance between incoming and outgoing radiation. The Sun provides the Earth with an average power of 1370 W/m^2 which is unevenly distributed over all latitudes because of the ellipticity and the tilt of the Earth's polar axis. Moreover, equatorial regions are heated more than the polar regions because of the low incident angle of solar rays at high latitudes. Part of the incoming solar radiation, also termed insolation, is absorbed and distributed between the components of the Earth's climate system. Some solar radiation is partly reflected and absorbed by atmosphere and clouds, and part is re-emitted. When the incoming and outgoing energy are balanced, the Earth's mean temperature remains constant.

The energy balance can be written as the balance between the insolation and the out-going radiation lost to space as a black body [26]:

$$\sigma T^4 = Q_0(1-\alpha) \tag{3.1}$$

where σ is the Stefan-Boltzmann constant, $Q_0 = 1367/4\ W/m^2$ is the mean annual insolation, and α is the mean annual planetary albedo (equal to 0.7) [75]. However, in this model, the Earth is treated as a black body. Considering the atmosphere, a fraction of the incident radiation is absorbed and causes the surface to warm. The warmed surface radiates energy back to space,

primarily in the infra-red (IR) region of the spectrum. Thus, Eq. (3.1) can be re-written as:

$$I_{IR} = Q_0(1-\alpha) \tag{3.2}$$

Following [75] and [73], a valid approximation for the the infra-red radiation is found. In fact, for small perturbations about some level, term I_{IR} in Eq. (3.2) can be written as a linear function of the surface temperature as follows:

$$I_{IR} = a + bT_0 \tag{3.3}$$

where a and b are constants that take into account cloudiness, infra-red absorbing gases and water vapour, deduced from observations. In particular, it is found that the values of a and b providing the best fit for observations in the northern hemisphere are 203.3 W/m^2 and 2.09 $W/m^2/°C$, respectively. Thus, substituting Eq. (3.3) into Eq. (3.1) and solving for T_0 leads to a global mean annual surface temperature of $14.97°C$, which is in agreement with observations [26, 75].

The model described in Eq. (3.1) is a zero-dimensional model since only annual average heat flows are considered. This model can then be improved by including heat transport between latitudes. The energy transported by a latitudinal element to its neighbours due to the movement of geophysical fluids is represented by a diffusion process where the transport is proportional to the gradient of the temperature field. Following [97], a one-dimensional model can be written as:

$$-\frac{d}{dx}D(1-x^2)\frac{dT(x)}{dx} + a + bT(x) = Q_0 S(x)\alpha(x) \tag{3.4}$$

where it is assumed that each term can be represented as a function of the zonally averaged temperature at sea level. This will form the basis of the analysis in Chapter 6.

In Eq. (3.4), x represents the sine of the latitude, and D is the diffusive term for heat transport, which can depend on x. However, considering D dependent on x would noticeably complicate the problem, thus it is usually considered as a free parameter to be adjusted empirically. In [75], it is found that $D = 0.649\ W/m^2/°C$ would provide a matching value of the temperature at the North pole as $-28°C$. The expressions $S(x)$ and $\alpha(x)$ are employed as the latitudinal distribution of insolation and co-albedo, given by [97]:

$$S(x) = 1 + S_2 P(2, x) \tag{3.5}$$

$$\alpha(x) = \alpha_0 + \alpha_2 P(2,x) \tag{3.6}$$

where $S_2 = -0.477$ is a constant, and $P(2,x) = \frac{1}{2}\left(3x^2 - 1\right)$ is the second Legendre polynomial [97]. In Eq. (3.6), $\alpha(x)$ represents the absorption losses due to the planetary albedo and allows the inclusion of ice-albedo feedback in the model. Ice-albedo feedback is a positive feedback which links changes in surface albedo with changes in snow and ice cover. With increasing temperature, the quantity of ice/snow decreases as well as the fraction of insolation absorbed/reflected by the system, therefore reinforcing the warming [98].

In order to avoid a non-physical solution diverging at the poles, it is required that the horizontal flux of heat vanishes at the poles and the equator. This condition is imposed by considering the following boundary condition:

$$-D(1-x^2)^{1/2}\frac{dT(x)}{dx} = 0 \qquad x = 0,1 \tag{3.7}$$

The effect of the heat conduction mechanism in the climate system results in the transport of heat from the equator to the poles, thus warming the poles and cooling the equator. It is important to highlight that the expression employed for the heat transport, given by the first term on the left in Eq. (3.4), is particularly convenient in this case because it represents the physical phenomenon of heat conduction, and therefore assures convergence of the solution.

Considering Eq. (3.6), a good fit for the mean annual values of albedo for the northern hemisphere is obtained by considering $\alpha_0 = 0.681$ and $\alpha_2 = -0.202$ [99]. Thus, the incoming solar radiation inclusive of albedo losses can be found in Fig. (3.1). Although Eqs. (3.5)-(3.6) provide a good fit only for the northern hemisphere, in Fig. (3.1), data has been extended to the southern hemisphere symmetrically for completeness. The plot in Fig. (3.1) is obtained considering the distribution of the function $Q_0 S(x)\alpha(x)$ with the sine of the latitude x and, as expected, it is not uniform over latitude and there is a difference greater than 200 W/m^2 between the annual mean insolation at the equator ($x = 0$) and at the poles ($x = \pm 1$). This phenomenon is key to understanding SRM requirements in order to counteract climate change.

Indeed, since SRM involves a reduction of the incoming solar radiation, its effect is largely dictated by the latitudinal distribution shown in Fig. (3.1). In the following chapters this phenomenon is taken into account in order to estimate the required insolation reduction for several radiative scenarios and to overcome issues related to regional disparities.

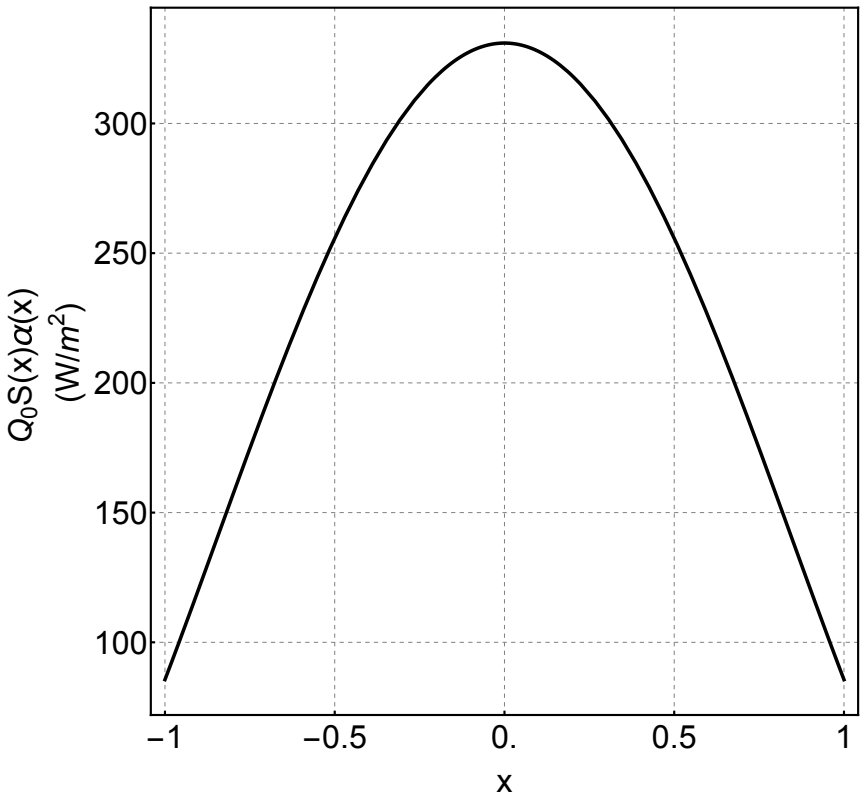

Figure 3.1: Latitudinal distribution of the annual mean insolation according to Eqs. (3.5)-(3.6).

Substituting the expressions considered for $S(x)$ and $\alpha(x)$, the system in Eq. (3.4) can be solved analytically as found in [75]. Equation (3.4) can be written as:

$$L[T] + a = Q_0 S(x)\alpha(x) \tag{3.8}$$

where L is a linear operator in T that can be written as:

$$L[T] = -D\frac{d}{dx}\left[(1-x^2)\frac{d}{dx}T(x)\right] + bT(x) \tag{3.9}$$

This is a non-uniform problem of heat conduction and can be solved with the formalism of the Green's function. Following the process described in [75], considering the boundary conditions in Eq. (3.7), the Green's function associated with the linear operator in Eq. (3.9) can be written as follows:

$$G(x,\xi) = \sum_{n(even)} \frac{(2n+1)P(n,x)P(n,\xi)}{L_n} \tag{3.10}$$

where the summation considers only even values of n. Also, $L_n = n(n+1)D + b$ represent the

eigenvalues associated with the linear operator of the system and $P(n,x)$ is the nth-degree Legendre Polynomial computed in x. Once the Green's function of the problem is known, the formal solution of the system can be written as:

$$T(x) = \int_0^1 G(x,\xi)(S(\xi)\alpha(\xi) - a(\xi))d\xi \tag{3.11}$$

Thus, developing the expression above, it is possible to obtain the latitudinal distribution of the surface temperature in the northern hemisphere.

Finally, the one-dimensional model in Eq. (3.4) can be extended to include time and longitude dependence. As in [75], in this case, an energy storage term depending on the heat capacity is added. The system can then be written as follows:

$$C(x,\ell)\frac{\partial T(x,t)}{\partial t} - D\frac{\partial}{\partial x}(1-x^2)\frac{\partial}{\partial x}T(x,t) + a + bT(x,t) = Q_0 S(x,t)\alpha(x,t) \tag{3.12}$$

where C is the heat capacity which, in general, depends on latitude x and longitude ℓ. According to [75], C can be expressed in terms of the infra-red parameter b and it is given by $0.16b$ years over land and $4.7b$ years over the ocean mixed layer. Also, in Eq. (3.12), terms for insolation and surface albedo depend on time, providing the possibility of including seasonal effects in the model.

The analytical expressions for $S(x,t)$ and $\alpha(x,t)$ that include seasonal effects are found in [75] and are summarised as follows:

$$S(x,t) = 1 + [0.006\ sin(2\pi t) - 0.796\ cos(2\pi t)]\,x - 0.477\ P(2,x) \tag{3.13}$$

$$\alpha(x,t) = 1 - \left(\frac{1}{100}[31.9 + (7.2\ cos(2\pi t) + 5.4\ sin(2\pi t))\,x + 20.2\ P(2,x)]\right) \tag{3.14}$$

where t is the time in years. Thus, the distribution of the insolation inclusive of albedo losses (the function $Q_0 S(x,t)\alpha(x,t)$) with time and latitude can be found in Fig. (3.2). In particular, for the southern hemisphere, the same functions are employed with a lag of 6 months [75].

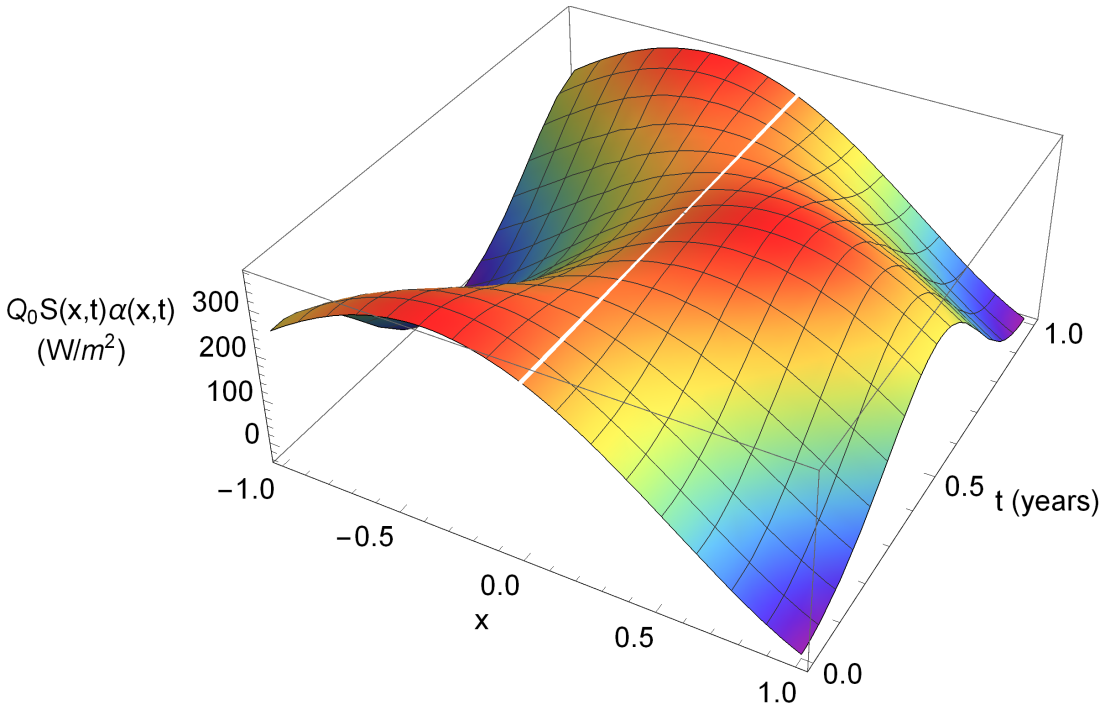

Figure 3.2: Distribution of seasonal insolation with latitude according to Eqs. (3.13)-(3.14).

3.2 Dynamics of the ice line

In this section the main principles required to investigate the dynamics of the ice line will be described, and used later in Chapter 7.

The ice line is defined as the latitude where the temperature reaches $T_s = -10°C$ and it is assumed that when the temperature is equal to or less than T_s the surface is ice-covered and higher surface albedo is expected. The term "ice-covered" represents one of the two stable equilibrium states of the climate system [100]. In the current climate state the ice line is at $x = x_{s0} = 0.95$ [75]. Considering the stationary perturbation theory in [75], it is possible to determine the variation of the ice line given a small perturbation in radiative forcing. As in [101], the temperature at the perturbed ice line is obtained by expanding the ice line condition to first order in small quantities as in Eq. (3.15):

$$T(x_s + \delta x_s, t) = T(x_s, t) + \left(\frac{\partial T}{\partial x}\right)_{x_s} \delta x_s \tag{3.15}$$

where $T(x_s,t) = T(x_s,\infty) + \delta T(x_s,t)$, δx_s is the variation of the ice line latitude and $T(x,\infty)$ is the temperature field at latitude x at equilibrium, i.e. for $t \to \infty$. Because of the ice line condition, Eq. (3.15) can also be written as $T(x_s + \delta x_s, t) = T_s = T(x_s,\infty)$, therefore the variation of the ice

line latitude is given by [101]:

$$\delta x_s(x,t) = \frac{\delta T(x,t)}{\left(\frac{\partial T(x,\infty)}{\partial x}\right)_{x_s}} \tag{3.16}$$

Thus, considering Eq. (3.16) in the time-dependent energy balance equation (Eq. (3.12)), a solution of the following form is expected:

$$\delta T(x,t) = \delta T(x) e^{-\lambda t/C} \tag{3.17}$$

where λ is the stability eigenvalue of the equilibrium solution $T(x,t)$ under a perturbation δT. Following the stationary perturbation theory in [75], the analytical expression of $\delta T(x)$, which includes the effect of the ice line shift, as a function of a generic small perturbation can be written as:

$$\delta T(x) = \int_{x_0}^{x_1} G_Z(x,\xi)\, U(\xi) d\xi \tag{3.18}$$

where U is the radiative forcing perturbation that causes the ice line shift. For the equator and the pole, respectively, the limits are set as $x_0 = 0$ and $x_1 = 1$. The term $G_Z(x,\xi)$ in Eq. (3.18) is given as follows:

$$G_Z(x,\xi) = G(x,\xi) + \frac{dx_s}{dQ} \frac{Q_0}{\left(S(x_{s0})\alpha(x_{s0})\right)} \left[\int_{x_0}^{x_1} G(x,\xi) S(\xi) \frac{\partial \alpha(\xi, x_{s0})}{\partial x_s} d\xi\right] G(x,\xi) \tag{3.19}$$

where G_Z represents the temperature response to a ring of heat added/subtracted at a given latitude and includes the effect of the ice line shift to first order, as found in [75]. In Eq. (3.19), the integral term represents the contribution of the ice-albedo feedback which is multiplied by the slope of the ice line dx_s/dQ.

The denominator of Eq. (3.16) depends on the stability eigenvalue λ and can be computed as follows:

$$\left(\frac{\partial T(x,\infty)}{\partial x}\right)_{x_{s0}} = \int_{x_0}^{x_1} G_\lambda(x_{s0},\xi) Q_0 S(\xi) \frac{\partial \alpha}{\partial x_s}(\xi, x_{s0})\, d\xi \tag{3.20}$$

where G_λ is a generalisation of G (see Section 3.1) and is given as:

$$G_\lambda(x,\xi) = \sum_{n=1}^{\infty} (2n+1) \frac{P(n,x)P(n,\xi)}{L_n - \lambda} \tag{3.21}$$

As can be seen in the expression above, $G_\lambda(x,\xi)$ is a continuous function of λ, except at the eigenvalues of L where it is not defined [75].

In order to understand the meaning of λ it is necessary to consider the linear stability of the 1-D model in [75]. A transcendental equation, which is satisfied only for the stability eigenvalues λ, can be developed and written as follows [75]:

$$\frac{dQ}{dx_s}(x_{s0}) = \lambda \frac{Q_0^2}{a+bT_s} \sum_n \frac{bS(x_s)\left(P(n,x_s)\right)^2}{L_n(L_n-\lambda)} = F_\lambda \tag{3.22}$$

where $L_n, P(n,x)$, a and b are given in Section 3.1 and the function F_λ is given by the right-hand side of Eq. (3.22). Again, this analysis is used later in Chapter 7.

3.3 Radiative forcing scenarios

As discussed in the previous sections, the climate system can be described by an energy balance model. If the incoming and outgoing radiation are balanced, a mean annual temperature of $14.9°C$ is maintained. However, climate change, and in particular the increasing concentration of carbon dioxide in the atmosphere, generates a radiative forcing leading to temperature anomalies. The relationship between the concentration of atmospheric carbon dioxide and the radiative forcing generated is given as follow [102]:

$$F_{CO_2} = \frac{F_{2xCO_2}}{ln(2)} ln\left(\frac{cc(t)}{cc_0}\right) \tag{3.23}$$

where F_{2xCO_2} is the radiative forcing associated with a doubling of CO_2 equal to 3.71 W/m^2 [26], cc_0 is the CO_2 concentration during pre-industrial times (278 ppm in 1775 [103, 104]) and cc_t is the CO_2 concentration at time t.

Moreover, long-term simulations have allowed the use of historical data to develop and update future projections. Therefore, it has been possible to reconstruct and simulate past climate conditions. On the basis of reconstructed data, forecasting of future emissions becomes possible. In particular, four scenarios for future radiative forcing due to GHGs and aerosols have recently been developed, i.e. the Representative Concentration Pathways (RCPs) [105], which can be found in Fig. (3.3). These scenarios are developed in [106] considering atmospheric concentration observations and emissions estimates for greenhouse gases between 1750 and 2005. In

particular, in [106], the reduced-complexity carbon cycle climate model MAGICC6 is employed to emulate the average response of models assessed in the IPCC Fourth Assessment Report. These scenarios provide assessment of future radiative forcing under unpredictable and uncertain conditions. The forcing scenarios are used to estimate future changes in climate forcing and provide useful references in order to compare different climate models. RCPs consider all sources of anthropogenic GHG emissions to describe the four radiative scenarios providing projections of GHGs concentrations, emissions of air pollutants such as aerosols and land use data. Carbon dioxide (CO_2) represents about 80 to 90% of the total anthropogenic forcing in all RCP scenarios up to the end of the 21st century.

The RCP scenarios are identified by stabilisation in terms of radiative forcing achieved at 2100. In fact, the weakest scenario, RCP2.6 has a peak forcing of 3 W/m^2 and then decreases to approximately 2.6 W/m^2 by 2100; the medium-low RCP4.5 and the medium-high RCP6.0 show stabilisation at 2100 of 4.5 and 6 W/m^2, respectively; and the most challenging scenario, RCP8.5 implies a radiative forcing of 8.5 W/m^2 at 2100 [9]. Thus, as can seen from Fig. (3.3), the most encouraging scenario is represented by RCP2.6, which considers effective mitigation of GHGs, followed by the RCP4.5 which considers a low-level mitigation strategy, whereas, the other two scenarios take very high GHG emissions into account and no mitigation is assumed [7]. The temperature change foreseen for the four scenarios is in the range $(0.3°C - 1.7°C)$ for RCP2.6, $(1.1°C - 2.6°C)$ for RCP4.5, $(1.4°C - 3.1°C)$ for RCP6.0 and $(2.6°C - 4.8°C)$ for RCP8.5 [76]. These Scenarios will be used in Chapter 4 and Chapter 6.

It is important to underline that these are one of the few radiative scenarios available and it was chosen amongst others because most of the literature employed in this research (for comparisons and validations of climate models and control strategies) uses RCP radiative scenarios. However, it is worth mentioning that there is a newer database named SSP (Shared Socioeconomic Pathways) [107, 108]. The SSPs are part of a new framework that the climate change research community has adopted to facilitate the integrated analysis of future climate impacts. In these scenarios, climate forcing is combined with socio-economic conditions. These two factors allow the evaluation of mitigation, adaptation and residual climate damage.

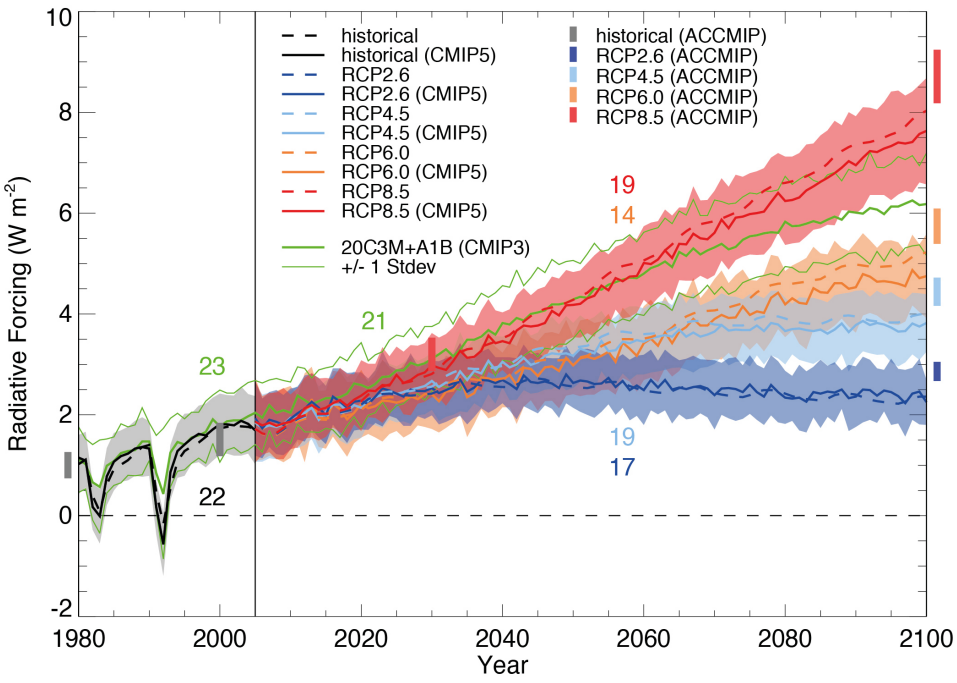

Figure 3.3: Trend of the Representative Concentration Pathways (RCPs) with related uncertainties as defined by Integrated Assessment Model (IAM)-based estimates. Figure reprinted from *Long-term Climate Change: Projections, Commitments and Irreversibility*. Fifth Assessment Report of the Intergovernmental Panel on Climate Change (IPCC), 2013, Retrieved from https://www.ipcc.ch/. Copyright (2013) by Cambridge University Press, Cambridge, United Kingdom and New York, NY, USA.

3.4 Stratospheric aerosol injection

Solar Radiation Management (SRM) techniques involve the intentional manipulation of the planetary surface or atmospheric albedo. SRM does not directly impact effects of elevated atmospheric CO_2 in the carbon cycle, but can affect the carbon and other biogeochemical cycles indirectly through their climate effects [109].

In this thesis, strategies such as the injection of scattering aerosols in the stratosphere [43] and the deployment of vast thin-film space reflectors to reduce direct solar insolation [42] are considered to reduce radiative forcing.

In this section, the main features of stratospheric aerosols injection are assessed. Sulphate Aerosols (SAs) are fine solid particles of a sulphate solution that are produced by reactions in the atmosphere from gaseous precursors. The main natural precursors are sulphur dioxide (SO_2) from volcanoes and anthropogenic sources and dimethylsulphide (DMS) from the terrestrial biosphere [110].

The injection of sulphur particles would essentially mimic the atmospheric effects that follow volcanic eruptions. The eruption of Mount Pinatubo in the Philippines in 1991 provided a good example of the effect of sulphur injection. This eruption is, in fact, often cited as the inspiration for this concept. Following the eruption, massive quantities of particulate matter and sulphur dioxide were ejected into the atmosphere. This aerosol layer was reported to have lowered average temperatures around the globe by about 0.5 degrees over the following three years.

SAs are able to interact with solar radiation through both absorption and scattering. When injection of sulphate aerosols into the stratosphere takes place, two main effects can be considered: the direct effect of the aerosol, given by the aerosol-radiation interaction, and the indirect Twomey effect [111] due to aerosol-cloud interactions. However, only direct radiative forcing is considered in this thesis because of large uncertainties in the modelling of aerosol-cloud interaction. The dynamical processes of atmospheric aerosols can alter their particle size distribution. Here, the model employed aims to reproduce aerosol behaviour after injection into the stratosphere in three latitude bands in Chapter 4 and then to compute the resulting radiative forcing.

The aerosol column in the stratosphere modifies incoming solar radiation. In order to quantify this effect, the direct radiative forcing ΔF as a function of time is computed through Eq. (3.24) [112]:

$$\Delta F = \frac{Q_0}{2} \mathcal{T}_a^2 (1 - A_c) \omega \beta (1 - R_s)^2 \tau(t) \tag{3.24}$$

The direct radiative forcing depends on the properties of the incident radiation, atmospheric optical properties (atmospheric transmission $\mathcal{T}_a = 0.76$, fractional cloud cover $A_c = 0.6$ and surface reflectance $R_s = 0.15$ [112]) and aerosol optical properties (single scattering albedo ω, aerosol optical depth $\tau(t)$, average up-scatter fraction β). In particular, the aerosols optical depth includes a time decay and latitudinal diffusion of particles and provides direct information regarding the influence of aerosols on radiative forcing.

The required radiative forcing through the aerosol optical depth can then be converted to an aerosol mass concentration (g/m^3) through Eq. (3.25) [113]:

$$M_a(t) = \frac{\tau(t)}{\int_{r_0}^{r_f} N(r)\, dr\, E_{ext}\, z} \tag{3.25}$$

or, as more commonly found in literature, the aerosol number density ($1/m^3$):

$$N_a(t) = \frac{M(t)}{\int_{r_0}^{r_f} \frac{4}{3}\pi(2r)^3 \rho \; N(r) \; dr} \tag{3.26}$$

where, r_0 and r_f define the range of particle radii set respectively to 0.1 μm and 1 μm. Additionally, ρ is the aerosol density (2 g/cm^3), z is the altitude of injection and E_{ext} is the extinction parameter which can be estimated through Mie Theory and for aerosol particles is usually given by 3.5 m^2/g [111].

In Eqs. (3.25)-(3.26), $N(r)$ represents the aerosol size distribution. Once precursors of the aerosol particles are injected in the stratosphere, the particles formed have a range of sizes, so the log-normal size distribution function $N(r)$ given is employed [114]:

$$N(r) = \frac{N_0}{\sqrt{2\pi}\; ln(\sigma)} \exp\left[-\frac{\left(log(r) - log(r_m)\right)^2}{2\; ln^2\sigma}\right] \tag{3.27}$$

where N_0 ($1/m^3$) is the number density of particles of mean radius $r_m = 0.05\ \mu m$ and standard deviation $\sigma = 2.03\ \mu m$ [57].

In particular, regarding the injection of aerosol particles, in [91, 92] a coupled atmosphere-ocean general circulation model with fully interactive stratospheric chemistry is employed to simulate aerosol injections at multiple locations to meet multiple simultaneous surface temperature objectives. Moreover in [96], multiple injection strategies are considered to achieve a desired radiative forcing profile using a two-dimensional chemistry-transport-aerosol model.

The production of such an artificial aerosol layer could be accomplished by releasing sulphur particles into the stratosphere from aircraft or by dispersing them from balloons. The required altitude to enter the stratosphere would be 11 km at the poles or 17 km at the equator [55]. Existing civil aircraft could be modified at relatively low cost to deliver sufficient amounts of the required material [115], whereas military cargo planes would have a limited payload for this task [116]. Moreover, while aircraft exhausts would also produce additional forms of pollution, this could potentially be avoided through the use of ground-based artillery (such as electromagnetic railguns) [116]. Finally, high-altitude balloons can in principle be used to lift precursor gases. However, thus far, no balloon has ever been deployed to the necessary altitude [57].

3.5 Orbital dynamics for space shields

3.5.1 Orbital parameters and Earth Centred Reference Frame (ECRF)

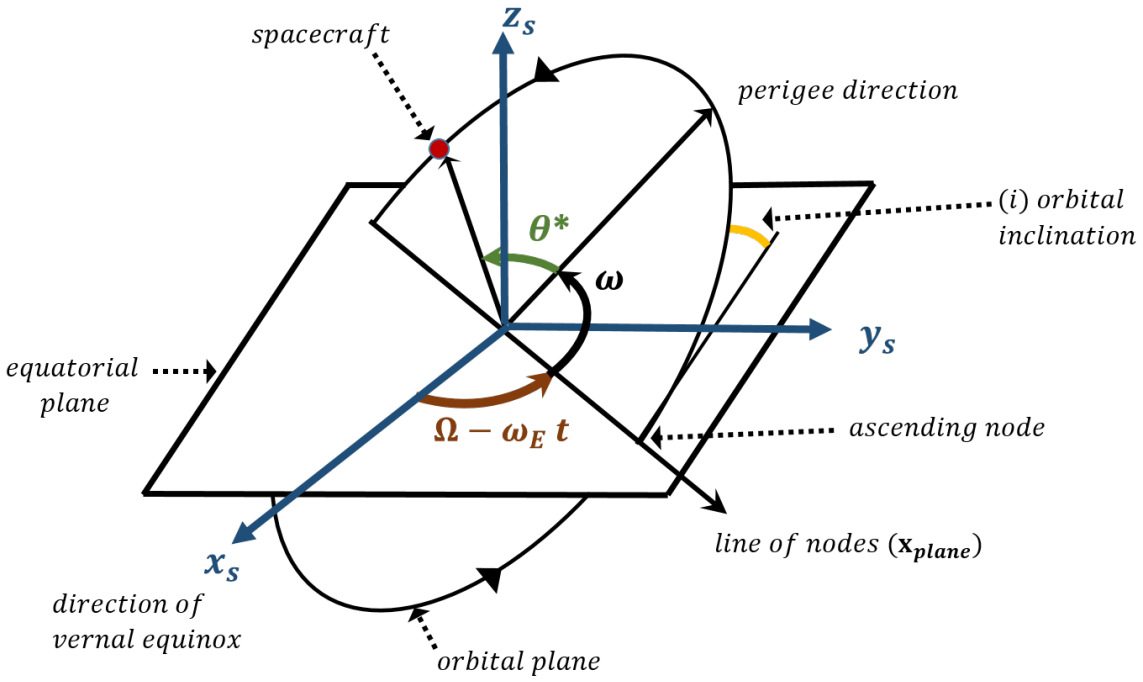

Figure 3.4: Representation of the orbital elements and the orbital plane with respect to the equatorial plane.

In this section, key elements of orbital dynamics will be considered and used later in Chapter 8. Considering a spacecraft which is in an elliptical orbit around the Earth with semi-major axis a, eccentricity e, orbit inclination i, longitude of ascending node Ω and argument of perigee ω, the true anomaly θ^* can be found as [117]:

$$sin(\theta^*) = (\frac{(\sqrt{1-e^2})sin(E(t))}{1 - e\ cos(E(t))} \tag{3.28}$$

$$cos(\theta^*) = (\frac{cos(E(t)) - e}{1 - e\ cos(E(t))} \tag{3.29}$$

In Eqs. (3.28)-(3.29), $E(t)$ is the eccentric anomaly found by solving Kepler's equation: $M(t) =$

$E(t) - e\ sin(E(t))$, where $M(t) = n_0(t - t_0)$ is the mean anomaly of the spacecraft at time t (t_0 initial time, $n_0 = \sqrt{\frac{\mu_E}{a^3}}$ is the mean motion with $\mu_E = 398600.4\ km^3/s^2$ the Earth's planetary constant [118]). As can be seen in Fig. (3.4), the true anomaly describes the angular position of the spacecraft in orbit measured from the perigee. Thus, considering the geometry described in Fig (3.4), the projection of the spacecraft position on the equatorial plane is given by:

$$x_{plane} = r(t)\ cos(\theta^*(t) + \omega) \tag{3.30}$$

$$y_{plane} = r(t)\ sin(\theta^*(t) + \omega) \tag{3.31}$$

Thus, the components of the position vector in an Earth Centred Rotating Frame can be written as:

$$x_s = x_{plane} cos(\Omega - \omega_E t) - r(t) - y_{plane} cos(i) sin(\Omega - \omega_E t) \tag{3.32}$$

$$y_s = x_{plane} sin(\Omega - \omega_E t) + r(t) + y_{plane} cos(i) cos(\Omega - \omega_E t) \tag{3.33}$$

$$z_s = y_{plane} sin(i) \tag{3.34}$$

where $r(t) = a[1 - e\ cos(E(t))]$ is the distance between the spacecraft and the Earth's centre at time t. Again, these expressions will be used later in Chapter 8.

3.5.2 Orbital perturbations

In this section, orbital perturbations due to the effect of the Earth's oblateness and solar radiation pressure (SRP) are investigated. These perturbations are crucial for the estimation of the actual position of a spacecraft in orbit. In particular, SRP perturbations are not negligible for high area-to-mass ratio objects such as large reflective space shields, as is considered in Chapter 8.

The three components of the acceleration perturbation due to SRP along the radial, transversal and normal direction can be written as [119]:

$$a_{SRP_R} = a_{SRP_0} \left\{ sin(\delta) \left[cos(\Omega) cos(\lambda_\odot) + sin(\Omega) sin(\lambda_\odot) cos(\epsilon) \right] + cos(\delta) sin(\lambda_\odot) sin(\epsilon) \right\} \tag{3.35}$$

$$a_{SRP_T} = a_{SRP_0}\left\{sin(\lambda_\odot)cos(\Omega)cos(\epsilon) - cos(\lambda_\odot)sin(\Omega)\right\} \tag{3.36}$$

$$a_{SRP_H} = a_{SRP_0}\left\{-cos(\delta)\left[cos(\Omega)cos(\lambda_\odot) + sin(\Omega)sin(\lambda_\odot)cos(\epsilon)\right] + sin(\delta)sin(\lambda_\odot)sin(\epsilon)\right\} \tag{3.37}$$

with $a_{SRP_0} = P_{SRP}\, C_r \frac{A_M}{m} sin^2(\gamma)$, where P_{SRP} is the solar pressure at 1 AU equal to 4.56×10^{-6} N/m^2 [120] and C_r is the reflectivity coefficient given by $1 + r_{sp}$ where r_{sp} is the reflectivity of the space shield material [121]. Also, A_M/m is the area-to-mass ratio of the reflector and γ is the incident angle (defined as the angle between incoming and reflected solar radiation).

Moreover, in Eqs. (3.35)-(3.37), δ is the spacecraft's declination that locates its position on the celestial sphere in the equatorial coordinate system. In particular, as can be seen in Fig. (3.5), the declination's angle is measured north or south of the celestial equator, along the hour circle defined by the right ascension (RA). Thus, considering Figs. (3.4) and (3.5), the declination can be written as:

$$\delta = arcsin\left[sin(i)sin(\theta^*(t))\right] \tag{3.38}$$

Also, $\lambda_\odot$ is the Sun's true ecliptic longitude described in Section 3.5.3, ω_E is the Earth's angular rate and ϵ is the ecliptic obliquity equal to 23.44°. The time dependency of terms δ and $\lambda_\odot$ is omitted in the expressions above for completeness.

With regards to the Earth's oblateness perturbations, two phenomena need to be taken into account: regression of the nodes and orbit precession. Thus, as found in [122], J_2 secular effects on Ω and ω can be written as:

$$\dot{\Omega}_{J_2} = -\frac{3}{2}\frac{J_2 R_E^2}{\bar{p}^2}\bar{n}cos(\bar{i}) \tag{3.39}$$

$$\dot{\omega}_{J_2} = \frac{3}{2}\frac{J_2 R_E^2}{\bar{p}^2}\bar{n}\left(2 - \frac{5}{2}sin^2(\bar{i})\right) \tag{3.40}$$

where the overbar represents the mean value of the parameter as can be found in [123]. Also, J_2 is the oblateness parameter (1.083×10^{-3}), R_E is the Earth's radius and $p = a(1-e^2)$ is the semi-parameter.

Equations (3.39-3.40) represent secular variations, due to the geopotential term J_2, of the

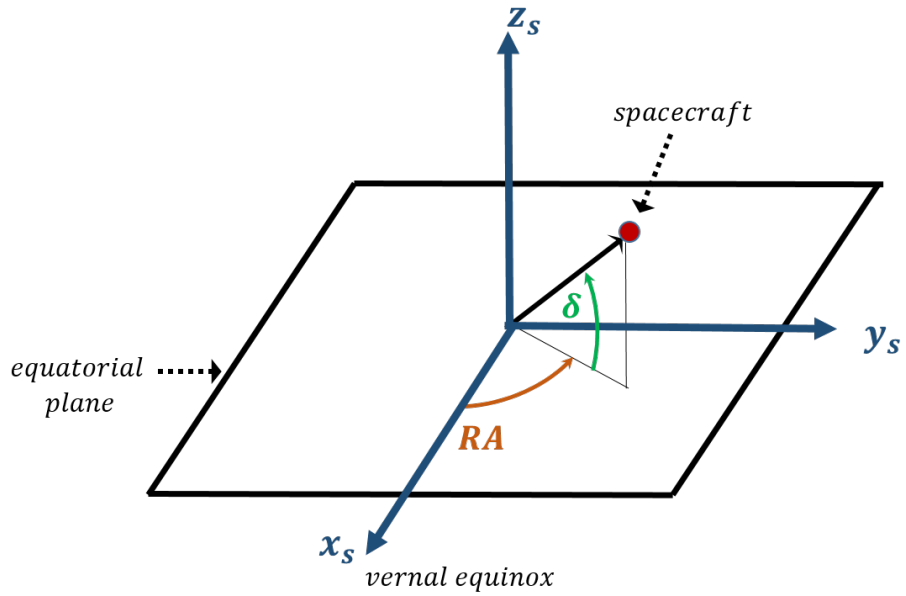

Figure 3.5: Representation of the spacecraft position in spherical coordinates on the celestial sphere.

longitude of ascending node and the argument of perigee of the orbit, respectively. In addition, small cyclic variations of semi-major axis, eccentricity and inclination are observed but they are not relevant when simulations are performed over a long duration.

3.5.3 The Sun's apparent motion around the Earth

The estimation of Sun's position in orbit with respect to Earth is required to estimate the grade of obscuration of solar shields in space in Chapter 8.

Given a Julian Ephemeris Date JD, it is possible to estimate the position of the Sun in ecliptic coordinates. Thus, time T, measured in Julian Centuries of 36525 ephemeris days from the epoch J2000.0 (2000 January 1.5 TD) is given by:

$$T = \frac{JD - 2451545.0}{36525} \tag{3.41}$$

where 2451545.0 is the Julian date corresponding to 2000 January 1.5. Then, the geometric mean longitude of the Sun, referred to the mean equinox of the date, can be written as:

$$L_0 = 280.46645° + 36000.76983°T + 0.0003032°T^2 \tag{3.42}$$

The mean anomaly of the Sun is then given by:

$$M = 357.52910° + 35999.05030°T - 0.0001559T^2 - 0.00000048T^3 \tag{3.43}$$

with L_0 and M constrained in the range $0° - 360°$. Then, the Sun's equation of centre C can be obtained as follow:

$$\begin{aligned} C = &\left(1.914600° - 0.004817°T - 0.000014°T^2\right) sin(M) + (0.01993° - 0.000101°T) sin(2M) \\ &+ 0.000290° sin(3M) \end{aligned} \tag{3.44}$$

where C provides the angular difference between the actual position of a body in its elliptical orbit and the position it would occupy if its motion was uniform and in a circular orbit of the same period. Then, the Sun's true ecliptic longitude and declination can be written as:

$$\lambda_\odot = L_0 + C \tag{3.45}$$

$$\delta_\odot = arcsin\left[sin(\epsilon) sin(\lambda_\odot)\right] \tag{3.46}$$

Once the Sun's true longitude and declination are known, it is possible to evaluate the Sun's rectangular equatorial coordinates as follow:

$$\mathbf{X}_\odot = \begin{pmatrix} x_\odot \\ y_\odot \\ z_\odot \end{pmatrix} = \begin{pmatrix} cos(\delta_\odot) cos(\lambda_\odot - \omega_E t) \\ cos(\delta_\odot) sin(\lambda_\odot - \omega_E t) \\ sin(\delta_\odot) \end{pmatrix} \tag{3.47}$$

Again, these key results is used later in Chapter 8.

3.6 Control techniques

3.6.1 PI control

In this section, a feedback control strategy designed with an unconstrained linear quadratic regulator (LQR) optimisation method is described, as is used in Chapter 5.

In common with other (single input) control analyses [1,4], a PI controller can be employed to design a feedback control scheme. The PI parameters can be obtained by LQR optimisation [124] which solves the algebraic Riccati equation. The LQR method aims to minimise a cost function J in Eq. (3.48) subject to the constraint $\dot{\mathbf{x}} = A\mathbf{x} + \mathbf{F} + B\mathbf{U}$ represented by the system's dynamics, where $\mathbf{x}$ is the state vector, $\mathbf{F}$ is the vector of external forcing, B is the control distribution matrix and $\mathbf{U}$ is a generic control vector. The cost function J is now defined as:

$$J = \int_0^\infty \left(\mathbf{x}^T Q\mathbf{x} + \mathbf{U}^T R\mathbf{U}\right) dt \tag{3.48}$$

where Q and R are positive definite weighting matrices. In particular, Q weights the state vector $\mathbf{x}$ and R weights the control effort. If R is large, the cost function is dominated by the control effort $\mathbf{U}$, otherwise when R is small J is dominated by the state error $\mathbf{x}$.

It is found that the optimal expression for the control $\mathbf{U}$ is given by [124]:

$$\mathbf{U}^* = -\left[R^{-1}B^T P\right]\mathbf{x} = -[K]\mathbf{x} \tag{3.49}$$

where P is the steady-state solution of the Riccati equation $PA + A^T Px + Q - PBR^{-1}B^T P = 0$.

Through the LQR method the poles of the closed-loop system are placed in stable, suitably-damped locations in the complex plane. The method also guarantees a phase margin larger than 60 degrees. Thus, the outputs of the process are the static gain matrix $K = \left[K_P\ K_I\right]$ and the control law which can be written as:

$$\mathbf{U} = -K_P\,\mathbf{x} - K_I \int_0^t \mathbf{x}\, dt \tag{3.50}$$

where K_P and K_I are proportional and integral gain matrices, respectively.

The controller matrices Q and R are regulated to achieve the required objective, i.e. the minimisation of the temperature anomaly, and so control the state vector. In particular, this PI controller is used in this thesis as a benchmark to compare results with adaptive control. This is

considered a valid choice because PI control is widely used for closed-loop control systems in climate engineering as explained in Sec. (2.4).

It is worth noting that, as will be seen in Chapter 5, matrices K_p and K_i are designed through the LQR method for a generic case where the temperature anomaly needs to be minimized in all latitudinal bands. After that, the same controller is tested in cases when changes occurs in either the plant model, or in the actuator dynamics, or in case of sudden perturbations. It needs to be highlighted that the controller has not been modified purposely for these new simulations in order to have insight on the sensitivity of PI control.

3.6.2 Adaptive control

The adaptive controller used later in Chapter 4 and Chapter 5 is the direct model reference adaptive control (MRAC) [125, 126]. As shown in Fig. (3.6), the main elements of this controller are: (1) a reference model which specifies the desired response to external commands; (2) a plant model whose general structure is known but its parameters are uncertain; (3) a controller that provides tracking; (4) adaptation laws to adjust the parameters of the control law during the process (feedforward and feedback).

This specific adaptive control technique has been selected against other robust control methods because of its simplicity and clear connection with the real world as well as the additional analytical insight it provides.

The goal of the MRAC is to create a closed loop controller with parameters that can be updated to change the response of the uncertain system to that of an ideal model.

The relationship between the key components of this controller and the real world can be easily outlined. The reference model in Fig. (3.6) represents the real world which is unknown, whereas the 3box model is a simplified model, whose structure represents current understanding of the general processes occurring in the real world, but its parameters are unknown. The adaptive control laws aim to minimize the difference between the real world model and the simple 3-box model. Therefore, model parameters are implicitly estimated and updated during every iteration, taking into account external inputs (CO_2 radiative forcing given by $r(t)$ in Fig. (3.6)), error between real world model and 3-box model (error term e) and uncertainties. Thus, this controller can then be considered a close relative of the model predictive controllers used in [88, 89]. However, an important difference between the two approaches needs to considered. In fact, as showed

in this section, convergence of the adaptation laws employed here is guaranteed through the Lyapunov stability criterion, whereas the same cannot be said for the method employed in [88, 89] (more details in Section 4.4).

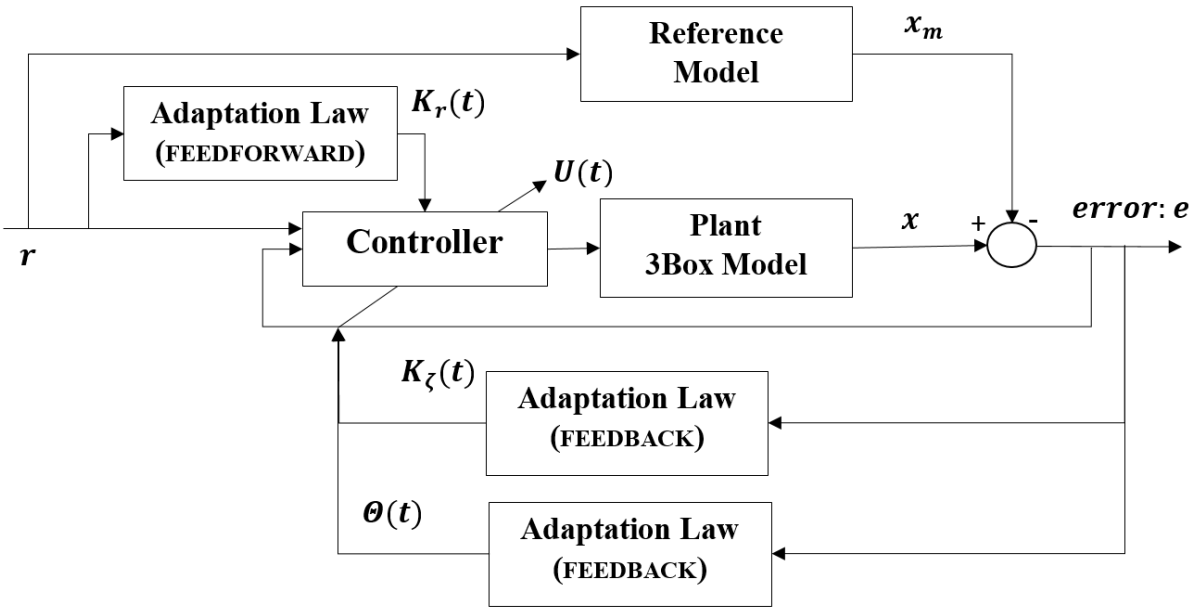

Figure 3.6: Model Reference Adaptive Control (MRAC) scheme.

Consider a system (given by the reference model in Fig. (3.6)) where the system matrix A_m and the output $\mathbf{x_m}$ are unknown and a stable system (given by the model provided to describe the dynamics) whose system matrix A and output $\mathbf{x}$ are provided. The goal is to find a control law $\mathbf{U}$ such that the error $\mathbf{e}$ in Fig. (3.6) between the output of the dynamical model ($\mathbf{x}$) and the reference model ($\mathbf{x_m}$) vanishes when $t \to \infty$. The known system employed to describe the dynamics is uncertain and can be written as:

$$\dot{\mathbf{x}} = A\mathbf{x} + B(\mathbf{U} + \Theta^T \mathbf{x}) + \mathbf{w} \tag{3.51}$$

where the term $\Theta^T \mathbf{x}$ is now used to match the uncertainties of the system, where Θ is an unknown parameter matrix that is part of the control law (see Eq. (3.52)) and $\mathbf{w}$ is a bounded disturbance.

The adaptive control law is parametrised as follows:

$$\mathbf{U} = K_x^T \mathbf{x} + K_r^T \mathbf{r} - \Theta^T \mathbf{x} \tag{3.52}$$

where K_x, K_r and Θ are the dynamical gain matrices whose parameters are estimated at each iteration and $\mathbf{r}$ is the external forcing.

This controller does not provide an explicit estimation of the plant parameters, but it is possible to show how these are updated at each iteration. Substituting Eq. (3.52) in Eq. (3.51) it is found that:

$$\dot{\mathbf{x}} = \left(A + BK_x^T\right)\mathbf{x} + BK_r^T\mathbf{r} + \mathbf{w} \tag{3.53}$$

Thus, as for any feedback controller, the plant dynamics, represented by A, are modified by term BK_x^T. However, in this case, as in [88, 89], matrix K_x is propagated with time according to its own dynamics (as will be seen later). Therefore the plant parameters are modified during every iteration. The main difference with respect to the approach employed in [88, 89] is that the Lyapunov stability criterion is used here to find laws for the controller matrices which guarantee asymptotic stability.

Moreover, it is worth noting that term $-\Theta^T\mathbf{x}$ is employed to deal with large uncertainties.

Thus, to estimate the dynamics of the controller matrices through the Lyapunov criterion, the error between the 3-box model and the reference model needs to be computed. According to [125], it can be shown that the error dynamics can be written as follow:

$$\dot{\mathbf{e}} = \dot{\mathbf{x}}(t) - \dot{\mathbf{x}}_m(t) = A_m\mathbf{e} + B\left(\Delta K_x^T\mathbf{e} + \Delta K_r^T\mathbf{r} + \Delta\Theta^T\mathbf{e}\right) \tag{3.54}$$

where $\mathbf{x_m}$ and A_m are the unknown state vector and the unknown system matrix of the reference model (see Fig. 3.6). Also, ΔK_x, ΔK_r and $\Delta\Theta$ are given by the difference between the estimated and the ideal gain matrices.

Through the method of Lyapunov [125,127] it is possible to choose adaptive laws, i.e. control laws to suitably update the gain matrices at each iteration. These adaptive laws are chosen such that the time-derivative of a Lyapunov function decreases along the error dynamics trajectory.

The Lyapunov function candidate for the design of an MRAC system of 3^{th} order is given by:

$$V(\mathbf{e}, \Delta K_x, \Delta K_r, \Delta\Theta) = \mathbf{e}^T P\mathbf{e} + Tr\left[\Delta K_x^T\Gamma_x^{-1}\Delta K_x\right] + Tr\left[\Delta K_r^T\Gamma_r^{-1}\Delta K_r\right] + Tr\left[\Delta\Theta^T\Gamma_\theta^{-1}\Delta\Theta\right] \tag{3.55}$$

where Γ_x, Γ_r and Γ_θ are symmetric positive definite matrices and P is a unique symmetric positive definite solution of the algebraic Lyapunov equation ($PA + A^T P = -M$ with M a symmetric positive definite matrix). If the adaptive control laws are chosen as follows:

$$\dot{K}_x = -\Gamma_x \mathbf{e}\mathbf{e}^T PB \tag{3.56}$$

$$\dot{K}_r = -\Gamma_r \mathbf{r}\mathbf{e}^T PB \tag{3.57}$$

$$\dot{\Theta} = -\Gamma_\theta \mathbf{e}\mathbf{e}^T PB \tag{3.58}$$

the time derivative of the Lyapunov function becomes negative semi-definite:

$$\dot{V}(\mathbf{e}(t), \Delta K_x(t), \Delta K_r(t), \Delta\Theta(t)) = -\mathbf{e}^T(t) M \mathbf{e}(t) \tag{3.59}$$

The invariant set theorems of La Salle and Barbalat's Lemma extend the concept of the Lyapunov function providing asymptotic stability analysis tools for autonomous and non-autonomous systems with a negative semi-definite time-derivative of a Lyapunov function [125]. Therefore, when $t \to \infty$, $\dot{V}(\mathbf{e}, t) = 0$ and it follows from Eq. (3.59) that $||\mathbf{e}(t)|| = 0$.

3.6.3 Optimal control

This section regards the description of open-loop optimal control, which is employed in Chapter 5. Optimal control involves the determination of control and state vectors for a dynamic system to minimise a performance index. Considering the following performance index:

$$J = \phi(\mathbf{x}(t_f)) + \int_{t_0}^{t_f} L(\mathbf{x}(t), \mathbf{u}(t), t)\, dt \tag{3.60}$$

the objective is to find the control vector $\mathbf{u}(t)$ so that J, subject to $\dot{\mathbf{x}}(t) = f(\mathbf{x}(t), \mathbf{u}(t), t)$ with initial condition $\mathbf{x}(t_0) = \mathbf{x_0}$ and constraint $\mathbf{u}(t) \leq \mathbf{u_{max}}$, is minimised.

In the case of climate engineering, the minimisation of the the performance index with constrained control variables allows minimisation of the temperature anomaly with a minimum given economic effort. It therefore represents the link between needed insolation reduction to achieve

a certain climate engineering objective and available resources.

The calculus of variations [128] provides an analytical method to solve this constrained optimisation problem. The index J can be adjoined with constraints through the time-varying Lagrange multiplier vector $\boldsymbol{\mu}$ (also called co-states). Thus, the augmented performance index becomes:

$$\bar{J} = \phi(\mathbf{x}(t_f)) + \int_{t_0}^{t_f} L(\mathbf{x}(t), \mathbf{u}(t), t) + \boldsymbol{\mu}(t)^T \left(f(\mathbf{x}(t), \mathbf{u}(t), t) - \dot{\mathbf{x}}\right)\, dt \tag{3.61}$$

The Hamiltonian function of the system can now be defined as:

$$H(\mathbf{x}, \mathbf{u}, t, \boldsymbol{\mu}) = L(\mathbf{x}, \mathbf{u}, t) + \boldsymbol{\mu}^T f(\mathbf{x}, \mathbf{u}, t) \tag{3.62}$$

where the time dependence of the vectors $\mathbf{x}$, $\mathbf{u}$ and $\boldsymbol{\mu}$ is omitted for simplicity. Thus, Eq. (3.61) becomes:

$$\bar{J} = \phi(\mathbf{x}(t_f)) + \int_{t_0}^{t_f} H(\mathbf{x}, \mathbf{u}, t, \boldsymbol{\mu}) - \boldsymbol{\mu}(t)^T \dot{\mathbf{x}}\, dt \tag{3.63}$$

The vector $\boldsymbol{\mu}$ is arbitrary and its components will be therefore chosen so that $\bar{J}$ is minimised. Following [128], the conditions required are summarised below. In particular, the co-state dynamics are given by:

$$\dot{\boldsymbol{\mu}}(t) = -\frac{\partial H}{\partial \mathbf{x}} \tag{3.64}$$

and the stationary condition for the Hamiltonian function is given by:

$$\left(\frac{\partial H}{\partial \mathbf{u}}\right)_{\mathbf{u}=\mathbf{u}^*} = 0 \tag{3.65}$$

The inequality constraints associated with the control variables require the use of the minimum principle of Pontryagin stating that the function H needs to be minimised over all admissible $\mathbf{u}$ in order to find optimal values of $\mathbf{x}^*$ and $\boldsymbol{\mu}^*$. The Pontryagin principle can be summarised as follows:

$$H\left(\mathbf{x}^*, \mathbf{u}^*, \boldsymbol{\mu}^*\right) \leq H\left(\mathbf{x}^*, \mathbf{u}, \boldsymbol{\mu}^*\right) \tag{3.66}$$

where $\mathbf{u}^*$ is the optimal control law that minimizes the Hamiltonian function.

Moreover, depending on the specific constraints of the problem, boundary conditions for the co-state and Hamiltonian functions can be defined. Specifically, for each state variable which is

not constrained at final time, the following condition can be written as:

$$\mu(t_f) = \left(\frac{\partial \phi(\mathbf{x}(t_f))}{\partial x} \right)_{t=t_f} \tag{3.67}$$

Also, if the final time is unconstrained, a transversality condition for the Hamiltonian can be written as:

$$H(t_f) = -\left(\frac{\partial \phi(\mathbf{x}(t_f))}{\partial t} \right)_{t=t_f} \tag{3.68}$$

The main issue of this method is solving the co-state dynamics with final conditions (3.67). Again, this optimal control strategy will be used later in Chapter 5.

Chapter 4

SRM Control strategies to minimize temperature in a three-box climate model

4.1 Introduction

In this Chapter, a 3-box model for the climate system is developed and, with respect to previous work [1–4], a new closed-loop strategy involving an adaptive controller is considered for climate engineering. This control strategy is able to deal with large uncertainties, which represent one of the main issues for the modelling of the climate system, as noted in Section 2.3.

Moreover, as seen in Section 2.2, SRM strategies are strictly linked to the latitudinal distribution of insolation and, therefore, uniform reductions would cause large regional disparities. To avoid this effect, multi-variable control methods are employed in a 3-box model, where largest latitudinal differences are taken into account. In particular, this chapter focuses on an evaluation of the effects of SRM methods considering a generic control function, representing a reduction of insolation (see Section 4.4), which is obtained by employing adaptive control methods as described in Section 3.6.2. Afterwards, in Chapter 5, following the procedure reported in Section 3.4, a simple dynamic model is considered for sulphur aerosols.

In Section 4.2, the 3-box model is described. The Earth is divided into three latitudinal bands to account for northern and southern zones and the equator, with heat transfer between the boxes to capture the poleward transport of energy from the equator. It is demonstrated that the model, with its simplicity, enables different control methods to be easily implemented and evaluated. The simple 3-box model provides clarity to assess the performance of these strategies.

The use of a simple 3-box model (rather than a single transfer function) allows latitudinal controllability and observability to begin to be investigated in Section 4.3. Indeed, the formal controllability of the problem is assessed using the 3-box model. In particular, in this context, the asymmetry of the northern and southern bands are found to play an important role.

Moreover, a Model-Reference Adaptive Controller (MRAC), already introduced in Section 3.6.2, is investigated for climate engineering and in Section 4.4 its performance is examined for three different control strategies. This type of controller overcomes issues related to the large uncertainties of the 3-box-model providing effective control, despite that the plant model is not well known. The stability of this control method is also investigated using Lyapunov methods. Finally, a concluding discussion can be found in Section 4.5.

4.2 Three-box model of the climate system

In Section 4.4, a non-uniform robust control strategy will be developed to minimise latitudinal disparities from climate engineering deployment using multiple control inputs. For this task a low order model of the climate system with three latitudinal bands is developed. The Earth's surface is divided in three bands: southern and northern bands (latitude bands in the ranges $(-65°,-90°)$, $(65°,90°)$) and a central band $(-65°,65°)$. In this way, coarse latitudinal dynamics are taken into account.

Considering the energy balance model in Eq. (3.12) (Section 3.1), the latitudinal subdivision can be represented through a 3-box model defined by Eq. (4.1-4.3). In particular, with respect to the model in Eq. (3.12), constant values of the heat capacity are considered taking into account land and water distributions, as will be described later. Also, a simplified expression is employed for the latitudinal heat transport rate, which is related to the temperature difference between the boxes. It is important to note that, in order to match observations, different values for the heat transport coefficients are employed for the latitudinal bands, and as a consequence the 3-box model cannot be considered an energy balance model. This outcome is likely to be related to the absence in the model of mean circulation in the atmosphere and ocean. This decision was taken in order to maintain a tractable problem. Finally, external forcing and control variables are included in the model.

It is important to note that the model is not considered a substitute for high fidelity General Circulation Models (GCM), but is used to assess the performance of adaptive control strategies

and to allow an investigation of formal controllability properties which are key to multi-variable control. Moreover, as will be shown later, adaptive control is robust to uncertainties in the climate model itself; therefore the importance of the model employed can be de-emphasised.

The subdivision of the system into three latitudinal bands is now developed to consider the use of three separate control processes. As noted earlier, this is motivated by the need to begin to investigate how to overcome issues associated with the largest latitudinal disparities of the impacts of SRM technologies.

In Eqs. (4.1-4.3) T_i is the surface temperature and $i = 1,2,3$ represents the northern band, the central band and the southern band, respectively. Also, a term F_{ext} considers external forcing due to anthropogenic GHGs emissions and a function U_i ($i = 1,2,3$) represents the generic reduction of insolation. In Section 5.4, the dynamics of stratospheric aerosols is considered for the function U_i ($i = 1,2,3$) in order to demonstrate the robustness of adaptive control to the choice of actuator dynamics.

The model is defined using 3 coupled linear equations which can be written as:

$$C_1 \frac{dT_1(t)}{dt} = Q_0 S_1(1-\alpha_1) - (a_1 + b_1 T_1) - k_1(T_1 - T_2) + F_{ext} + U_1 \tag{4.1}$$

$$C_2 \frac{dT_2(t)}{dt} = Q_0 S_2(1-\alpha_2) - (a_2 + b_2 T_2) - \frac{1}{2}k_2(T_2 - T_1) - \frac{1}{2}k_2(T_2 - T_3) + F_{ext} + U_2 \tag{4.2}$$

$$C_3 \frac{dT_3(t)}{dt} = Q_0 S_3(1-\alpha_3) - (a_3 + b_3 T_3) - k_3(T_3 - T_2) + F_{ext} + U_3 \tag{4.3}$$

where, $Q_0 S_i$ and α_i (i=1,2,3) are the mean annual insolation and the planetary albedo in each latitudinal band, respectively. These are assumed to be fixed, although time-dependent seasonal variation could in principle be included.

The expression in Eq. (3.3) found in Section 3.1 is employed for the outgoing infra-red radiation. Specifically, it is noted that values of a and b from [75] reported in Section 3.1 describe well the infra-red radiation of the central band of the 3-box model ($a_2 = 203.3\ W/m^2$, $b_2 = 2.09\ W/m^2/°C$), whereas, a more specific infra-red parametrisation for the northern and southern hemispheres is used for the northern band (a_1, b_1) and southern band (a_3, b_3) [73]. According

to work in [73] the out-going infra-red radiation can be represented as:

$$a + b\,T(t) = A_1 + A_2 A_c + (B_1 + B_2 A_c) T(t) \tag{4.4}$$

where $A_1 = 257\ W/m^2$, $A_2 = -91\ W/m^2$, $B_1 = 1.63\ W/m^2/°C$, $B_2 = -0.11\ W/m^2/°C$ for the northern band and $A_1 = 262\ W/m^2$, $A_2 = -81\ W/m^2$, $B_1 = 1.64\ W/m^2/°C$, $B_2 = -0.09\ W/m^2/°C$ for the southern band, whereas A_c is the cloud cover fraction set to 0.5 [75]. Through climatological records of zonal surface temperature and satellite observations this fit has been proven to be quite accurate [129].

Moreover, C_i (i=1,2,3) is the effective heat capacity for each latitudinal band, which is largely determined by the different hemispherical distributions of land and water. The heat capacity over land is approximately 1/30 of the capacity over the ocean mixed layer [75], therefore, since a larger fraction of water is found in the southern hemisphere a larger heat capacity is expected. Considering the fraction of water and land in each hemisphere (oceans cover 61% of the northern hemisphere and the 82% of the southern hemisphere) the heat capacity, in terms of b_1 and b_3, is 2.88 b_1 years for the northern hemisphere and 3.79 b_3 years for the southern hemisphere. The values of the heat capacities are given in years as in [75] to show the combination of the time-scales of land and oceans for the southern and northern hemisphere. From Eq. (4.4) $b_1 = 1.575\ W/m^2/°C$ and $b_3 = 1.595\ W/m^2/°C$, therefore $C = 4.542\ W yr/m^2/°C$ and $C_2 = 6.048\ W yr/m^2/°C$. As for the infra-red radiation, these values for the heat capacity are employed for the northern band (C_1) and the southern band (C_3) and their average is used for the central band (C_2).

The term for the latitudinal heat transport rate is considered proportional to the temperature difference between two contiguous latitudinal zones, which provides coupling between the boxes. In accordance with the 2^{nd} law of thermodynamics, it is the transport of heat from warmer tropical to colder polar regions that leads to a downgrading of energy and an increase of the Earth's global entropy [130]. In this case, the poleward heat transport can be approximated by a transport coefficient k given by $k_1 = 0.549\ W/m^2/K$ [75] for the northern band and $k_3 = 0.649\ W/m^2/K$ for the southern band. For this specific model, the values of k_1 and k_3 are selected so that the mean annual temperature at the equator represents the current climate ($T \simeq 30\ °C$ [75]). With regard to the central band, the transport coefficient needs to be larger at the equator than the higher latitudes [75], therefore a value of $0.73\ W/m^2/K$ is considered for k_2.

Considering variations of temperature around the equilibrium state of each latitudinal band T_{eq_i} $(i = 1,2,3)$, the following transformation can be used for each band:

$$\zeta_i = \frac{T_i - T_{eq_i}}{T_{eq_i}} \qquad i = 1,2,3 \tag{4.5}$$

Moreover, since Eqs. (4.1-4.3) form a linear system of differential equations, they can be written in the form $\frac{d\boldsymbol{\zeta}}{dt} = A\boldsymbol{\zeta} + \mathbf{F} + \mathbf{U}$ where $\boldsymbol{\zeta}$ is the 3x1 state vector defining the temperature anomalies and where A is the system matrix and $\mathbf{F}$ is a forcing vector given by:

$$A = \begin{pmatrix} j_{11} & j_{12} & 0 \\ j_{21} & j_{22} & j_{23} \\ 0 & j_{32} & j_{33} \end{pmatrix} \tag{4.6}$$

$$\mathbf{F}(t) = \begin{pmatrix} Q_0 S_1(1-\alpha_1) - (a_1 + b_1 T_1) - k_1\left(T_{eq_1} - T_{eq_2}\right) + F_{ext}(t) \\ Q_0 S_2(1-\alpha_2) - (a_2 + b_2 T_2) - k_2\left(T_{eq_2} - \frac{1}{2}T_{eq_1} - \frac{1}{2}T_{eq_3}\right) + F_{ext}(t) \\ Q_0 S_3(1-\alpha_3) - (a_3 + b_3 T_3) - k_3\left(T_{eq_3} - T_{eq_2}\right) + F_{ext}(t) \end{pmatrix} \tag{4.7}$$

with $j_{ii} = -\frac{(b_i + k_i)}{C_i}$ $(i = 1,2,3)$, $j_{12} = \frac{k_1}{C_1} h_{21}$, $j_{21} = \frac{1}{2}\frac{k_2}{C_2} h_{12}$, $j_{23} = \frac{1}{2}\frac{k_2}{C_2} h_{32}$, $j_{32} = \frac{k_3}{C_3} h_{23}$ where $h_{ij} = \frac{T_{eq_i}}{T_{eq_j}}$ $(i, j = 1,2,3)$. Considering these transformations, it is possible to write the transfer function scheme for the 3-box model represented by 3 connected transfer functions, as can be seen in Fig. (4.1). In particular, the external inputs ($\mathbf{F}(t)$) are highlighted in yellow whereas the temperature anomalies represent the outputs ($\zeta(t)$) and are highlighted in green. Moreover, the scheme in Fig. (4.1) shows distinctly the interactions between the boxes: the first box (northern band) receives the contribution j_{12} (light blue) from the second box (central band); the second box receives contributions j_{21} (orange) from the first box and j_{23} (red) from the third box (southern band), whereas the third box receives the contribution j_{32} (light blue) from the second box. The elements internal to each band are given by terms j_{ii} $(i = 1,2,3)$ and are highlighted in grey in Fig. (4.1). The equilibrium temperatures in the three zones can be computed considering the

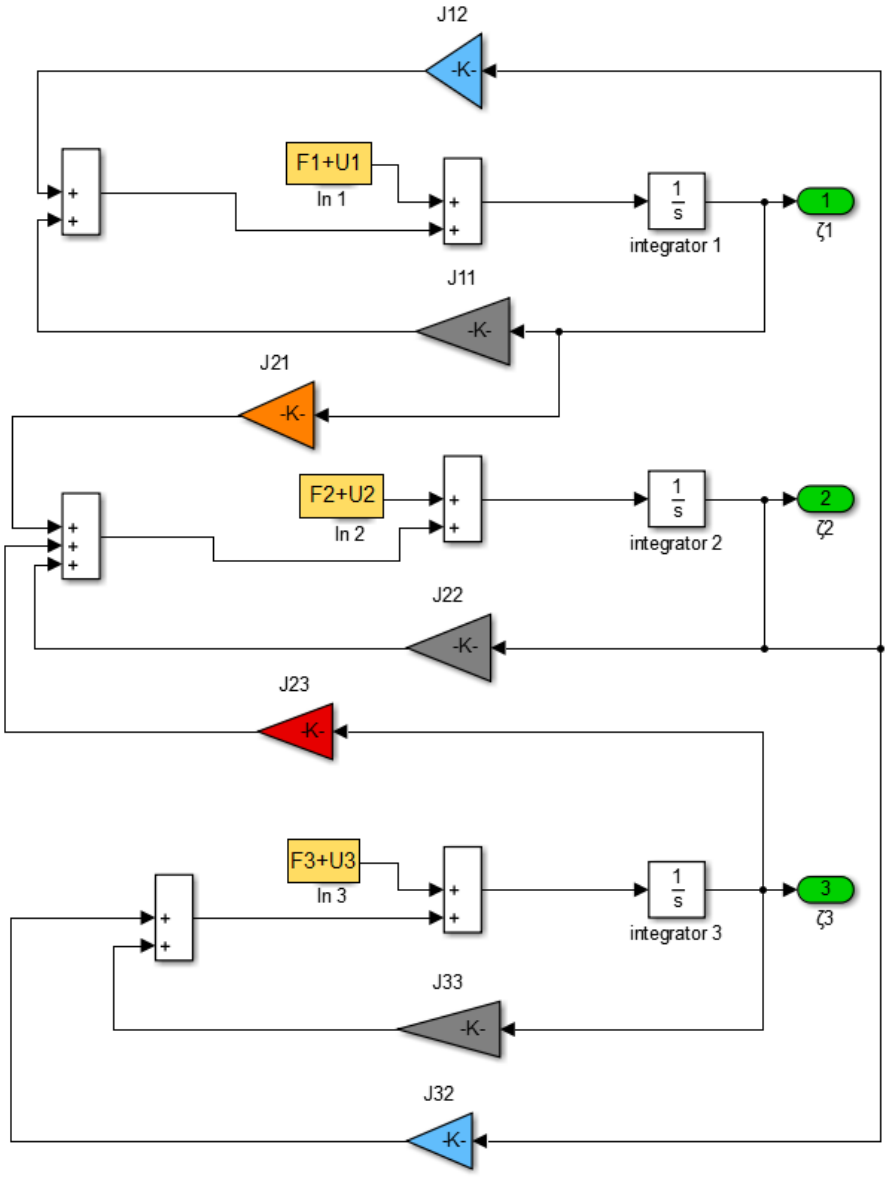

Figure 4.1: Scheme for the three-box energy model described by $\frac{d\zeta}{dt} = A\zeta + \mathbf{F} + \mathbf{U}$.

equilibrium state of the system in Eqs. (4.1-4.3). External forcing is then ignored so that:

$$\mathbf{F}(0) = \begin{pmatrix} Q_0 S_1(1-\alpha_1) - (a_1 + b_1 T_{eq_1}) - k_1\left(T_{eq_1} - T_{eq_2}\right) \\ Q_0 S_2(1-\alpha_2) - (a_2 + b_2 T_{eq_2}) - k_2\left(T_{eq_2} - \frac{1}{2}T_{eq_1} - \frac{1}{2}T_{eq_3}\right) \\ Q_0 S_3(1-\alpha_3) - (a_3 + b_3 T_{eq_3}) - k_3\left(T_{eq_3} - T_{eq_2}\right) \end{pmatrix} \tag{4.8}$$

The system defined by Eq. (4.8) can then be solved to obtain the equilibrium temperatures of the three bands given by $(T_{eq_1}, T_{eq_2}, T_{eq_3}) = (-28.9°C, 14.7°C, -34.5°C)$ [75]. The terms S_i $(i = 1,2,3)$ are constants related to the latitudinal distribution reported in Eq. (3.5) (Section 3.1).

Table 4.1: Values of S_i and the Earth's albedo for the three latitudinal bands [131].

	Northern Band	Central Band	Southern Band
S_i	0.60625	1.0882	0.545625
α_i	0.498	0.281	0.498

Specifically, data considered for S_i and for the Earth's albedo α_i are reported in Table (4.1) and are the average of values reported by Warren [131]. The terms S_i are weight functions that determine the quantity of incoming solar radiation in each latitudinal band and are not necessarily bounded between 0 and 1 since Q_0 is only the average value of the incoming solar radiation, not the maximum value.

Now that the terms j are defined and the matrix A is completely defined, it is possible to write the 3 transfer functions for the three-box model as follow:

$$\frac{\zeta_1(t)}{F_1(t)+U_1(t)} = \frac{j_{23}j_{32} - j_{12}j_{23} + j_{12}j_{33} - j_{22}j_{33}}{\left[(j_{11}-s)(j_{22}-s) - j_{12}j_{21}\right](j_{33}-s) + j_{23}j_{32}(s-j_{11})} \tag{4.9}$$

$$\frac{\zeta_2(t)}{F_2(t)+U_2(t)} = \frac{j_{11}j_{23} - j_{11}j_{33} + j_{21}j_{33} + (j_{11} - j_{21} - j_{23} + j_{33})s - s^2}{\left[(j_{11}-s)(j_{22}-s) - j_{12}j_{21}\right](j_{33}-s) + j_{23}j_{32}(s-j_{11})} \tag{4.10}$$

$$\frac{\zeta_3(t)}{F_3(t)+U_3(t)} = \frac{j_{12}j_{21} - j_{11}j_{22} + j_{11}j_{32} - j_{21}j_{32} + (j_{11} + j_{22} - j_{32})s - s^2}{\left[(j_{11}-s)(j_{22}-s) - j_{12}j_{21}\right](j_{33}-s) + j_{23}j_{32}(s-j_{11})} \tag{4.11}$$

Applying the external input $F_i(t)+U_i(t)$ $(i=1,2,3)$ to the transfer functions in Eqs. (4.9-4.11) the response of the system is obtained in terms of temperature anomalies in the three latitudinal bands ζ_i $(i=1,2,3)$. Substituting values of j_{ij}, j_{ii} $(i=1,2,3)$ in Eqs. (4.9-4.11), the expressions above become:

$$\frac{\zeta_1(t)}{F_1(t)+U_1(t)} = \frac{(0.374367+s)(0.650065+s)}{(0.322541+s)(0.430703+s)(0.617928+s)} \tag{4.12}$$

$$\frac{\zeta_2(t)}{F_2(t)+U_2(t)} = \frac{(0.404076+s)(0.572404+s)}{(0.322541+s)(0.430703+s)(0.617928+s)} \tag{4.13}$$

$$\frac{\zeta_3(t)}{F_3(t)+U_3(t)} = \frac{(0.462339+s)(0.64512+s)}{(0.322541+s)(0.430703+s)(0.617928+s)} \tag{4.14}$$

As expected, the denominator in Eqs. (4.12-4.14) is the same for the three bands since it depends only on the system matrix A in the state space model. Indeed, the roots of the denominators are given by the eigenvalues of the system which are also its poles. For the three-box model, as can be seen from the expressions above, the eigenvalues are real and negative as expected $(-0.6179, -0.4307, -0.3225)$, demonstrating that the system is asymptotically stable.

The zeros of the system are given by the roots of the numerator of each transfer function and depend on how inputs and outputs are coupled to the states. The zeros thus depend on the matrices A, B (control distribution matrix), and Ψ (measurement matrix) in the state space description (matrices B and Ψ are described in more detail in Section 4.3). In particular, the zeros are different for the three bands because the measured quantity is $\zeta_1(t)$ in Eq. (4.12) with $\Psi = [1\ 0\ 0]$, $\zeta_2(t)$ in Eq. (4.13) with $\Psi = [0\ 1\ 0]$ and $\zeta_3(t)$ in Eq. (4.14) with $\Psi = [0\ 0\ 1]$.

4.2.1 Validation of the model

The response of the model described above to the four RCPs scenarios defined in Section 3.3 is shown in Fig. (4.2) where the average temperature between the three latitudinal bands is reported for the four cases.

This result is obtained considering $U_i = 0$ $(i = 1, 2, 3)$ in Eqs. (4.1-4.3) and is comparable with other simulations in the literature, for example in [132] where the behaviour of the CMIP5 model under the RCPs scenarios is reported. In particular, in Fig. (4.2), the uncertainty range of the temperature anomaly at $t = 2100$ is reported as found in Fig. 1 from Ref. [132] for each radiative scenario and in every case the response of the model is within the relevant uncertainty range (see also the values of temperature anomaly forecast for the 4 scenarios in [76] reported in Section 3.3). Also, it is worth noticing that, according to the data reported in Fig. (4.2), the value of the temperature anomaly in 2018 is found to be $\approx 0.48°C$ which is in agreement with observation from HadCRUT.4.6 data set [1]. In particular, the annual average of the global surface temperature data set is considered for the comparison.

This approach is considered as the verification of the general correctness and usefulness of the model developed. Also, considering the step response to a doubling of CO_2, the climate

[1] Met Office Hadley Centre observations datasets, `https://www.metoffice.gov.uk/hadobs/hadcrut4/data/current/download.html#gridded_fields`.

sensitivity of the 3-box model is estimated to be $2.3°C$, which is within the acceptable range of values found for other climate models [133].

Moreover, in Fig. (4.2) as in all the other simulations, Gaussian noise (w) with a normal distribution (zero mean and 25% standard deviation, considering a 50% uncertainty range for the temperature anomaly as in [76, 87]) is added to the signal later to simulate climate variability.

Now that the 3-box model has been presented and validated, the development of the adaptive control strategies for climate engineering can proceed. In the following sections the investigation of the stability of the system, the controllability and the observability of the strategies considered and the assessment of adaptive control strategies for highly-uncertain systems is presented.

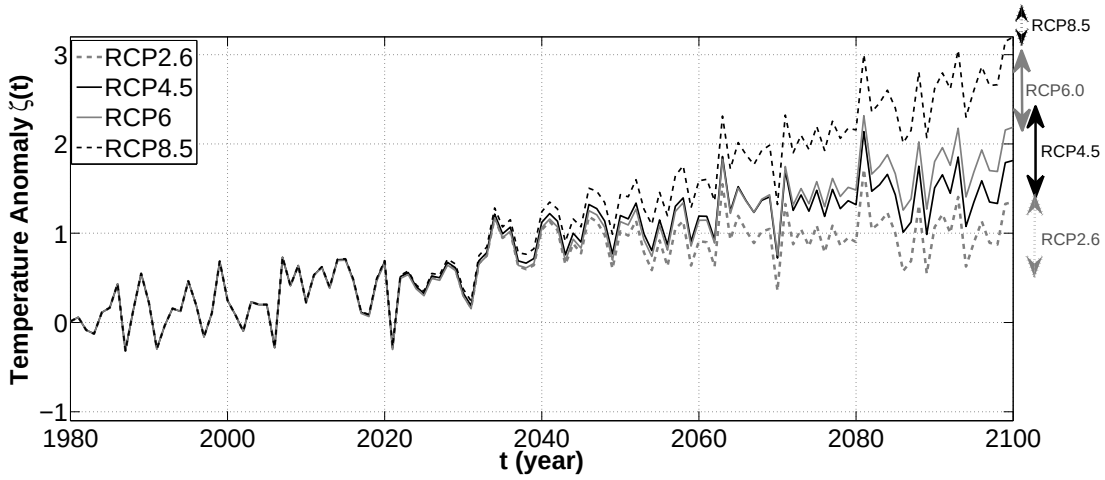

Figure 4.2: Response of the 3-box model described in Eqs. (4.1-4.3) to RCP scenarios. Uncertainty ranges for RCP scenarios found in [132] are reported on the right-hand side.

4.3 Controllability and observability of the three-box model

The stability of the 3-box model defined by Eqs. (4.1-4.3) has been investigated in Section 4.2 and it is found that the system is asymptotically stable.

From the point of view of the control system, low order models with more than one input and one output, such as the 3-box model, are of particular interest since it allows for the investigation of some important properties of the system. In particular, in this section, the formal controllability and observability of the system is investigated by exploring the control architecture.

Four cases are investigated: reduction of the temperature anomaly (a) in the northern band, (b) in the northern and southern band, (c) in all the three zones and (d) in the central band only.

The four strategies are summarised in Table (4.2) where the area of deployment provides the latitudinal band in which the deployment of SRM takes place, the number of controllers (or actuators) indicates the number of latitudinal bands in which SRM is deployed and the objective to minimise represents the latitudinal band where the temperature anomaly is driven to zero. In particular, the latter indicates the objective of each strategy in the cases when the system is controllable.

Table 4.2: Summary of the four control strategies investigated.

Case	Area of deployment	# Controllers	Objective to minimise
a	Northern band	1	Northern band
b	Northern and Southern bands	2	Northern and Southern bands
c	Northern, Southern and Central bands	3	all 3 bands
d	Central band	1	all 3 bands

The system in Section 4.2 now becomes $\frac{d\boldsymbol{\zeta}}{dt} = A\boldsymbol{\zeta} + \mathbf{F} + B\mathbf{U}$ where B is the control distribution matrix, with as many columns as the number of controllers and 3 rows equal to the dimension of the system. The number of controllers (or actuators) are different for each strategy (a-d) as reported in Table (4.2).

For each strategy, the controllability of the system can be verified. Since A is a non-singular 3×3 matrix, the controllability matrix [134] associated with the system in Eqs. (4.1-4.3) is given by:

$$\Sigma = [B \; AB \; A^2B] \tag{4.15}$$

where Eq. (4.15) is used to evaluate when $rank(\Sigma) = rank(A)$. In that case the system is fully controllable and so it is in principle possible to drive the three internal states of the system from any initial state to any other final state in a finite time interval.

The matrix Σ is determined for cases (*a-d*) and the system is found always to be controllable for strategies (*a-c*) and for strategy (*d*) only if the asymmetries of the poles are taken into account in the model, as will be discussed later. The controllability matrices for cases (a-c) are reported

below:

$$\Sigma_a = \begin{pmatrix} 1 & -0.4896 & 0.2463 \\ 0 & 0.0391 & -0.0345 \\ 0 & 0 & 0.0026 \end{pmatrix} \tag{4.16}$$

$$\Sigma_b = \begin{pmatrix} 1 & 0 & -0.4896 & 0 & 0.2463 & 0.0065 \\ 0 & 0 & 0.0391 & 0.0385 & -0.0345 & -0.0274 \\ 0 & 1 & 0 & -0.3187 & 0.0026 & 0.1041 \end{pmatrix} \tag{4.17}$$

$$\Sigma_c = \begin{pmatrix} 1 & 0 & -0.4896 & 0.1693 & 0 & 0.2463 & -0.1492 & 0.0065 & \\ 0 & 1 & 0 & 0.0391 & -0.3920 & 0.0385 & -0.0344 & 0.1628 & -0.0274 \\ 0 & 0 & 1 & 0 & 0.0661 & -0.3187 & 0.0026 & -0.0469 & 0.1041 \end{pmatrix} \tag{4.18}$$

The actuator matrices, $\boldsymbol{B}_a$, $\boldsymbol{B}_b$ and $\boldsymbol{B}_c$, used to compute the controllability matrices above, are given by:

$$\boldsymbol{B}_a = \begin{pmatrix} 1 \\ 0 \\ 0 \end{pmatrix} \quad \boldsymbol{B}_b = \begin{pmatrix} 1 & 0 \\ 0 & 0 \\ 0 & 1 \end{pmatrix} \quad \boldsymbol{B}_c = \begin{pmatrix} 1 & 0 & 0 \\ 0 & 1 & 0 \\ 0 & 0 & 1 \end{pmatrix} \tag{4.19}$$

With regard to strategy (d), it has been noted that if the asymmetries of the southern band with respect to the northern band are neglected and the same climate parameters are used for both latitudinal bands ($C_1 = C_3$, $b_1 = b_3$, $k_1 = k_3$), it can be demonstrated that the system is uncontrollable. In this case, if only the central band is controlled and so the matrix $\boldsymbol{B}$ is given by the vector $(0,1,0)^T$ then, according to Eq. (4.15), the controllability matrix of the system is:

$$\Sigma_d = \begin{pmatrix} 0 & j_{21} & j_{11}j_{21} + j_{21}j_{22} \\ 1 & j_{22} & j_{12}j_{21} + j_{22}^2 + j_{23}j_{32} \\ 0 & j_{23} & j_{22}j_{23} + j_{23}j_{33} \end{pmatrix} = \begin{pmatrix} 0 & 0.1185 & -0.0941 \\ 1 & -0.3973 & 0.1678 \\ 0 & 0.1203 & -0.0955 \end{pmatrix} \tag{4.20}$$

The numerical values for the components of Σ_d in Eq. (4.20) are obtained considering $C = 7.3\ W\ yr/m^2/K$, $b = 2.17\ W/m^2/°C$ and $k = 0.73\ W/m^2/K$ for both poles [75].

In this case, the uncontrollability of the system is due to the symmetry of the central band with respect to poles: the poles are not significantly different to each other, therefore the associated rows $\left(1^{st} \text{ and } 3^{rd}\right)$ are not independent. For this reason, $rank(\Sigma) < rank(A)$ and the system cannot be controlled.

However, when the asymmetry of the poles (mainly due to the different fraction of land and water) are taken into account and the climate parameters in Section 4.2 are considered, the controllability matrix for strategy (d) can be written as:

$$\Sigma_d = \begin{pmatrix} 0 & 0.1693 & -0.1492 \\ 1 & -0.3920 & 0.1628 \\ 0 & 0.0661 & -0.0470 \end{pmatrix} \tag{4.21}$$

The system is now controllable and this means that a temperature anomaly can in principle be driven to zero in all the three latitudinal bands, even if SRM is deployed only in the central band. This case has been considered to investigate the limits of controllability of the system, however it is not investigated further in this thesis.

In a similar way it is possible to investigate the observability of the system in each case. This feature is also useful to understand the number of observable states when not all measurements are available. This could in principle occur, for example, if some measurements cannot be considered reliable or even if a geopolitical disagreement causes degraded data. The observability matrix of a system is given by:

$$\mathcal{O} = [\Psi \;\; \Psi A \;\; \Psi A^2] \tag{4.22}$$

where Ψ is the matrix of measurements with as many rows as the number of sensors and 3 columns equal to the dimension of the system. The model is completely observable if the matrix $\mathcal{O}$ has full rank 3. Considering the cases in Table (4.2), as expected, the results confirm the outcomes from the analysis of controllability: the system is fully observable in cases (a-c) and in case (d) if asymmetries of the poles are taken into account.

4.4 Adaptive controller for multi-variable control strategies

In this section, adaptive control strategies which are able to deal with large uncertainties are considered. The adaptive controller employed in this work is the direct model reference adaptive control (MRAC) [125, 126] which has been introduced in Section 3.6.2. In this control strategy, control parameters are updated in real time to modify the response of the system as required, which guarantees convergence in the case of large uncertainties.

It is worth noting that in [88], a model predictive controller is considered. This method involves the minimisation of a cost function over the prediction horizon to compute the new system inputs at every iteration. This method implements a concept which is similar to an adaptive controller. However, recursive least squares (RLS) estimation is employed and, in principle, this may lead to the estimation of parameters which generate an unstable control scheme when non-stochastic phenomena affect the dynamical system.

Otherwise, the convergence of the MRAC employed in this thesis is guaranteed through the implementation of the Lyapunov stability criterion, which is used to estimate the structure of the control gains dynamics (as was seen in Section (3.6.2)).

Moreover, adaptive controllers are of particular interest for their simple representation and the clear linkage with the real world. It is in fact possible to add perturbing forcings, representing natural phenomena or possible dangerous circumstances, to the system without making any change in the structure of the controller and demonstrating that the controller adjusts itself to most situations. This cannot be guaranteed a priori with a model predictive controller.

Equation (3.51) is now considered to describe the 3-box model. In this case, $\mathbf{x} = \boldsymbol{\zeta}$ (i.e. vector of temperature anomalies), Eq. (4.6) is considered to be the system matrix A and $\mathbf{r}$ is given by the radiative forcing $\mathbf{F}_{CO_2}(t)$. Then, the system in Eqs. (4.1-4.3) can be written as:

$$\dot{\boldsymbol{\zeta}} = A\boldsymbol{\zeta} + B(\mathbf{U} + \Theta^T \boldsymbol{\zeta}) + \mathbf{w} \tag{4.23}$$

where the matrix Θ takes uncertainties in the system into account, as noted in Section 3.6.2. Also, $\mathbf{w}$ represents Gaussian noise with a normal distribution (with 0 mean and 25% standard deviation, as discussed in Section 4.2).

According to [125], the control law $\mathbf{U}$ in Eq. (3.52) can be employed so that the error $\mathbf{e} = \boldsymbol{\zeta} - \boldsymbol{\zeta}_m$ (where subscript m refers to the reference model) is equal to zero for $t \to \infty$. The standard MRAC is usually known to become unstable in the presence of time delay. However, in

this specific problem, since the external forcing ($\mathbf{r}(t)$) is persistently exciting the system ($RCP4.5$ scenario [135]), it is demonstrated in [125] that MRAC systems are robust despite uncertainties. Comparisons of the adaptive control strategy to conventional PI control is provided later in Chapter 5.

Control strategies with PI control in feedback have been employed for climate engineering [1, 4, 90] as discussed in Section 3.6.1. Such control strategies can handle certain classes of parametric and dynamic uncertainties. However, adaptive control can tolerate much larger uncertainties because of the on-line estimation of the control law gains. Adaptive control therefore represents the natural solution for problems where only a nominal model of the real-world plant is available for control design and the plant parameters can vary [136]. Adaptive control appears therefore to be of significant benefit for climate engineering. Moreover, it is demonstrated that adaptive control is also able to deal with unforeseen major perturbations, that are likely to occur when SRM is deployed, and also uncertainty in the actuator dynamics.

The method is based on the dynamical estimation of the parameters of the gain matrices and it has been proved that, despite the uncertainties on the parameters of the plant (the climate model), a suitable control strategy can always be developed. Even if the actual gains deviate from the nominal control gains, adaptive control guarantees that the values for the control gain matrices are always included in the admissible domain that would not result in loss of system stability.

The adaptive control strategy is now applied in all the three cases reported in Table (4.2). As noted in Section 4.3, the dimensions of $\boldsymbol{B}$ depend on the configuration of the control strategy (i.e. on the number of actuators) and for this reason a different controllability matrix is obtained in each case. Equations (3.56-3.58) are employed to adjust the control matrices K_x,K_r and Θ at each iteration.

The symmetric matrices Γ_ζ, Γ_r, Γ_Θ and $\boldsymbol{M}$ are chosen so that all the system's variables have the same order of magnitude and are comparable during the estimation of the adaptive control laws. It is important to note that these matrices are set before the beginning of the control process and it is not necessary to modify them despite changes in external inputs because of the on-line update of the control laws. The chosen values for these matrices for cases (a-c) (Table (4.2)) are

reported below.

$$\Gamma_{\zeta_A} = \begin{pmatrix} 3^9 & 10^8 & 2\times10^8 \\ 10^8 & 1 & 1 \\ 2\times10^8 & 1 & 3\times10^9 \end{pmatrix} \quad \Gamma_{r_A} = \begin{pmatrix} 10^9 & 10^5 & 10^5 \\ 10^5 & 1 & 1 \\ 10^5 & 1 & 10^9 \end{pmatrix} \tag{4.24}$$

$$\Gamma_{\zeta_B} = \begin{pmatrix} 10^9 & 2\times10^8 & 10^9 \\ 2\times10^8 & 10^{-10} & 1 \\ 10^9 & 1 & 1 \end{pmatrix} \quad \Gamma_{r_B} = \begin{pmatrix} 10^8 & 10^8 & 10^8 \\ 10^8 & 1 & 1 \\ 10^8 & 1 & 1 \end{pmatrix} \tag{4.25}$$

$$\Gamma_{\zeta_C} = \begin{pmatrix} 10 & 10 & 10 \\ 10 & 10 & 10 \\ 10 & 10 & 10 \end{pmatrix} \quad \Gamma_{r_C} = \begin{pmatrix} 100 & 10 & 100 \\ 10 & 10 & 10 \\ 100 & 10 & 100 \end{pmatrix} \tag{4.26}$$

$$\Gamma_{\Theta_A} = \begin{pmatrix} 3\times10^3 & 10^5 & 10^5 \\ 10^5 & 1 & 1 \\ 10^5 & 1 & 3\times10^3 \end{pmatrix} \Gamma_{\Theta_B} = \begin{pmatrix} 100 & 1 & 1 \\ 1 & 1 & 1 \\ 1 & 1 & 100 \end{pmatrix} \Gamma_{\Theta_C} = \begin{pmatrix} 10 & 10 & 10 \\ 10 & 20 & 10 \\ 10 & 10 & 10 \end{pmatrix} \tag{4.27}$$

Moreover, the matrices M and P, given by the solution of the Lyapunov equation (see Section 4.4) are given below for cases (a-c).

$$M_A = 10^{-11} \begin{pmatrix} 1 & 0 & 0 \\ 0 & 0.1 & 0 \\ 0 & 0 & 0.9 \end{pmatrix} \quad P_A = 10^{-10} \begin{pmatrix} 0.1092 & 0.0092 & 0.0028 \\ 0.0092 & 0.0120 & 0.0111 \\ 0.0028 & 0.0111 & 0.1250 \end{pmatrix} \tag{4.28}$$

$$M_B = 10^{-9} \begin{pmatrix} 0.01 & 0 & 0 \\ 0 & 10^{-5} & 0 \\ 0 & 0 & 1 \end{pmatrix} \quad P_B = 10^{-8} \begin{pmatrix} 0.0011 & 0.0004 & 0.0016 \\ 0.0004 & 0.0014 & 0.0108 \\ 0.0016 & 0.0108 & 0.1379 \end{pmatrix} \tag{4.29}$$

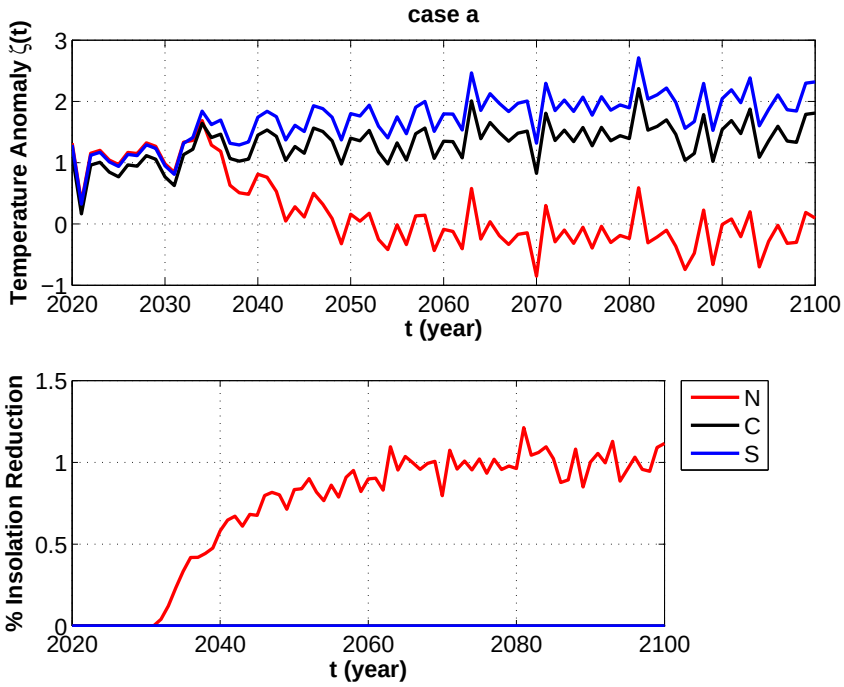

Figure 4.3: Case A: response of the temperature perturbation $\zeta(°C)$ (top) in the 3 latitudinal bands and required insolation reduction (bottom) under the $RCP4.5$ radiative scenario with SRM (adaptive control strategy) deployed in 2030 in the northern band (number of actuators=1). N is the northern band, C the central band and S the southern band.

$$M_C = \begin{pmatrix} 10^{-4} & 0 & 0 \\ 0 & 10^{-4} & 0 \\ 0 & 0 & 2\times 10^{-3} \end{pmatrix} \qquad P_C = 10^{-4}\begin{pmatrix} 1.1136 & 0.2564 & 0.3621 \\ 0.2564 & 1.2678 & 2.2847 \\ 0.3621 & 2.2847 & 27.6137 \end{pmatrix} \tag{4.30}$$

The matrices $M, \Gamma_\zeta, \Gamma_r$ and Γ_Θ depend on the control strategy and their values are chosen in order to control the temperature anomaly in the northern band in case (a), in both northern and southern bands in case (b) and in all the latitudinal bands in case (c).

The temperature anomaly, defined in Eq. (4.5), and the required insolation reduction are shown in Figs (4.3-4.5) for each of the three cases using the adaptive control strategy. In the first case (Fig. (4.3)) the insolation reduction is considered in the northern band. In this case, the temperature anomaly in the northern band is reduced after approximately 15 years from the deployment of SRM and a maximum of 1% insolation reduction is required.

It can be noted that in the second case (Fig. (4.4)) two controllers (or actuators) are considered and SRM is deployed in both northern and southern bands. The temperature in the central band is influenced by the heat transport between the boxes and approaches $1.2°C$. Again, the control

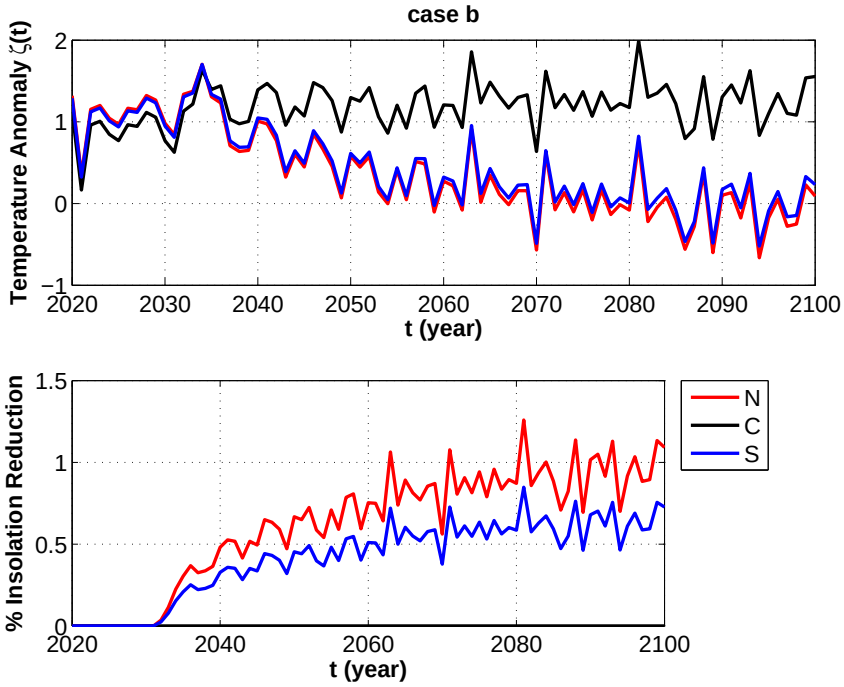

Figure 4.4: Case B: response of the temperature perturbation $\zeta(°C)$ (top) in the 3 latitudinal bands and required insolation reduction (bottom) under the $RCP4.5$ radiative scenario with SRM (adaptive control strategy) deployed in 2030 in the northern and southern bands (number of actuators=2).

law is able to minimise the temperature anomaly in both Northern and Southern bands by 2050-2060 with a maximum insolation reduction of 1% in the northern band and 0.7% in the southern band. The third case (Fig. (4.5)) regards the full system where SRM is deployed in all bands. It is important to note that the main objective of case (c) is to minimise the temperature in the central band, although effort has been made during the control design so that the temperature anomaly in the other two bands do not become negative. In particular, in this case, the temperature anomaly in all the latitudinal bands is minimised within approximately 10 years. As can be seen, the minimisation in the central band is also connected with the decline of the temperature in the other two bands. A maximum insolation reduction of approximately 0.8% and 0.6% is required in the northern and southern bands, respectively, and 0.2% in the central band.

As can be seen, adaptive control provides the necessary control of radiative forcing in the 3-box model to counteract human-driven climate change under the $RCP4.5$ scenario with a 50% uncertainty range for the temperature anomaly due to climate variability [76,87], as discussed in Section 4.2. Moreover, the overall insolation reduction required in case c is approximately 1.6% which is broadly comparable with literature [87].

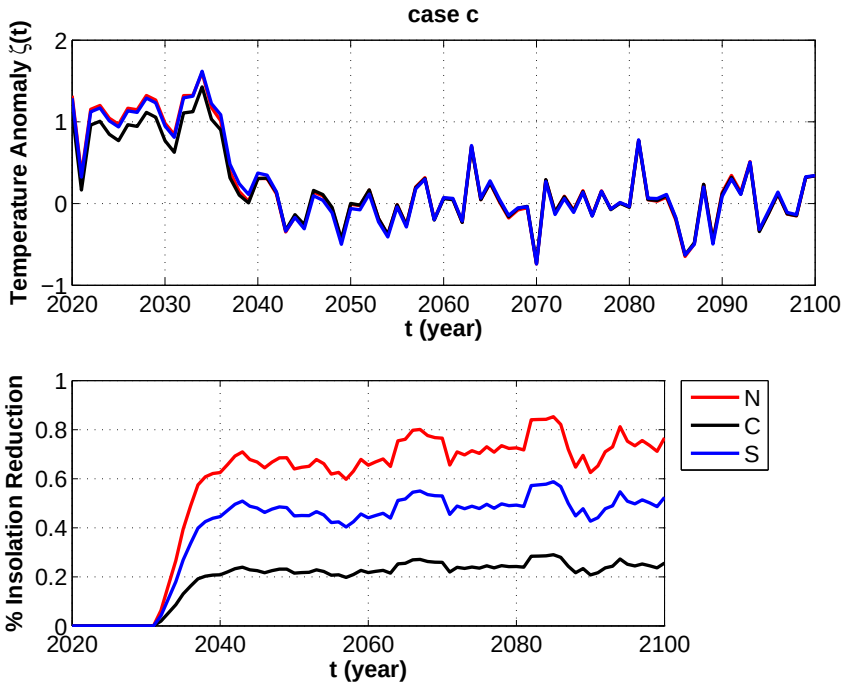

Figure 4.5: Case C: response of the temperature perturbation $\zeta(^{\circ}C)$ (top) in the 3 latitudinal bands and required insolation reduction (bottom) under the $RCP4.5$ radiative scenario with SRM (adaptive control strategy) deployed in 2030 in all the latitudinal bands (number of actuators=3).

In this section, it has been demonstrated that adaptive control, as with PI control (see [87]), deals well with uncertainties due to climate variability. However, in the next Chapter, the robustness of adaptive control to large uncertainties in the parameters of the climate model, to unforeseen perturbations and to the choice of the actuator is demonstrated. Comparisons of the results from these investigations with the implementation of PI control are reported for each case and key differences between the two approaches are noted.

4.5 Conclusions

A 3-box model for the climate system has been employed: the Earth's surface is divided into the northern, southern and central latitude bands to account for temperature disparities between mid and high latitudes. Assuming independent climate engineering interventions in each band, the model provides a multiple input control system to explore strategies to mitigate latitudinal climate warming and provide clarity to assess the performance of adaptive and PI control strategies. A new control strategy involving an adaptive controller is considered for the first time for climate engineering to counteract human-driven climate change.

The 3-box model does not aim to be a substitute for high fidelity General Circulation Models (GCM) models for the description of the climate system. However, for the purposes of this thesis (i.e. to establish a control strategy able to overcome issues related to large uncertainties), it is a useful tool to demonstrate the performance of adaptive control strategies.

The multi-variable approach with the 3-box model also allows for an investigation of the formal controllability and observability of the system for the first time. The controllability analysis demonstrates that three of the strategies considered are always controllable with the 3-box model. The fourth strategy involving the control of the three latitudinal bands through the deployment of SRM in the central band only shows that the system can be controlled only if the asymmetries of the northern and southern bands are taken into account. Considering the controllability matrix, it is demonstrated that if the same climate parameters are considered for these two bands, the matrix has two linearly-dependent rows and is therefore uncontrollable. Otherwise, considering the largely different fraction of land and water in the two hemispheres the system then becomes controllable.

Chapter 5

Performance of adaptive control in a three-box model

5.1 Introduction

The 3-box model for the climate system developed in the previous chapter is now considered to investigate the performance and robustness of the adaptive control strategy described in Section 3.6.2 and employed in Chapter 4. The performance is compared with a proportional-integral (PI) controller in feedback and an optimal control strategy. Importantly, it is demonstrated that adaptive control can compensate for large uncertainties in the climate model parameters, in the dynamics of the actuators considered as well as in cases of abrupt perturbations. It therefore offers a robust strategy for closed-loop deployment of SRM. In particular, the method is demonstrated to be of critical importance in the case of unknown perturbations, such as lack of information on key parameters of the climate model or a partial failure of the actuators.

Robustness is demonstrated through introducing significant changes in the model parameters in Section 5.2 and comparing the results of two different control strategies. Moreover, the robustness of the adaptive controller is further tested in Section 5.3 where a scenario involving an abrupt perturbation is considered and in Section 5.4 where the dynamics of stratospheric aerosols is considered. Again, the 3-box model with multiple control inputs allows such issues to begin to be addressed, albeit at coarse length-scales.

Moreover, in Section 5.5, a constrained optimal control strategy is applied to the 3-box model considering the theory of calculus of variations. This section provides insight on feasible SRM

strategies with a given constrained economic effort. In particular, a generic control law, representing the trend of required insolation reduction, is found for case (c) described in Chapter 4 and results are discussed and compared with the adaptive control performance.

Finally, in Section 5.6, the 3-box model is expanded to 5 boxes to provide higher resolution of the polar bands. This modification of the model is employed to investigate effects of a collapse of the Arctic ice sheet and the required insolation reduction to counteract the resulting change of albedo. The analysis also demonstrates the utility of low order models to quickly investigate new climate engineering feedback control strategies.

5.2 Management of uncertain parameters in the three-box model

Simulations developed in this section are used to illustrate a comparison between the implementation of PI and adaptive control in case (3) of Table (4.2).

In particular, an ideal PI controller is designed and tuned in order to minimise the temperature anomaly in the three latitudinal bands for case (3) of Table (4.2). This analysis is employed as a base-line in order to later compare its performance with adaptive control methods. PI control is used for this purpose in order to make easy comparisons with results from the literature where PI control is widely employed.

It is important to highlight that matrices K_p and K_i are designed with the LQR method for a generic case where the temperature anomaly needs to be minimised in all latitudinal bands (case (c)). After that, the same controller is tested in cases when changes occur in either the plant model, or in the actuator dynamics, or in case of sudden perturbations. It needs to be noted that the controller has not been modified purposely to have insight on the sensitivity of PI control with respect to adaptive control.

The control law employed is given by the expression in Eq. (3.50), which can be rewritten as:

$$\mathbf{U} = -K_P\,\boldsymbol{\zeta} - K_I \int_0^t \boldsymbol{\zeta}\; dt \tag{5.1}$$

with K_P and K_I matrices (3x3), given by the proportional and integral gain matrices, whose components are found through linear quadratic regulator (LQR) optimisation (see Section 3.6.1 for details). In this case, because of the coupling between the three boxes in the climate model,

both the matrices are completely full. Their expressions are:

$$K_P = \begin{pmatrix} 3.214 & 0.084 & -0.00084 \\ 0.3191 & 0.4606 & 0.151 \\ -0.00082 & 0.0399 & 0.0399 \end{pmatrix} \tag{5.2}$$

$$K_I = \begin{pmatrix} 0.053 & 0.0025 & -0.00027 \\ -0.01494 & 0.0312 & -0.0071 \\ -0.0003 & 0.0012 & 0.0533 \end{pmatrix} \tag{5.3}$$

It will be showed that adaptive control is able to tolerate larger uncertainties in the parameters of the plant model with respect to a PI controller, providing good performance in all circumstances.

Thus, simulations are performed where the three main parameters of the 3-box model (the heat capacity C_i ($i = 1,2,3$), the transport coefficient k_i ($i = 1,2,3$) and the infra-red parameter b_i ($i = 1,2,3$)) are modified and the system's response is investigated in the cases when the adaptive and the PI controller are employed. In particular, three sets of climate parameters are reported in Table (5.1) for the northern and southern band and the central band. Values in Table (5.1) are obtained considering slight variations around the nominal values considered in Section 4.2 and values of the climate parameters found in [157], where the global thermal properties of 16 AOGCMs participating in phase 5 of the Coupled Model Intercomparison Project (CMIP5) are determined.

Table 5.1: Sets of climate parameters considered for the three latitudinal bands in order to compare adaptive and PI control strategies.

Case	C_1	k_1	b_1	C_3	k_3	b_3	C_2	k_2	b_2
I	3.2	0.649	1.675	7.04	0.2325	1.195	5.12	0.44	1.8
II	6	1.049	2.675	10.04	0.5325	1.995	8.02	0.79	2.9
III	10.54	1.249	2.175	12.04	0.6325	2.045	11.29	0.94	2.5

As will be seen, the PI control shows deteriorated performance when the model parameters drift from their nominal values. In particular, an issue is found in the minimisation of the temperature anomaly in the northern and southern bands: plots in the bottom of Figs. (5.1-5.3-5.5)

show that control with the PI controller in feedback is not able to correctly track the dynamics of the state and drive the anomalies to zero. Although the temperature anomaly for the central band is minimised, the control strategy is not considered successful because it is not effective in the other latitudinal bands. Moreover, it is noticeable that with a larger drift of the model parameters it is more unlikely that the control is effective (see case I in the bottom plot of Fig. (5.1)), therefore PI control is considered unreliable with major uncertainties in the climate model. Whereas, plots in the top of Figs. (5.1-5.3-5.5) indicate that adaptive control provides good performance in all cases considered and no marked variations are reported with respect to the nominal case.

Therefore, as expected, the simulations with PI control demonstrate that the controller is rather sensitive to the parametrisation of the climate model. The results do not provide acceptable solutions and the control methods cannot be considered as robust as adaptive control techniques in dealing with the inevitable large (and unknown) uncertainties of the climate system.

As can be seen in Figs. (5.1-5.5), when comparing PI and adaptive control, the temperature anomaly is not completely minimised in any of the three cases. In particular, in case I, where the smallest drift of parameters is considered, the temperature anomaly is reduced in the central band but, at the same time, becomes negative in the northern band and does not decrease to zero in the southern band. In fact, as can be seen in Fig. (5.2), the controller overestimates the amount of insolation reduction needed in the northern band and underestimate the amount needed in the southern band. Whereas, in cases II and III the solution does not converge and, as can be seen in Figs. (5.4,5.6), the required insolation reduction is wrongly evaluated in the northern and southern bands because the control gains are not chosen purposely for this task.

Thus, Pi control cannot be considered as reliable as adaptive control in dealing with highly-uncertain models.

A key point to note is that, since adaptive control demonstrates robustness to large uncertainties in the climate model employed, the fidelity of the model used is of less importance if this control strategy is considered.

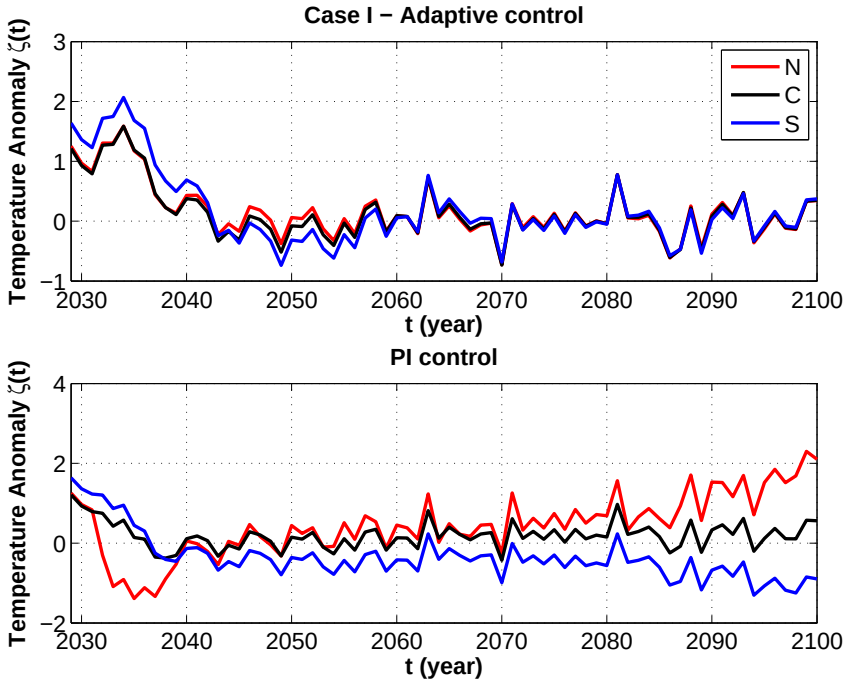

Figure 5.1: Trend of temperature anomaly with adaptive control (top) and PI control (bottom) applied to the three latitudinal bands for the first sets of climate parameters (see case I in Table (5.1)).

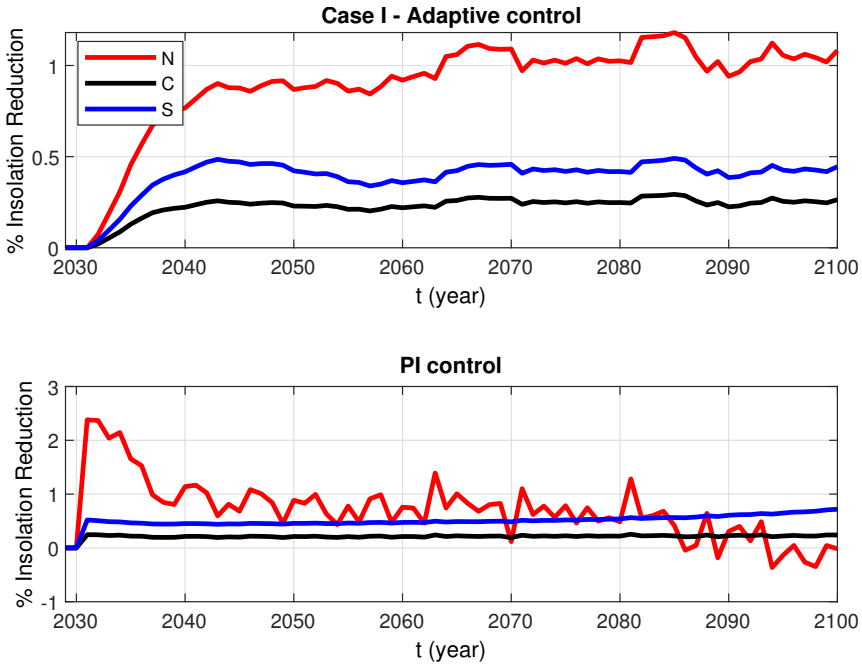

Figure 5.2: Insolation reduction required when adaptive control (top) and PI control (bottom) are applied to the three latitudinal bands for the first sets of climate parameters (see case I in Table (5.1)).

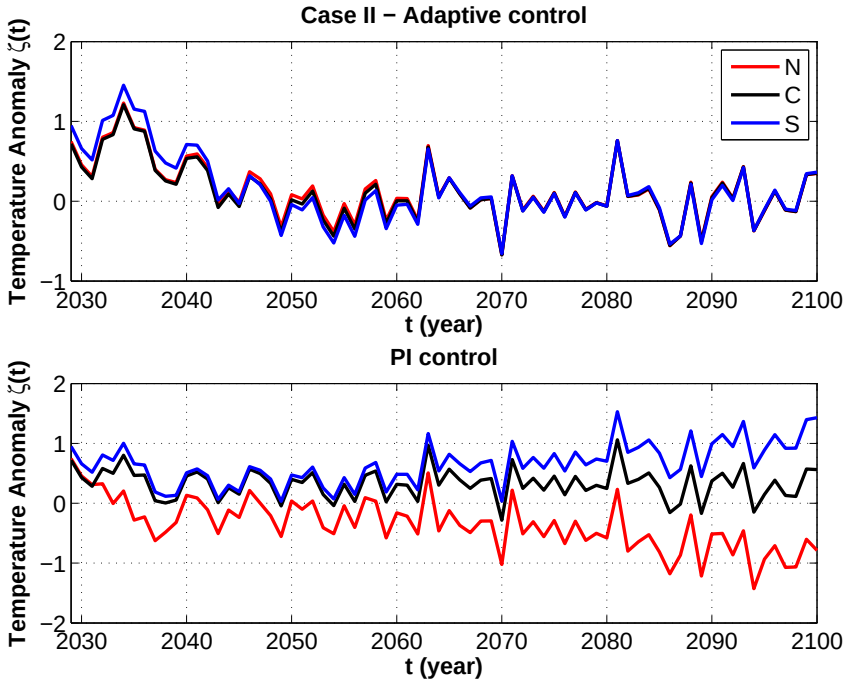

Figure 5.3: Trend of temperature anomaly with adaptive control (top) and PI control (bottom) applied to the three latitudinal bands for the second sets of climate parameters (see case II in Table (5.1)).

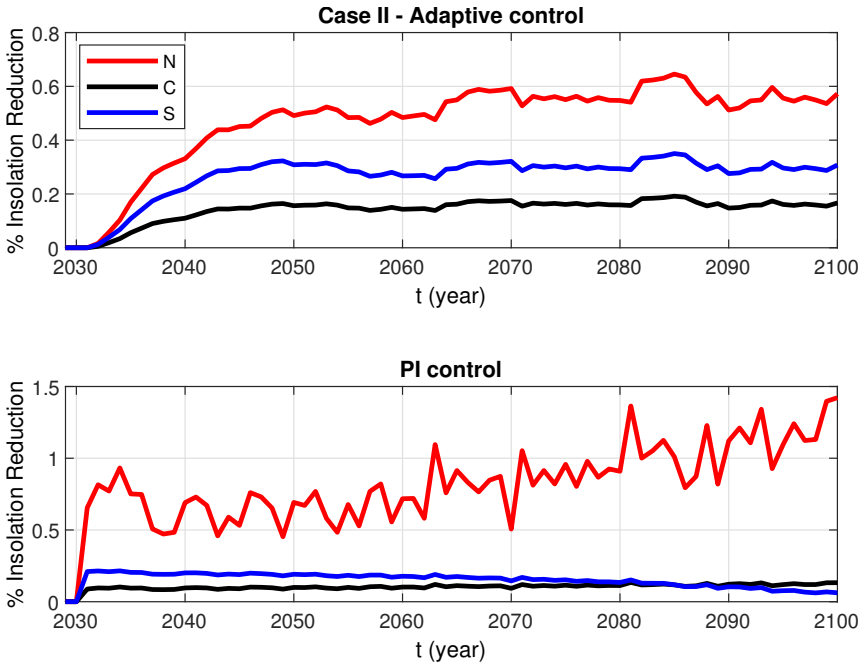

Figure 5.4: Insolation reduction required when adaptive control (top) and PI control (bottom) applied to the three latitudinal bands for the second sets of climate parameters (see case II in Table (5.1)).

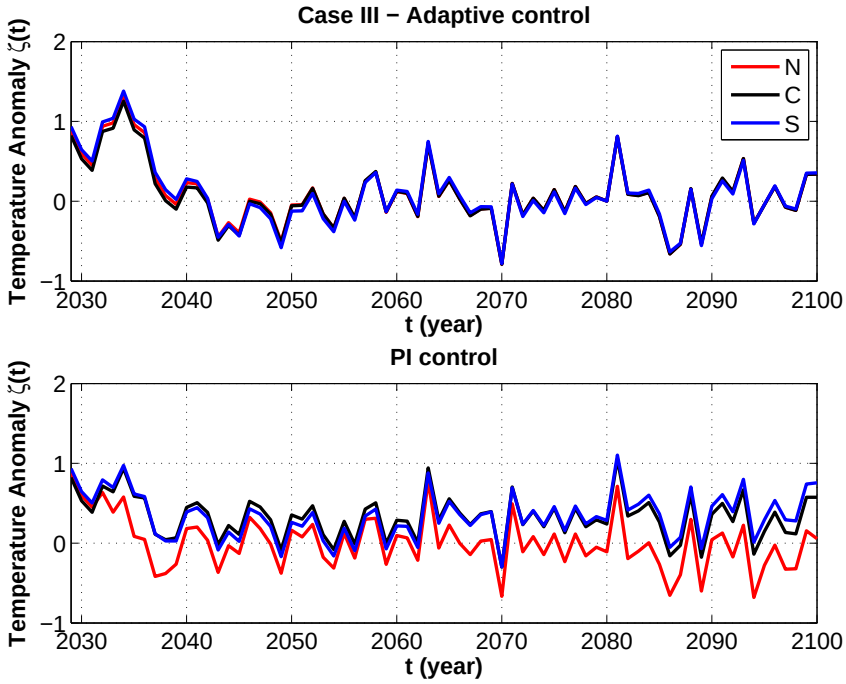

Figure 5.5: Trend of temperature anomaly with adaptive control (top) and PI control (bottom) are applied to the three latitudinal bands for the third sets of climate parameters (see case III in Table (5.1)).

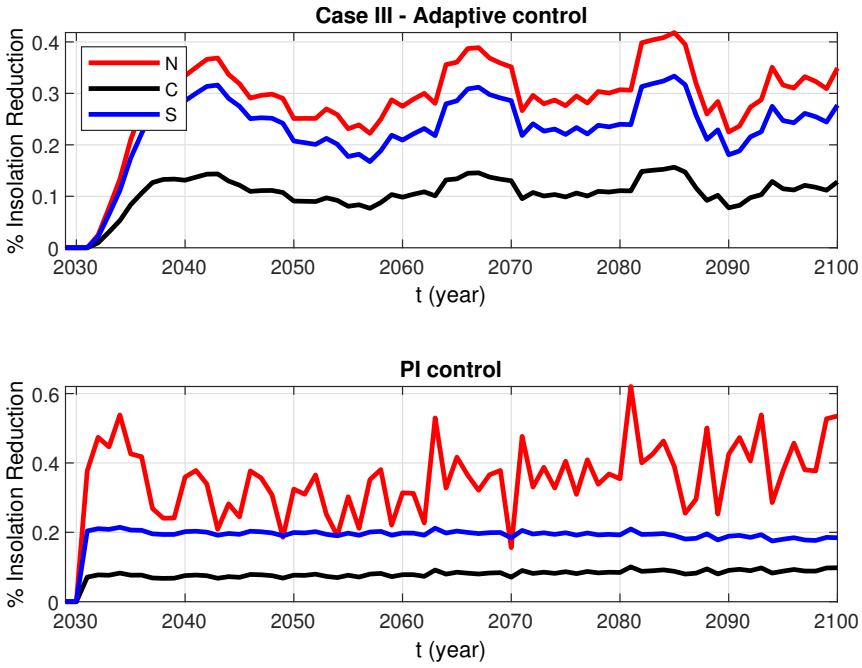

Figure 5.6: Insolation reduction required when adaptive control (top) and PI control (bottom) are applied to the three latitudinal bands for the third sets of climate parameters (see case III in Table (5.1)).

5.3 Unforeseen major perturbations

In the previous section it was demonstrated that adaptive control is able to deal with large uncertainties in the climate model by up-dating the control parameters as required to minimise the temperature anomalies. A further interesting analysis regards the possible occurrence of unforeseen major perturbations, such as a sudden partial failure of the climate engineering intervention. In principle this event could be caused, for example, by the deterioration or failure of one or more actuators (of whatever type) during the course of the implementation of the climate engineering strategy.

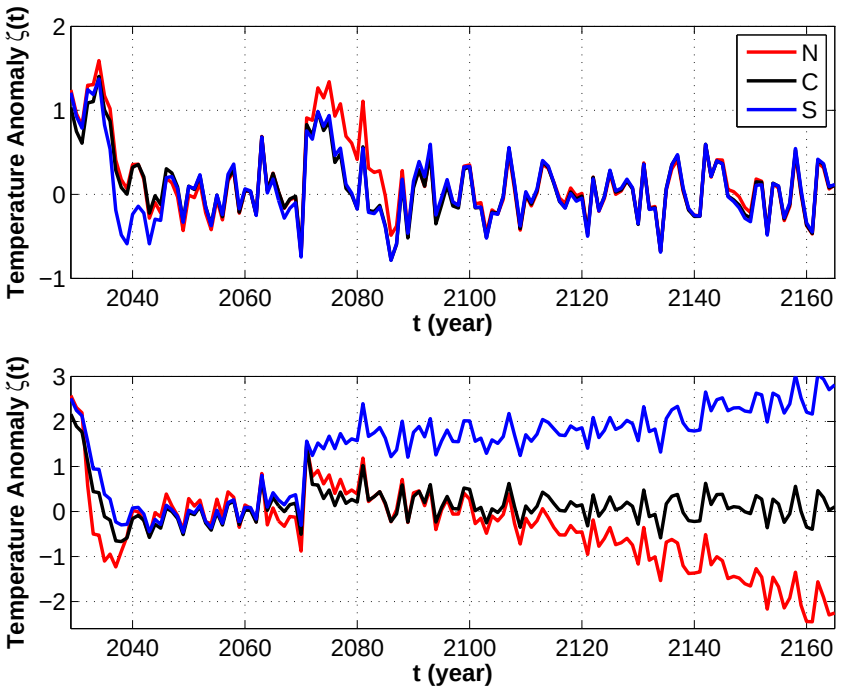

Figure 5.7: Temperature anomalies for the three latitudinal bands with a sudden disruption of SRM occurring at 2065 with the application of adaptive control (top) and PI control (bottom).

In particular, in this section, employing the control law in Eq. (3.50) with the gain matrices in Eq. (5.2), it is assumed that in 2065 the actuators in the northern and southern latitudinal bands become only 50 % efficient (actuator effectiveness is only 50% of the commanded effort).

In these circumstances, the performance of adaptive control and PI control are considered and the results found in top and bottom of Fig. (5.7), respectively. In the simulations, in both cases, a large perturbation occurs at 2065, where the control effectiveness of the temperature anomaly in the northern and southern bands is reduced by 50%. In the case of the adaptive control, the controller parameters are automatically adjusted in order to counteract the perturbation in these

new circumstances. Specifically, the adaptive control registers the change, increases the control effort in the central band and so provides the required control in the northern and southern bands through the coupling between the boxes via heat diffusion. Whereas, when PI control is applied (bottom of Fig. (5.7)), the temperature anomaly in the central band is minimised but in the other bands diverges reaching approximately $-2.1°C$ in the northern band and $3°C$ in the southern band.

In this section it is demonstrated that adaptive control is of critical importance in effectively compensating unforeseeable perturbations and failures in the climate engineering system, whereas the PI controller is not able to deal with these abrupt changes.

5.4 Adaptive and PI controller with aerosol dynamics

Hitherto, a generic control function ($\mathbf{U}$) representing the reduction of the incoming solar radiation has been considered in the closed loop control system and the performance of adaptive and PI control have been considered in several scenarios (variation of the system's parameters in Section 5.2, and abrupt disruption of SRM in Section 5.3).

In this section, the robustness of adaptive and PI control methods is investigated in the case when a specific actuator is chosen. Among SRM methods, the emission of sulphate aerosols in the stratosphere is now considered in the closed-loop control system.

Here, the model employed considers the decay process of aerosol particles from the stratosphere in each latitudinal band and the poleward diffusion of aerosols injected in the central band. More detailed models describing the aerosols dynamics can be found in [91, 92, 96].

Therefore, considering the latitude-average aerosol radiative forcing described in Section 3.4 [112], the first-order dynamics of the control inputs can be written as a 3-components vector as follow:

$$\frac{dU_i}{dt} = \frac{S_i}{2}\mathcal{T}_a^2(1-A_c)\omega_i\beta_i(1-R_s)^2\tau_{0_i}(t)\, e^{-t/\Gamma_i} \qquad i = 1,2,3 \tag{5.4}$$

where U_i are the components of the control vectors also found in Eqs. (4.1-4.3) and Γ_i (i=1,2,3) denotes the time constant associated with the rate of removal of aerosols, which is of order 1 *year* for stratospheric aerosols in the central band (Γ_2) and 3 *months* for aerosols in the northern and southern bands (Γ_1, Γ_3) [59]. As can be seen from Eq. (5.4), aerosol dynamics depends on the

incident radiation properties (S_i is the incoming solar radiation in the i^{th} band, as discussed in Section 4.2), the optical properties of the atmosphere ($\mathcal{T}_a$, A_c and R_s are defined in Section 3.4) and the optical properties of aerosols (single scattering albedo $\omega_1 = \omega_3 = 0.9$, $\omega_2 = 0.5$ [113], aerosol optical depth $\tau_i(t)$ $(i = 1,2,3)$, average up-scatter fraction $\beta_1 = \beta_3 = 0.21$, $\beta_2 \notin^{\smile} = 0.27$ [111]).

Considering Eq. (5.4), the dynamics associated with the removal of the aerosol particles can be expressed through a first order transfer function for each latitudinal band that links the actuated and the commanded control, U_{ai} and U_{ci} (i=1,2,3) respectively. A simple proportional term is considered for the diffusion from the central band to the northern and southern bands. These relationships are summarised for each latitudinal band as follow:

$$U_{a_1}(s) = \frac{1}{\Gamma_1 s + 1} U_{c_1}(s) + k_d U_{a_2}(s) \tag{5.5}$$

$$U_{a_2}(s) = \frac{1}{\Gamma_2 s + 1} U_{c_2}(s) - 2k_d U_{a_2}(s) \tag{5.6}$$

$$U_{a_3}(s) = \frac{1}{\Gamma_3 s + 1} U_{c_3}(s) + k_d U_{a_2}(s) \tag{5.7}$$

where k_d is a diffusion coefficient set to 0.05 as in [158], where the latitudinal diffusion of the aerosol particles ejected after the eruption of El Chicon is considered.

These expressions are used directly in the closed-loop system for the three latitudinal bands in order to take into account the decay process of aerosol particles and their poleward diffusion while the control laws are estimated. The altitude of injection is set to 25 km for the central band and to 20 km for the northern and southern bands [59].

Finally, in order to make comparisons with results from the literature, the emission rate of the aerosol particles ($Tg/year$) is estimated through the following expression [159]:

$$E_{a_i} = \frac{d B_{a_i}(t)}{dt} \qquad i = 1,2,3 \tag{5.8}$$

where $B_{a_i}(t)$ is the mass (Tg) of aerosol particles (or sulphur burden [112]) in the i^{th} latitudinal

band and is given by:

$$B_{a_i}(t) = M_{a_i}(t)A_i \qquad i = 1,2,3 \tag{5.9}$$

Here, $M_{a_i}(t)$ is the aerosol mass concentration of the i^{th} band reported in Eq. (3.25) and A_i ($i = 1,2,3$) is the area covered given by 13.9% for the poles (from $65°N$ to $90°N$ and from $65°S$ to $90°S$) and 72.2% (from $65°S$ to $65°N$) for the central band. In order to compare the results with data in the literature, the mass of aerosol particles is converted into units of sulphur according to [57], where the following equivalence is reported: $4\ Tg\ S = 1\ Tg$ of aerosol particles.

Therefore, applying adaptive control and PI control to case (c) of Table (4.2) and considering the aerosol dynamics described above in the closed-loop control system, Figs. (5.8-5.9) are obtained.

In particular, Fig. (5.8) shows the trend of the temperature anomalies and the time history of the required sulphur burden for each band when adaptive control is applied. Whereas, Fig. (5.9) shows results when the PI control is applied.

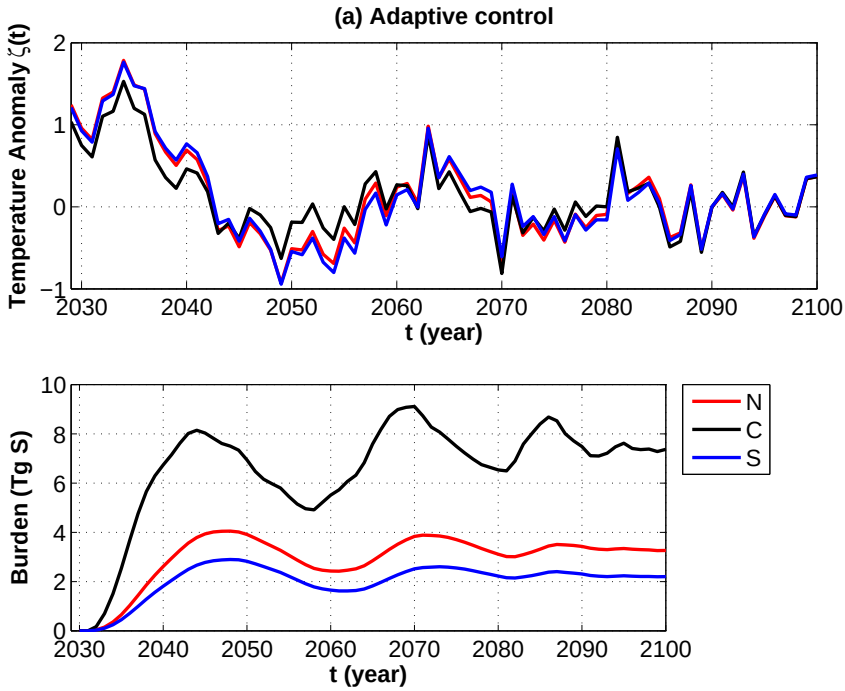

Figure 5.8: Trend of the temperature anomalies for the three latitudinal bands (top) and required sulphur burden ($Tg\ S$) (bottom) when adaptive control is applied to the 3-box model.

It is important to note that the control parameters employed for the two control methods are

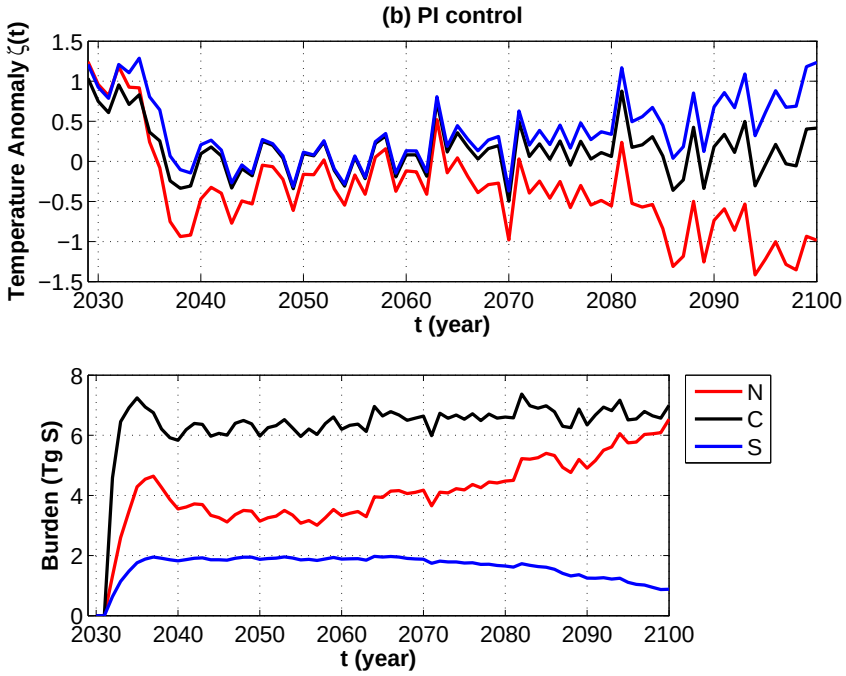

Figure 5.9: Trend of the temperature anomalies for the three latitudinal bands (top) and required sulphur burden ($Tg\ S$) (bottom) when PI control is applied to the 3-box model.

the same used to minimise the temperature anomalies with a generic SRM control function as in Chapter 4 and Section 5.2. Specifically, the control parameters reported in Eqs. (4.26)-(4.27.c)-(4.30) are employed for the adaptive control and those found in Eq. (5.2) for the PI control.

The analysis aims to demonstrate that the control parameters for the adaptive control do not depend on the SRM strategy considered, demonstrating that this method is robust to the choice of the actuator employed. This result is shown in Fig. (5.8) where the temperature anomalies are minimised in all latitudinal bands when adaptive control is employed. Whereas, for the PI control, it can be seen in Fig. (5.9), that the temperature anomalies largely diverge, specifically in the northern and southern bands, where they reaches $\approx -1°C$ and $\approx 1.3°C$, respectively. Adaptive control is able to deal with aerosol diffusion because the control gains are updated during every iteration in order to minimise the temperature anomaly while also considering the actuator dynamics. For this reason, it is also expected that in case the aerosol dynamics are different from that assumed here, or another actuator is considered, an adaptive controller would be able to minimise the temperature anomaly and to estimate the required SRM effort. In the case of PI control, the control gains need to be selected for every specific case because once chosen they are not automatically up-dated; therefore, when different actuator dynamics are considered, the

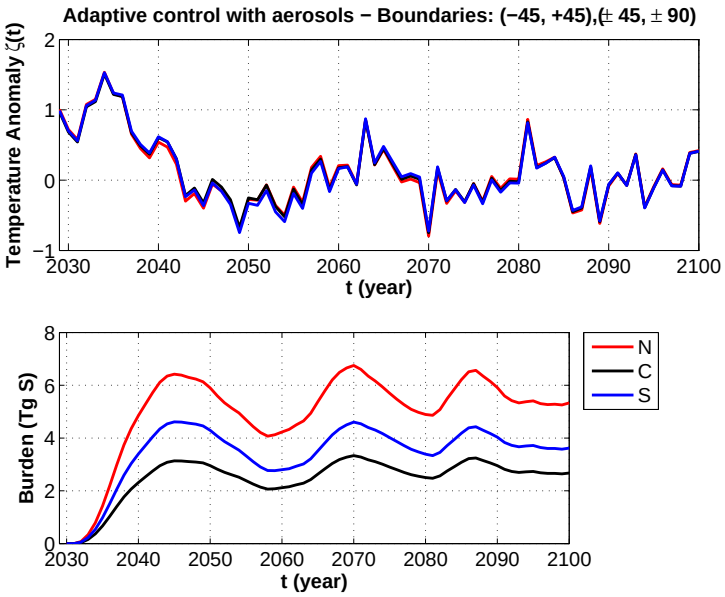

Figure 5.10: Trend of the temperature anomalies for the three latitudinal bands (top) and required sulphur burden ($Tg\ S$) (bottom) when adaptive control is applied to the 3-box model with new regional boundaries: $(-45°, +45°)$ for the central band and $(\pm 45°, \pm 90°)$ for northern and southern band.

PI control does not deliver the same performance.

With regards to the sulphur burden, in order to offset the radiative forcing from the $RCP4.5$ scenario (see Fig. (4.2)), the time-decay of the aerosol particles and their poleward diffusion from the central band, the aerosol mass needs to increase with time. In particular, at the bottom of Fig. (5.8), the aerosol mass shows a periodic trend with a steady increase up to $\approx 8\ Tg\ S$ in the central band, whereas the concentration in the northern and southern bands rises up to only $2-3\ Tg\ S$. Otherwise, in Fig. (5.9), the trend of the aerosol burden (bottom figure) reaches a peak of $6\ Tg\ S$ for the central band, providing sufficient insolation reduction to minimise the temperature anomaly. Whereas, with PI control an incorrect estimation of the required control is found for the northern and southern bands due to the fact that the control parameters are not taking the aerosol dynamics into account.

Values of the sulphur burden in Fig. (5.8) are in accordance with values found in [160] (see Table (2) in [160]) for a given value of the optical depth for aerosol deployed at approximately 25 km ($30hP$).

Case (c) of Table (4.2) is the most critical because it involves the control of the temperature anomaly in the central band, which is higher than the other two bands. However, the required

emission rates are still within an acceptable range of values: around $0.6 - 0.4\ Tg\ S$ per year in the northern and southern bands, respectively, and around $2\ Tg\ S$ per year in the central band. Although comparison with the literature is complicated because the experiments differ in size, area of injection and environment, in [161] a similar experiment with the $RCP4.5$ scenario has been performed and an emission rate of $6\ Tg\ S/yr$ found (in an open-loop simulation) to counteract radiative forcing [160].

Moreover, GeoMIP (Geoengineering Model Intercomparison Project) experiment G3 considers an emission rate of $5\ TgSO_2$ per year ($2.5\ Tg\ S/yr$) on the equator to balance the $RCP4.5$ scenario with stratospheric aerosols for the period between 2020 and 2070 [162].

Moreover, the 3-box model can be employed to evaluate the influence of the boundaries chosen for the three latitudinal bands. Thus, assuming the new boundaries, given by $(-45°, 45°)$ for the central band and $(\pm 45°$ to $\pm 90°)$ for northern and southern bands, the analysis of adaptive control with sulphur aerosols dynamics is performed again. The results are reported in Fig. (5.10) and it is found that, choosing boundaries closer to mid-latitudes causes the behaviour of each box to become similar to each other, loosing some information on the most important differences between the polar and central regions. This effect is particularly visible for the northern and southern bands in Fig. (5.10).

Also, as expected, considering the new boundaries, it is found that the distribution of aerosols required is different in each band with respect to the previous case investigated, but the overall quantity of aerosols is estimated to be the same in both cases, as expected (see Fig. (5.10) for comparison). This result highlights the independence of the aerosol injection strategy from the boundaries of the 3-box model.

5.5 Comparison of adaptive and constrained optimal control

This section considers the implementation of the optimal control theory described in Section 3.6.3 with constraints on the magnitude of the control variables. This analysis will be used to assess the possibility of enforcing engineering constraints on the closed-loop system and to compare the results with the outcomes from the implementation of adaptive control in Chapter 4. The constrained variable U represents the economic effort needed to accomplish the SRM strategy, such as the deployment of space shields or the injection of sulphur aerosol. It is therefore an index of the global cost required to implement climate engineering through SRM.

Using the calculus of variations [128] a functional J of the form reported in Eq. (3.60) can be minimised. Considering the system summarised by Eqs. (4.6)-(4.7) and Eq. (3.60), the index of performance to be minimised under the constraint $\dot{\boldsymbol{\zeta}} = A\boldsymbol{\zeta} + \mathbf{F}(t) + B\mathbf{U}$ can be written as:

$$J(\boldsymbol{\zeta}, \mathbf{U}, t) = \boldsymbol{\zeta}(t_f) + \int_{t_0}^{t_f} \frac{1}{2}\mathbf{U}^2(t) + \boldsymbol{\mu}^T(t)(A\mathbf{x} + B\mathbf{u} + \mathbf{F}(t) - \dot{\mathbf{x}}) \;\; dt \tag{5.10}$$

with $\mathbf{0} < \mathbf{U} < \mathbf{U}_{max}$ and where the state $\boldsymbol{\zeta}$ at the final time t_f and the integrated state variables and controls between t_0 and t_f are considered. The vector $\mathbf{U}_{max}$ is the maximum insolation reduction allowed in the three latitudinal bands which can be used to enforce engineering constraints.

The variables $\mathbf{U}_i$ $(i = 1,2,3)$ are constrained between 0 and the maximum control value $U_{i_{max}}$ $(i = 1,2,3)$. Reasonable values are chosen for $U_{i_{max}}$ $(i = 1,2,3)$ as follow:

$$\mathbf{U}_{max} = \begin{pmatrix} 0.012 \\ 0.012 \\ 0.012 \end{pmatrix} \tag{5.11}$$

As will be seen later, the maximum required reduction in solar insolation does not rise above 1.2%, enforcing the required constraint defined by Eq. (5.11).

The Hamiltonian function can now be written as follow [128]:

$$H(\boldsymbol{\zeta}, \mathbf{U}, \boldsymbol{\mu}, t) = \mathbf{U}^2 + \boldsymbol{\mu}^T(t)(A\mathbf{x} + B\mathbf{u} + \mathbf{F}(t)) \tag{5.12}$$

Following Section 3.6.3, conditions to satisfy in order to minimise Eq. (5.10) involve the co-state dynamics, stationary condition of the Hamiltonian function and boundary conditions. The co-state dynamics (from Eq. (3.64)) for this problem are summarised as:

$$\dot{\mu_1} = -\frac{\partial H}{\partial \zeta_1} = -\left(j_{11}\lambda_1 + j_{21}\lambda_2\right) \tag{5.13}$$

$$\dot{\mu_2} = -\frac{\partial H}{\partial \zeta_2} = -\left(j_{12}\zeta_1 + j_{22}\zeta_2 + j_{32}\zeta_3\right) \tag{5.14}$$

$$\dot{\mu_3} = -\frac{\partial H}{\partial \zeta_3} = -\left(j_{23}\zeta_2 + j_{33}\zeta_3\right) \tag{5.15}$$

where the j-terms are given by the components of the state matrix (A) in Eq. (4.6). The stationary

condition (from Eq. (3.65)) provides:

$$\begin{aligned} \mu_1(t) &= -u_1^*(t)C_1 \\ \mu_2(t) &= -u_2^*(t)C_2 \\ \mu_3(t) &= -u_3^*(t)C_3 \end{aligned} \tag{5.16}$$

where $u_i^*(t)$ $(i = 1,2,3)$ are the optimal control laws for the three bands that minimize the Hamiltonian function, as seen in Eq. (3.66).

Furthermore, Eq. (3.67) becomes:

$$\begin{aligned} \mu_1(t_f) &= 1 \\ \mu_2(t_f) &= 1 \\ \mu_3(t_f) &= 1 \end{aligned} \tag{5.17}$$

According to Pontryagin's minimum principle, the optimal control $\mathbf{U}^*$ is given by the vector $\mathbf{U}$ that minimizes the Hamiltonian function according to Eq. (3.66).

Thus, in order to solve the optimisation problem it is necessary to solve the state dynamics with initial conditions on the temperature anomaly ζ_i $(i = 1,2,3)$ and the co-state dynamics with the final conditions for μ_i, $(i = 1,2,3)$ reported in Eq. (5.17). Then, once the co-state dynamics are known, following Eq. (5.16), it is possible to estimate the optimal control law (u^*).

This control strategy is applied to case (c) of Table (4.2), for which the objective is to minimise the temperature anomalies in all the three bands. An appropriate control law that minimizes the functional $J(\boldsymbol{\zeta}, \mathbf{U}, t)$ in Eq. (5.10) is obtained. Results of the simulation can be found in Fig. (5.11), where the trend of the temperature anomaly under the $RCP45$ scenario in the three latitudinal bands is found for the period between 2030, when SRM is deployed, and 2045, when the temperature anomalies are reduced in all the latitudinal bands. It is found that the control law provides the required insolation reduction which minimises the temperature anomaly in all latitudinal bands in 15 years and requires a maximum reduction in insolation of 1.2% (in the northern band) as specified in Eq. (5.11). The reduction of the temperature anomaly in Fig. (5.11) is obtained considering a maximum reduction in solar insolation of 1.2% in each band, which provides a negative radiative forcing of 13.43 W/m^2 in the central band and $5.38 - 6.36$ W/m^2 in the northern and southern band, respectively. The main difference that can be noted with respect to results from adaptive control applied in case (c) is that the temperature anomaly

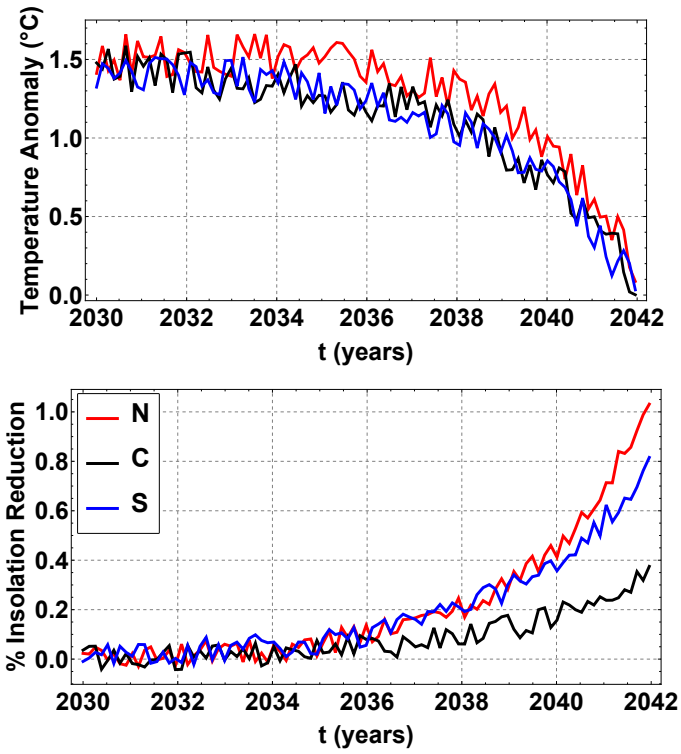

Figure 5.11: Trend of the temperature anomaly and required insolation reduction when a constrained optimal controller ($\boldsymbol{U}_{max} = (0.012, 0.012, 0.012)$) is applied to the 3-box model to minimise the temperature anomalies of all the latitudinal bands (case (c) in Table (4.2)).

is minimised by 2050 when adaptive control is applied, i.e. within 20 years from the implementation of SRM, whereas it requires only 15 years when constrained optimal control is employed. This is justified by the higher insolation reduction required for the optimal control case. Indeed, comparing Fig. (4.5) and Fig. (5.11), it can be noted that only a 0.8-0.6% reduction of insolation is required in the northern and southern bands against 1.2-1% when optimal control is employed. This last value for insolation reduction can be easily reduced by decreasing the maximum control magnitude allowed ($\boldsymbol{U}_{max}$). As can be seen in Fig. (5.12), when a smaller $\boldsymbol{U}_{max}$ is considered, more time is required to minimise the temperature anomaly; in fact ≈ 24 *years* are required if a maximum insolation reduction of 0.9% is considered.

Moreover, as for PI and adaptive control in Section 5.2, performance of the constrained optimal control and, in particular, robustness to uncertainties are investigated for the three set of climate parameters in Table (5.1). However, since optimal control is not known to be robust to uncertainties, this analysis is considered of secondary importance with respect to the implementation of PI and adaptive control and results are only briefly discussed in this section. Indeed, the estimation of the co-states, described in this section, is a difficult process that needs to be

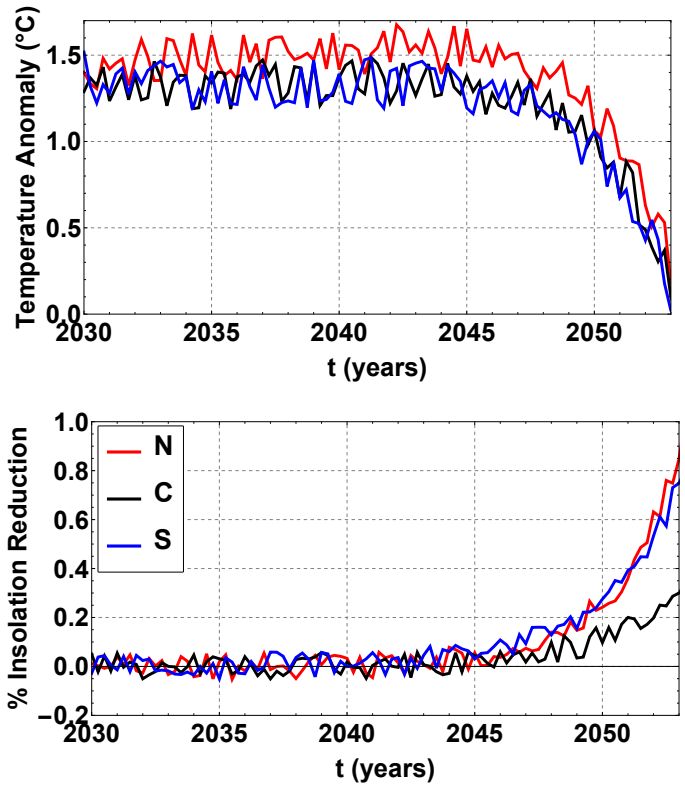

Figure 5.12: Constrained optimal control ($\boldsymbol{U}_{max} = (0.009, 0.009, 0.009)$) applied to the 3-box model to minimise the temperature anomalies of all the latitudinal bands (case (c) in Table (4.2)).

developed with high accuracy. Therefore, it is expected that this control strategy would be susceptible to large uncertainties. It is found that, in case I, where the smallest drift of parameters is considered, the temperature anomaly begins to be reduced in the three bands (from $\sim 3°C$ to $\sim 0.8 - 1°C$) only in the final years of the simulation. Whereas, in cases II and III the optimisation does not converge and it is not possible to estimate the required control. Thus, as expected, optimal control is not able to deal with highly uncertain models.

5.6 Performance of adaptive control with collapsing ice-sheet in a 5-box climate model

In this section, the 3-box model is modified in order to take into account the climate conditions near the North Pole and South Pole. In fact, between $\pm 70°$ and $\pm 90°$ ice sheets provide a considerably different albedo with respect to any other region on Earth with the Arctic and Antarctic albedo as high as 0.6-0.7 [100]. Several analytical climate models in the literature consider a

step function albedo in order to model the insolation of these regions [97], but these are difficult to manage and can easily generate mathematical artefacts [149].

Otherwise, the 3-box model can be easily expanded to n-boxes, following the structure in Eqs. (4.1-4.3), and so provides a useful tool to quickly investigate the effect of climate engineering over the polar regions and their interaction with the other latitudinal bands.

Thus, the 3-box model becomes a 5-box model considering the following subdivision: southern polar band $(-90°, 70°)$, southern band $(-70°, -50°)$, central band $(-50°, 50°)$, northern band $(50°, 70°)$, northern polar band $(70°, 90°)$. This model can be written as follow:

$$C_n \frac{dT_n(t)}{dt} = Q_0 S_n(1-\alpha_n) - (a_n + b_n T_n) - k_n(T_n - T_1) + F_{ext} + U_n \tag{5.18}$$

$$C_1 \frac{dT_1(t)}{dt} = Q_0 S_1(1-\alpha_1) - (a_1 + b_1 T_1) - \frac{1}{2}k_1(T_1 - T_n) - \frac{1}{2}k_1(T_1 - T_2) + F_{ext} + U_1 \tag{5.19}$$

$$C_2 \frac{dT_2(t)}{dt} = Q_0 S_2(1-\alpha_2) - (a_2 + b_2 T_2) - \frac{1}{2}k_2(T_2 - T_1) - \frac{1}{2}k_2(T_2 - T_3) + F_{ext} + U_2 \tag{5.20}$$

$$C_3 \frac{dT_3(t)}{dt} = Q_0 S_3(1-\alpha_3) - (a_3 + b_3 T_3) - \frac{1}{2}k_3(T_3 - T_2) - \frac{1}{2}k_3(T_3 - T_s) + F_{ext} + U_3 \tag{5.21}$$

$$C_s \frac{dT_s(t)}{dt} = Q_0 S_s(1-\alpha_s) - (a_s + b_s T_s) - k_s(T_s - T_3) + F_{ext} + U_s \tag{5.22}$$

In particular, for the northern polar band the model parameters are $C_n = 4.2\ W\ yr/m^2/°$, $S_n = 176.56\ W/m^2$, $\alpha_n = 0.6665$, $b_n = 1.45\ W/m^2/°$, $k_n = 0.52\ W/m^2/K$; and for the southern polar band $C_s = 6.5\ W\ yr/m^2/°$, $S_s = 194.21\ W/m^2$, $\alpha_s = 0.7095$, $b_s = 1.47\ W/m^2/°$, $k_s = 0.76\ W/m^2/K$ [100, 131].

As before the $RCP4.5$ radiative scenario is considered as a uniformly distributed external disturbance. However, in this case, for example, it is now assumed that in 2060 a major collapse of the ice sheet in the Arctic (northern polar band) occurs. Consequently, a rapid reduction of the Arctic albedo (1% per year) takes place. In this simulation, SRM is deployed in 2030 with an adaptive controller. Thus, it is expected that the controller adjusts the control gains to counteract the radiative forcing due to increasing CO_2 as well as providing the necessary

insolation reduction in the north polar band when the change in the albedo occurs in 2060.

Results of the simulation can be found in Fig. (5.13), where it can be seen that adaptive control is able to deal with the sudden change in albedo due to the collapsing ice sheets in the Arctic and rapidly provides the required insolation reduction to counteract all external disturbances.

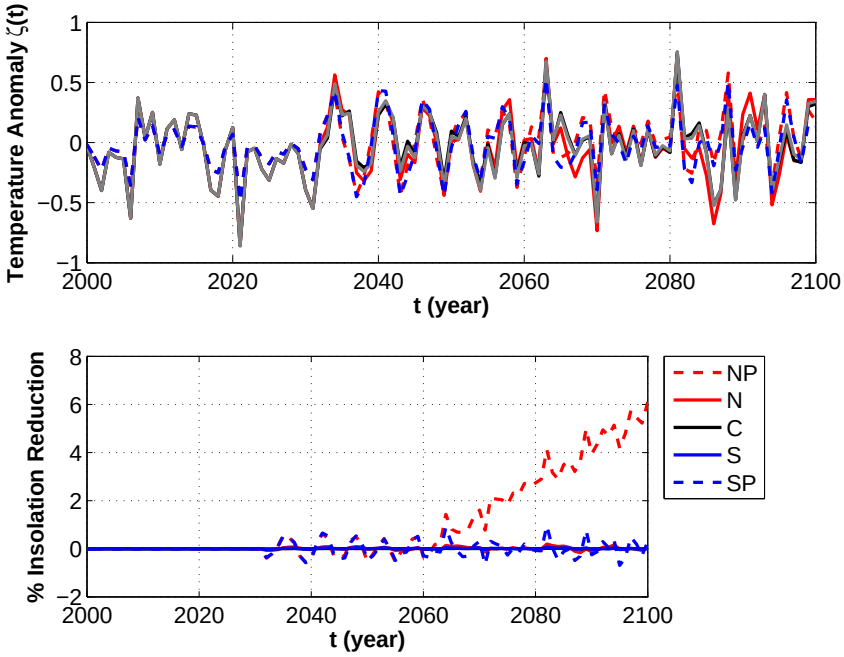

Figure 5.13: Temperature anomalies (top) due to the RCP4.5 scenario and insolation reduction (bottom) for the five latitudinal bands with adaptive control deployed in all the latitudinal bands in 2030 and a collapse of the ice sheet in the northern polar band occurring in 2060.

5.7 Conclusions

Performance and robustness of an adaptive controller for climate engineering has been evaluated and compared with a PI controller and an optimal control strategy. Considering variations of the three main model parameters of the 3-box model, adaptive, PI control and constrained optimal control methods have been analysed in order to investigate the susceptibility of the control strategies to uncertainties in the model. Results show that adaptive control is robust to large uncertainties in the climate model itself, de-emphasizing therefore the importance of the model employed. Whereas, as expected, PI control and constrained optimal control show poor performance when large variations from the nominal model parameters are considered and, therefore, they do not provide satisfactory results in any of the cases investigated.

Moreover, adaptive control shows excellent performance in case of unforeseen perturbations, such as a sudden partial failure in the climate engineering intervention in the northern and southern bands. In fact, the controller parameters are automatically adjusted in order to counteract the perturbation in these new circumstances. In this case results from the implementation of the PI control show poor performance in the northern and souther bands.

Finally, it has been demonstrated that adaptive control is also robust to the choice of the method employed to deploy SRM. When the dynamics of stratospheric sulphur aerosols is considered as the actuator in the closed loop system, without modifying the adaptive control parameters, again, the controller is able to respond properly in order to minimise the temperature anomalies in all the latitudinal bands. Also, no significant changes are found with respect to the case where a generic control function is used.

Results indicate that the temperature anomaly under the $RCP4.5$ scenario could be offset in all the three latitudinal bands injecting 0.6-0.4 $Tg\ S/yr$ in the northern and southern bands, respectively, and 2 $Tg\ S/yr$ in the central band. The values estimated for the emission rates are within acceptable bounds and are broadly comparable with results from the literature.

Applying a PI controller in the same circumstances, it is noted that the estimated sulphur burden required to minimise the temperature anomalies is incorrectly estimated in the northern and southern bands leading to poor performance.

Thus, since adaptive control has shown superior performance in several scenarios, it has been chosen as the controller for the last simulation, involving a collapse of the ice-sheets in the Arctic. In particular, in this case extreme climatic conditions of northern and southern polar bands are considered by adding two additional latitudinal bands to the model. Again, adaptive control provided the necessary insolation reduction to counteract radiative forcing due to carbon dioxide as well as a rapid change in albedo caused by the melting ice in the Arctic region.

Therefore, as expected, these simulations demonstrate that adaptive control works well with large uncertainties in the climate model, with unforeseeable perturbations and does not depend on the method chosen to deploy SRM. Since the control gain matrices are updated during every iteration, adaptive control guarantees the convergence of the strategy.

Finally, optimal control strategies have been employed to minimize the temperature anomalies in the three latitudinal bands with two different boundary conditions for the control variables. This control method allows the finding of solution strategies with limited global costs. In particular, it is found that the maximum economic effort required (in terms of insolation reduction)

is directly linked to the time required to accomplish the objective. It is found that, reducing the maximum insolation reduction allowed, more time is required to minimize the temperature anomaly in all latitudinal bands. Thus, this method can be employed to quickly determine the insolation reduction required to minimize the temperature anomaly within a specific period of time.

Chapter 6

Continuous latitudinal climate model for closed-loop control

6.1 Introduction

This chapter aims to approximate the complexity of the climate system with a simple model that takes into account its main features as described in [75], and to develop continuous control laws for climate engineering as a function of latitude. The work therefore builds on the 3-box (and 5-box) models of Chapter 4. Efforts have been made to develop a continuous-time system with latitudinal resolution with which it is possible to explore control strategies to investigate issues related to latitudinal disparities and the side effects of SRM interventions. The use of efficient analytical methods provides a useful tool to rapidly assess SRM strategies with latitudinal resolution and allows efficient application of multi-objective analyses.

Moreover, through this procedure the latitudinal impact of SRM can be directly addressed. In general, the pattern of insolation reduction that can be generated using SRM does not match the pattern of climate change impacts due to increased CO_2.

In fact, despite the simplicity of the model, results which are broadly comparable with the literature [4] are found. This demonstrates the utility of the model in rapidly assessing new climate engineering strategies and control laws. The model can assess the trade-off between the number of degrees of freedom of SRM and the RMS error in latitudinal temperature compensation, for example.

Section 6.2 addresses a mathematical model to describe the climate system with a single

partial differential equation (PDE); here, the analytical solution to compute the temperature perturbation due to atmospheric carbon dioxide (CO_2) is developed. Moreover, several control functions are applied to the model in open-loop control strategies in Section 6.3.2 to analyse the response of the model and show disadvantages of these strategies with respect to closed-loop control methods.

In Section 6.3 a multi-objective control analysis is undertaken with a PI feedback control and the trade-off between number of the considered degrees of freedom and the resulting RMS error in temperature compensation is investigated. Thus, considering the deployment of climate engineering through a reduction of incoming solar radiation, a control law to drive the temperature perturbation to zero is developed. In particular, although in Chapter 5 the superior performance of adaptive control has been demonstrated, a PI control is employed in this section in order to show that the PDE model is able to deliver comparable results with respect to GCMs employed in the literature with PI control.

Finally, in Section 6.4 the PDE model is employed to find the analytical control law to achieve a desired temperature profile when the concentration of carbon dioxide in the atmosphere doubles.

6.2 PDE model for non-uniform climate engineering

In this section, an analytical solution of the dynamical model for the climate system with latitudinal resolution in Eq. (3.12) is found. With respect to [75], where the analytical solution of a one-dimensional equilibrium model with diffusive heat transfer was developed to investigate ice feedback mechanisms, here temperature is also considered as a function of time. Moreover, both hemispheres are considered and differences in land and oceans are taken into account for the computation of capacity. The model is then employed to explore control strategies based on a reduction of insolation. Again, the model is an extension of the multiple box model of Chapter 4, in the asymptotic limit of an infinite number of boxes.

As described in Section 3.1, an energy model [26] is used to describe the main dynamics of the Earth's climate and the diffusion of heat between latitudinal bands. This allows for an evaluation of non-uniform climate engineering strategies. In particular, the model has the advantage of being analytically tractable, allowing new strategies to be efficiently assessed prior to more detailed analysis. Following Eq. (3.12), the PDE system investigated in this chapter can

be summarised as:

$$C\frac{\partial T(x,t)}{\partial t} = Q_0 S(x)\alpha(x,x_s) - (a + bT(x,t)) + \frac{\partial}{\partial x} D(1-x^2)\frac{\partial T(x,t)}{\partial x} \tag{6.1}$$

where the terms have already been defined in Section 3.1.

In general, Eq. (6.1) allows for the computation of the zonally-averaged surface temperature T, as function of the time t and the sine of latitude x. Importantly, the model allows for a range of forcing terms, therefore the presence of CO_2 forcing and a control function representing the deployment of SRM strategies can be included. The solution is constrained by Neumann boundary conditions (Eq. (3.7)) at the poles ($x = \pm 1$) and the equator ($x = 0$).

Increasing the forcing in one hemisphere relative to the other causes a shift of the latitude of zero heat-flux inducing large precipitation anomalies. However, this effect is not taken into account in this chapter in order to keep the analysis manageable. In fact, it is worth noting that the problem in Eq. (6.1) represents a specific non-homogeneous heat equation with boundary conditions which has a known Green function and an analytical solution can be found. This cannot in general be said if other terms depending on time or latitude are included.

Equation (6.1) represents an EBM where the incoming and outgoing energy are balanced and an equilibrium temperature distribution with latitude is reached. Specifically, $T(x,t)$ represents the annual zonally-averaged temperature field. The incoming energy is the solar radiation and the energy losses are given by the effect of the Earth's albedo and the infra-red radiation leaving the top of a latitudinal element. The energy transported by a latitudinal element to its neighbours due to the movement of geophysical fluids is represented by a diffusion process where the transport is proportional to the gradient of the temperature field. In this Chapter, as is shown later, some of these parameters are taken from data in the literature [26, 73, 75] and others are chosen in order to match the time-domain step response of high-fidelity numerical models. In this way it is possible to regulate the equilibrium climate sensitivity of the system which is a key parameter for comparison between climate models. Therefore, the goal of this model is emulating the behaviour of complex numerical models with a more convenient analytical structure to easily (and rapidly) implement climate engineering strategies based on SRM.

The problem is split in two separate processes for the two hemispheres, with the solution found for the Northern hemisphere when $0 < x < 1$ and for the Southern hemisphere when $-1 < x < 0$. This operation allows for a more specific description of the physical processes

in each hemisphere through the use of appropriate parameters. The expression in Eq. (4.4) is employed for the outgoing infra-red radiation, with values for the empirical constants a and b for the Northern and Southern hemispheres reported in Section 4.2.

Moreover, $S(x)$ again describes the distribution of the incident solar radiation averaged over 1 year for which the expression in Eq. (3.5) is considered. Then, $\alpha(x, x_s)$ is the planetary co-albedo at latitude x [75] for which a smooth albedo formulation, that includes the definition of the ice line at $x = x_s$, is considered [137]:

$$\alpha(x, x_s) = \frac{\alpha_w + \alpha_i}{2} + \frac{\alpha_i - \alpha_w}{2} \, tanh\left(M(x - x_s)\right) \tag{6.2}$$

where α_w is the co-albedo of water set to $1 - 0.32$, α_i is the co-albedo of ice set to $1 - 0.55$ and the parameter M represents the steepness of the albedo function near the ice line and is set to 12. The value of x_s for the current climate is set to $x_{s0} = \pm 0.95$ for the Northern and Southern hemisphere, respectively. Moreover, in Eq. (6.1) D is an empirical constant describing the latitudinal transport of energy. Its value for the Northern hemisphere is given by $0.649 \; W/m^2/^\circ C$ [75], whereas the value for the Southern hemisphere is found in order to satisfy the condition $T_N(0, \infty) = T_S(0, \infty)$, where $T_{N/S}(x, \infty)$ are the temperature fields at latitude x for the Northern and Southern hemispheres in the equilibrium state ($t \to \infty$). Thus, the value of D for the Southern hemisphere that satisfies this condition is $0.322 \; W/m^2/^\circ C$.

Different values of the transport coefficient are employed for the PDE model in this chapter and the 3-box model in Chapter 4. This choice is related to the different parametrisation employed for the distribution of solar insolation and co-albedo as well as the different latitudinal resolution of the two climate models.

Finally, C is the effective heat capacity for which values employed for the Northern and Southern band in the 3-box model in Section 4.2 are considered. It is worth noting that the model neglects the mean circulation in both the atmosphere and oceans but includes the heat transport due to circulation. This approach allows for tractable mathematics and analytical solutions.

The system in Eq. (6.1) with the boundary conditions in Eq. (3.7) can be identified as the non-homogeneous heat equation with Neumann boundary conditions and has an analytical solution [139]. As in [75] for the one-dimensional model, an efficient, straightforward approach for solving such problems and obtaining an analytical solution is provided by the Green's function formalism as noted in Section 3.1. Green's functions are constructed by utilizing the eigenfunc-

tions and eigenvalues of the differential operators from which the system is constructed [138]. Once the Green's function for a given problem is known, the solution for the latitudinal distribution of the temperature is immediately computed from the analytical expression for the Green's function [139].

The general solution in terms of the Green's function can be written as [138]:

$$T(x,t) = \int_{\xi_0}^{\xi_f} T(\xi,0)\, G(x,\xi,t,0) d\xi + \int_0^t \int_{\xi_0}^{\xi_f} G(x,\xi,t,\tau)\Phi(\xi,\tau)\, d\xi d\tau \tag{6.3}$$

where $G(x,\xi,t,\tau)$ is the Green's function associated with the differential operators in Eq. (6.1) with Neumann boundary conditions and can be written as [138]:

$$G(x,\xi,t,\tau) = G(x,\xi)G_t(t,\tau) = \sum_{n=1}^{\infty}(2n+1)\frac{P(n,x)P(n,\xi)}{L_n}\frac{1}{C}\exp\left(-\frac{t-\tau}{L_t}\right) \tag{6.4}$$

where L_n are the eigenvalues of the linear operator given in Section 3.1 and L_t is the time constant given approximately by $C\beta_0/b$, where β_0 is the climate sensitivity of the model as determined later. The Green's function $G(x,\xi,t,\tau)$ represents the temperature perturbation $\delta T(x,t)$, at latitude x, at time t, due to an instantaneous heat source of unit strength, located at ξ, releasing its energy instantaneously at time τ. Therefore, the argument 'ξ,τ' in Eq. (6.4) represents an impulse, given by the heat source term [139], whereas 'x,t' represent the resulting effect. Moreover, Φ is the external forcing of the system which in this case depends only on x and can be written as:

$$\Phi(x) = Q_0 S(x)(\alpha(x,x_s)) - a \tag{6.5}$$

In general, the first term on the right-hand side of Eq. (6.3) is the contribution of the initial condition given by the Green's function, evaluated at $\tau = 0$, multiplied by $T(x,0)$ and integrated over the hemisphere. The second term then represents the contribution of the forcing to the temperature profile. Then $T(x,0)$ is the latitudinal distribution of the temperature (at initial time $t = 0$) which can be found by Eq. (3.11) considering the 1-dimensional model.

The annual zonally-averaged surface equilibrium temperature for the two hemispheres can be obtained considering $T(x,t)$ in Eq. (6.3) at the final time $t = t_f$. The result is reported in Fig. (6.1) and is consistent with the literature [73, 75, 140].

Considering the combination of the behaviour in the two hemispheres, the step response of the PDE model for the climate system can be found in Fig. (6.2) together with the response

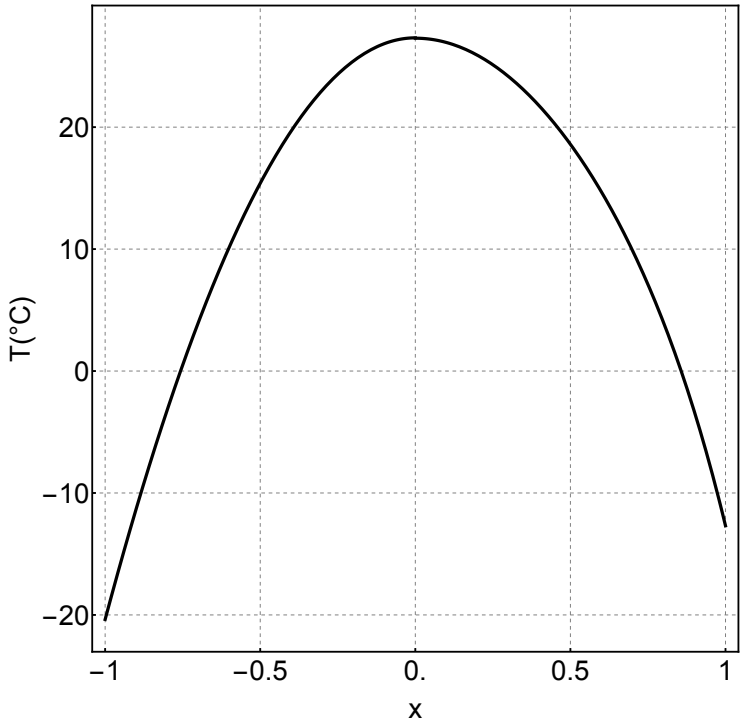

Figure 6.1: Latitudinal distribution of the annual zonally-averaged surface equilibrium temperature for Northern and Southern hemispheres.

from a first order linear model (dashed line) [90] and a semi-infinite diffusion model [142]. The behaviour of the PDE model is comparable with the semi-infinite diffusion model. In particular, the two curves (continuous black thick and thin lines) reach the same equilibrium temperature, although the relaxation profile is different. In the semi-infinite diffusion model, the overall heat capacity is given by 4.063 years with an equilibrium climate sensitivity of $2.71°C$ [142], which is comparable with the HadCM3L model. As can be seen in Fig. (6.2), in this case, the perturbation is considered with respect to the equilibrium temperature. This version of the model, where only the temperature anomaly with respect to the equilibrium state is considered, is described in detail in the next section. According to [101] and [75], the fundamental sensitivity of the system can be estimated for the PDE model as follows:

$$\beta_0 = \frac{Q_0}{100}\left(\int_0^1\int_0^1 G_x(x,\xi)S(\xi)\left(\alpha(\xi,x_{s0}) + Q_0\frac{dx_s}{dQ}\frac{\partial\alpha(\xi,x_s)}{\partial x_s}\right)d\xi\,dx\right) \tag{6.6}$$

where dx_s/dQ is the slope surface of the ice line (x_s), i.e. the latitude where the temperature is $-10°C$ (ice line) and the surface is assumed to be covered by ice. Again, in the current climate the ice line is at $x_{s0} = \pm 0.95$. The value for the slope of the ice line can be found considering

Eq. (2.9) in [75]. The term $\partial\alpha(x, x_s)/\partial x_s$ is the derivative of the co-albedo function in Eq. (6.2) with respect to the ice line calculated at x_{s0}. Computing Eq. (6.6) for the Southern and Northern hemisphere, it can be demonstrated that the averaged sensitivity of the PDE model in Eq. (6.1) with the chosen parameters is $2.32°C$.

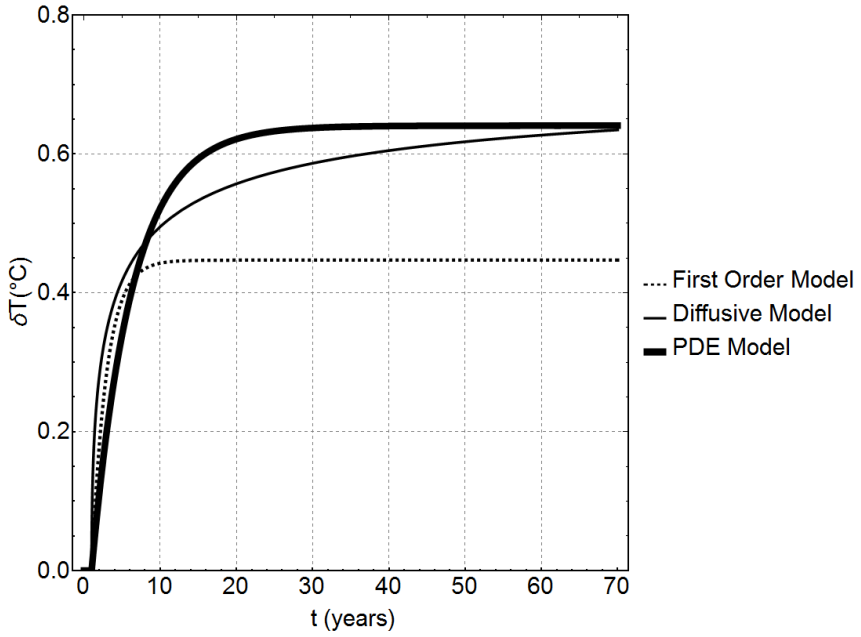

Figure 6.2: Step response for the global mean temperature in the time domain due to the step change in radiative forcing of 1 W/m^2 at $t = 1$ year of the climate model reported in Eq. (6.1) (black thick solid line), a first-order model (dashed line) [90] and a semi-infinite diffusion model (black thin solid line) [90], [142].

6.3 Multi-objective control strategies with a PI controller

6.3.1 Methodology

It is important to highlight that the expression for the external forcing $\Phi(x, t)$ is a generic function; therefore, it can be used to implement climate engineering strategies and analyse the behaviour of the PDE model. In this section a slightly modified version of the model in Eq. (6.1), where the system is considered in the neighbourhood of its equilibrium state, is presented.

This version includes external forcing which represents the excess of carbon dioxide in the atmosphere. This forcing term (F_{CO_2}) causes an imbalance in the radiative forcing in Eq. (6.1) producing an anomaly in the latitudinal temperature profile. In particular, the 1pctCO_2 scenario

[143] is considered in this section, where a constant increase in carbon dioxide concentration of 1% per year is assumed.

Assuming the deployment of a climate engineering strategy consisting of a reduction of insolation (SRM), a control function is defined as $U(x,t)Q_0\ S(x)\alpha(x,x_s)$, which in general depends on both latitude and time. This term is included in the model through Eqs. (6.7)-(6.8) and aims to reduce the temperature anomaly generated by the excess of atmospheric CO_2.

Thus, considering a small radiative perturbation δF_{CO_2}, it is possible to solve the equation governing the temperature perturbation as follows:

$$\delta T(x,t) = \int_{\xi_0}^{\xi_f} \int_0^t G(x,\xi,t,\tau)\Phi(x,t)\ d\tau\ d\xi \tag{6.7}$$

where, in this case, Φ is given by the forcing due to atmospheric CO_2 and the deployment of climate engineering intervention:

$$\Phi(x,t) = \delta F_{CO_2}(x,t) - U(x,t)Q_0 S(x)\alpha(x,x_s) \tag{6.8}$$

As can be noted, since only perturbations around the equilibrium temperature of the system are considered, the term depending on $T(x,0)$ is equal to zero and only the perturbation term of Eq. (6.3) is considered in Eq. (6.7).

The analytical expression for the temperature distribution, obtained through the Green's function approach, allows for a fast and efficient investigation of the effects of SRM deployment on the climate system. The advantages of using such an approximate mathematical model for closed-loop control purposes can be summarised as follow: (1) capturing latitudinal disparities in induced cooling; (2) easy application of optimisation processes and multi-objective analyses; (3) clearer understanding of the key climatic processes involved and the effects of closed-loop control on them; (4) the possibility of developing an analytical control function with latitudinal resolution; (5) the efficient assessment of new climate engineering strategies, prior to more detailed analysis.

The 1pctCO_2 scenario assumes that the CO_2 concentration in the atmosphere rises steadily at 1% per year; therefore, considering Eq. (3.23), the associated radiative forcing can be obtained

through the following relationship:

$$F_{CO_2}(t) = \frac{F_{2\text{x}CO_2}}{ln(2)} \log\left(\frac{cc}{cc_0} \mathrm{e}^{\log(1.01)t}\right) \qquad (W/m^2) \tag{6.9}$$

where the expression found in [144] for the radiative forcing due to atmospheric CO_2 is considered. Here, cc is the current CO_2 concentration in the atmosphere (400 ppm [104]) and log(1.01) represents the 1% per year growth rate.

The model described offers an analytical approach to the design of control strategies to counteract radiative forcing on a latitudinal basis. Following the same approach used in [90], a multi-objective control strategy is applied to the system. The objectives regard the minimisation of changes in the global mean temperature, the temperature gradient and the equator-to-pole temperature gradient due to increasing CO_2. For this purpose the functions to minimise are defined by the projection of the temperature distribution $\delta T(x,t)$ onto the first three Legendre polynomial functions [90, 145] that are reported below:

$$L_0 = 1 \tag{6.10}$$

$$L_1(x) = x \tag{6.11}$$

$$L_2(x) = \frac{1}{2}(3x^2 - 1) \tag{6.12}$$

Considering Eqs. (6.10-6.12) and the analytical solution of the PDE system for the temperature anomaly in Eq. (6.7), the three outputs can be defined as follow:

$$\delta T_i(t) = \int_{x_0}^{x_f} \delta T(x,t) L_i(x)\, dx \qquad i = 0,1,2 \tag{6.13}$$

with $x_0 = sin(\phi_0)$ and $x_f = sin(\phi_f)$, where subscripts 0 and f represent the extremes of the hemispheric integration.

The latitudinal distribution of $\delta T_0(x,t)L_0$, $\delta T_1(x,t)L_1(x)$ and $\delta T_2(x,t)L_2(x)$ under the 1pctCO_2 scenario when SRM is not deployed ($U(x,t) = 0$) can be found in Figs. (6.3- 6.5).

It is important to note that the integration for the Southern hemisphere is necessary in all three cases since the function $\delta T(x,t)$ is distinct for the Northern and Southern hemisphere because

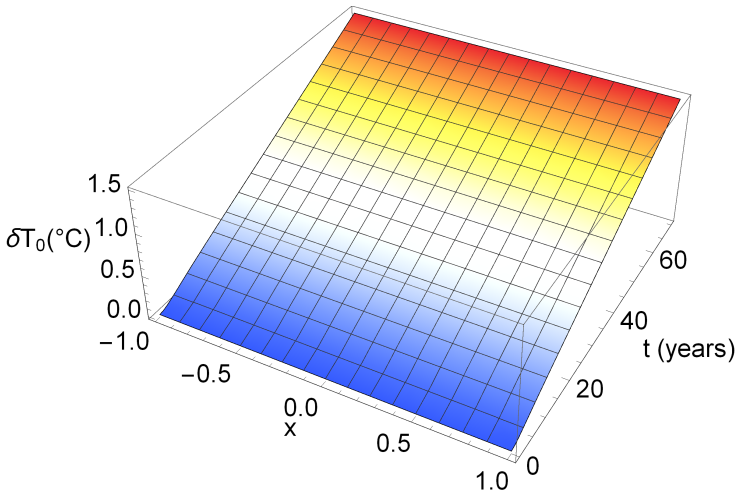

Figure 6.3: Latitudinal distribution of the global mean temperature anomaly $\delta T_0(^\circ C)$ with time under the $1pctCO_2$ scenario.

of the parameters selected (see Section 6.2 for details). Therefore, the process described in this section needs to be undertaken for both hemispheres.

As in [90], the first goal will now consider the minimisation of the global mean temperature $\delta T_0(t)$ (case 1), the second case also considers the minimisation of the temperature gradient $\delta T_1(t)$ (case 2), and the third case investigates the full problem where all the three objectives are taken into account (case 3).

6.3.2 Implementation of a PI controller

The general analytical solution of the PDE model in Eq. (6.3) allows for any type of control function $U(x,t)$. Thus, the response of the PDE model to several open-loop control laws under the 1pctCO_2 scenario can be investigated. In Figs (6.6-6.9) the temperature anomaly is reported when several functions $U(x,t)$ are employed in a open-loop control system.

In particular, Fig. (6.6) shows the effect of the 1pctCO_2 scenario on $\delta T(x,t)$ when a latitudinally-uniform constant control is considered ($U = 1\%$, $U = 2\%$) and when no control is applied (brown surface with $U = 0$). As can be seen, the system never reaches an equilibrium state because of the time-variation of the radiative forcing that is not compensated for by the constant value of the control function. Also, the latitudinal pattern of the insolation ($S(x)\alpha(x,x_s)$) causes the control function to have a non-uniform distribution with larger cooling effects at the equator with respect to the poles.

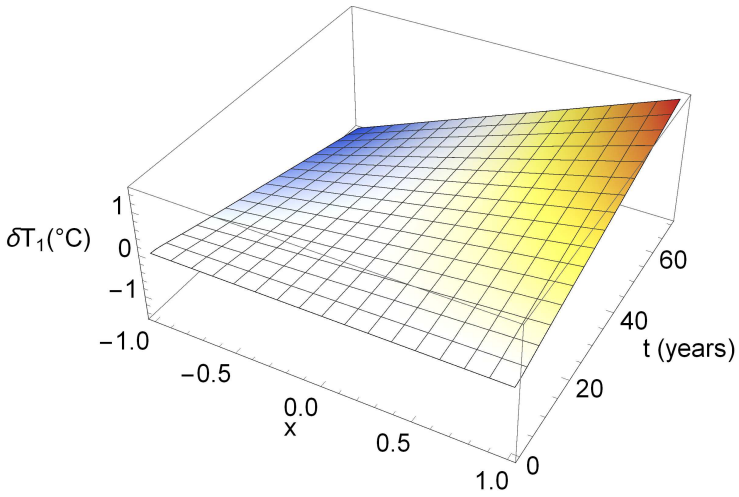

Figure 6.4: Latitudinal distribution of the temperature anomaly gradient $\delta T_1(^\circ C)$ with time under the $1pctCO_2$ scenario.

Moreover, in Figs (6.7-6.8), several linear and quadratic profiles from the poles to equator are considered ($U = 1.5x$ %, $U = 2.5x$ %, $U = 2x^2$ %, $U = 3x^2$ %) and compared with the uncontrolled case (brown surface). These functions represent time-independent reductions of insolation which are latitudinally non-uniform, thus latitudinal variations can be noted but the temperature anomaly continues to increase due to CO_2 forcing. Moreover, although in both cases $U = 0$ at the equator ($x = 0$), Fig. (6.7) shows insolation reduction toward the north and insolation growth toward the south, whereas Fig. (6.8) shows a reduction near both poles due to the quadratic nature of the control function employed.

Finally, in Fig. (6.9), the effect of temporal variations of latitudinally-uniform control laws are investigated ($U = 0.01t$ %, $U = 0.03t$ % where t is measured in an years). Again, latitudinally uniform control laws show the effects of the distribution of insolation. Although the temperature anomaly decreases everywhere an over-cooling of the tropics and under-cooling of the high latitudes regions can be noted.

In conclusion, this analysis shows that the climate system never reaches an equilibrium state when generic open-loop control systems are employed. It is also suggested that the required control law is a combination of the control functions used for the open-loop control schemes (function depending on x, x^2 and t) which should be specifically chosen for the each radiative scenario. This is a task that can be accomplished with the PDE model. Therefore, a PI controller in feedback will be employed with the PDE model to minimise the temperature anomaly for several multi-objective control strategies as summarised later in Table (6.1).

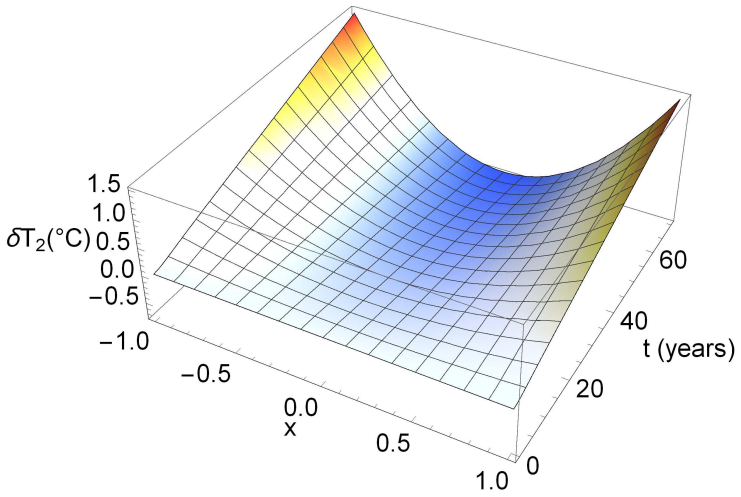

Figure 6.5: Latitudinal distribution of the equator-to-pole temperature anomaly gradient $\delta T_2(^\circ C)$ with time under the $1pctCO_2$ scenario.

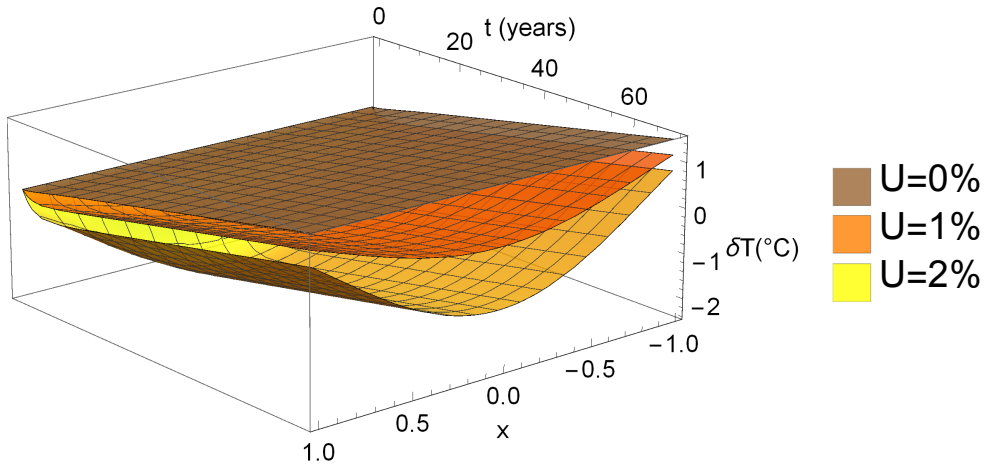

Figure 6.6: Response of the temperature anomaly under 1pctCO_2 scenario with constant values of the control law: $U = 0\%$ (brown surface), $U = 1\%$ (orange surface), $U = 2\%$ (yellow surface)

A Proportional-Integral (PI) controller is now employed to achieve the required control objectives. This control structure is a feedback control strategy with delay, where the control at time t depends on the state δT_i at the previous time $(t-1)$ (years). This approach is justified since observations of the temperature distribution during year t would be used to estimate the quantity of material required, for example if the injection of stratospheric aerosol is used. The time to collect data, implement decision-making processes are then assumed to cause a delay between the time of observation and the deployment of the climate engineering strategy. As in [1], in this analysis a time-delay of 1 year is considered. Other important properties of feedback control

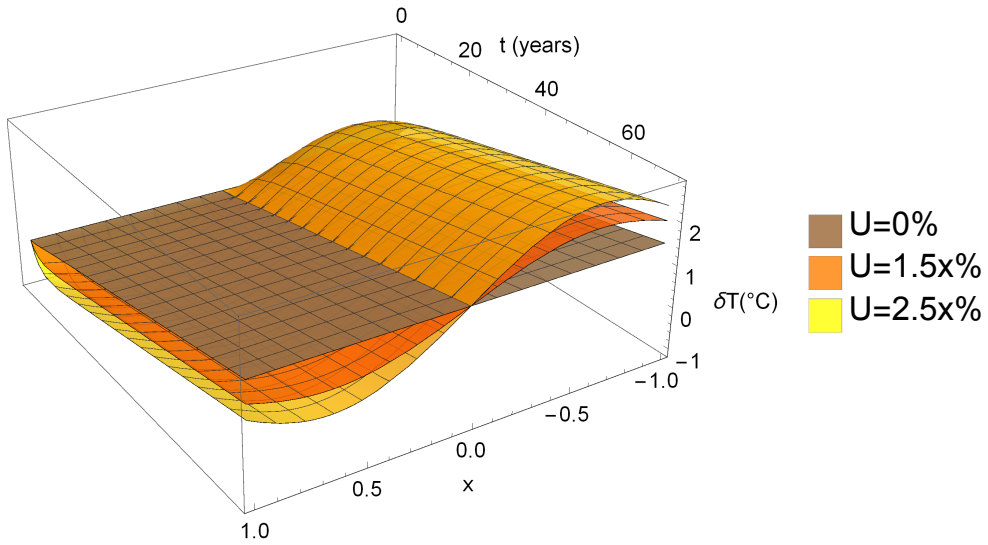

Figure 6.7: Response of the temperature anomaly under 1pctCO_2 scenario with linear relationships of the control law with the latitude: $U = 0\%$ (brown surface), $U = 1.5x$ % (orange surface), $U = 2.5x$ % (yellow surface)

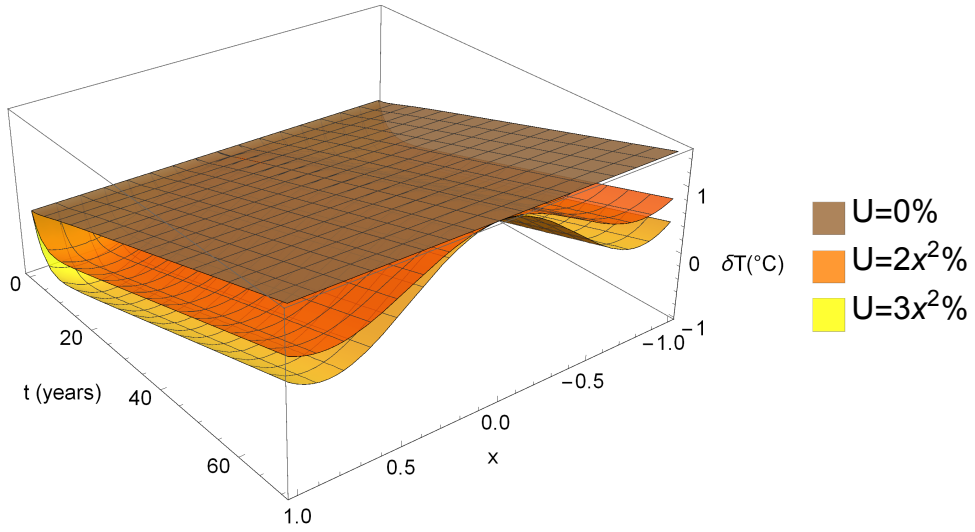

Figure 6.8: Response of the temperature anomaly under 1pctCO_2 scenario with quadratic relationships of the control law with the latitude: $U = 0\%$ (brown surface), $U = 2x^2$ % (orange surface), $U = 3x^2$ % (yellow surface)

systems and advantages of their use in climate engineering can be found in [4] and [1].

Following Section 3.6.1, the general structure of the PI control used to achieve the objectives can be defined as:

$$U_i(t) = k_{Pi}\,\delta T_i(t-1) + k_{Ii}\int_0^t \delta T_i(t-1)\,dt \qquad i = 0,1,2 \tag{6.14}$$

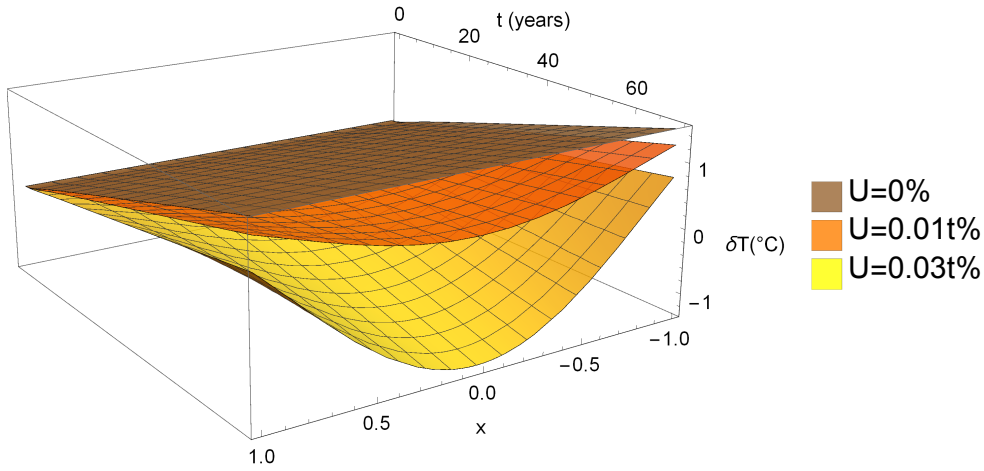

Figure 6.9: Response of the temperature anomaly under 1pctCO_2 scenario with time-dependent control laws: $U = 0\%$ (brown surface), $U = 0.01t$ % (orange surface), $U = 0.03t$ % (yellow surface)

where $U_0(t)$ aims to minimise the global mean temperature $\delta T_0(t)$, $U_1(t)$ regards the control of $\delta T_1(t)$ and $U_2(t)$ of $\delta T_2(t)$, respectively. The control functions for cases (1), (2) and (3) can be written as:

$$U_{1x1}(t) = U_0(t)L_0 \tag{6.15}$$

$$U_{2x2}(x,t) = U_0(t)L_0 + U_1(t)L_1(x) \tag{6.16}$$

$$U_{3x3}(x,t) = U_0(t)L_0 + U_1(t)L_1(x) + U_2(t)L_2(x) \tag{6.17}$$

where L_i $(i = 1,2,3)$ are again the first three Legendre polynomial functions. As can be seen from Eqs. (6.15-6.17), the control functions are given by a combination of the functions $U_i(t)$, describing the time-history of the control (given by the outcomes of the PI control strategy) and the functions $L_i(x)$, characterizing the latitudinal distribution of the control. The results of this investigation are presented in detail in the following section.

6.3.3 Results of multi-objective control strategies

Considering the analytical solution of the PDE system in Eq. (6.7), the three outputs, $\delta T_0(t)$, $\delta T_1(t)$ and $\delta T_2(t)$, can be computed through Eq. (6.13). As noted earlier, climate engineering through the reduction of insolation is deployed in case (1) to minimise the global mean temper-

ature, in case (2) to drive both $\delta T_0(t)$ and the temperature gradient $\delta T_1(t)$ to zero and, finally, in case (3), all three outputs are controlled. Again, in this analysis the 1pctCO_2 scenario is considered. To achieve these strategies, the control functions reported in Eqs. (6.15-6.17) are employed.

The three control strategies are summarised in Table (6.1). Specifically, the controlled outputs are indicated with the symbol "$\star$" in the first three columns, whereas, in the last column the control function employed is reported for each case. Values for k_{Pi} and k_{Ii} $(i = 1, 2, 3)$ are chosen

Table 6.1: Summary of the control strategies considered.

case	$\delta T_0(t)$	$\delta T_1(t)$	$\delta T_2(t)$	Control function
1	$\star$	-	-	$U_{1x1}(t)$
2	$\star$	$\star$	-	$U_{2x2}(x,t)$
3	$\star$	$\star$	$\star$	$U_{3x3}(x,t)$

in order to ensure a fast response whilst avoiding excessively increasing the system's sensitivity to natural variability [4]. In particular, a response time of 3 years is assumed to select the gains for U_0, U_1 and U_2 in Eq. (6.14). As can be seen in [4], higher gains would provide a quicker response to changes, but also a higher amplification of natural variability. Moreover, one of the purposes of this section is the comparison with results found in [4], therefore an effort is made to reproduce the scenario employed in [4].

The PI-control scheme is now fully defined and the control functions, in terms of the reduction of insolation, are obtained. Figure (6.10) shows the time-history of $U_{1x1}(t)$, which has a uniform distribution at every latitude since the first Legendre polynomial L_0 does not depend on x. This strategy shows the effect of a latitudinally-uniform reduction of insolation that increases with time. However, although the increase of atmospheric CO_2 is uniformly distributed there is an amplified effect at the poles. Therefore, when uniform cooling is applied as in case (1), a overcooling of the tropics and an undercooling of the poles occurs with the northern hemisphere cooler than the southern hemisphere (see also [90]). This result can be seen from Fig. (6.18) where the latitudinal distribution of the zonal mean temperature at the final time is reported for the three cases.

Hemispheric differences are related to the different distribution of ocean and land between the two hemispheres and, in particular, to the impact of the ocean on heat transport [146]. These

effects are taken into account in the PDE model through the values of the heat capacities and the transport coefficients employed for the northern and southern hemispheres.

Figure (6.11) shows the function $U_{2x2}(x,t)$, employed in the case (2), which is given by the combination of the feedback control of $\delta T_0(t)$ and $\delta T_1(t)$. Its latitudinal distribution is dictated by the first and the second Legendre polynomial expressions in order to minimize the global mean temperature as well as the temperature gradient.

The additional feedback control of the inter-hemispheric temperature gradient in case (2) reduces disparities between the temperature residuals in the north pole and the south pole and decreases over-cooling of the tropics. Therefore, as can be seen in Fig. (6.11), a larger cooling effect is required in the southern hemisphere.

As noted in [90], the additional feedback control of the inter-hemispheric temperature gradient in case (3) reduces disparities between the temperature residuals in the north pole and the south pole and decreases over-cooling of the tropics. Again, these effects are also confirmed in Fig. (6.18).

Finally, Fig. (6.12) shows the distribution of the control function employed in the full case (3), where the equator-to-pole temperature gradient is also minimized.

In all three cases the control strategy employed is consistently comparable with the numerical results obtained in [90], where multi-objective control strategies are applied to two fully coupled atmosphere-ocean general circulation models (AOGCM) that participated in CMIP5, the CESM 1.0.2 (Community Earth System Model) and the GISS ModelE2 (the Goddard Institute for Space Studies) in order to minimize $\delta T_0(t)$, $\delta T_1(t)$ and $\delta T_2(t)$. In particular, the control responses obtained with the analytical solution of the PDE model are comparable with those obtained through the CESM. However the model shows low sensitivity to the control of L_1 as occurs for the GISS model.

The results regarding the three outputs of the multi-objective control strategy simulations are reported in Figs. (6.13-6.15). In particular, the output time-history of $\delta T_0(t)$ is reported in Fig. (6.13), whereas Fig. (6.14) and Fig. (6.15) show $\delta T_1(t)$ and $\delta T_2(t)$, respectively. Each figure includes three curves: the black line represents case (1), the dark-grey line represents case (2) and the light-grey line shows the full case (3). Therefore, it is possible to analyse the effect of every control strategy on each output. Moreover, a Gaussian noise (zero mean and standard deviation set to 10^{-2}) is added to the outputs of the temperature level to simulate measurement noise and climate variability.

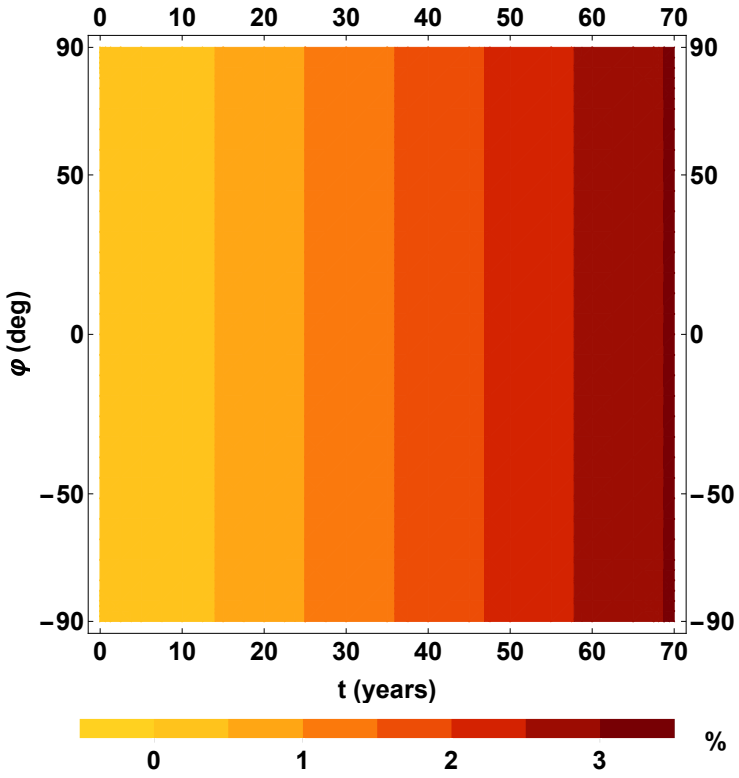

Figure 6.10: Latitudinal distribution of the control function U_{1x1} with the time.

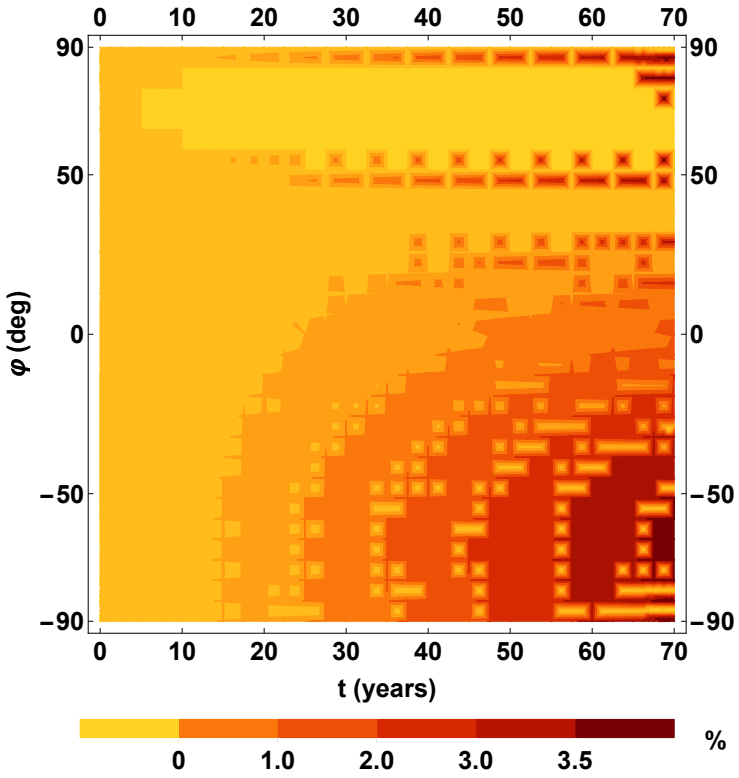

Figure 6.11: Latitudinal distribution of the control function U_{2x2} with the time.

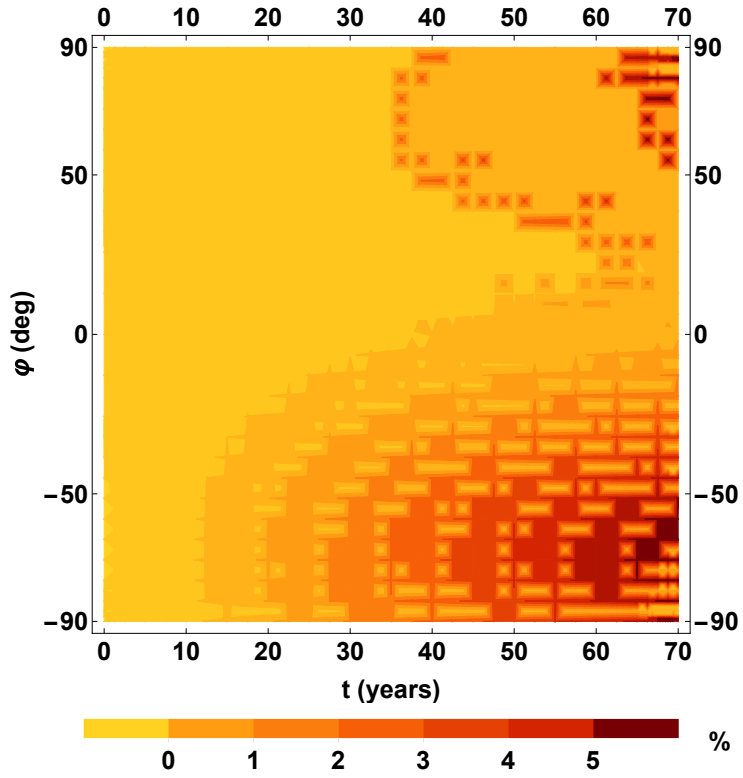

Figure 6.12: Latitudinal distribution of the control function U_{3x3} with the time.

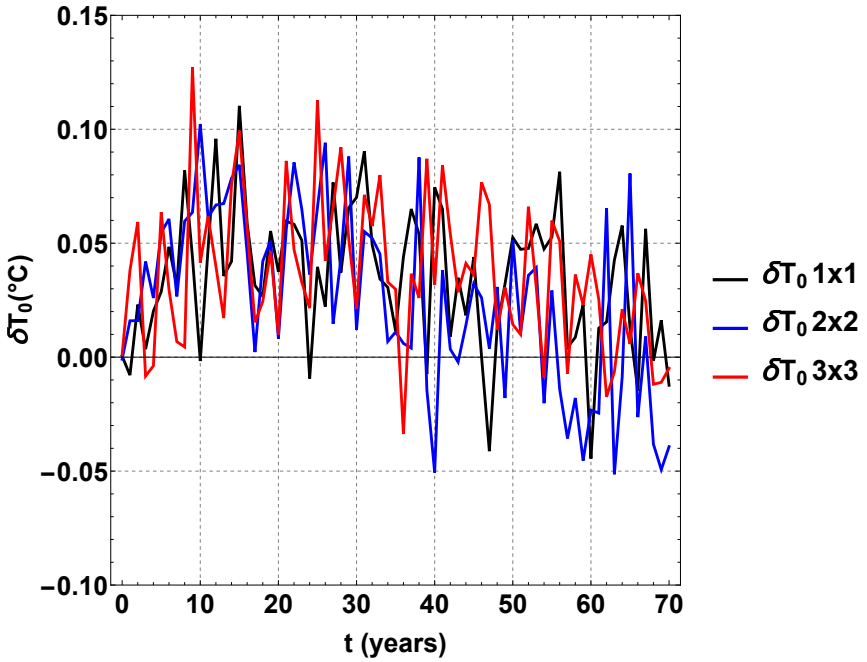

Figure 6.13: Perturbation of the global mean temperature $\delta T_0(^\circ C)$ (panel a) in cases 1 (black line), 2 (blue line), 3 (red line).

It can be seen from Figs. (6.13-6.15) that, in all the cases considered, the objective of each specific requirement is achieved. In fact the global mean temperature in case (1), the inter-

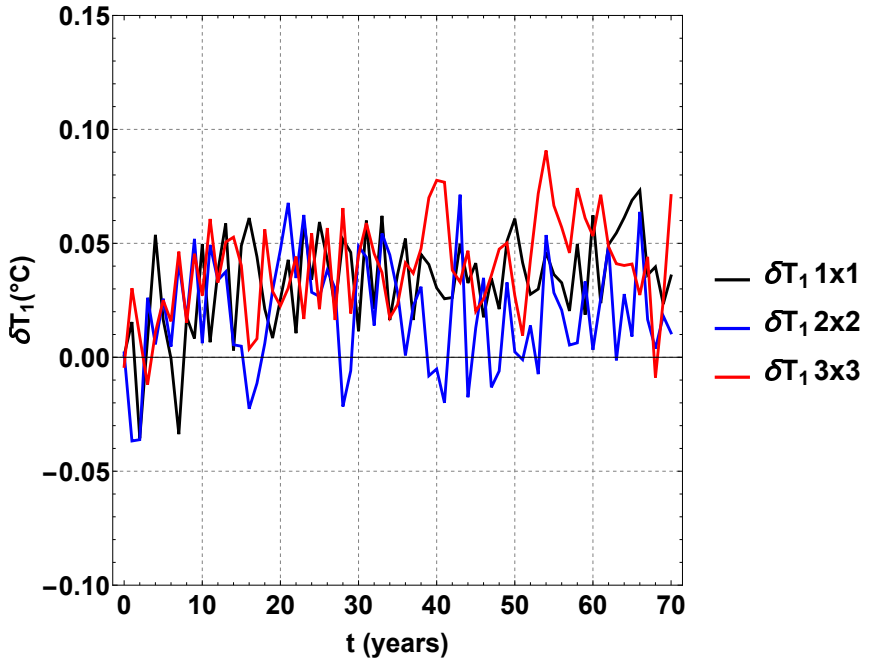

Figure 6.14: Perturbation of the inter-hemispheric temperature gradient δT_1 ($^\circ C$) (panel b) in cases 1 (black line), 2 (blue line), 3 (red line).

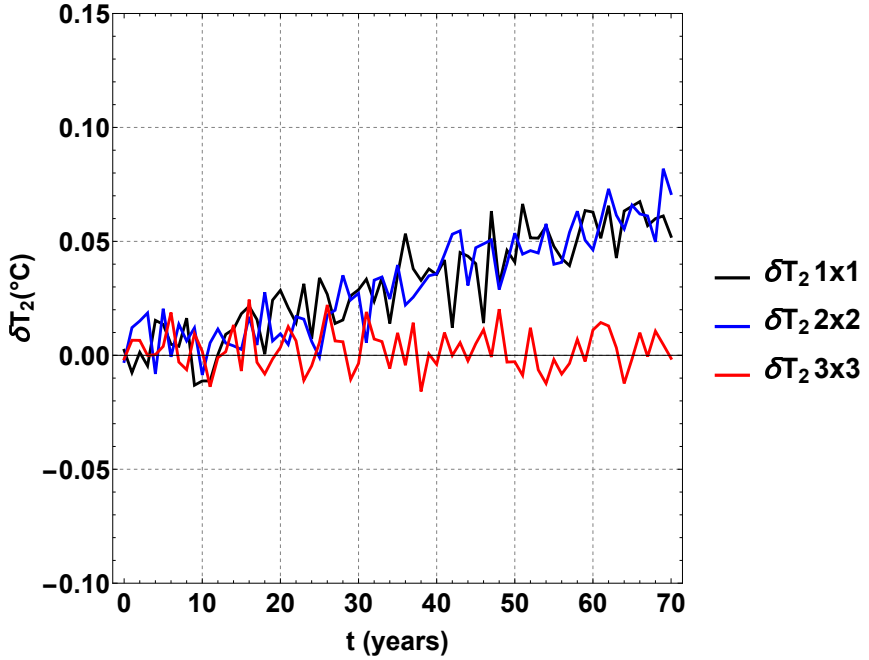

Figure 6.15: Perturbation of the equator-to-pole temperature gradient δT_2 ($^\circ C$) in cases 1 (black line), 2 (blue line), 3 (red line).

hemispheric temperature gradient in case (2) and the equator-to-pole temperature gradient in case (3) are minimized. Although, from Fig. (6.14), it can be noted that the system is not very sensitive to U_1 and it is found that δT_1 is reduced to a mean value of approximately $0.02^\circ C$. This

result is comparable with the outcome from the GISS model found in [90]. Moreover, negative effects are found for the objectives that are not managed in a particular case, such as δT_1 in cases (1) and (3) and δT_2 in cases (1) and (2).

In accordance with results from the literature [90, 147], the required latitudinally-uniform reduction of insolation increases linearly with time as the atmospheric CO_2 concentration grows (see Fig. (6.10)) and mainly aims to decrease the global mean temperature δT_0.

With respect to similar simulations from the literature, the results for $\delta T_0(t)$, $\delta T_1(t)$ and $\delta T_2(t)$ are comparable with results reported in [90]. Finally, in a rather similar way to the literature the equator-to-pole temperature gradient (δT_2) in Fig. (6.15) shows convergence to zero steady-state error in case (3), while in case (1) it shows large sensitivity to climate variability (noise). It is therefore clear that the analytic PDE model can provide an efficient and effective means of investigating non-uniform climate engineering strategies.

Moreover, the model described in this chapter also allows for an analysis of the zonal mean temperature. Therefore, a trade-off between the number of controlled degrees of freedom of SRM and the compensation of the zonal mean temperature is performed. Considering Eq. (6.7), the zonal mean temperature anomaly is computed and it is found that the rms error in compensating δT is $0.84°C$, $0.81°C$ and $0.31°C$ when U_{1x1}, U_{2x2} and U_{3x3} are applied to the system respectively. These results are shown in Fig. (6.18), where the zonal mean temperature at the final time is reported with latitude for the three cases considered. As can be seen, the temperature anomaly is noticeably lower in case (3). This result demonstrates that the zonal mean temperature is not completely minimized in any case, but that the overall rms error decreases when more degrees of freedom are managed. In fact, in the case when SRM is not deployed ($U = 0$) the overall rms error due to the 1pctCO_2 scenario is $1.41°C$. Thus, the computed control functions are able to manage the reduction of the global mean temperature anomaly, the temperature gradient and equator-to-pole temperature gradient, and greater benefits are found for the zonal mean temperature in all the three cases. In particular, case 3 is the most advantageous and indicates larger residuals of the zonal mean temperature anomaly when 3 degrees of freedom are considered.

This outcome is also confirmed in [145], where several combinations of the L_0, L_1 and L_2 distributions are employed for SRM. In particular, it is found that the rms zonal mean land temperature change from a doubling of CO_2 is reduced when more degrees of freedom are considered. Also, it is found that with a uniform SRM distribution and increased control closer to the poles, there is a more nearly uniform offsetting of CO_2-induced warming that restores global mean tem-

perature without over-cooling the equatorial regions and under-cooling the polar regions. This

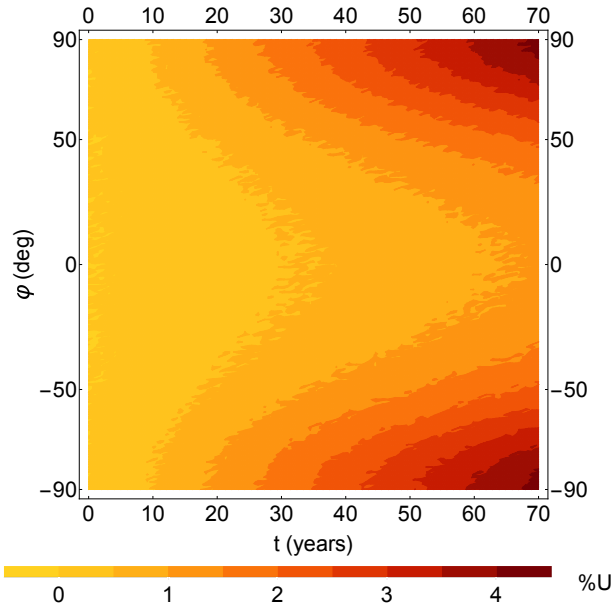

Figure 6.16: Contour Plot of the control law estimated to minimise the rms zonal mean temperature anomaly due to the 1pctCO_2 scenario over 70 years.

can also be demonstrated through the PDE model when the $1pctCO_2$ scenario is considered. As will be noted in Sec. (6.4), the PDE model can be employed to find a control law with latitudinal resolution to obtain a desired temperature profile. Therefore, the analytical solution reported in Eq. (6.3) is used to reduce to zero the rms zonal mean temperature and so Figs. (6.17-6.16) are obtained. In particular, the control law has been found by setting the expression of the rms zonal mean temperature provided through the PDE model to zero. As expected, the radiative forcing required to counteract the 1pctCO_2 scenario increases with time (see Fig. (6.16)) and is larger at the poles than the equator in order to avoid the under-cooling that would be caused by a uniform deployment of SRM. In particular, this can be noted from Fig. (6.17), where the latitudinal distribution of the control law at the final time of the simulation (when the radiative forcing is at its maximum) is reported. This method is equivalent to the selection of the necessary combination of L_0, L_1 and L_2. In particular, it is found that small levels of control over L_1 are required. As can be seen, the PDE model quickly produces the control function required to achieve the required goals. Other quantitative analysis of PI, or other control laws, can again be efficiently performed using the PDE model.

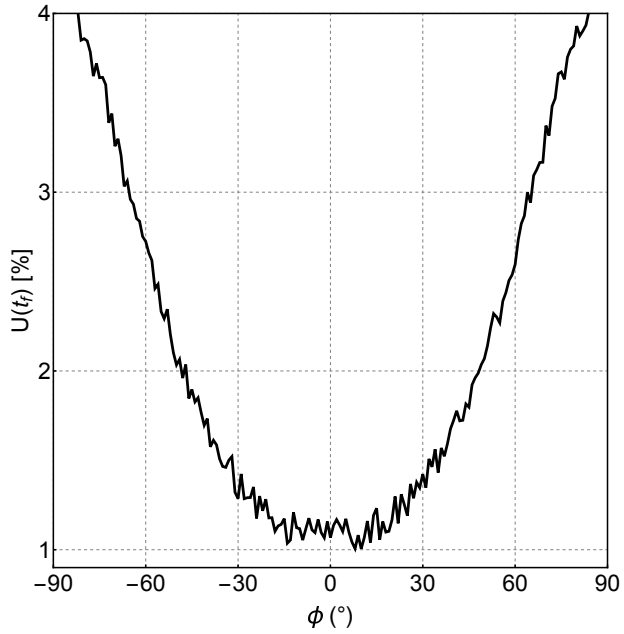

Figure 6.17: Latitudinal distribution of the control law estimated to minimise the rms zonal mean temperature anomaly at the final time $t_f = 70$ years.

6.4 Analytical control law to counteract a doubling of CO_2

The analytical solution of the PDE model reported in Eq. (6.3) can be employed to find a control law with latitudinal resolution to obtain a desired temperature profile. As demonstrated in the previous section, PI control is used in a closed-loop scheme to achieve the minimisation of the required objectives. The final outcome is the appropriate time-dependent control function that takes latitudinal disparities into account.

In this section, a more generic case is investigated first, where a control function is estimated in order to achieve a specific temperature profile. Assuming a doubling of CO_2 (which amounts to a forcing of $F_{2\times CO_2} = 3.71\ W/m^2$) the necessary reduction of solar radiation to drive the temperature back to the pre-industrial profile is evaluated and expressed through a control law with latitudinal resolution.

The analytical solution of the system in Eq. (6.7), i.e. the case when small variations of temperature around the equilibrium state are assumed, is considered as well as an external forcing that accounts for a doubling of CO_2 and the climate engineering intervention as given below:

$$\Phi(x,t) = F_{2\times CO_2} - U(x,t)Q_0 S(x)\alpha(x,x_s) \tag{6.18}$$

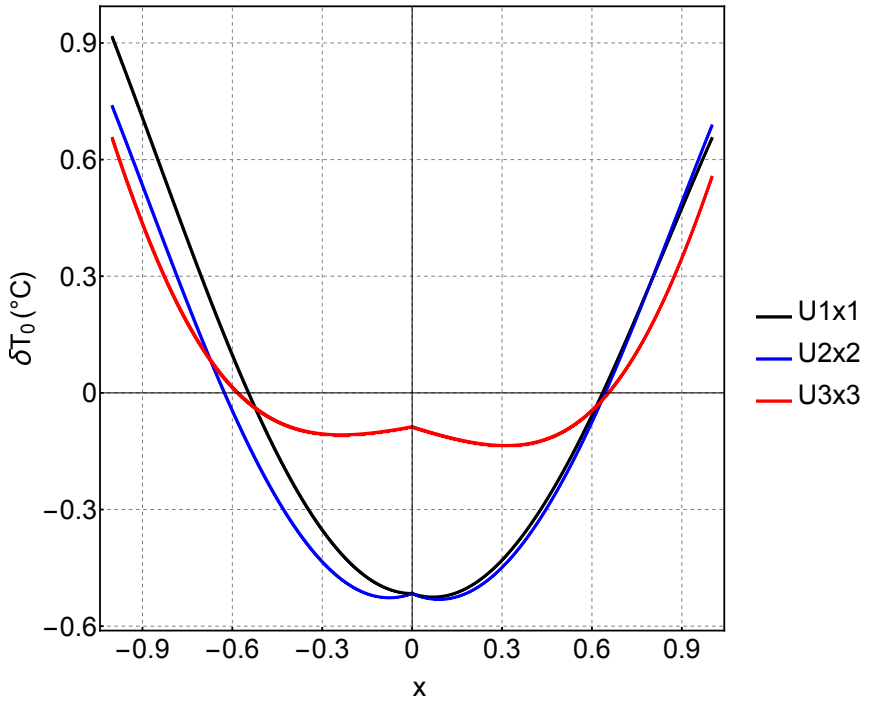

Figure 6.18: Latitudinal distribution of the zonal mean temperature at final time ($t_f = 70$ *years*) for the three considered cases.

Although the radiative forcing $F_{2\times CO_2}$ is constant with latitude, the climate engineering intervention consists in the fractional reduction of the incoming solar radiation (given by the term $Q_0 S(x)\alpha(x, x_s)$, see Fig.(3.1) in Section 3.1) and therefore depends on its latitudinal distribution. In this context, the control function $U(x,t)$, required to counteract the effect of $F_{2\times CO_2}$, can now be found by setting $\Phi(x,t)$ to zero.

6.4.1 Results

Unlike the 1pctCO_2 scenario used in Section 6.3.2, in this section a doubling of CO_2 concentration in the atmosphere is considered. In particular, two cases are considered for this simulation: in the first case a gradual change from the pre-industrial level up to a doubling of CO_2 occurs over 70 years (with a time constant equal to 34.4 years and $F_{CO_2} = F_{2\times CO_2}$ when $t = 70$ *years*), whereas, in the second case, the external forcing consists of a step change in radiative forcing equal to $F_{2\times CO_2}$.

The output of the first control strategy is given by the control law in Fig. (6.19.a), where the required fractional reduction of insolation is reported for the Northern and Southern hemisphere. As expected, the required control to counteract F_{CO_2} increases with time up to approximately 4%

of insolation at higher latitudes.

In the second case (Fig. 6.19.b), a constant radiative forcing equal to a doubling of CO_2 is assumed and a slightly larger control effort is necessary overall. In fact the maximum value of $U(x,t)$ required is 4.5% of the incoming solar radiation. This is due to the larger temperature anomaly caused by the steady radiative forcing with respect to the gradual change investigated in the first case. Moreover, integrating $U(x,t)$ over latitude, it is possible to estimate the global mean solar insolation reduction required to counteract a doubling of CO_2. This is found to be 1.78 %, which is comparable with the value of 1.8% found in literature where the global temperature is investigated for a doubling of the atmospheric CO_2 content, such as in [46] and [54].

The increase in atmospheric CO_2 concentration causes warming everywhere but requires a larger cooling at the poles. This can be justified considering the pattern of the incoming solar radiation (see Fig. (3.1)). When SRM is considered, the latitudinal distribution of the control law is always related to the pattern of insolation and the response of the climate system, which in this chapter is given by the PDE model described in Section 6.2.

Since the insolation is larger at the equator and lower at the poles, in order for the term $U(x,t)Q_0S(x)\alpha(x,x_s)$ to be constant over latitude and balance $F_{2\times CO_2}$, in both cases investigated, the pattern of $U(x,t)$ is required to have an inverse latitudinal distribution with respect to the incoming solar radiation. Therefore, it is found that the required control is larger at the poles than at the equator. This result is again widely comparable with the literature, for example [44,46,145].

6.5 Conclusions

The analytical solution of a time-dependent model for the climate system with latitudinal resolution has been developed in this chapter to assess multi-objective closed-loop climate engineering strategies. The system investigated is a PDE model which is analytically solved for any external forcing providing the latitudinal distribution of the temperature perturbation with time.

The model can be employed to investigate climate engineering strategies taking into account latitudinal disparities. High-fidelity numerical models for the climate can also be used to evaluate climate engineering strategies, but these models are computationally expensive. In contrast, the use of the PDE model provides a useful tool to rapidly assess SRM strategies, providing a clear understanding of the climate dynamics involved.

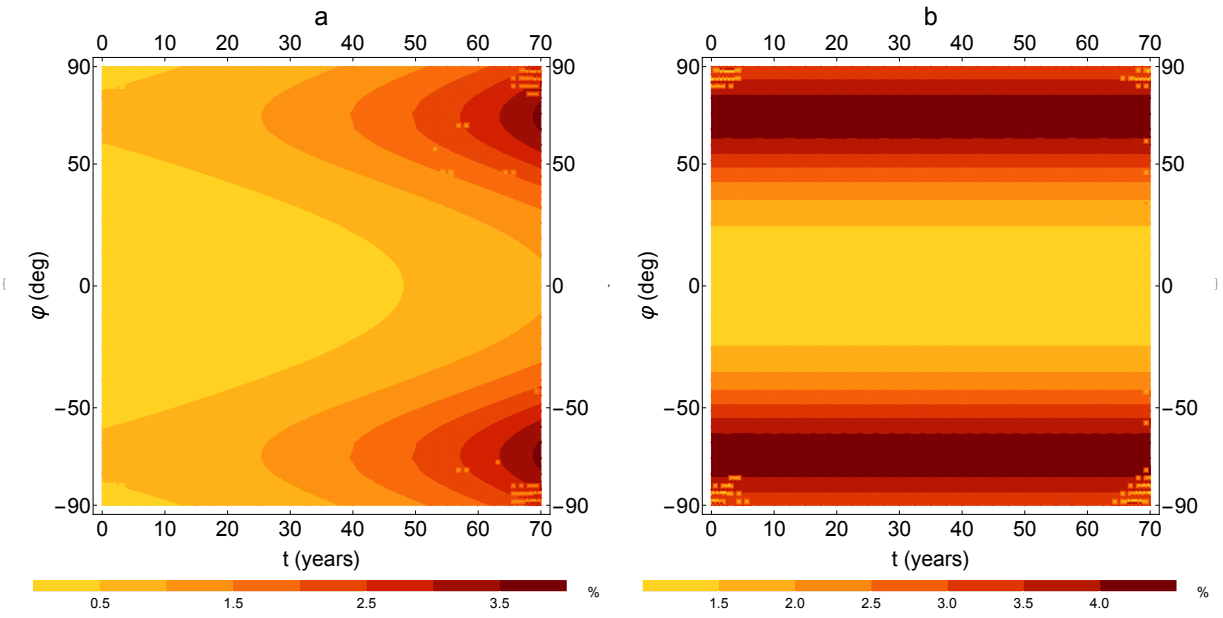

Figure 6.19: Control law to counteract (panel a) a time-increasing radiative forcing that reaches $F_{2\times CO_2} = 3.71\ W/m^2$ in 70 years and (panel b) a constant radiative forcing equal to $F_{2\times CO_2}$.

The PDE model developed in this chapter is employed in three simulations (cases (1), (2), (3)) to explore multi-objective strategies with a PI feedback control. Several objectives were simultaneously minimised and the latitudinal response investigated considering a steady increase of CO_2 concentration in the atmosphere (1pctCO_2 scenario). The model provided analytical expressions for suitable control functions for three strategies, and proved to be effective when multi-objective analyses are considered. In fact, despite the simplicity of the model, results which are broadly comparable with the literature are found. The distributions of the control functions with latitude are obtained using the analytical solution of the PDE model and are again consistently comparable with the literature. In particular, the control responses and the temperature trends obtained with the analytical solution of the PDE model are comparable with those achieved through the CESM 1.0.2 (Community Earth System Model). This approach is considered as the verification of the general correctness and usefulness of the model developed.

Moreover, the model is used for the analysis of the zonal mean temperature. In agreement with the literature, it is found that the rms zonal mean temperature anomaly caused by the 1pctCO_2 scenario decreases when more degrees of freedom are managed. Also, the PDE model can be employed to find the exact control law required and reduce the zonal mean temperature perturbation to zero. It is found that a non-uniform SRM distribution with increased control closer to the poles provides a more uniform offsetting of CO_2-induced warming and restores the mean temperature without over-cooling equatorial regions and under-cooling polar regions.

Chapter 7

Constraints on Solar Radiation Management

7.1 Introduction

In the previous chapter it has been demonstrated that the PDE model is a useful tool for climate engineering and can be used to develop analytical control laws for multi-objective strategies. In this chapter the PDE model is employed to explore constraints on SRM. In particular, the model can be used to investigate ice line dynamics, providing extreme operational limits on SRM obtained through the latitudinal model. Through this investigation, it is possible to compare the estimated SRM necessary to counteract anthropogenic climate change with the insolation reduction which would cause instability of the climate system through bifurcation to an ice-covered state.

With respect to other similar calculations in the literature [75, 99, 140], the insolation reduction that would trigger climate instability is given as a function of both latitude and time, providing more information for appropriate comparisons with commonly considered SRM strategies. Moreover, as found in [140], climate models which include the dependence from time produce an output which is less sensitive to changes in the solar constant. Also, for the purposes of this thesis, a time-dependent model allows time-dependent control functions for insolation reduction to be estimated. As will be seen later, this is a fundamental issue with the dynamics of the ice line and for SRM investigations in general.

In Section 7.2, considering the PDE model in the previous chapter, the ice line dynamics

are modelled and in Section 7.3 constraints on SRM are investigated by exploring the effect of climate engineering on the dynamics of the ice line. Moreover, in Section 7.4, it is assumed that the upper limit of SRM is exceeded and the climate system has fallen into a ice-covered state. In these conditions the recovery from the new climate state is investigated estimating the insolation increment needed. Finally, a concluding discussion and main results can be found in Section 7.5.

7.2 Modelling the ice line dynamics

In this section the dynamics of the ice line is investigated using the analytical solution of the PDE model in Eq. (6.1). Climate engineering involves the manipulation of the climate system, therefore the analysis of the stability of the global climate system (related to ice line dynamics) is of critical relevance for the study of the impact of climate engineering interventions.

This analysis is also of key importance for climate engineering involving SRM since it demonstrates that the extent of the insolation reduction commonly considered for SRM is far from triggering large-scale instability of the climate system. However, the definition of such boundaries is a requirement for engineering ventures. It will be shown that the PDE can be readily adapted for such analysis.

The Lyapunov stability criterion is now used to find the critical climate engineering intervention that would lead the current climate towards an ice-covered state. An upper limit on SRM is therefore found by exploring the effect of climate engineering on the dynamics of the ice line. While this limit is of course highly unlikely to be reached, the analytical PDE model provides insight into the extreme operational boundaries of SRM.

For simplicity, this strategy is employed for the Northern hemisphere only, therefore $x_1 = 1$ always refers to the North pole and the value employed in this section for the climate sensitivity takes into account only the Northern hemisphere ($\beta_0 = 2.735°C$).

As discussed in Section 3.2, the ice line represents the latitude where $T_s = -10°C$, and so for any $T \leq T_s$, the surface is entirely covered by ice and the albedo is as high as 0.55 [75].

As can be seen from Eq. (3.17), $\delta T(x,t)$ depends on the stability eigenvalue λ of the 1-dimensional model found in [75], where λ can be obtained through the investigation of the transcendental equation given in Eq. (3.22).

According to [75], one means of obtaining dQ/dx_s is a relationship depending on the climate

sensitivity of the model (β_0) as given below:

$$\frac{dQ}{dx_s}(x_s) = \frac{Q_0^2 S(x_s)\Delta\alpha}{100B\beta_0 - (a + bT_\infty)} \tag{7.1}$$

where, $\Delta\alpha$ is the change of albedo at the ice line equal to $|a_i - a_w| = 0.23$, and where a_i and a_w are ice and water albedo coefficients defined in Section 6.2. In particular, expression of the smooth albedo in Eq. (6.2) is employed.

Thus, the functions $\frac{dQ}{dx_s}(x_{s0})$ and F_λ can be plotted as a function of λ as shown in Figure (7.1). The intersections of the curves provide the roots λ of Eq. (3.22). In the case when $\frac{dQ}{dx_s}(x_{s0}) < 0$ the lowest root is negative and the solution is unstable. This condition represents state II and is equivalent to the transition between state I given by the present climate and state III representing the ice-covered Earth, according to the notation in [75].

The three equilibrium states are shown in Figure (7.2), where the potential function Π normalised with respect to Q_0 is illustrated as a function of T_0. Here, T_0 is the global equilibrium temperature, which is defined as the integral of $T(x,0)$ (see Eq. 3.11) with respect to latitude.

The expression of $\Pi(T_0)$ can be found in [75] and it is reported in Eq. (7.2):

$$\Pi(T_0) = aT_0 + \frac{1}{2}bT_0^2 - Q_0 \int_0^{T_0} H_0(T_0')\ dT_0' \tag{7.2}$$

Here, $H_0(T_0)$ is the planetary co-albedo which is defined by:

$$H_0(x_s(T)) = a_i + (a_w - a_i)(x_s(T) + \frac{1}{2}S_2(x_s(T) - x_s(T)^3)) \tag{7.3}$$

where the expression $x_s(T)$ represents the ice line given as a function of the temperature for which Eq. (3.16) is employed with δT used as the independent variable. Thus, with respect to Eq. (6.2), Eq. (7.3) includes the ice-albedo feedback. In fact, according to [75], the position of the iceline depends on the global mean temperature as follows:

$$\begin{aligned} x_s &= 1 && T_0 > 15°C \\ x_s &= 0 && T_0 < -15°C \\ x_s &= 1 - \tfrac{(T_0 - 15)}{30} && -15°C < T_0 < 15°C \end{aligned} \tag{7.4}$$

Solving Eq. (3.22) for λ with $\frac{dQ}{dx_s} < 0$, the lowest root is found to be $\lambda = -0.3086$. As will be

shown in Section 7.3, the value found for λ determines the reduction of insolation required to drive the climate system from state I to II. Since state II is unstable (as can be seen in Figure (7.2)) any larger reduction of insolation would make the system fall into state III; therefore, the estimated insolation reduction represents the reduction of insolation required before an ice-covered state is in principle achieved.

In Figure (7.3) the lowest root of Eq. (3.22) is reported for several climate sensitivities and it can be seen that the greater the sensitivity of the model, the closer to zero the value of λ. The PDE model has a sensitivity of $2.74°C$ for the Northern hemisphere, again with $\lambda = -0.3086$. In other cases, λ can be less than -1 if the climate model has a sensitivity of $2°C$. Thus, as expected, in a more sensitive model a smaller change in insolation is necessary to reach the condition for instability.

Therefore a value of λ equal to -0.3086 is employed in Section 7.3 in order to estimate the limiting control function $U_{ice}(x,t)$ so that the solution $T(x,t)$ approaches the ice-covered stable solution.

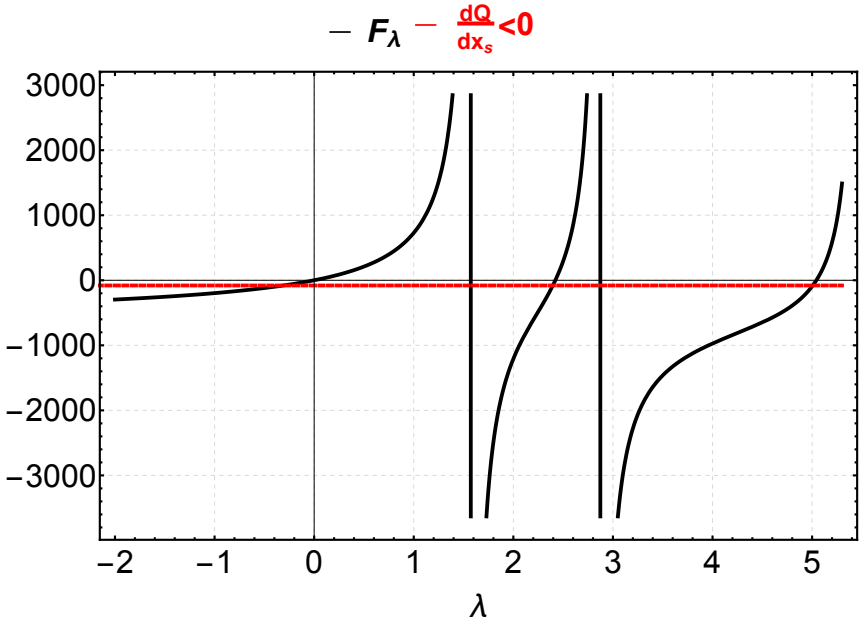

Figure 7.1: Plot of functions $\frac{dQ}{dx_s}$ and F_λ versus the stability parameter λ.

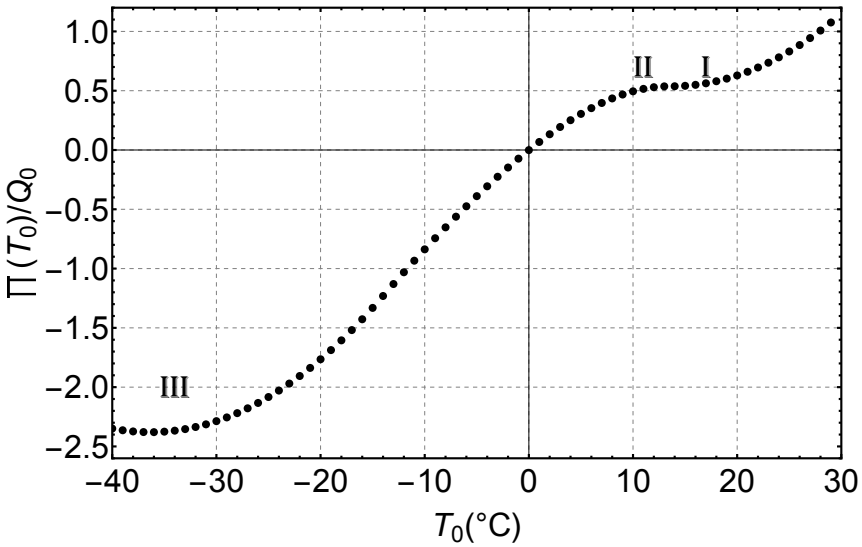

Figure 7.2: Normalised potential function with respect to the global equilibrium temperature T_0. Labels I, II and III represent the equilibrium states of the climate system, i.e. the current climate condition, an intermediate unstable equilibrium state and the ice-covered state, respectively.

7.3 Estimation of SRM Constraints

In Sections 3.2 and 7.2, the approach to determine the constraint on SRM through the ice line stability analysis has been detailed. Investigating the dynamics of the ice line and employing the Lyapunov stability criterion, it is now possible to estimate the form of $U_{ice}(x,t)$ to move the ice line from its current position to the equator ($x_s \to 0$).

Therefore, the result of this investigation provides the limit of SRM in terms of the maximum reduction of insolation applicable before the Earth's climate approaches a new ice-covered state. Again, this provides an extreme operational boundary for SRM, which can be obtained from the analytic PDE model developed in Section 6.2. However, it is clearly unlikely that such a control boundary would be reached.

Substituting Eq. (3.17) and Eq. (3.20) found in Section 3.1 in Eq. (3.16), an expression for δx_s as a function of the control variable U is obtained.

In order to estimate the reduction of solar radiation required to destabilise the climate system and then achieve the condition of an ice-covered state ($x_s \to 0$), the quadratic expression in Eq. (7.5) is considered as a candidate Lyapunov function:

$$v(x_s(x,t,U)) = \frac{1}{2}x_s(x,t,U)^2 = \frac{1}{2}(x_{s0} + \delta x_s(x,t,U))^2 \tag{7.5}$$

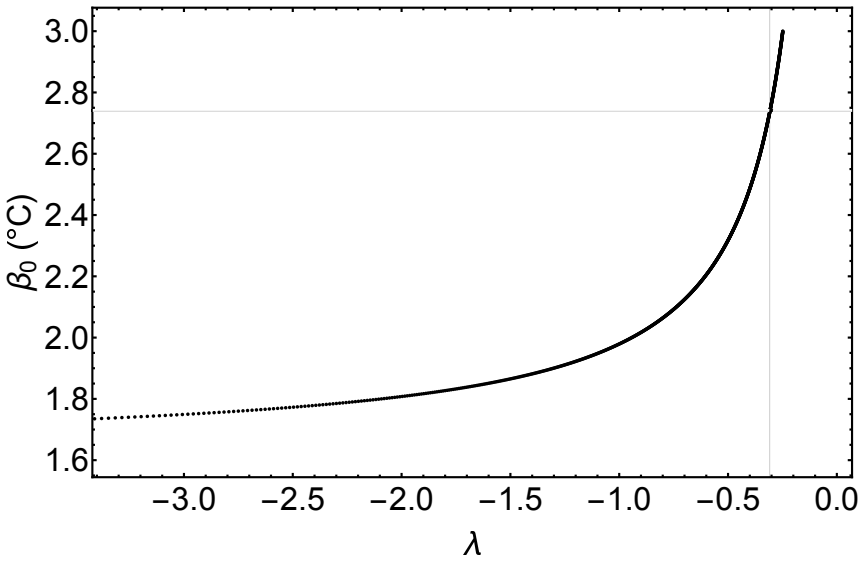

Figure 7.3: Values of the lowest root of Eq. (3.22), i.e. the stability eigenvalue λ, for several values of the climate sensitivity. The intersection of the grey lines represents the value of λ associated to the climate sensitivity of the PDE model.

The Lyapunov stability criterion [141] states that the dynamical system $\dot{x_s} = f(x_s(x,t,U))$ is unstable at x_{s0} in the sense of Lyapunov if:

(a) $v(x_{s0}) = 0$

(b) $v(x_s(x,t,U)) > 0$ for $x_s \neq x_{s0}$

(c) $\frac{\partial}{\partial t} v(x_s(x,t,U)) > 0$

In particular, relationship (c) provides the unstable condition if reversed. In order to satisfy condition (a), a function $v(x_s(x,t,U))$ is computed at $x_{s0} = 0.95$ and the Lyapunov function becomes:

$$V(x_s(x,t,U)) = v(x_s(x,t,U)) - v(x_{s0}) \tag{7.6}$$

Since the quadratic expression in Eq. (7.5) is considered, the Lyapunov function is locally positive and therefore condition (b) is satisfied. For condition (c) the first time-derivative of V is developed. Substituting Eq. (3.16) in Eq. (7.5), the analytical expression for $V(x_s(x,t,U))$ can

then be developed as follow:

$$V(x_s(x,t,U)) = U e^{-\frac{\lambda t}{C}} f_6 \frac{\left(F_1(x)\left(f_5 x_{s0} - f_6 T_0 + F(x_{s0})\left(f_6 T_0 - f_5 x_{s0}\right)\right)\right)}{f_5^2} + \frac{1}{2} U^2 e^{-\frac{2\lambda t}{C}} f_6^2 \frac{F_1(x)^2 - F_1(x_{s0})^2}{f_5^2} \quad (7.7)$$

As can be seen in the expression above, $V(x_s(x,t,U))$ is given by the multiplication of a series of analytical functions which can be found in Appendix (A). These expressions are obtained using symbolic computing. In particular, $F_1(x)$ depends on the system parameters, such as the planetary albedo, insolation, outgoing infra-red radiation, transport coefficient and the slope of the ice line, whereas, $f_5(\lambda)$ and $f_6(\lambda)$ depend on the stability eigenvalue λ.

Computing the first time derivative of Eq. (7.7), which also includes the time-dependence of U, and solving the inequality $\frac{\partial}{\partial t} V(x_s(x,t,U)) > 0$ for the variable U the following condition is obtained:

$$U_{ice}(x,t) \geq -\frac{f_{U1}(x)}{f_{U2}(x)} + \frac{\sqrt{f_{U2}(x) C_1 + \frac{f_{U1}^2(x) e^{-\frac{2\lambda t}{C}}}{f_{U2}(x)}}}{f_{U2}(x)\sqrt{\frac{e^{-\frac{2\lambda t}{C}}}{f_{U2}(x)}}} \quad (7.8)$$

where the analytical expressions for functions $f_{U1}(x)$ and $f_{U2}(x)$ can be found in Appendix (B).

As can be seen from Eq. (7.8), condition (c) of the Lyapunov stability criterion is satisfied by an infinite number of control functions. Each of these functions is identified by a specific value of the parameter C_1, which enables the selection of the initial condition for the control function U. In Fig. (7.4), control functions with values of C_1 between 0 and 3 can be found.

If C_1 is set to zero in Eq. (7.8), the boundary control function, labelled U_{bound}, is obtained. Combining $U_{bound}(x,t)$ with the latitudinal distribution of the albedo and the insolation, it is possible to estimate the minimum insolation reduction required to achieve an ice-covered state. Therefore, $U_{bound}(x,t)\, S(x)\alpha(x,x_s)$ (see Fig. (7.5)) is the minimum reduction of insolation which would force a transition to an ice-covered equilibrium state.

Thus, if the cooling applied is below one of the curves reported in Fig. (7.4), the current climate will converge to the new ice-covered equilibrium state. Considering the boundary function $U_{bound}(x,t)$, as expected, the required insolation reduction is larger at the equator ($U/Q_0 \simeq -11.5\%$ for $x = 0$) than at high latitudes ($U/Q_0 \simeq -4.16\%$ for $x = 0.90$) and in particular $U/Q_0 = 0$ for $x \geq 0.95$ since that region is already covered by ice. Considering $U_{bound}(x,t)$

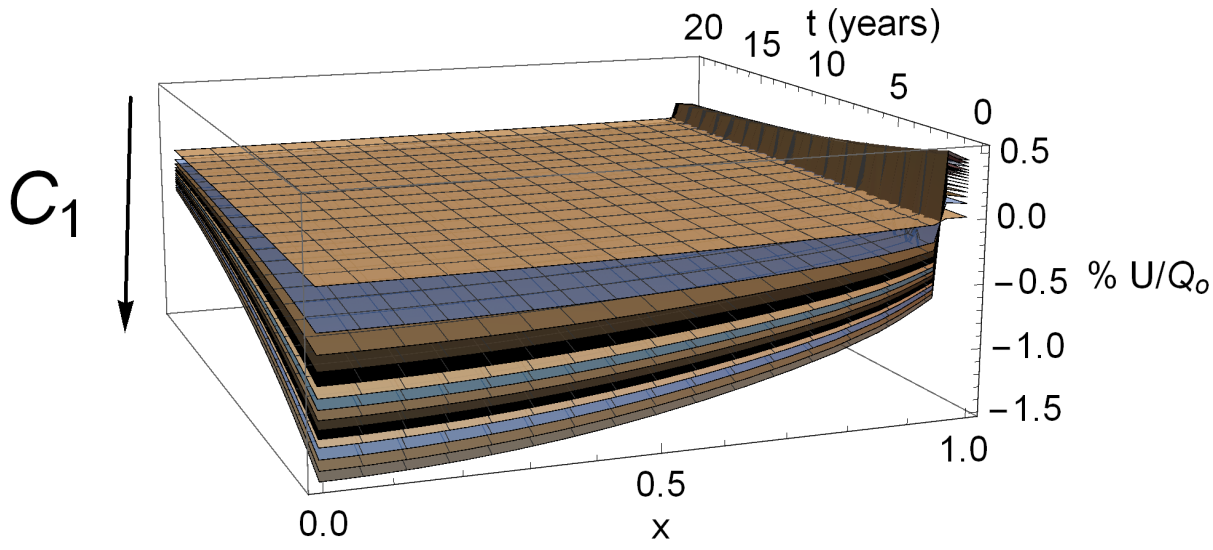

Figure 7.4: Family of control ($0 < C_1 < 3$) functions satisfying condition in Eq. (7.8).

at $t = 0$, it is estimated that a minimum overall reduction of insolation of approximately 8.8% is required to achieve an unstable state (equilibrium condition II in Fig. (7.2)) with $x_{s0} = 0.55$. This result is consistent with the literature [99, 148, 149], for example in [99] Fig.(3), where it can be seen that a decrease of $8-9\%$ of the solar constant is required to achieve $x_s \simeq 0.5$.

As seen in Fig. (6.19), in order to counteract a doubling of CO_2, a reduction of insolation of $4-4.5\%$ is required at the poles and only $1-1.5\%$ at the equator. Comparing this result with Fig. (7.5), although the cooling required at the equator to achieve the ice-covered state is considerably higher than 1.5%, the required deployment of SRM at the poles to counteract F_{2xCO_2} is in principle sufficient to move the ice line to lower latitudes. However, if the energy input to the tropics is left nearly constant, as in this case, changes in the albedo of the middle and upper latitudes can eventually be mitigated by the exporting of energy from the tropics [140]. Therefore, the instability of the system would not be triggered. This analysis is of importance to climate engineering involving SRM since it demonstrates that the extent of the insolation reduction commonly considered for SRM is rather far from such a catastrophic boundary.

In order to compute the new temperature profile, representing the third equilibrium state (see Fig. (7.2)), a small perturbation δU with $\lambda < -1$ is considered. The perturbed temperature obtained by the reduction of insolation given by $U_{bound}(x,t)$ to drive the system from the current

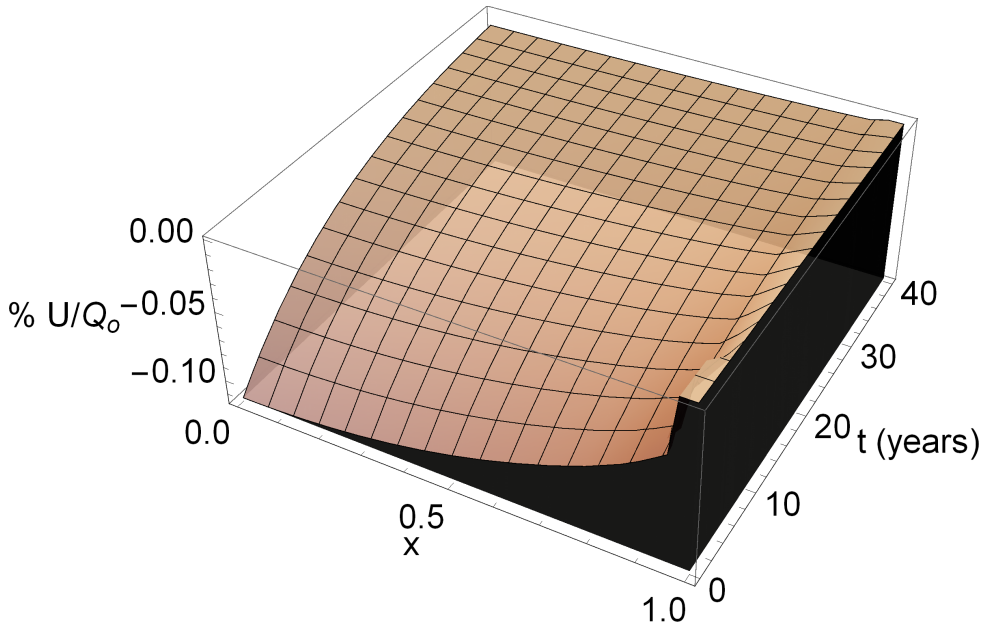

Figure 7.5: Boundary control function obtained setting $C_1 = 0$ in Eq. (7.8), where any SRM profile within the surface which satisfies Eq. (7.8) will lead to an ice-covered state.

climate state (I) to the unstable state (II) can therefore be computed as follow:

$$\delta T_{12_{ice}}(x,t) = \int_0^t \delta T_{12}(x,\tau) G_t(t,\tau)\, d\tau \tag{7.9}$$

with δT_{12} given by Eq. (3.18), where the expression for U is substituted from U_{bound} and G_t is reported in Eq. (6.4) in Section 6.2.

To describe the transition from state II to an ice-covered state (III), Eq. (7.9) becomes:

$$\delta T_{23_{ice}}(x,t) = \int_0^t \delta T_{23}(x,\tau) G_t(t,\tau)\, d\tau \tag{7.10}$$

with δT_{23} given by Eq. (3.18), where the expression for U is substituted from $U_{bound}(x,t) + \delta U(x,t)$.

Figure (7.6) shows the latitudinal distribution of $T_{12_{ice}}(x,t)$ and $T_{23_{ice}}(x,t)$ given by:

$$T_{12_{ice}}(x,t) = T(x,t) + \delta T_{12_{ice}}(x,t) \tag{7.11}$$

$$T_{23_{ice}}(x,t) = T(x,t) + \delta T_{23_{ice}}(x,t) \tag{7.12}$$

where $T_{12_{ice}}$ and $T_{23_{ice}}$ represent the equilibrium temperatures reached after the perturbations $\delta T_{12_{ice}}$ and $\delta T_{23_{ice}}$ are applied to the system. In particular, $\delta T_{23_{ice}}$ achieves the climate state III, i.e. the condition of an ice-covered Earth with $x_s = 0$. However, for any $U(x,t)$ smaller than $U_{bound}(x,t)$ the climate system would remain in state I (current climate with $x_{s0} = 0.95$). Also, in Fig. (7.6), $T(x,t)$ is given by the equilibrium solution describing the current climate (Eq. (6.3)).

In accordance with the literature [150], in this new climate state the maximum temperature obtained is $-20.44°C$, whereas the global average temperature given by the integration over latitude of $T(x,\infty)$, i.e. the equilibrium temperature, is $-31.77°C$, as expected from the investigation of the potential function for state III (see Fig. (7.2)). This result can be also seen in Fig. (7.7), where the contours show equilibrium temperatures between $-30°C$ and $-35°C$ for $x_s \leq 0.4$ and specific values of $(Q_0+U)/Q_0$. As seen in Fig. (7.7), another important feature for

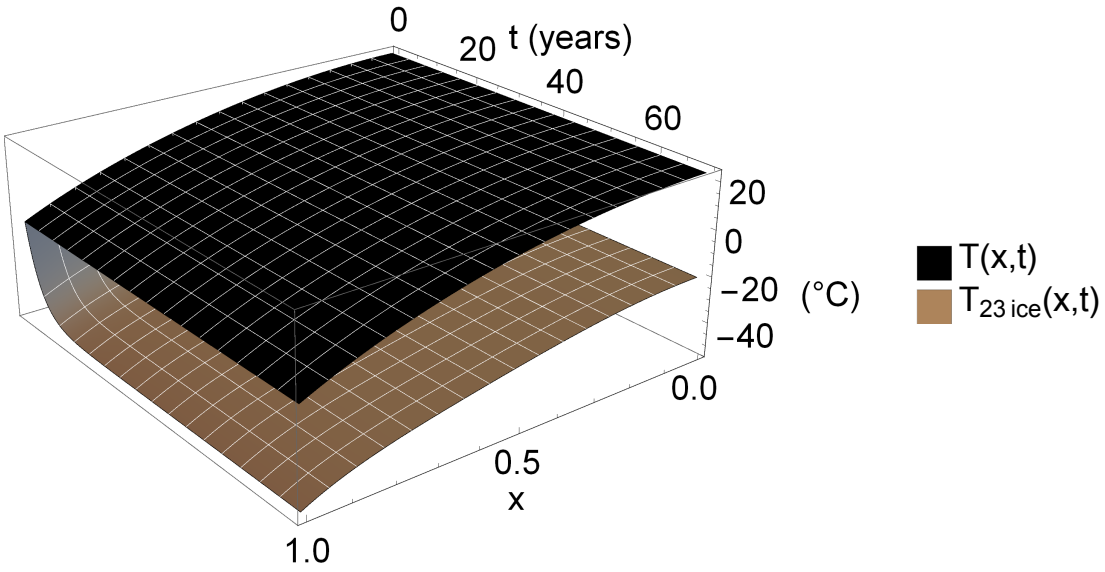

Figure 7.6: Trend of the equilibrium temperature of the current climate ($T(x,t)$) and the equilibrium temperatures obtained after the perturbation $U_{bound}(x,t)+\delta U(t)$ is applied to the system, respectively.

the investigation of the dynamics of the ice line is the trend of x_s for a given change of insolation ($(Q_0+U)/Q_0$). This can be obtained through Eq. (50) in [75] where the parameters of the PDE model, averaged between the Southern and Northern hemisphere in order to better imitate the diffusive model in [75], are considered.

Despite the differences between the PDE model and the model described in [75], such as the overall climate sensitivity and the parametrisation of the albedo (in [75] a step function is

employed for $\alpha(x, x_s)$), the results, reported in Fig. (7.7) of this work and in Fig. (8) in [75], are broadly comparable. In both cases the climate system shows two equilibrium states for current insolation conditions. As can be seen from Fig. (7.7), if the normalised insolation is decreased to 0.94, the unstable equilibrium state is reached and although if the normalised insolation is increased again the ice line decreases further and the ice-covered state is reached. As it will be seen later, a much larger warming perturbation is required to lead the system back to the current climate state if an ice-covered state is reached. This outcome is in agreement with the literature where steady-state climate models are considered and suggests that only a 6% reduction of insolation is required to trigger the instability. Otherwise following the approach developed in this Chapter, with the PDE model in Section 6.2, it is found that the overall reduction needs to be 8.8% to drive the system to instability (Section 6.4). This discrepancy is due to the time-dependency of the PDE model employed [140].

The change of sign of the curve for $x_s > 0.8$ in [75] is an artefact of the mathematical form of the albedo step function, as explained by North et al. in [75], and it is therefore not visible in Fig. (7.7) because a smooth function is considered for the albedo. Another similar model, where the same function in Eq. (6.2) is employed for the albedo, can be found in [137]. In particular, in [137], the graph of Fig. (7.7) is obtained through numerical simulations (and can be found in Fig. (4.2) of [137]). Although the models employ different system parameters, the values of Q are broadly comparable with the normalised values shown in Fig. (7.7).

7.4 Recovery from an ice-covered state

Finally, the recovery from an ice-covered state is investigated for completeness. The procedure described in Section 7.2 is applied again in order to estimate the variation of insolation necessary to drive the Earth's climate from an ice-covered state (III) to its previous state (the current climate state I). Therefore, in this case, $x_{s0} = 0$, $T_s = -20.44°C$ and $\lambda = -0.28$ (obtained through Eq. (3.22)) are employed. Again, a family of control functions which would trigger a recovery is found. In Fig. (7.8), several control functions are reported for values of C_1 between 0 and 3. As before, the minimum control function can be found setting $C_1 = 0$ and Fig. (7.9) is obtained.

Therefore, considering the minimum control function reported in Fig. (7.9), it is estimated that an overall increase of $U/Q_0 = 30\%$ is required to move the ice line from $x_s = 0$ back to $x_s = 0.95$. In particular, a maximum increase of 30.1% is required at the equator and a minimum

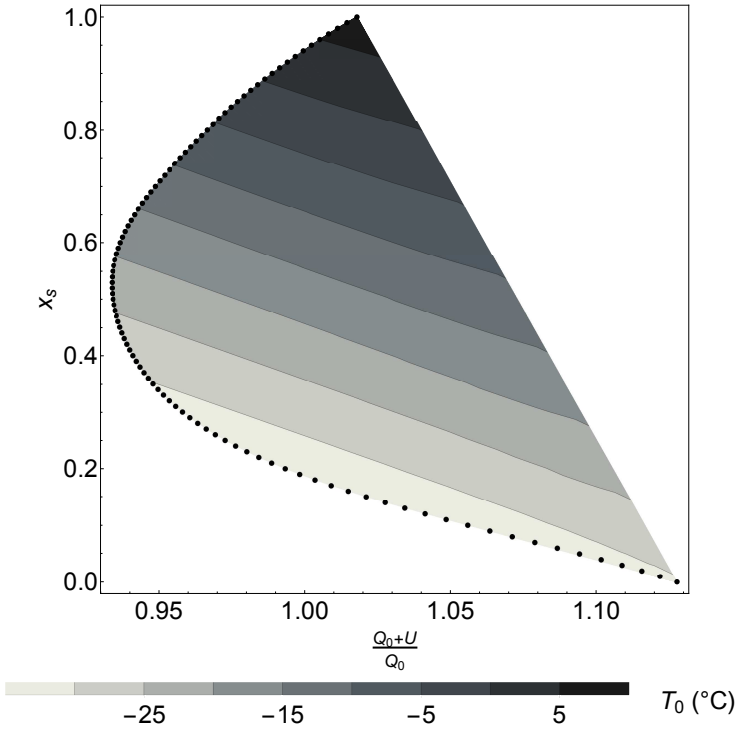

Figure 7.7: Dotted curve represents the trend of the position of the ice line x_s with the variation of the insolation (normalised over the current value of the solar constant Q_0). The values of x_s are obtained computing Eq. (50) in [75] with the parameters of the PDE model (see Section 6.2). The contours give information on the equilibrium temperature for a given insolation ($(Q_0+U)/Q_0$) and ice line position (x_s).

of 10.6% at the pole. This result can be also found in [148].

The family of functions $U_r(x,t)$ (r stands for recovery) provides the distribution of insolation increase required to move the climate system back to current conditions. In particular, $U_r(x,t)$ is obtained considering Eq. (3.16) and applying the Lyapunov stability criterion as for the previous case. As before, the new equilibrium temperature can be computed through Eq. (7.9) and Fig. (7.10) is then obtained. In particular, the trend of the temperature of the ice-covered climate state is given by T_{23ice} whereas the new climate state reached is represented by T_{rec}.

It can be noted that the value of the equilibrium temperature at $x = 0.95$ is $-10°C$ and the overall equilibrium temperature of the new climate state is $24.1°C$. In accordance with other results from the literature [75], the new equilibrium state is found to be much warmer than the previous state with a global equilibrium temperature of order $13°C$, despite that the ice line is at $x_{s0} = 0.95$ in both cases. This is due to latitudinal diffusion of heat towards the poles and the strong ice-albedo feedback. Because of these phenomena, a considerable increase of solar radiation is required near the equator to move the ice line back to the pole and this causes a

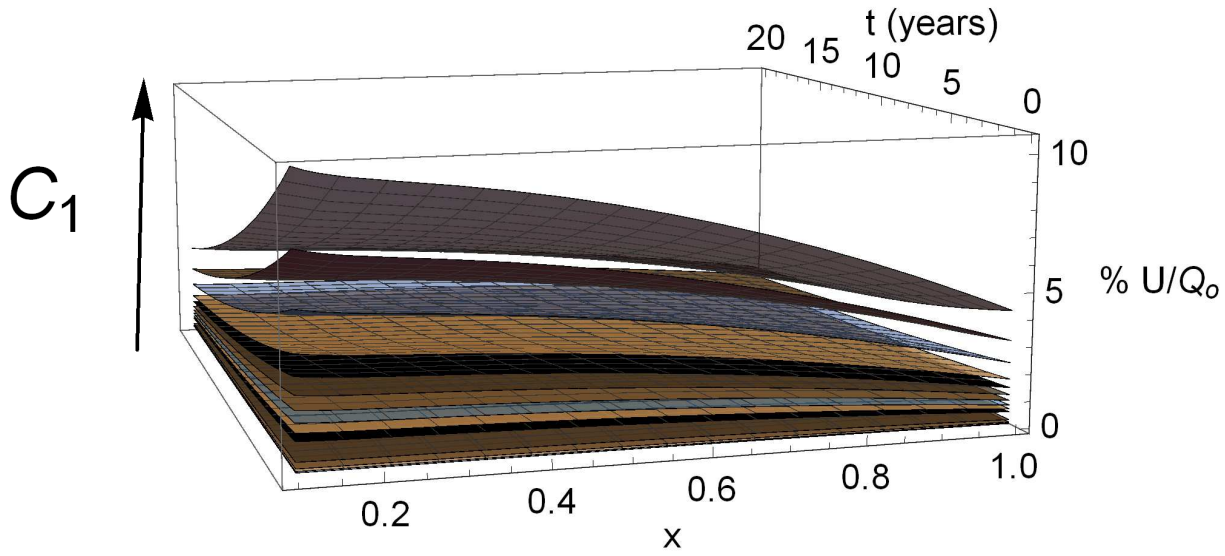

Figure 7.8: Family of control functions ($0 < C_1 < 3$) for the recovery from an ice-covered state.

resulting warmer equilibrium climate state.

7.5 Conclusions

In this Chapter, the PDE model investigated in Chapter 6 is employed in order to investigate the upper limit on SRM through the analysis of the ice line dynamics. This analysis is of importance for climate engineering involving SRM since it demonstrates that the extent of the insolation reduction commonly considered for SRM is far from the insolation reduction required to trigger instability of the climate. However, the definition of such boundaries are of importance for any engineering venture. With respect to other similar analysis in the literature, where the insolation reduction required to achieve an ice-covered state is estimated, in this case, the whole family of control functions which would destabilise the climate system is found and analytical expressions are provided as a function of both latitude and time.

Results of the analysis show that the minimum overall control effort required for an ice-covered state is approximately 8.8%, which decreases towards zero as the climate cools. In particular, the maximum insolation reduction is required at the equator (11.5%) and the minimum at high latitudes (4.2%). The system then falls into a stable ice-covered state, where the global equilibrium temperature is estimated to be $-32°C$.

The use of the PDE model allows a clear and quick assessment of the boundaries of SRM,

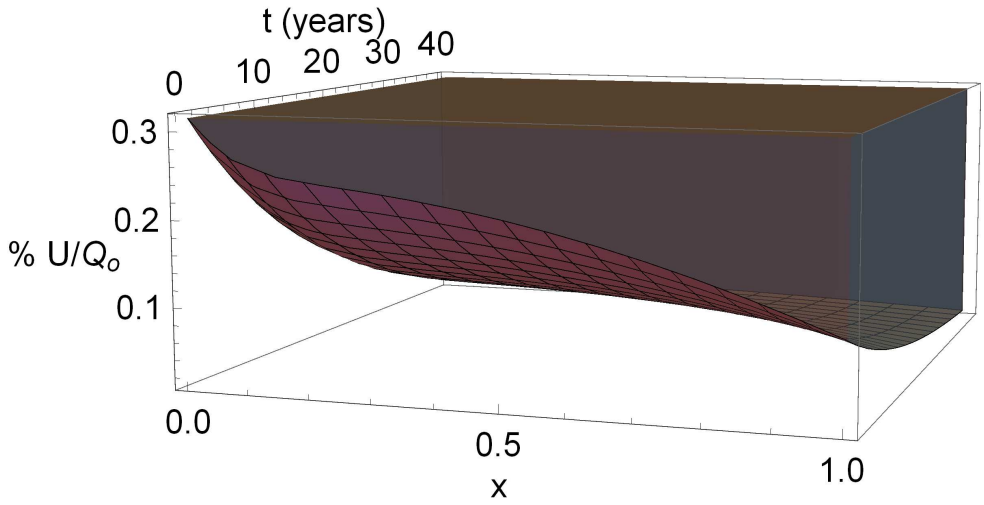

Figure 7.9: Minimum control function required to recover from an ice-covered state obtained setting $C_1 = 0$, where any SRM profile within the surface, which is also part of the family of functions in Fig. (7.8), will lead to the current climate state

.

proving that the insolation reduction required to move the ice line to the equator is much larger than that considered for SRM deployment. Again, it is highly unlikely to accidentally force an ice-covered state.

Finally, the recovery from the ice-covered state is investigated, again through the approach of the Lyapunov stability criterion. In this case, in accordance with the literature, an overall increase of insolation of 30% (of which a maximum of 30.1% at the equator and a minimum of 10.6% at the pole) is required to restore the ice line to its previous position. The equilibrium temperature of the new climate state is found to be approximately $24.1°C$, which is greater than the equilibrium temperature for the current climate. This is due to the effect of the latitudinal diffusion towards the pole and the strong ice-albedo feedback that requires a large increase of the insolation near the equator.

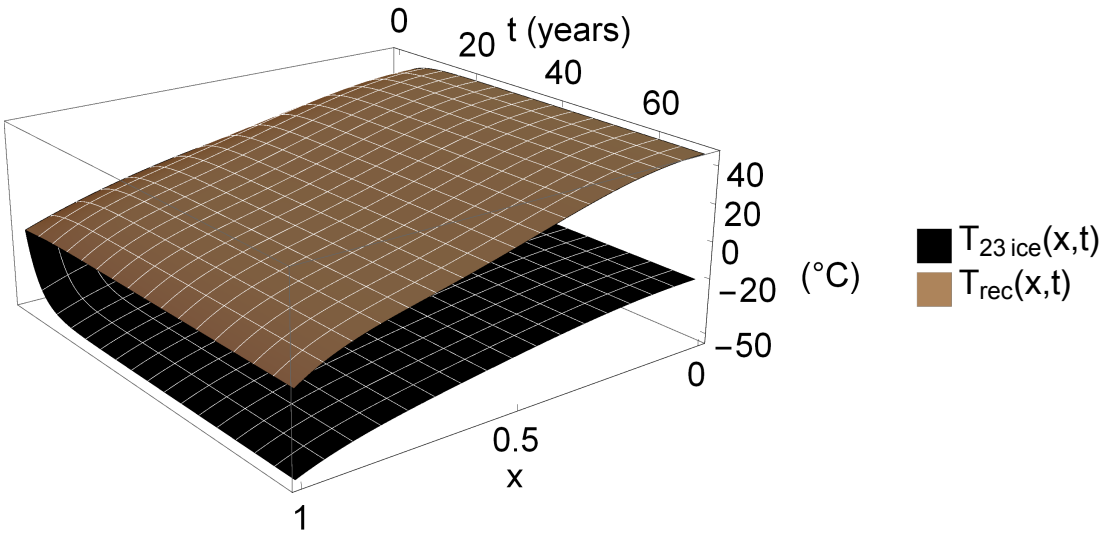

Figure 7.10: Trend of the temperature of the ice-covered climate state ($T_{23ice}(x,t)$) and the temperature obtained after the perturbation $U_r(x,t)S(x)\alpha(x,x_{s0})$ is applied to the system, which is given by $T_{rec}(x,t)$.

Chapter 8

Space solar shields to counteract climate change in a latitudinal Energy Balance Model

8.1 Introduction

Concepts for SRM, such as aerosol injection in the stratosphere or deployment of space-shields, is generally seen as the fastest-acting and most efficient climate engineering scheme, particularly compared to CDR. SRM strategies involving the deployment of large shields in Earth orbit to reflect back a fraction of insolation, and therefore decrease global mean temperatures [42, 48], are investigated in this chapter to counteract radiative forcing from a doubling of CO_2 within less than 2 decades.

With respect to prior work [42, 43, 49, 52, 151], in this chapter a continuous climate model with latitudinal resolution is employed using the PDE model of Chapter 6. It is therefore possible to analytically estimate the insolation reduction required at every latitude and determine the most suitable orbit for the shield. Moreover, orbital perturbations are included in the analysis to estimate the shield position in orbit.

In order to counteract a doubling of CO_2, equivalent to an insolation reduction of 1.78 %, it is found in [50] that an occulting solar disk of radius 915 km would be required, whereas, in [152] it is estimated that an interception area of $2\times10^6\ km^2$, or a disk approximately 800 km in radius would be required. However, these strategies do not take into account latitudinal disparities due

to SRM.

The strategy employed in this chapter considers a shield in Earth orbit capable of providing discontinuous shade on a latitudinal scale, which aims to match the required latitudinal profile of insolation reduction needed to counteract a doubling of CO_2 concentration. The main goal of the chapter is to provide a strategy for SRM which takes into account the orbit of the shield, latitudinal disparities as well as seasonal effects.

In Section 6.4, a continuous latitudinal PDE model with analytical solution is employed to estimate the latitudinal insolation reduction required to counteract a doubling of CO_2 concentration. In this chapter, the PDE model is revised in order to include the grade of obscuration provided by the space shields and then estimate the resulting effect on the temperature profile.

In Section 8.2, a formulation for the grade of obscuration is derived and is employed in the PDE model to demonstrate the validity of the strategy by reproducing results from the literature. Also, in Section 8.4, an analytical expression for the shield radius required is obtained and, in Section 8.5, the geometry between Sun and shield is determined.

The design of the optimal orbit to provide a matching of the required latitudinal obscuration pattern is also discussed in Section 8.5, where the description of an optimisation process is provided. In particular, the optimization is performed to minimise the shield's size as well as to provide large obscuration at high latitudes (requirement of the problem as found in Section 6.4). Moreover, since space shields are high area-to-mass ratio objects, the effects of solar radiation pressure (SRP), and also J_2 perturbations, on the orbit need to be investigated. Therefore, in Section 8.6.2, the effect of these perturbations are quantified.

Results of the optimisation are reported in Section 8.6, where the efficiency of the strategy employed is demonstrated investigating its effect upon the latitudinal temperature profile when a single shield (Section 8.6.1) or a constellation of shields (Section 8.6.3) are deployed. Indeed, when more than one shield is considered the radius of each shield can be largely reduced.

8.2 Grade of obscuration provided by a solar shield

Following Sections 3.1 and 6.2, the PDE model in Eq. (6.1) is employed in this chapter to describe the climate system and to assess the effects of space shields. Equation (6.1) can be summarised as:

$$C\frac{\partial T(x,t)}{\partial t} = \frac{\partial}{\partial x}D(1-x^2)\frac{\partial T(x,t)}{\partial x} - bT(x,t) + \Phi(x) \tag{8.1}$$

where terms and parameters are defined in Section 6.2 for each hemisphere. In particular, the formulation in Eq. (4.4) is employed for the infra-red parameters a and b. Moreover, Φ is the external forcing of the system which in this case depends only on x and can be written as:

$$\Phi(x) = (1-U)\,Q_0 S(x)(\alpha(x,x_s)) - a + F_{2\times CO_2} \tag{8.2}$$

In addition, with respect to Eq. (6.1), the radiative forcing due to a doubling of carbon dioxide ($F_{2\times CO_2} = 3.71\ W/m^2$) is included in Eq. (8.2).

The necessary reduction of insolation $U(x)$ to drive the temperature back to pre-industrial levels has been estimated in Section 6.4 and expressed through a control law with latitudinal distribution in Fig. (6.19). As can be seen, the required control has a distinctive latitudinal distribution which depends strictly on the latitudinal pattern of insolation (see Section 6.4 for further details).

As seen in Fig. (6.19), in order to counteract a doubling of CO_2, an insolation reduction of $3-4.5\%$ is required near the poles, i.e. between latitudes $\pm 50°$ to $\pm 90°$, whereas only $1-2\%$ is necessary at lower latitudes. Therefore, the optimal orbit should provide a larger coverage of the polar regions with respect to the low-latitude regions. Before initiating the optimisation process which provides the optimal parameters for the shield's orbit, it is necessary to estimate the grade of obscuration provided by the shield. A shield in Low-Earth-Orbit (LEO) is assumed so that a larger number of obscuration events would occur. This choice will be confirmed later through the optimisation process.

Thus, in this section, a computation of the area of the shaded region on the Earth's surface is performed. Since the altitude of the orbit is rather low (LEO), it is necessary to consider the shaded region as a spherical cap whose area is given by [153]:

$$A_e = 2\pi R_E^2 \left(1 - cos\left(\frac{R_s}{R_E}\right)\right) \tag{8.3}$$

where R_s is the radius of the shield and R_E is the Earth's radius.

The grade of obscuration at time t and latitude x is given by the ratio of A_e to the area of the Earth's sphere and can be written as:

$$\mathcal{O}(x,t) = \frac{1}{2}\left(1 - cos\left(\frac{R_s}{R_E}\right)\right) S(x(t),t)\alpha(x(t),t) \tag{8.4}$$

where, the terms $S(x,t)$ and $\alpha(x,t)$ represent the latitudinal distribution of insolation and the planetary albedo at time t and latitude x as described in Eqs. (3.13)-(3.14). These terms take seasonal effects into account. In the PDE model in Eq. (8.1), the yearly-averaged functions $S(x)$ and $\alpha(x,x_s)$ from Eqs. (3.5)-(3.6) are employed to describe the latitudinal distribution of the insolation in the PDE model since the behaviour of the climate system will be investigated over several decades. However, in this case, the grade of obscuration provided by the shield throughout one year is explored in conjunction with its orbital elements and the Sun's position. Seasonal variations are therefore of critical importance.

8.3 Validation of the strategy with the PDE latitudinal model

In this section the PDE model is employed to compute the required shield radius to counteract a doubling of CO_2. In particular, since the objective of this section is the reproduction of the results from the literature [51], seasonal effects will be neglected and the annual average insolation $(S(x)(\alpha(x,x_s)))$, with terms found in Eqs. (3.5)-(3.6), is considered for the obscuration function in Eq. (8.4).

Thus, the expression for the grade of obscuration is largely simplified and can be analytically solved considering the analytical solution of the PDE model found in Section 6.2. It is then found that in order to quickly minimise the temperature anomaly, the radius of the shield needs to be between 1350 km and 2600 km (depending on latitude) equivalent to an area of $5.7\times10^6 - 2.1\times 10^7\ km^2$ which is comparable with the area $55000\times100\ km^2 = 5.5\times10^6$ estimated in [51] for a large cloud of $100/km^2$ reflectors. As can be seen, employing the PDE model, the latitudinal resolution is maintained, therefore the analysis provides greater insight to the estimation of the shield radius with respect to the literature. In fact, as expected, in principle the shield radius required to minimise the temperature anomaly due to a doubling of CO_2 concentration is not constant and depends on the latitude as can be seen in Fig. (8.1). As expected, a smaller shield is required at low latitudes because of the larger mean insolation received in those regions.

In the next section, an optimization process will be performed in order to find the ideal orbit for the shield and provide sufficient obscuration at high latitudes. As will be seen, the optimization process includes the orbital dynamics of the shield and it will be demonstrated that, choosing an orbit which provides matching of the insolation reduction, it is possible to use a shield of fixed size.

Results from the literature can therefore be reproduced neglecting seasonal and latitudinal effects and without purposely designing the shield orbit through an optimisation process. In the next section, the method employed to select the ideal orbit for the shield, taking into account latitudinal disparities due to the pattern of insolation and seasonal effects, will be developed.

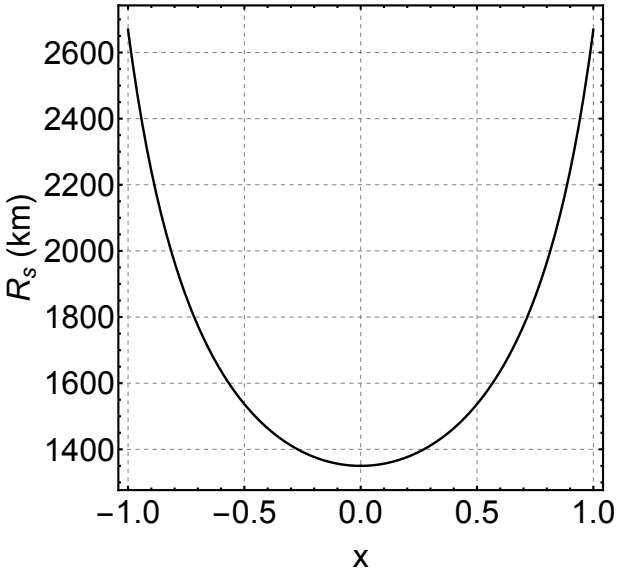

Figure 8.1: Required shield radius to counteract a doubling of CO_2 with latitude obtained without optimisation and neglecting seasonal effects.

8.4 Estimation of the shield radius

In this section, a relationship to estimate the dimensions of the shield is found. In particular, the radius of the shield is estimated considering the insolation reduction required at high latitudes and then the orbit is designed in order to minimize the presence of the shield at low latitudes. This strategy provides the matching insolation reduction to counteract a doubling of CO_2 at each latitude.

Thus, taking into account Eq. (8.4) with seasonal effects, discussed in Section 3.1, it is possible to find the shield radius required to achieve the insolation reduction required at high latitudes ($> \pm 50°$) to counteract a doubling of CO_2. Again, the coverage of high latitude regions is considered the main objective to find the shield size whereas the minimization of the time spent at lower latitudes is achieved through the orbit design. Also, the value of $\pm 50°$ was chosen to identify the limit between high and low latitudes because, as can be seen in Fig. (6.19), the most relevant variations for required insolation reduction occur near $\pm 50°$.

Integrating Eq. (8.4) over a year (t_f), the yearly-averaged obscuration function $\mathcal{O}_y$ at high latitudes x_e is obtained:

$$\mathcal{O}_y = \frac{1}{2}\left(1 - cos\left(\frac{R_s}{R_E}\right)\right)\int_0^{t_f} S(x_H,t)\alpha(x_H,t)\,dt \tag{8.5}$$

where x_H represents the latitude of a point on the Earth's surface within the shaded area which is higher than a latitude of $\pm 50°$. Using Eq. (8.5), the required shield radius which would provide the necessary change in solar radiation at x_H during each obscurating event may be obtained through the following expression:

$$R_s(x_H) = R_E\ arccos\left(1 - \frac{2\,\mathcal{O}_y}{\int_0^{t_f} S(x_H,t)\alpha(x_H,t)\,dt}\right) \tag{8.6}$$

The required value of $\mathcal{O}_y$ can be written as:

$$\mathcal{O}_y = \frac{F_{2xCO_2}}{Q_0} n_{obsH} = 1.086\%\ n_{obsH} \tag{8.7}$$

where 1.086% is the radiative forcing reduction required to counteract a doubling of CO_2 ($3.71\ W/m^2$) normalised with respect to the solar constant. Radiative forcing due to carbon dioxide is uniformly distributed over all latitudes, therefore this value is constant. Also, n_{obsH} is the number of obscuration events occurring at high latitudes throughout each year. In particular, the number of obscuration events at high latitudes is considered in order to guarantee that the minimum obscuration needed is provided at all latitudes. Selecting the final value of the shield through this method would guarantee that there are no under-cooled regions. In this way, Eq. (8.6) can be employed to estimate the shield radius to provide the necessary radiative forcing reduction during every obscuration event, taking seasonal variations into account. In fact, the latitudinal dependence of the control law is found in the terms $S(x(t),t)\alpha(x(t),t)$, which also defines n_{obsH}, and provides the latitudinal distribution of insolation reduction.

As will be seen in the Section 8.5, the estimation of the shield's size is linked to the orbit elements of the shield since these are employed to determine the geometry between Sun and shield. The geometry is then employed to determine coordinates of the shaded regions as a function of time as well as the time of the year when obscuration occurs. Again, these contributions can be found in the term $S(x_H,t)\alpha(x_H,t)$ in Eq. (8.6).

Moreover, the distinction between obscuration events occurring in winter and summer is of relevance because, for example, as can be seen in Fig (3.1), in the northern hemisphere, during summer months a larger quantity of insolation would be reflected back to space with respect to the case when the shield is employed during winter months. As will be seen later, this response is also considered in the optimisation process.

8.5 Design of the ideal shield orbit

In order to design the orbit of the solar shield, the geometry in Fig. (8.2) is considered. In particular, $\mathbf{X_s}$ and $\mathbf{X}_\odot$ are the position vectors of shield and Sun, respectively. Their expressions can be found in Eqs. (3.32)-(3.47), where distances are measured in astronomical units (AU). Specifically, the shield coordinates in the Earth centred rotating frame can be computed following the process described in Section 3.5 for a given set of orbital elements (a_s, e, i_s, Ω_s, ω_s). This procedure is included in the optimisation process performed to find the best combination of orbital elements for the shield's orbit. Moreover, as discussed in Section 3.5.2, long-term perturbations due to J_2 and solar radiation pressure have a non-negligible effect on the longitude of ascending node and argument of perigee. Therefore these perturbations are taken into account in the optimisation process and are computed at every iteration in order to correctly estimate the shield position.

The equation of the line connecting the Sun and shield is $\mathbf{X} = \mathbf{X}_\odot + d\mathbf{l}$, where d is the distance along the line centred at the Sun and $\mathbf{l}$ is a unit vector representing the direction of the line which can be written as:

$$\mathbf{l} = \left(\frac{x_s - x_\odot}{D_{s\odot}}, \ \frac{y_s - y_\odot}{D_{s\odot}}, \ \frac{z_s - z_\odot}{D_{s\odot}} \right) \tag{8.8}$$

In Eq. (8.8), $D_{s\odot}$ is the distance between Sun and shield in astronomical units. Combining the line's equation with an expression for the Earth's sphere, it is possible to calculate the intersection points ($\mathbf{X}_{e1}$ and $\mathbf{X}_{e2}$) on the Earth's surface as shown in Fig. (8.2). One of these points represents the location where a partial obscuration occurs, whereas the other is located on the other side of Earth, as can be seen in Fig. (8.2). Thus, solving the resulting equation for d, the following expression is obtained:

$$d^* = -\mathbf{l} \cdot \mathbf{X}_\odot \pm \sqrt{\left(\mathbf{l} \cdot \mathbf{X}_\odot\right)^2 - |\mathbf{X}_\odot|^2 + R_e^2} \tag{8.9}$$

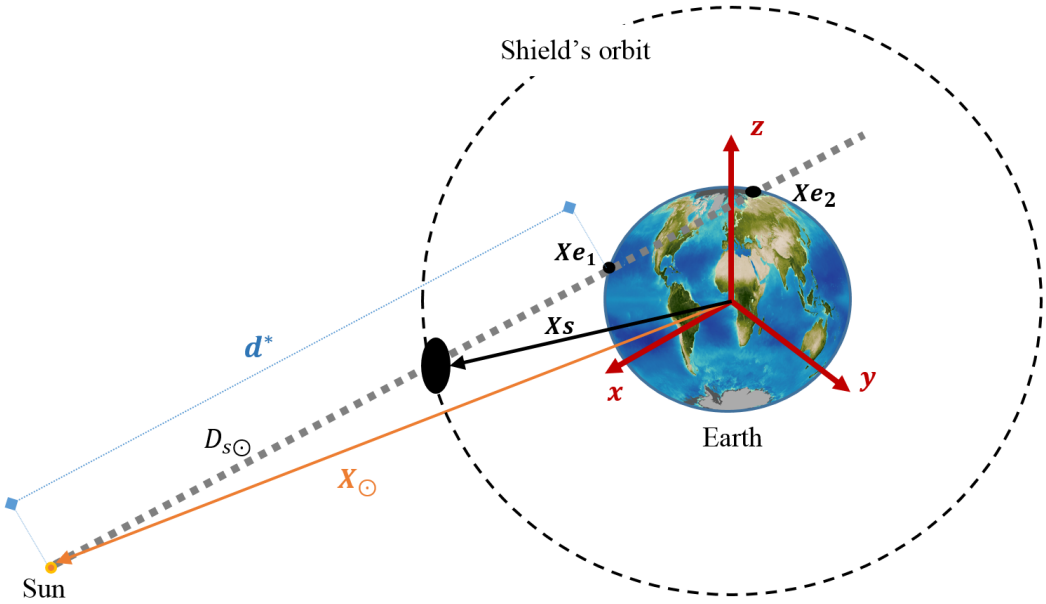

Figure 8.2: Geometry of the obscuration of a location on the Earth's surface provided by a space-based solar shield.

where d^* is the distance between the Sun and the two intersections on the Earth's surface. The Earth's radius is also measured in AU in Eq. (8.9).

When the term under the radical sign in Eq. (8.9) is larger than or equal to zero and $\mathbf{X}_\odot \cdot \mathbf{X_s} > 0$, i.e. the Sun and shield are on the same side with respect to the Earth, a partial obscuration occurs at:

$$\mathbf{X_{e1}} = \left(x_{e1}, y_{e1}, z_{e1}\right)^T = \mathbf{X}_\odot + d^*\mathbf{l} \tag{8.10}$$

In particular, d^* is computed considering the negative sign in Eq. (8.9) to find the coordinates of $\mathbf{X_{e1}}$ and to neglect $\mathbf{X_{e2}}$. Thus, the latitude of the intersection point can be written as:

$$\phi_e = arcsin\left(\frac{z_{e1}}{R_e}\right) \tag{8.11}$$

This expression provides the link between the orbit elements of the shield and the latitudinal distribution of the obscuration pattern.

Then, considering the expression in Eq. (8.11), a process of maximisation is performed to find the most suitable combination of orbital elements for the solar shield that would provide the required insolation reduction to counteract a doubling of CO_2 concentration as well as minimise the size of the shield. The objective function, which attempts to maximize the latitude of the

obscuration events while minimising the shield radius, may be written as follows:

$$\mathcal{F}\left(a_s, i_s, e, \Omega_s, \omega_s, A_s/m\right) = \frac{\bar{\phi}_e}{\phi_e^*} - \frac{R_s}{R_s^*} \tag{8.12}$$

where $\bar{\phi}_e$ is the average latitude of the intersection point in a year which can be written as:

$$\bar{\phi}_e = \sum_{i=0}^{n_{obs}} \frac{\phi_{e_i}}{n_{obs}} \tag{8.13}$$

here, n_{obs} is the number of obscuration events occurring throughout the year. Moreover, in Eq. (8.12), ϕ_e^* is equal to 90°, i.e. the highest achievable latitude which represents the ideal case in order to provide more obscuration at high latitudes. Thus, term $\bar{\phi}_e/\phi_e^*$ is maximized when $\bar{\phi}_e$ approaches ϕ_e^*. Similarly, R_s^* represents the worst case scenario for the shield radius. After several iterations, the most suitable value for R_s^* was found to be 490 km. This value guarantees that the terms in Eq. (8.12) maintain the same order of magnitude throughout the simulation. Thus, term $-R_s/R_s^*$ is maximized when R_s is much smaller than R_s^*.

It is worth noting that, ϕ_e and R_s in Eq. (8.12) are normalised with respect to the respective ideal/worst case to compare different quantities and combine them in a single expression. In fact, both terms are in the range $(0, 1)$.

Finally, it was pointed out in Eq. (8.12) that the objective function depends on the orbital elements of the shield and A_s/m, i.e. the area-to-mass ratio of the shield, which affects perturbations due to solar radiation pressure (see Section 3.5.2 for details).

It is important to note that ϕ_e (and therefore $\mathcal{F}$) exists only when the geometry required for an obscuration event is satisfied. Therefore, the conditions for existence of an obscurating event are verified at every iteration of the optimisation process.

8.6 Results

In this section, results from the optimisation process described in Section 8.5 are reported. In particular, in Section 8.6.1 a strategy involving only one large shield in Earth orbit is considered, whereas in Section 8.6.3 several smaller shields are considered to provide the insolation reduction required to counteract a doubling of CO_2.

8.6.1 Single shield

The results of the optimisation are summarized in Fig. (8.3), where values for Ω_s, ω_s, M_0 and i_s which maximise the objective function $\mathcal{F}$ are reported for 64 different sets of initial conditions used with the optimiser. Specifically, the initial conditions considered can be summarized as:

$$\begin{aligned} \Omega_s(0) &= [0\ 90\ 250\ 300]^\circ \\ \omega_s(0) &= [0\ 90\ 250\ 300]^\circ \\ M_0(0) &= [0\ 90\ 250\ 300]^\circ \end{aligned} \tag{8.14}$$

The optimized solutions are provided for the 64 combinations of initial conditions given in Eq. (8.14) for the orbital elements. For the other orbital elements, the initial conditions considered are $i_s = 70°$, $a_s = 7500\ km$, $e = 0.01$ and $A_s/m = 10\ m^2/kg$. These values are then modified during the optimization process to find the maximum of the objective function in Eq. (8.12).

Through this approach, it is possible to obtain reliable results which do not depend on the initial guess. Thus, the global maximum of the objective function can be found. The optimal values found for the semi-major axis and eccentricity of the orbit are approximately 7500 km and 0.01, respectively, whereas, for the orbit inclination and longitude of the ascending node, values can be found in Fig. (8.3). As can be seen, they are mostly in the following ranges: $60° < i_s < 70°$ and $0° < \Omega_s < 40°$. Values of the other orbital elements are rather spread but mostly distributed as follows: $\omega_s = (0°, 30°, 250°)$ and $M_0 = (0°, 250°, 300°)$. Moreover, employing Eq. (8.6), it is possible to estimate the shield radius in order to provide the necessary insolation reduction. This investigation is performed for every set of orbital elements obtained through the maximisation of the function $\mathcal{F}$ and Fig. (8.4) is therefore obtained.

The best solution, which provides the smallest shield radius, is chosen. Thus, it is found that the the ideal orbit has the following orbital elements: semi-major axis of 7875.6 km, orbit inclination of 88.1°, longitude of ascending node of 282°, argument of the perigee of 252°, mean anomaly of 0° and area-to-mass ratio of 29 m^2/kg. In this case, the minimum value found for the shield radius required to provide the necessary latitudinal distribution of solar reduction is estimated to be 1467 km. From Fig. (8.4), it can be seen that for any other combination of values of inclination and longitude of the ascending node, larger values of the shield radius, ranging from 1470 to 1540 km, are found.

Considering the result reported in Fig. (8.1), it can be noted that the optimal value found for

the shield radius is close to the lowest estimate for the shield radius which would be enough to achieve the insolation reduction required at low latitudes, but it would be too small to counteract a doubling of CO_2 concentration at high latitudes. However, as will be demonstrated, considering the orbital elements found through the optimization process, the shield orbit and size defined, it is possible to provide the necessary insolation reduction at every latitude.

Considering the optimal result achieved from the optimisation, the obscuration function may be computed through Eq. (8.4) and the distribution of $\mathcal{O}$ as a function of time and latitude is obtained (see Fig. (8.5)). In particular, the blue dots represent obscurating events at high latitudes, whereas grey dots portray events at latitudes between $-50°$ and $50°$. In addition to the

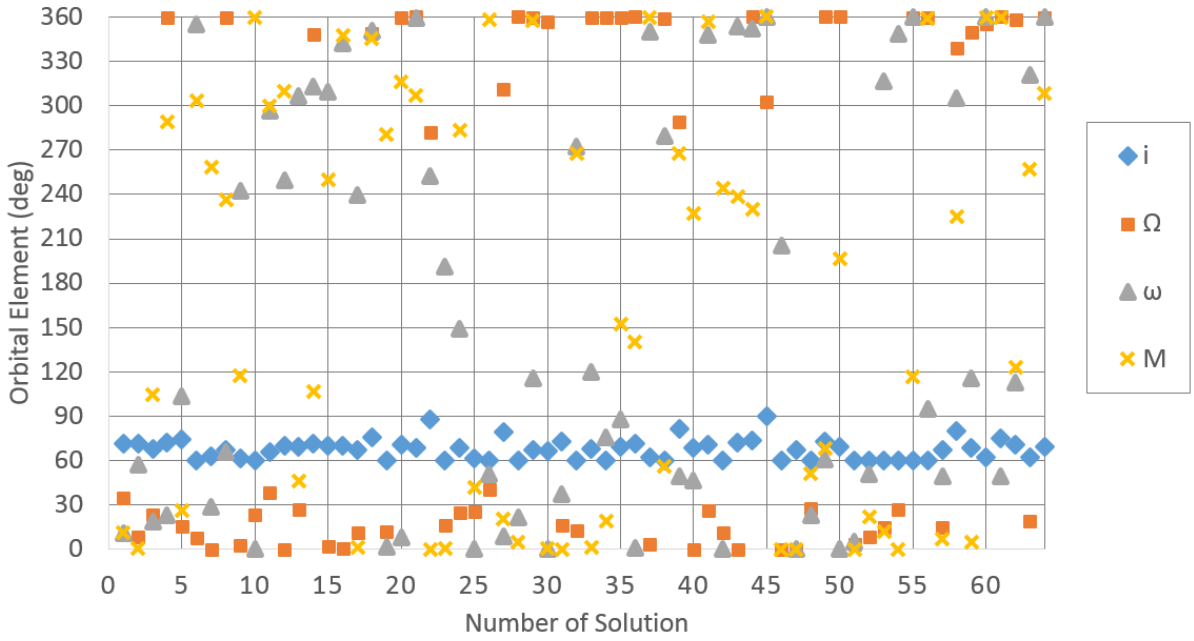

Figure 8.3: Values of the orbital elements resulting from the maximisation of function $\mathcal{F}$ for 64 different sets of initial conditions.

minimization of the shield radius, the goal of the optimisation process is the maximisation of the obscuration at high latitudes and its minimisation between $-50°$ and $50°$ in order to achieve a pattern of insolation reduction which would match the distribution reported in Fig. (6.19). In fact, it can be seen in Fig. (6.19) that a much smaller reduction of insolation is required at low latitudes. Specifically, integrating the function $U(x)$, found in Section 6.4, at low (L) and high (H) latitudes in each hemisphere as follows:

$$U_L = \int_0^{50°} U(sin(\phi))d\phi \tag{8.15}$$

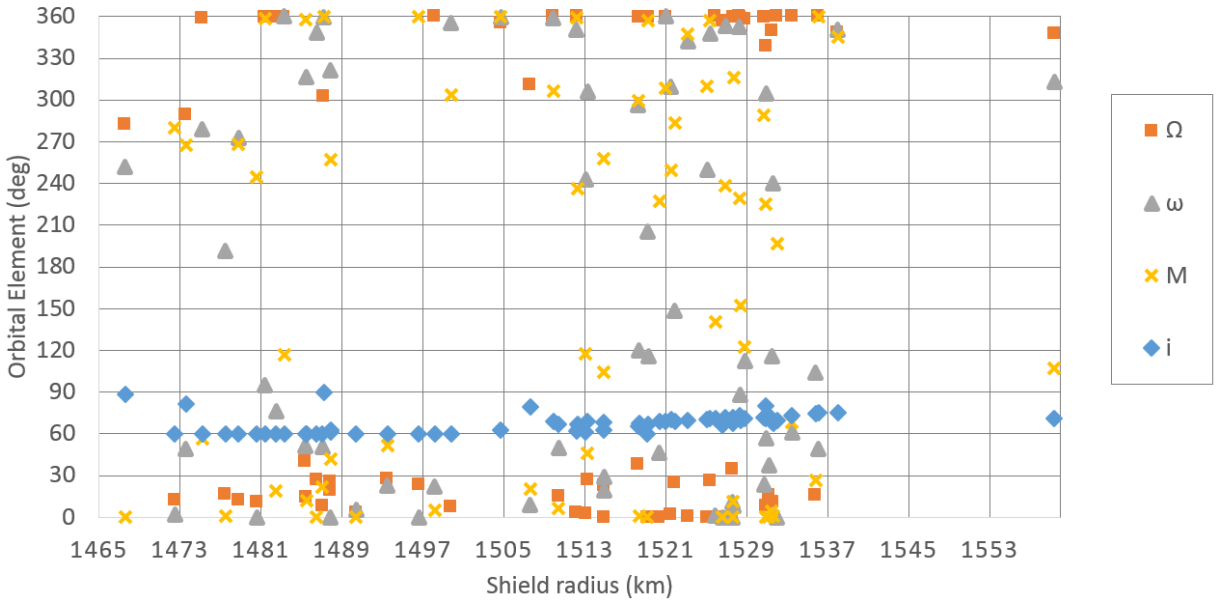

Figure 8.4: Values of the set of orbital elements resulting from the maximisation of the function $\mathcal{F}$ versus the value of the shield radius estimated to counteract a doubling of CO_2 concentration.

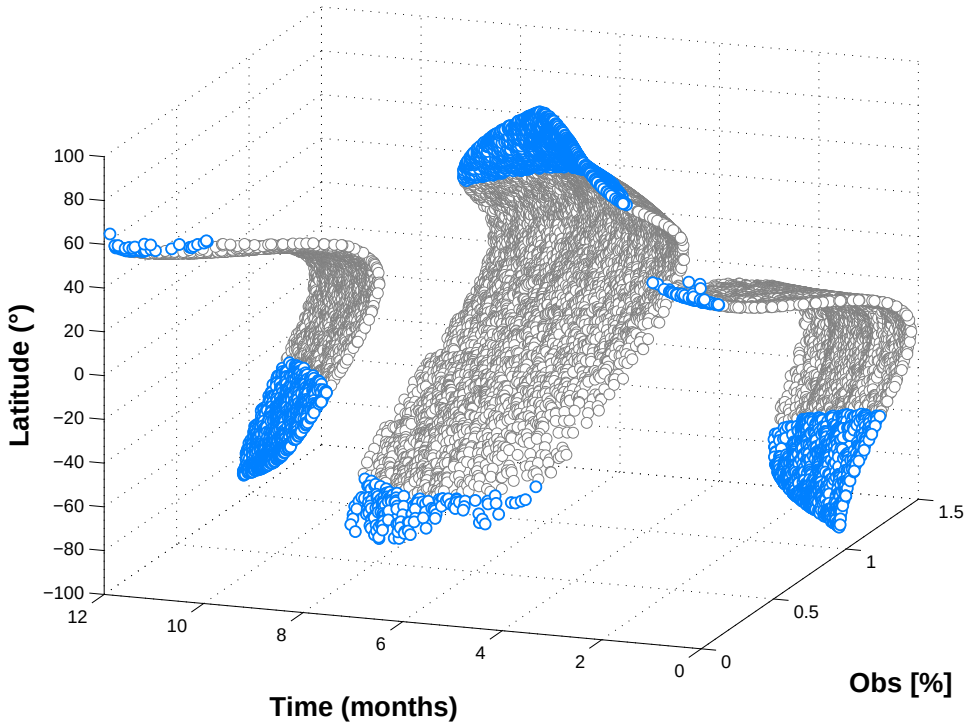

Figure 8.5: Latitudinal distribution of the obscuration function throughout a year provided by a shield orbiting the Earth ($a_s = 7875.6\ km$, $e = 0.01$, $i_s = 88.1°$, $\Omega_s = 282.24°$, $\omega_s = 252.17°$, $M_0 = 0°$, $A_s/m = 29.13\ m^2/kg$, $R_s = 1467\ km$).

$$U_H = \int_{50°}^{90°} U(sin(\phi))d\phi \tag{8.16}$$

It is estimated that only a 1.25 % insolation reduction is required at low latitudes (U_L) and as much as 3.5 % at high latitudes (U_H).

Results show that, for the case considered above which provides the minimum shield radius, the shield would cover high-latitude regions for the 8.8 % of the year, whereas for the 29.4 % of the year would provide obscuration at low latitudes ($\phi < \pm 50°$).

Although high latitudes are covered for a smaller fraction of time, as can be seen in Fig. (8.5), the polar regions are mostly obscured when the largest insolation is received, i.e. from May to September in the northern hemisphere and from October to April in the southern hemisphere. In this way, each obscurating event is more effective with respect to the case when the shield is employed during the winter months. Therefore, if this strategy is employed, then a smaller shield of fixed size would be necessary to provide the required insolation reduction at each latitude and counteract a doubling of CO_2 concentration. Specifically, this result is noted in Fig. (8.6), where the latitudinal obscuration function can be found for both hemispheres. It can be seen then that the obscuration provided by the shield is similar to the required insolation reduction estimated previously.

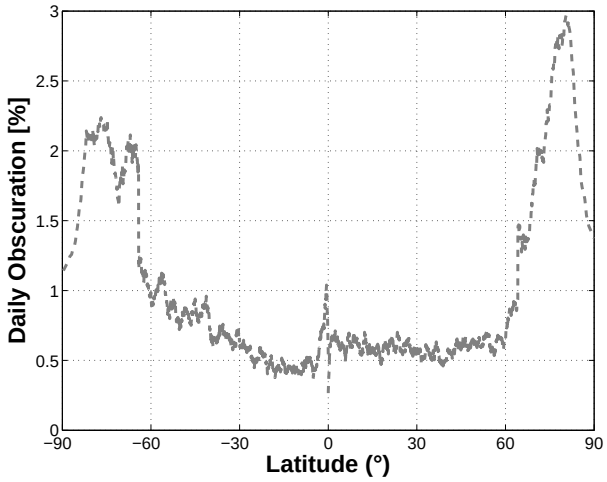

Figure 8.6: Latitudinal distribution of the obscuration function provided by a shield each day ($a_s = 7875.6\ km$, $e = 0.01$, $i_s = 88.1°$, $\Omega_s = 282.24°$, $\omega_s = 252.17°$, $M_0 = 0°$, $A_s/m = 29.13\ m^2/kg$, $R_s = 1467\ km$).

The estimated obscuration function obtained in Fig. (8.5) can be substituted in the PDE

model by considering:

$$U(x,t) = \frac{\mathcal{O}(x,t)}{S(x)(\alpha(x,x_s))} \tag{8.17}$$

where can be noted that the obscuration function already includes terms due to insolation, therefore it needs to be divided by $S(x)(\alpha(x,x_s))$. Employing (8.17) in Eqs. (8.1-8.2), it is possible to investigate the trend of the temperature anomaly due to a doubling of CO_2 concentration in the case when the space shield is deployed. Specifically, it is assumed that a step-change, representing a doubling of CO_2, occurs in 2030 whereas the deployment of SRM starts from 2050.

In Fig. (8.7), the latitudinal distribution of the temperature profile under the F_{2xCO_2}-scenario is reported when SRM is not yet deployed (grey line) and when the shield is deployed in a orbit described by the orbital elements that provided the minimum value of shield's radius (black line). In particular, it is possible to note from Fig. (8.7) that the effect of the shield provides a larger

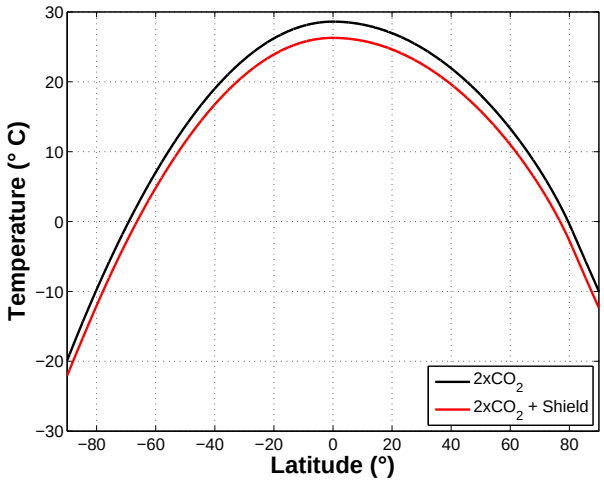

Figure 8.7: Latitudinal distribution of the temperature under a doubling of CO_2 concentration with (red line) and without (black line) deployment of the space shield ($a_s = 7875.6\ km$, $e = 0.01$, $i_s = 88.1°$, $\Omega_s = 282.24°$, $\omega_s = 252.17°$, $M_0 = 0°$, $A_s/m = 29.13\ m^2/kg$, $R_s = 1467\ km$).

temperature reduction at low latitudes. As previously discussed, this is due to the larger quantity of solar radiation reaching those regions throughout the year.

Moreover, Fig. (8.8) shows the trend of the global equilibrium temperature throughout the simulation. As can be seen, when the shield is deployed in 2050, the equilibrium temperature starts decreasing and is driven back to its initial value of $14.37°C$ within 15 years.

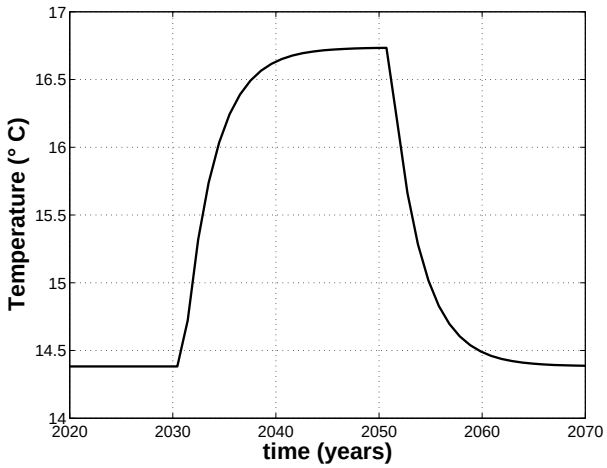

Figure 8.8: Trend of the global equilibrium temperature when a doubling of CO_2 step-change occurs in 2040 and the deployment of a space shield.

8.6.2 Orbital perturbations

Space shields are high are-to-mass ratio objects; therefore, orbital perturbations, such as solar radiation pressure (SRP) need to be assessed for the design of the optimum orbit. Thus, considering Section 3.5.2, Eqs. (3.35)-(3.37) are computed to calculate the SRP acceleration at every iteration of the optimisation process. Specifically, the area-to-mass ratio of the shield (A_s/m) is a variable of the optimisation procedure, as shown in Section 8.5, and is found to be 29 m^2/kg for the optimal solution found in Section 8.6.1. Also, the incident angle (defined as the angular distance between the shield surface and direction of sun rays) is set to $\gamma = 0°$ since the normal to the shield is always perpendicular to the Sun. This is a reasonable assumption considering that the goal is to maximize the area shaded. With regards to perturbations due to Earth's oblateness, as found in [122], J_2 secular effects on Ω_s and ω_s are given by Eqs. (3.39)-(3.40).

The variations of the orbital elements estimated through the Gauss variational equations [118] were taken into account in the optimization process to compute the equatorial coordinates of the shield (x_s, y_s, z_s). Indeed, variations of longitude of the ascending node and argument of perigee are key to estimate the actual position of the shield and determine the geometry between the Earth and shield (see Fig. (8.2)).

In particular, it is expected that only the trend of the argument of perigee and longitude of ascending node are affected whereas variation of inclination, semi-major axis and eccentricity are negligible. Since these perturbations have been considered in the optimization process, the choice of the optimal orbit has been influenced by the presence of these perturbations. Combining

the effect of Earth's oblateness and solar radiation pressure each year,, the total yearly effect can be summarized by $\Delta\omega_s = -57.67°$ and $\Delta\Omega_s = -864.64°$. Also, resulting variations of a_s, i_s, Ω_s, ω_s and eccentricity can be found in Fig. (8.9).

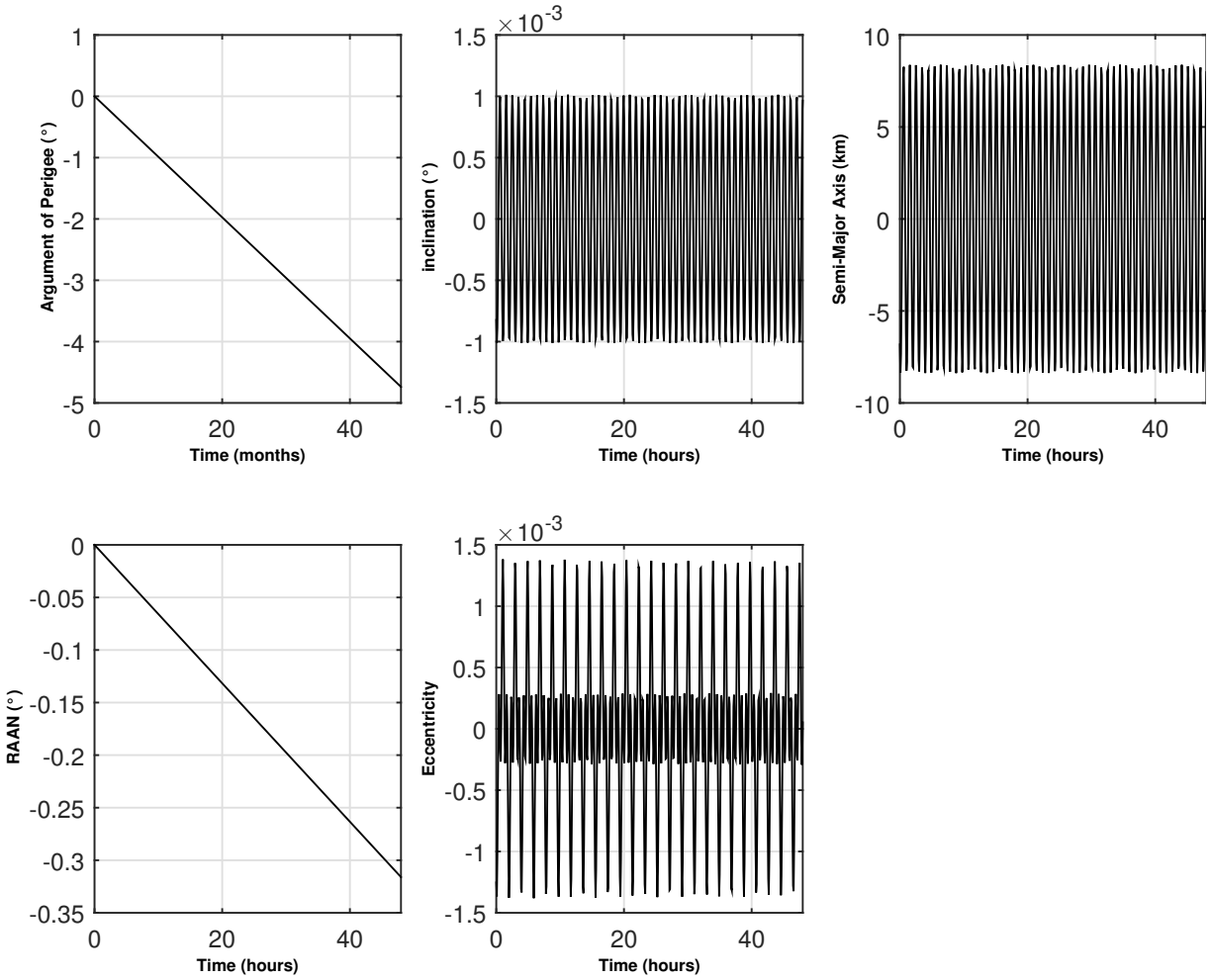

Figure 8.9: Variation of shied's orbital elements ($a_s = 7500\ km,\ i_s = 70°,\ e = 0.01$) due to the Earth's oblateness and SRP perturbations (1 year simulation).

8.6.3 Multiple shields

In reality, it is very impractical to deploy a surface of radius 1467 km in space. Thus, it is important to discuss how it is possible to further reduce the shield size. As in other work [51], this can be accomplished by considering several smaller shields in a constellation and provide the same obscuration pattern found in Section 8.6.1. It is worth noting that this new strategy would not necessarily represent a cheaper option, but surely a more feasible solution. In fact, smaller

shields would be provided with their own attitude control and independent steering capacity with respect to other shields in the constellation.

Assuming the deployment of N shields, each of which provides a grade of obscuration equal to $\mathcal{O}_y/N$ per year, then the required radius for each shield can be obtained through Eq. (8.6). Thus, Fig. (8.10) can be obtained, where the shield radius required to counteract a doubling of CO_2 with the number of shields to deploy is shown. It can be seen that only 25 shields are required, for example, to reduce the radius of each shield to 290 km, but 100 shields need to be deployed to decrease the radius to approximately 175 km. This behaviour is due to the fact that,

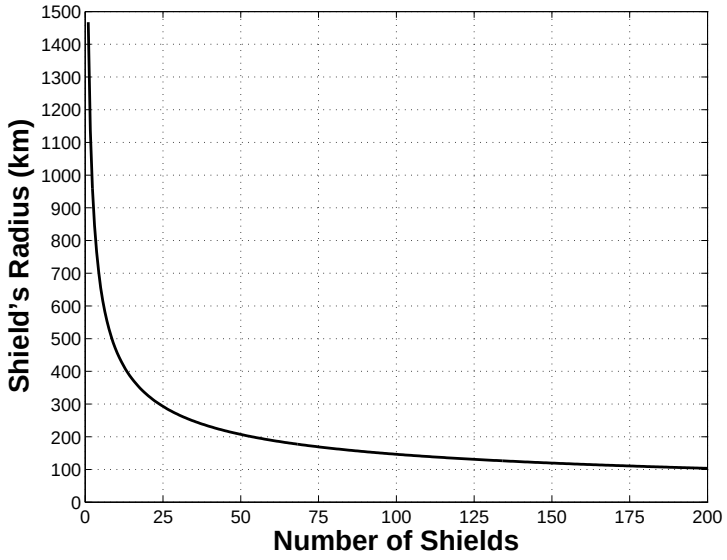

Figure 8.10: Shield radius versus the number of shields required to counteract a doubling of CO_2.

despite the number of shields deployed, the number of obscuration events is ultimately dictated by a suitable geometry between Sun, Earth and shield. This condition represents an operational limit on this SRM strategy.

As can be seen from Fig. (8.4), there are several combinations of the orbital elements found which would result approximately in the same value for the shield's radius. Those solutions from Fig. (8.4) which can be considered the most interesting are reported in detail in Fig. (8.11) and in Table (8.1) alongside with a list of the corresponding orbital elements and yearly perturbation of longitude of ascending node and argument of perigee due to secular effects of J_2 and solar radiation pressure. In Fig. (8.12) the grade of obscuration provided by the 10 shields considered is shown for a year-long simulation. As expected, a larger obscuration is provided around June

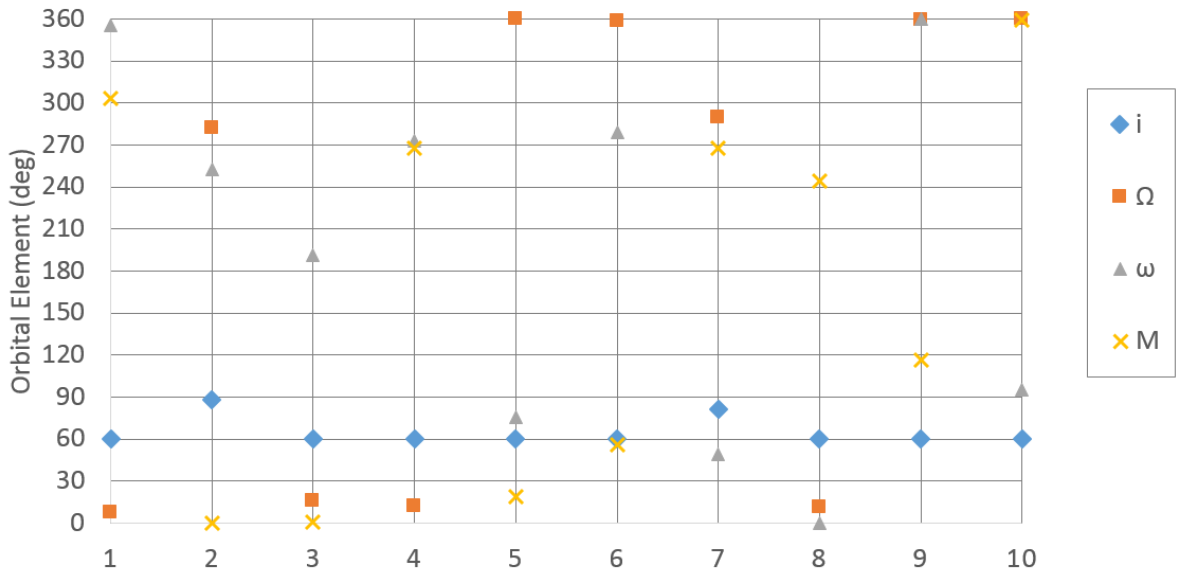

Figure 8.11: Orbital elements of the 10 cases selected from the optimisation results.

for the northern hemisphere and around December for the southern hemisphere because of the larger quantity of incoming solar radiation reaching the Earth's surface at those times of the year. As noted before, as a result of the optimisation, the orbital elements of the shields are chosen so that obscuration of the high latitude regions is provided during those times of the year. This can be seen in Fig. (8.12), where the obscuration of high latitude regions is identified by blue markers, whereas black markers represent the obscuration of the low-latitude regions.

Table 8.1: Orbital elements, shield radius (if a single shield is employed) and orbital perturbations (over 1 year) for 10 cases selected from the optimisation results.

	$a_s(km)$	i_s (°)	Ω_s (°)	ω_s (°)	M_0 (°)	R_s (km)	A/m (m^2/kg)	$\Delta\Omega_s$(°)	$\Delta\omega_s$(°)
1	7875.6	88.1	282.2	252.2	0	1467	29.1	-57.67	-864.9
2	7450.4	60	40.4	51	357.9	1485.4	2	-1056	264
3	7450	60	16.2	191.4	0.74	1477.5	15.8	-1056	264
4	7450	60.3	12.5	272.6	267.9	1478.8	2	-1046.4	240.13
5	7450	60	359.9	75.9	19.3	1482.5	18.8	-1056	264
6	7450	60	358.6	279.3	56.2	1475.2	8.6	-1056	264
7	7631.8	81.2	289.2	49	267.8	1473.6	12.3	-296.96	-856.98
8	7877.7	60	11	0.01	244.6	1480.6	2.6	-868.6	217.15
9	7669.9	60	359.4	360	116.8	1483.3	35.25	-953.79	238.45
10	7487.5	60	359.8	95	358.8	1481.4	8.5	-1037	259.4

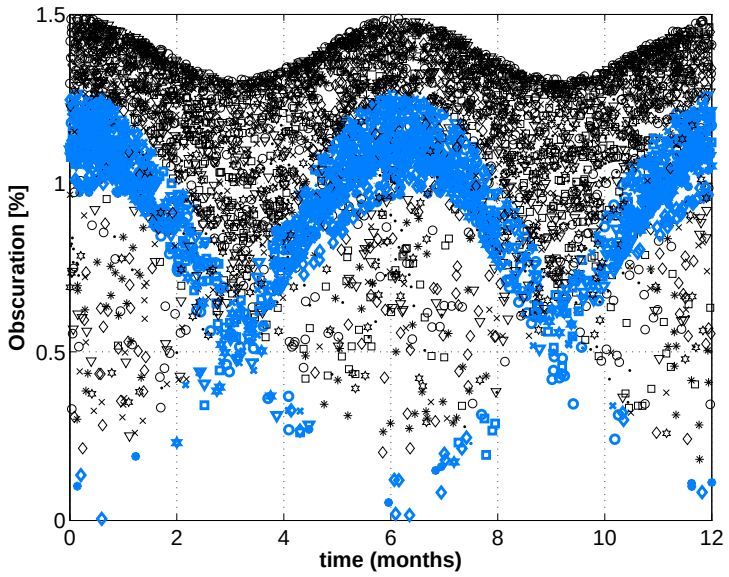

Figure 8.12: Trend of the grade of obscuration throughout 1 year provided by the first 10 shields reported in Table (8.1).

8.7 Conclusions

The deployment of space shields for climate engineering has been investigated as a Solar Radiation Management (SRM) strategy. In particular, the objective of this chapter is to find a feasible strategy that takes into account latitudinal disparities due to SRM and provide the required insolation reduction to counteract a doubling of CO_2 through large space shields deployed in LEO.

Employing a continuous PDE model for the climate system, it was found that a larger cooling near is required near the poles with respect to the equator. This is justified considering that the latitudinal distribution of the control law is strictly related to the pattern of insolation.

The grade of obscuration provided by a shield deployed in LEO (altitude of approximately 1100 km) is quantified through geometrical considerations in relationship to its orbit.

The expression for the grade of obscuration has been employed in the PDE model to match results from the literature. As expected, it was found that a shield of different size is required at each latitude to provide the required insolation reduction to avoid latitudinal over-cooling/under-cooling. In particular, a shield radius of 1350 km would be required at low latitudes, whereas a shield radius as large as 2600 km would be required at high latitudes to counteract a doubling of CO_2.

Thus, with respect to prior work, in this chapter, an optimization process is performed to design the ideal orbit for the shield taking into account latitudinal variation and seasonal effects.

Thus, a strategy involving a shield with fixed size which is able to provide the necessary insolation reduction at every latitude is found.

The optimisation process provides the optimal orbit which would provide the matching latitudinal obscuration pattern to counteract a doubling of CO_2 concentration. In particular, the goals of the optimisation process are the minimisation of the shield radius and the maximisation of the obscuration of high-latitude regions in order to provide a larger cooling near the poles.

Indeed, as a result of the optimisation process, it is found that the required shield radius is 1467 km and the ideal orbit presents the following orbital elements: $a_s = 7875.6\ km$, $e = 0.01$, $i_s = 88.1°$, $\Omega_s = 282.24°$, $\omega_s = 252.17°$, $M_0 = 0°$. These orbital elements are selected through the optimisation process so that the obscuration of the polar regions, i.e. latitudes $\geq 50°$, occurs when the largest quantity of solar radiation is received, thus between May and September in the northern hemisphere and between October and April in the southern hemisphere. This design allows the deployment of a smaller shield to reflect a larger quantity of insolation back to space during a single obscurating event.

Thus, it is demonstrated through this strategy that, it is possible to provide the necessary latitudinal distribution of insolation reduction to minimise the latitudinal temperature anomaly due to a doubling of CO_2. In particular, with respect to other strategies previously considered in the literature, which would involve a uniform distribution of insolation reduction, if this strategy is employed no over-cooling of the tropics or under-cooling of the poles would occur.

Finally, it is found that the shield's size can be further reduced if a constellation of shields is considered instead. For example, if 25 shields are deployed, then it is estimated that each of them should have a radius of 290 km to provide the required insolation reduction during each obscuration event.

Chapter 9

Conclusions

This thesis has developed methods to quickly assess a range of new control strategies for Solar Radiation Management (SRM). The main issues of SRM were identified to be (1) regional disparities in induced cooling due to the non-uniform distribution of insolation; and (2) management of uncertainties in climate modelling due to poor knowledge of some physical processes and forecast radiative scenario.

The conclusions drawn from each chapter can be found in the following sections.

9.1 Chapter 3

In Chapter 4, a 3-box climate model was developed where Earth is divided in three latitudinal bands. This model, with its simplicity, takes the largest latitudinal disparities into account and provides a useful tool to evaluate new multi-variable control methods. External forcing due to an excess of atmospheric carbon dioxide and SRM control were included in the formulation. Moreover, heat transport from the warmer central band to the colder northern and southern bands was considered, related to the temperature difference between contiguous boxes. This term provided coupling between the three boxes.

The correctness of the 3-box model was demonstrated considering its response to four Radiative Concentration Paths (RCPs) scenarios. It was found that the averaged temperature anomaly between the three latitudinal bands which results from the radiative scenarios is within the relevant uncertainty range for all four cases. In particular, the final outcomes were compared with the behaviour of the CMIP5 model from the literature.

Moreover, since independent control variables are included for each latitudinal band, formal

controllability and observability were investigated for the first time. Four different control strategies were evaluated and it was found that it is possible to control the temperature anomaly in all of the latitudinal bands deploying SRM only in the central band only if northern and southern bands are dissimilar from each other, i.e. when differences in the two hemispheres, such as land and water distribution, are considered in the model.

The structure of the 3-box model is particularly useful for the implementation of closed-loop control strategies. The model was then employed to develop an adaptive control strategy for climate engineering. This control strategy represents a means to deal with uncertain systems. With respect to PI control, widely employed in the literature, adaptive control uses dynamic gains which are updated during every iteration in order to compensate for uncertainty. In this chapter, a model reference adaptive control was designed in order to minimize the temperature anomaly with a 50% uncertainty range (zero mean and 25% standard deviation of the temperature) and 3 different scenarios were considered. As expected, adaptive control was able to deal with uncertainties and minimize temperature anomalies.

9.2 Chapter 4

Adaptive control was further explored in Chapter 5, where it was compared with SRM approaches from the literature, involving PI control, and with an optimal control strategy with constrained control variables.

Simulations were performed demonstrating that adaptive control is robust to large uncertainties in the parameters of the climate model, to sudden perturbations of the system, such as actuator failure or rapid collapse of ice sheets, and to the dynamics of the SRM method considered. It was shown that, despite choosing different sets of the climate model parameters, adaptive control always delivers good performance. Otherwise, PI control and optimal control strategies do not always provide satisfactory results. In particular, these control methods are not able to minimize the temperature anomaly in all latitudinal bands simultaneously if the model parameters are uncertain. In all cases, it was not possible to minimize the anomaly in the central band without causing under/over cooling in the northern or southern band. This result is not seen in 1-box models when only global dynamics are investigated, but it is otherwise verifiable through the 3-box model. Interestingly, due to the robustness of adaptive control to large uncertainties in the model employed, less importance can given to the details of the model used when this control

strategy is considered.

Moreover, adaptive and PI control were compared in the case when a sudden partial failure of an actuator occurs. It was assumed that the effectiveness of the SRM actuators in the northern and southern bands was abruptly reduced by 50 % and it was found that only adaptive control is able to cope with this event, whereas the temperature anomaly diverged greatly when PI control was employed. Another case investigated regarded the implementation of specific aerosol dynamics, including the modelling of poleward diffusion and time decay. It was shown that adaptive control is not susceptible to changes in the actuator dynamics and it is able to estimate the required aerosol mass, providing results widely comparable with the literature. However, PI control underestimated the aerosol mass required with diverging values of the temperature anomaly in the northern and southern bands. Finally, adaptive control was considered in an expanded version of the 3-box model with 5 latitudinal bands, where additional polar bands were considered in the northern and southern hemisphere. This model was employed to demonstrate the performance of the controller in case of collapse of the Arctic ice-sheet causing a rapid reduction of the albedo in the northern polar band. Again, it was shown that adaptive control provides the insolation reduction required to remove the temperature anomalies in all latitudinal bands.

9.3 Chapter 5

The 3-box model was extended to n-boxes to obtain the limiting case of a continuous latitudinal PDE model which was explored in Chapter 6. An analytical solution for the PDE model was derived through the Green's function approach and the time-dependent temperature profile was obtained as a function of latitude. The model provided an efficient application of optimisation processes and multi-objective analyses.

Importantly, the parameters of the PDE model were chosen for each hemisphere in order to replicate observed temperature profiles at equilibrium and to match the step response of high fidelity models from the literature. In fact, it was demonstrated that the behaviour of the PDE model is comparable with results from the HadCM3L model. In this way, it has been possible to provide useful results with an efficient, analytical approach to investigate SRM strategies.

A PI control in feedback was employed with the PDE model to minimise several objectives simultaneously. The objectives were the minimisation of changes in the global mean temperature, the temperature gradient and the equator-to-pole temperature gradient due to a 1% increase

of CO_2 concentration per year. As in other similar work from the literature, the latitudinal distribution of the control functions was obtained as a combination of the first three Legendre polynomial functions. Three cases were investigated and successfully compared with results from the literature, demonstrating that the PDE model is a valid method of quickly implementing multi-objective analyses. In particular, it was found that the temperature trends obtained employing the analytical solution of the PDE model are comparable with results of the CESM 1.0.2 model. Moreover, through the PDE model, it was possible to investigate the overall rms zonal mean temperature and an analytical control law was obtained to reduce the zonal mean temperature perturbation to zero. In accordance with the literature, it was found that increased control effort near the poles with respect to the tropics is required to counteract warming induced by the excess of atmospheric CO_2. This result is directly linked to the latitudinal pattern of incoming solar radiation which governs the SRM control mechanism.

As was noted, the use of an analytical climate model allowed for the development of analytical control laws to obtain a required latitudinal temperature profile. Moreover, since the model allows for any forcing term to be considered, the response of the PDE model was investigated under a doubling of CO_2. Again, it was found that the required control law was strictly related to the insolation distribution and the resulting overall insolation reduction was in agreement with values found in the literature.

9.4 Chapter 6

In Chapter 7 the extreme operational limits of SRM were investigated. Employing the PDE model developed in Chapter 6, it was possible to investigate the dynamics of the ice line, and its stability, in order to determine the conditions for which the climate would reach an ice-covered state. This analysis illustrated the size of the required SRM intervention for climate engineering in comparison with the insolation reduction that would be required to trigger such an instability of the climate system, demonstrating that this limit is far beyond expected SRM interventions.

The Lyapunov stability criterion was employed for this study. A quadratic expression depending on the variation of the ice line position with time was found to be a good candidate function. In particular, this expression was derived analytically through the solution of the PDE model. Thus, the analytical expression of the Lyapunov function was employed to estimate the family of control functions which satisfy a Lyapunov stability criterion. The infinite number of

control functions are bounded by a minimum function which defines the minimum reduction of insolation which would force the climate system to an ice-covered state. As expected, it was estimated that the required insolation reduction to trigger the instability is larger near the equator than at high latitudes. Moreover, it was also found that the stability limit largely depends on the climate sensitivity of the model. Employing the boundary control function found in the PDE model, it was possible to estimate the latitudinal profile of the surface equilibrium temperature for the new climate state. Results are broadly comparable with the literature

Results from this analysis were also compared with the SRM intervention required to counteract a doubling of CO_2 concentration and it was found that the insolation reduction required near the poles could in principle be enough to extend the ice line to lower latitudes. Nevertheless, a small insolation reduction to counteract a doubling of CO_2 concentration is required at the tropics, therefore, the poleward transport of energy from low to high latitudes would eventually mitigate the insolation reduction occurring near the poles and the instability would not be triggered.

Finally, again following the Lyapunov stability criterion, recovery from an ice-covered state was investigated. It was found that a large increase in insolation was required near the equator to move the ice line back to the pole. In fact, it was estimated that the increase of insolation required to recover from an ice-covered state is 3.5 times more than the reduction of insolation required to trigger the instability. This result is in agreement with the literature and is due to the latitudinal transport of heat towards the poles and the strong ice-albedo feedback. As a consequence, the global equilibrium temperature of the new state achieved after the recovery would be approximately $10°C$ higher than that associated with the current climate state.

9.5 Chapter 7

In the last technical chapter of this thesis, SRM methods involving the deployment of large shields in space have been investigated. Through the use of the PDE model described in Chapter 6, an new concept for the optimal deployment of space shields in Low Earth Orbit was developed.

Because of the latitudinal disparities induced by SRM methods, in order to counteract a doubling of CO_2 concentration in principle, a smaller shield is required at low latitudes with respect to that needed at high latitudes. Therefore, an optimisation process was performed to design the optimal orbit for a fixed shield and provide sufficient obscuration at high latitudes. In particular,

including the orbital dynamics of the shield and seasonal effects in the optimisation process it was shown that, selecting a suitable orbit which provides a matching insolation reduction, it is possible to use a shield of fixed size.

Also, the optimisation included non-negligible orbital perturbations for high area-to-mass ratio objects in Low Earth Orbit, such solar radiation pressure, and the J_2 effect.

The geometrical configuration between the Sun and shield, along with latitudinal and seasonal effects were taken into account and an expression for the required latitudinal distribution of the grade of obscuration with time was found. Through this expression, the relationship between the shield radius required to counteract a doubling of CO_2 and the orbital elements of the shield was computed. This expression was included in the optimisation process. The main objectives of the optimisation were: the minimisation of the shield radius and the maximisation of the obscuration at high latitudes.

Therefore, developing the optimisation process for different sets of initial conditions, it was possible to find the global maximum of the objective function and obtain a solution independent from the initial guess.

As a result of the optimisation process, seasonal effects were exploited in order to maximize obscuration at high latitudes. In fact, although high-latitude regions are obscured for less time with respect to the tropics, the regions near the poles are obscured when the largest quantity of solar radiation is received, i.e. from May to September in the northern hemisphere and from October to April in the southern hemisphere. Therefore, each obscurating event is more effective.

It has also been demonstrated that results from the literature can be reproduced through the PDE model if latitudinal and seasonal effects are neglected and without specifically designing the shield orbit. This outcome is considered as confirmation that seasonal and latitudinal variations and the design of the optimal orbit are key processes.

Finally, a strategy involving multiple smaller shields was considered. It was found that by increasing the number of shields deployed it was possible to further reduce the radius of each shield. It was demonstrated that this method has a limit related to the number of shields deployable in suitable orbits. In fact, the number of obscuration events is dictated by the required geometry between the Sun, Earth and shield. This provides an operational limit for this SRM strategy.

9.6 Summary of findings

The conclusions are now drawn for each objective stated in the introduction:

- Two climate models with latitudinal resolution were developed to overcome the regional disparities caused by SRM, and to deal with large uncertainties associated with climate model parameters. These climate models are not designed to replace complex General Circulation Models (GCM), which have millions of degrees of freedom, but they provide a clear understanding of the main climatic processes. Moreover, these models speed up and facilitate the assessment of new closed-loop control strategies.

- An adaptive controller for climate engineering is introduced. This controller is able to tolerate high uncertainties and deal with abrupt perturbations. The controller is tuned during each iteration according to a control law found through the Lyapunov stability criterion. Implementing this method guarantees the asymptotic stability of the controller. Comparisons with PI control show that adaptive control is able to provide excellent results where PI control shows poor performance when not purposely tuned. As a result of this analysis, the importance of using an accurate model to describe the climate system is de-emphasised.

- It is demonstrated that a continuous energy balance PDE model with latitudinal resolution has analytical solution and can be employed to evaluate multi-objective closed-loop control strategies. Considering similar simulations from the literature, where high fidelity numerical models are used, comparable results are found. Moreover, because of the analytical formulation employed, analytical control laws representing the pattern of insolation reduction required, can be easily found for many different radiative scenarios. Thus, the PDE model represents a useful tool to quickly assess many different SRM strategies with any radiative scenario.

- The PDE model was further employed to investigate the dynamics of the ice line. The position of the ice line gives information on the equilibrium states of the climate system. It is known that the Earth's climate has two equilibrium states, the current state and an ice-covered state. An unstable equilibrium state is located between these two conditions. In this study, the conditions to reach this unstable state are found in terms of insolation reduction required at each latitude. This study provided the upper limit of SRM strategies for

climate engineering. Importantly, it is demonstrated that this limit would not be surpassed by most SRM strategies generally considered.

- Finally, a new strategy regarding the deployment of large shields in space to reflect a fraction of insolation back to space is proposed. Again, the PDE model has been employed to assess the required obscuration pattern under a doubling of CO_2 and an optimisation process was performed to find the ideal orbit for the shield. Finally, in order to increase the feasibility of this strategy, a constellation of shields is considered and a detailed description of the family of orbits employed is provided. Importantly, orbital perturbations due to solar radiation pressure and Earth's oblateness are taken into account to outline the optimal orbits.

9.7 Future developments

The research presented in this thesis satisfied the objectives described in Chapter 1, by presenting practical solutions to overcome issues related to latitudinal disparities caused by SRM strategies and large uncertainties associated with the climate system. However, the study presented in this thesis represents only the first step into potentially rich new paths of research and there is the opportunity for further investigation in several areas.

Two climate models have been presented. In particular, a 3-box energy model for the climate system has been employed to demonstrate the advantages of adaptive control strategies for climate engineering and its ability to deal with highly uncertain climate models. This new control strategy provides flexibility for future SRM deployments. Also, it was demonstrated that adaptive control can be easily implemented in other models such as a 5-box model that was considered to investigate collapse of the Arctic ice sheets.

Moreover, a continuous PDE model with latitudinal resolution was developed and it has been demonstrated that it can be used to provide analytical control laws to achieve any desired temperature profile. Moreover, taking into account the main climatic processes, it has been found that the PDE model is able to successfully replicate the behaviour of high fidelity numerical models.

In future research, it would be of interest to consider the implementation of adaptive control within the PDE model through numerical simulation. This approach would provide a methodology to extrapolate continuous control laws with latitudinal resolution for any radiative scenario. The main benefits would be the prompt evaluation of SRM control strategies, the capability of

managing model uncertainties and unforeseeable perturbations, and the possibility of overcoming issues associated with regional disparities. Implementing adaptive control in a full GCM would also be of great interest.

Another interesting development would be the inclusion of aerosols dynamics in the PDE model with adaptive control. For example, the Global Aerosol Models (GAM) [154] or Transport Chemical Aerosol Model (TCAM) [155] is already available in the literature and could be employed. In this way, the mass of aerosols required at each latitude could be dynamically estimated through adaptive control, taking into account the lifetime and latitudinal diffusion of aerosol particles. In addition to the future work proposed above, suggestions to improve the PDE model regard the inclusion of longitudinal resolution so that a detailed distribution of land and ocean could be considered.

Moreover, although heat transport due to circulation is included, in order to maintain a tractable problem, the assumption of negligible mean circulation in the atmosphere and ocean is used. This simplification allowed for analytical solutions of the PDE model, but if numerical simulations are considered the PDE model could be improved by including mean circulation terms. In addition, latitudinal dependence of the heat capacity coefficients and transport coefficients for the northern and southern hemispheres could be taken into account to better define inter-hemispheric disparities.

Regarding the study of the ice line stability, it is worth noting that the method employed for investigation of the ice line dynamics provided in this thesis represents a general approach and can be implemented through any climate model. In fact, the Lyapunov stability criterion can be employed for both linear and non linear dynamical systems without any specific limitation.

Finally, regarding the deployment of space shields, the optimisation process developed in this thesis could be implemented to design suitable orbits for other external forcing. The approach considered in this thesis regarding space shields provides interesting SRM strategies to counteract only constant radiative forcing scenarios. If other radiative scenarios are considered, such as the RCP scenarios, time variation of the radiative forcing could require the shields to change orbit (orbit plane, altitude, etc.) in order to provide the required latitudinal obscuration. In order to introduce a more flexible strategy, several active shields, whose orbit can be controlled using solar radiation pressure, should be taken into account.

Indeed, it would be interesting to develop future research on an adaptable orbit design strategy with a constellation of shields. In this case, an optimisation process could be considered to find

the most suitable orbit configurations, at several intervals of time, which can be achieved with the smallest orbit control effort for the shields.

Finally, shields with variable cross-sectional area (or reflectivity) could be considered to provide a dynamical control of the latitudinal insolation reduction. Examples regarding the possibility of developing parabolic mirrors with adjustable focal lengths can be found in the literature [156]. This feature could also be included in simpler strategies with the employment of membrane materials capable of becoming transparent for active reflectivity control.

Bibliography

[1] MacMartin DG, Kravitz B, Keith DW. *Geoengineering: The world's largest control problem*. In American Control Conference (ACC), 2014 2014 Jun 4 (pp. 2401-2406). IEEE. DOI: 10.1109/ACC.2014.6858658.

[2] Weller SR, Schulz BP. *Geoengineering via solar radiation management as a feedback control problem: Controller design for disturbance rejection*. In Control Conference (AUCC), 2014 4th Australian 2014 Nov 17 (pp. 101-106). IEEE. DOI:10.1109/AUCC.2014.7358684.

[3] Jarvis A, Leedal D, Taylor CJ, Young P. *Stabilizing global mean surface temperature: A feedback control perspective*. Environmental Modelling & Software. 2009 May 31;24(5):665-74.

[4] MacMartin DG, Kravitz B, Keith DW, Jarvis A. *Dynamics of the coupled human climate system resulting from closed-loop control of solar geoengineering*. Climate Dynamics. 2014 Jul 1;43(1-2):243-58.

[5] Twomey, S., 1977: *Influence of pollution on shortwave albedo of clouds*. Journal of Atmospheric Science, 34, 1149âĂŞ1152.

[6] Albrecht, B. A., 1989: *Aerosols, cloud microphysics, and fractional cloudiness*. Science, 245, 1227âĂŞ1230.

[7] IPCC, 2014: *Climate Change 2014: Synthesis Report*. Contribution of Working Groups I, II and III to the Fifth Assessment Report of the Intergovernmental Panel on Climate Change [Core Writing Team, R.K. Pachauri and L.A. Meyer (eds.)]. IPCC, Geneva, Switzerland, 151 pp.

[8] Sacks, W. J., B. I. Cook, N. Buenning, S. Levis, and J. H. Helkowski, 2009: *Effects of global irrigation on the near-surface climate*. Clim. Dyn., 33, 159âĂŞ175.

[9] Cubasch, U., D. Wuebbles, D. Chen, M.C. Facchini, D. Frame, N. Mahowald, and J.-G. Winther, 2013: *Introduction*. In: Climate Change 2013: The Physical Science Basis. Contribution of Working Group I to the Fifth Assessment Report of the Intergovernmental Panel on Climate Change [Stocker, T.F., D. Qin, G.-K. Plattner, M. Tignor, S.K. Allen, J. Boschung, A. Nauels, Y. Xia, V. Bex and P.M. Midgley (eds.)]. Cambridge University Press, Cambridge, United Kingdom and New York, NY, USA.

[10] Houghton, R. A. (2003), *Why are estimates of the terrestrial carbon balance so different?*. Global Change Biology, 9: 500-509. doi:10.1046/j.1365-2486.2003.00620.x.

[11] A. Foley, J. & Defries, R. & Asner, G. & Barford, C. & Bonan, G. & Carpenter, S. & Chapin III, F. Stuart & Coe, M. & Daily, G. & Gibbs, H. & H. Helkowski, J. & Holloway, T. & A. Howard, E. & Kucharik, C. & Monfreda, C.& Patz, J. & Prentice, I. & Ramankutty, N. & K Snyder, Peter. (2005). *Global Consequences of Land Use*. Science (New York, N.Y.). 309. 570-4. 10.1126/science.1111772.

[12] Smithson, P. A. (2002), IPCC, *2001: climate change 2001: the scientific basis. Contribution of Working Group 1 to the Third Assessment Report of the Intergovernmental Panel on Climate Change*, edited by J. T. Houghton, Y. Ding, D. J. Griggs, M. Noguer, P. J. van der Linden, X. Dai, K. Maskell and C. A. Johnson (eds). Cambridge University Press, Cambridge, UK, and New York, USA, 2001. No. of pages: 881. ISBN 0–521–80767–0 (hardback).. International Journal of Climatology, 22: 1144-1144. doi:10.1002/joc.763.

[13] IPCC, *2007: Climate Change 2007: Impacts, Adaptation and Vulnerability. Contribution of Working Group II to the Fourth Assessment Report of the Intergovernmental Panel on Climate Change*, M.L. Parry, O.F. Canziani, J.P. Palutikof, P.J. van der Linden and C.E. Hanson, Eds., Cambridge University Press, Cambridge, UK, 976pp.

[14] Rial, J.A., R.A. Pielke, M. Beniston, M. Claussen, J. Canadell, P. Cox, H. Held, N. De Noblet-Ducoudre, R. Prinn, J.F. Reynolds and J.D. Salas, 2004: *Nonlinearities, feedbacks and critical thresholds within the EarthâĂŹs climate system*. Climatic Change, 65, 11-38.

[15] Jansson, P., R. Hock and T. Schneider, 2003: *The concept of glacier storage: a review*. J. Hydrol., 282, 116-129.

[16] Forster, P., et al., 2007: *Changes in atmospheric constituents and in radiative forcing*. In: Climate Change 2007: The Physical Science Basis. Contribution of Working Group I to the Fourth Assessment Report of the Intergovernmental Panel on Climate Change [Solomon, S., D. Qin, M. Manning, Z. Chen, M. Marquis, K. B. Averyt, M. Tignor and H. L. Miller (eds.)]. Cambridge University Press, Cambridge, United Kingdom and New York, NY, USA, 131âĂŞ234.

[17] Matthews, H., and K. Caldeira, 2008: *Stabilizing climate requires near-zero emissions*. Geophys. Res. Lett., 35, L04705.

[18] Solomon, S., G. Plattner, R. Knutti, and P. Friedlingstein, 2009: *Irreversible climate change due to carbon dioxide emissions*. Proc. Natl. Acad. Sci. U.S.A., 106, 1704âĂŞ1709.

[19] Keller DP, Feng EY, Oschlies A. *Potential climate engineering effectiveness and side effects during a high carbon dioxide-emission scenario*. Nature Communications. 2014 Feb 25;5.

[20] Blackstock JJ, Battisti DS, Caldeira K, Eardley DM, Katz JI, Keith DW, Patrinos AA, Schrag DP, Socolow RH, Koonin SE. *Climate engineering responses to climate emergencies*. 2009 Jul 29. DOI: 10.1088/1755-1307/6/5/452015.

[21] Vaughan NE, Lenton TM. *A review of climate geoengineering proposals*. Climatic change. 2011 Dec 1;109(3-4):745-90. DOI: 10.1007/s10584-011-0027-7.

[22] Hallegatte, S., 2005: *The long timescales of the climate-economy feedback and the climatic cost of growth*. Environ. Model. Assess., 10, 277-289

[23] Schneider, Stephen H. *Earth systems engineering and management.* Nature 409.6818 (2001): 417.https://doi.org/10.1038/35053203.

[24] Barrett, Scott. (2008). *The Incredible Economics of Geoengineering*. Environmental & Resource Economics. 39. 45-54. 10.1007/s10640-007-9174-8.

[25] Schimel, D.S., 1995. *Terrestrial ecosystems and the carbon cycle*. Global Change Biology, 1(1), pp.77-91.

[26] McGuffie K, Henderson-Sellers A. *A climate modelling primer*. John Wiley & Sons; 2005 Mar 11. DOI: 10.1002/0470857617.ch6.

[27] Keith DW (2000) *Geoengineering the climate: history and prospect*. Annual Review of Energy and the Environment 25:245–284.

[28] Olson JS, Watts JA, Allison LJ (1985) *Major world ecosystem complexes ranked by carbon in live vegetation*. Carbon Dioxide Information Analysis Center, Oak Ridge, Tenn. USA, NDP-017.

[29] Lenton TM, Vaughan NE (2009) *The radiative forcing potential of different climate geoengineering options*. Atmos Chem Phys 9:5539–5561.

[30] Goldemberg J, Guardabassi P (2009) *Are biofuels a feasible option?* Energy Policy 37:10–14.

[31] Read P, Parshotam A (2007) *Holistic greenhouse gas management: mitigating the threat of abrupt climate change in the next few decades (with reviewers comments and author rejoinders)*. Institute of Policy Studies Working Paper 07/1, Victoria University of Wellington, Wellington, New Zealand.

[32] Koppmann, R. (Ed.). (2008). *Volatile organic compounds in the atmosphere*. John Wiley & Sons.

[33] Ciais, P., C. Sabine, G. Bala, L. Bopp, V. Brovkin, J. Canadell, A. Chhabra, R. DeFries, J. Galloway, M. Heimann, C. Jones, C. Le QuÃľrÃľ, R.B. Myneni, S. Piao and P. Thornton, 2013: *Carbon and Other Biogeochemical Cycles*. In: Climate Change 2013: The Physical Science Basis. Contribution of Working Group I to the Fifth Assessment Report of the Intergovernmental Panel on Climate Change [Stocker, T.F., D. Qin, G.-K. Plattner, M. Tignor, S.K. Allen, J. Boschung, A. Nauels, Y. Xia, V. Bex and P.M. Midgley (eds.)]. Cambridge University Press, Cambridge, United Kingdom and New York, NY, USA.

[34] Zhou S Flynn PC (2005) *Geoengineering downwelling ocean currents: a cost assessment*. Climatic Change 71(1–2):203–220.

[35] Jin X, Gruber N, Frenzel H, Dooley SC, McWilliams JC (2008) *The impact on atmospheric CO_2 of iron fertilization induced changes in the ocean's biological pump*. Biogeosciences 5:385–406.

[36] Zeebe RE, Archer D (2005) *Feasibility of ocean fertilization and its impact on future atmospheric CO_2 levels*. Geophysical Research Letter 32:L09703.

[37] Gnanadesikan A, Sarimento JL, Slater RD (2003) *Effects of patchy ocean fertilization on atmospheric carbon dioxide and biological production*. Global Biogeochemical Cycles 17(2):1050.

[38] Cao L, Caldeira K (2008) *Atmospheric CO_2 stabilization and ocean acidification*. Geophysical Research Letter 35:L19609.

[39] IPCC (2005) *Carbon dioxide capture and storage*. Cambridge University Press, Cambridge.

[40] Keith DW, Ha-Duong M, Stolaroff JK (2006) *Climate strategy with CO_2 capture from the air*. Climatic Change 74:17–45.

[41] Zeman F (2007) *Energy and material balance of CO_2 capture from ambient air*. Environmental Science and Technology. 41:7558–7563.

[42] McInnes CR. *Space-based geoengineering: challenges and requirements*. Proceedings of the Institution of Mechanical Engineers, Part C: Journal of Mechanical Engineering Science. 2010 Mar 1;224(3):571-80.

[43] Teller, E., Wood, L. and Hyde, R., 1997. *Global warming and ice ages: I. Prospects for physics-based modulation of global change*. Report UCRL-231636/UCRL JC 128715 (Lawrence Livermore National Laboratory, Livermore, CA).

[44] Govindasamy, B., Caldeira, K., Duffy, P., *Geoengineering Earth's radiation balance to mitigate climate change from a quadrupling of CO_2*. Global and Planetary Change 37(1), 157-168 (2003).

[45] Lunt, D. J., A. Ridgwell, P. J. Valdes, and A. Seale (2008), *"Sunshade World": A fully coupled GCM evaluation of the climatic impacts of geoengineering*, Geophysical Research Letter, 35, L12710, doi: 10.1029/2008GL033674.

[46] Bala, Govindasamy and Duffy, PB and Taylor, KE, *Impact of geoengineering schemes on the global hydrological cycle*, Proceedings of the National Academy of Sciences, 105, number 22, 7664-7669 (2008), National Acad Sciences.

[47] Andy Parker and Peter Irvine. 3/11/2018. *The Risk of Termination Shock From Solar Geoengineering.* Earth's Future, 6, Pp. 456-467.

[48] Seifritz, Walter. *Mirrors to halt global warming?.* Nature 340 (1989): 603.

[49] Angel, Roger. *Feasibility of cooling the Earth with a cloud of small spacecraft near the inner Lagrange point (L1).* Proceedings of the National Academy of Sciences 103.46 (2006): 17184-17189.

[50] Sánchez, Joan-Pau, and Colin R. McInnes. *Optimal sunshade configurations for space-based geoengineering near the Sun–Earth L1 point.* PloS one 10.8 (2015): e0136648.

[51] Committee on Science, and Public Policy (US). *Panel on Policy Implications of Greenhouse Warming. Policy implications of greenhouse warming: mitigation, adaptation, and the science base*. National Academies Press, 1992.

[52] Pearson, J., Oldson, J., & Levin, E. (2006). *Earth rings for planetary environment control*. Acta Astronautica, 58(1), 44-57.

[53] Matthews HD, Caldeira K (2007) *Transient climate-carbon simulations of planetary geoengineering*. Proceedings of the National Academy of Sciences of the United States of America 104(24):9949–9954.

[54] Govindasamy, Bala and Caldeira, Ken, *Geoengineering Earth's radiation balance to mitigate CO_2-induced climate change*, Geophysical Research Letters, 27, number 14, 2141-2144 (2000), Wiley Online Library.

[55] Crutzen PJ (2006) *Albedo enhancement by stratospheric sulphur injections: a contribution to resolve a policy dilemma?* Climatic Change 77(3–4):211–219.

[56] Stenchikov GL, Kirchner I, Robock A, Graf HF, Antuna JC, Grainger RG, Lambert A, Thomason L (1998) *Radiative forcing from the 1991 Mount Pinatubo volcanic eruption*. Journal of Geophysical Research Atmospheres 103(D12):13837–13857.

[57] Rasch PJ, Tilmes S, Turco RP, Robock A, Oman L, Chen CC, Stenchikov GL, Garcia RR. *An overview of geoengineering of climate using stratospheric sulphate aerosols*. Philosophical Transactions of the Royal Society of London A: Mathematical, Physical and Engineering Sciences. 2008 Nov 13;366(1882):4007-37.

[58] Wigley TML (2006) *A combined mitigation/geoengineering approach to climate stabilization*. Science 314:452–454.

[59] Robock A, Oman L, Stenchikov GL. *Regional climate responses to geoengineering with tropical and Arctic SO_2 injections*. Journal of Geophysical Research: Atmospheres. 2008 Aug 27;113(D16).

[60] Tilmes S, Muller R, Salawitch R (2008) *The sensitivity of polar ozone depletion to proposed geoengineering schemes*. Science 320:1201–1204.

[61] IPCC (2007) *Climate Change 2007: the physical science basis*. Contribution of Working Group I to the Fourth Assessment Report of the Intergovernmental Panel on Climate Change. Cambridge University Press, Cambridge.

[62] Charlson RJ, Lovelock JE, Andreae MO, Warren SG (1987) *Oceanic phytoplankton, atmospheric sulphur, cloud albedo and climate*. Nature 326:655–661.

[63] Salter S (2006) *Sea-going hardware for the implementation of the cloud albedo control method for the reduction of global warming*. In: EIC climate change conference, Ottawa, Canada.

[64] Salter S, Sortino G, Latham J (2008) *Sea-going hardware for the cloud albedo method of reversing global warming*. Philosophical Transactions of the Royal Society A 366:3989–4006.

[65] Latham J (1990) *Control of global warming?* Nature 347:339–340. https://doi.org/10.1038/347339b0.

[66] Latham J, Rasch P, Chen C-C, Kettles L, Gadian A, Gettelman A, Morrison H, Bower K, Choularton T (2008) *Global temperature stabilization via controlled albedo enhancement of low-level maritime clouds*. Phil Trans R Soc A 366:3969–3987.

[67] Wingenter OW, Elliot SM, Blake DR (2007) *New directions: enhancing the natural sulphur cycle to slow global warming*. Atmospheric Environment 41(34):7373–7375.

[68] Hamwey RM (2007) *Active amplification of the terrestrial albedo to mitigate climate change: an exploratory study*. Mitigation and Adaptation Strategies for Global Change 12 (4):419–439.

[69] Ridgwell A, Singarayer JS, Hetherington AM, Valdes PJ (2009) *Tackling regional climate change by leaf albedo bio-geoengineering*. Current Biology 19:146–150.

[70] Akbari H, Menson S, Rosenfeld A (2009) *Global cooling: increasing world-wide urban albedos to offset* CO_2. Climatic Change 94:275–286.

[71] Gaskill, A. (2004). *Summary of Meeting with US DOE to discuss Geo-engineering options to prevent abrupt and long-term climate change*. In http://www. global-warming-geo-engineering. org/DOE-Meeting/DOE-Geoengineering-Climate-Change-Meeting/ag1. html.

[72] Randall, D.A., et al., 2003: *Confronting models with data: The GEWEX Cloud Systems Study*. Bull. Am. Meteorol. Soc., 84, 455âĂŞ469.

[73] Budyko MI. *The effect of solar radiation variations on the climate of the Earth*. Tellus. 1969 Oct 1;21(5):611–9. DOI: 10.1111/j.2153-3490.1969.tb00466.x.

[74] Sellers, W.D., *A global climatic model based on the energy balance of the Earth-Atmosphere System*. Journal of Applied Meteorology 8(3), 392-400 (1969). DOI https://doi.org/10.1175/1520-0450(1969)008<0392:AGCMBO>2.0.CO;2.

[75] North GR, Cahalan RF, Coakley JA. *Energy balance climate models*. Reviews of Geophysics. 1981 Feb 1;19(1):91-121. DOI: 10.1029/RG019i001p00091.

[76] Collins, M., R. Knutti, J. Arblaster, J.-L. Dufresne, T. Fichefet, P. Friedlingstein, X. Gao, W.J. Gutowski, T. Johns, G. Krinner, M. Shongwe, C. Tebaldi, A.J. Weaver and M. Wehner, *2013: Long-term Climate Change: Projections, Commitments and Irreversibility.* In: IPCC Climate Change 2013: The Physical Science Basis. Contribution of Working Group I to the Fifth Assessment Report of the Intergovernmental Panel on Climate Change [Stocker, T.F., D. Qin, G.-K. Plattner, M. Tignor, S.K. Allen, J. Boschung, A. Nauels, Y. Xia, V. Bex and

P.M. Midgley (eds.)]. Cambridge University Press, Cambridge, United Kingdom and New York, NY, USA.

[77] Matthews, H Damon & Weaver, Andrew. (2010). *Committed climate warming*. Nature Geoscience. 3. 10.1038/ngeo813.

[78] Hansen, J., Johnson, D., Lacis, A., Lebedeff, S., Lee, P., Rind, D., & Russell, G. (1981). *Climate Impact of Increasing Atmospheric Carbon Dioxide*. Science, 213(4511), 957-966. Retrieved from http://www.jstor.org/stable/1687038.

[79] Rohling, E. J., Sluijs, A., Dijkstra, H. A., Köhler, P., van de Wal, R. S., von der Heydt, A. S., & Deconto, R. (2012). *Making sense of palaeoclimate sensitivity*. Nature, 2012 Nov 29;491(7426):683-91. doi: 10.1038/nature11574.

[80] Meehl, G.A., T.F. Stocker, W.D. Collins, P. Friedlingstein, A.T. Gaye, J.M. Gregory, A. Kitoh, R. Knutti, J.M. Murphy, A. Noda, S.C.B. Raper, I.G. Watterson, A.J. Weaver and Z.-C. Zhao, *2007: Global Climate Projections*. In: Climate Change 2007: The Physical Science Basis. Contribution of Working Group I to the Fourth Assessment Report of the Intergovernmental Panel on Climate Change [Solomon, S., D. Qin, M. Manning, Z. Chen, M. Marquis, K.B. Averyt, M. Tignor and H.L. Miller (eds.)]. Cambridge University Press, Cambridge, United Kingdom and New York, NY, USA.

[81] Hansen, J., et al. (2005), *Efficacy of climate forcings*, J. Geophys. Res., 110, D18104, doi:10.1029/2005JD005776.

[82] Le Treut, H., R. Somerville, U. Cubasch, Y. Ding, C. Mauritzen, A. Mokssit, T. Peterson and M. Prather, *2007: Historical Overview of Climate Change. In: Climate Change 2007: The Physical Science Basis. Contribution of Working Group I to the Fourth Assessment Report of the Intergovernmental Panel on Climate Change* [Solomon, S., D. Qin, M. Manning, Z. Chen, M. Marquis, K.B. Averyt, M. Tignor and H.L. Miller (eds.)]. Cambridge University Press, Cambridge, United Kingdom and New York, NY, USA.

[83] Cubasch, U., D. Wuebbles, D. Chen, M.C. Facchini, D. Frame, N. Mahowald, and J.-G. Winther, 2013. *Introduction. In: Climate Change 2013: The Physical Science Basis. Contribution of Working Group I to the Fifth Assessment Report of the Intergovernmental Panel*

on Climate Change. Cambridge University Press, Cambridge, United Kingdom and New York, NY, USA.

[84] Collins, M. and M.R. Allen, 2002: *Assessing the Relative Roles of Initial and Boundary Conditions*. in Interannual to Decadal Climate Predictability. J. Climate, 15, 3104–3109, https://doi.org/10.1175/1520-0442(2002)015<3104:ATRROI>2.0.CO;2.

[85] Nakicenovic, N., J. Alcamo, G. Davis, H.J.M. de Vries, J. Fenhann, S. Gaffin, K. Gregory, A. Grubler, T.Y. Jung, T. Kram, E.L. La Rovere, L. Michaelis, S. Mori, T. Morita, W. Papper, H. Pitcher, L. Price, K. Riahi, A. Roehrl, H-H. Rogner, A. Sankovski, M. Schlesinger, P. Shukla, S. Smith, R. Swart, S. van Rooijen, N. Victor, and Z. Dadi. N. Nakicenovic and R. Swart (Eds.), *Special Report on Emissions Scenarios*, IPCC, Cambridge University Press, Cambridge, UK, 2000. pp. 570.

[86] Hawkins, E. and R. Sutton, 2009: *The Potential to Narrow Uncertainty in Regional Climate Predictions*. Bull. Amer. Meteor. Soc., 90, 1095–1108, https://doi.org/10.1175/2009BAMS2607.1.

[87] Kravitz, B., MacMartin, D. G., Leedal, D. T., Rasch, P. J., Jarvis, A. J. (2014). *Explicit feedback and the management of uncertainty in meeting climate objectives with solar geoengineering*. Environmental Research Letters, 9(4), 044006.

[88] Jarvis, A. and Leedal, D. (2012), *The Geoengineering Model Intercomparison Project (GeoMIP): a control perspective*. Atmosph. Sci. Lett., 13: 157-163. doi:10.1002/asl.387

[89] Jackson L, Crook J, Jarvis A, Leedal D, Ridgwell A, Vaughan N, Forster PM. 2015. *Assessing the controllability of Arctic sea ice extent by sulfate aerosol geoengineering*. Geophysical Research Letters. 42(4), pp. 1223-1231.https://doi.org/10.1002/2014GL062240 .

[90] Kravitz, B., MacMartin, D. G., Wang, H., and Rasch, P. J. *Geoengineering as a design problem*, Earth System Dynamics, 7, 469-497, DOI: https://doi.org/10.5194/esd-7-469-2016, 2016.

[91] Kravitz, B., MacMartin, D. G., Mills, M. J., Richter, J. H., Tilmes, S., Lamarque, J.-F., Tribbia, J. J.,Vitt, F. (2017). *First simulations of designing stratospheric sulfate aerosol geoengineering to meet multiple simultaneous climate objectives*. Journal of Geophysical Research: Atmospheres, 122,12,616 – 12,634. https://doi.org/10.1002/2017JD026874.

[92] MacMartin, D. G., Kravitz, B., Tilmes, S., Richter, J.H., Mills, M. J., Lamarque, J.-F., Tribbia, J. J., & Vitt, F. (2017). *The climate response to stratospheric aerosol geoengineering can be tailored using multiple injection locations*. Journal of Geophysical Research: Atmospheres, 122, 12, 574 – 12, 590. https://doi.org/10.1002/2017JD026868.

[93] Heyen, D., Wiertz, T., Irvine, P., *Regional disparities in SRM impacts: the challenge of diverging preferences* (2015). DOI 10.1007/s10584-015-1526-8. URL http://EconPapers.repec.org/RePEc:spr:climat:v:133:y:2015:i:4:p:557-563.

[94] Moreno-Cruz, J.B., Ricke, K.L., Keith, D.W., *A simple model to account for regional inequalities in the effectiveness of solar radiation management*. Climatic Change 110(3), 649-668 (2012). DOI 10.1007/s10584-011-0103-z. URL http://dx.doi.org/10.1007/s10584-011-0103-z.

[95] MacMartin, D., Keith, D., Kravitz, B., Caldeira, K., *Managing tradeoffs in geoengineering through optimal choice of non-uniform radiative forcing*. Nature Climate Change 3, 365-368 (2012). DOI 10.1038/*nclimate*1722.

[96] Dai, Z., Weisenstein, D. K., & Keith, D. W. (2018). *Tailoring meridional and seasonal radiative forcing by sulfate aerosol solar geoengineering*. Geophysical Research Letters, 45, 1030 – 1039. https://doi.org/10.1002/2017GL076472.

[97] North, G.R., *Analytical solution to a simple climate model with diffusive heat transport*. Journal of the Atmospheric Sciences 32(7), 1301-1307 (1975).

[98] Curry, Judith A., et al. *Sea Ice–Albedo Climate Feedback Mechanism*. Journal of Climate, vol. 8, no. 2, 1995, pp. 240–247. JSTOR, JSTOR, www.jstor.org/stable/26199877.

[99] Coakley Jr, James A, *A study of climate sensitivity using a simple energy balance model*, Journal of the Atmospheric Sciences, 36, number 2, 260-269 (1979).

[100] Winton, M. (2013). *Sea Ice-Albedo Feedback and Nonlinear Arctic Climate Change. In Arctic Sea Ice Decline: Observations, Projections, Mechanisms, and Implications* (eds E. T. DeWeaver, C. M. Bitz and L. Tremblay). doi:10.1029/180GM09.

[101] Robert, F., North, G.R., *A stability theorem for energy-balance climate models*. Journal of the Atmospheric Sciences 36, 1205-1216 (1979).

[102] Myhre G, Highwood EJ, Shine KP, Stordal F. *New estimates of radiative forcing due to well mixed greenhouse gases*. Geophysical Research Letters. 1998 Jul 15;25(14):2715-8.

[103] Prather, M., G. Flato, P. Friedlingstein, C. Jones, J.-F. Lamarque, H. Liao and P. Rasch (eds.). *Annex II: Climate System Scenario Tables* . In: IPCC Climate Change 2013: The Physical Science Basis. Contribution of Working Group I to the Fifth Assessment Report of the Intergovernmental Panel on Climate Change [Stocker, T.F., D. Qin, G.-K. Plattner, M. Tignor, S.K. Allen, J. Boschung, A. Nauels, Y. Xia, V. Bex and P.M. Midgley (eds.)]. Cambridge University Press, Cambridge, United Kingdom and New York, NY, USA.

[104] Dlugokencky, E., Tans, P., *Trends in atmospheric carbon dioxide: Recent global* CO_2 (2016). URL http://www.esrl.noaa.gov/gmd/ccgg/trends/.

[105] van Vuuren, D.P., Edmonds, J., Kainuma, M. et al. *The representative concentration pathways: an overview* Climatic Change (2011) 109: 5. https://doi.org/10.1007/s10584-011-0148-z.

[106] Meinshausen, Malte et al. (2011). *The RCP greenhouse gas concentrations and their extensions from 1765 to 2300*. Climatic Change. 109. 213-241. 10.1007/s10584-011-0156-z.

[107] van Vuuren, D.P., Kriegler, E., O'Neill, B.C. et al. *A new scenario framework for Climate Change Research: scenario matrix architecture*. Climatic Change (2014) 122: 373. https://doi.org/10.1007/s10584-013-0906-1.

[108] O'Neill, B.C., Kriegler, E., Riahi, K. et al. *A new scenario framework for climate change research: the concept of shared socioeconomic pathways*. Climatic Change (2014) 122: 387. https://doi.org/10.1007/s10584-013-0905-2

[109] Kelly DL, Kolstad CD. *Integrated assessment models for climate change control*. International Yearbook of Environmental and Resource Economics. 1999;2000:171-97.

[110] Bruhl, C., Lelieveld, J., Crutzen, P.J. and Tost, H., 2012. *The role of carbonyl sulphide as a source of stratospheric sulphate aerosol and its impact on climate*. Atmospheric Chemistry and Physics, 12(3), pp.1239-1253.

[111] Penner JE, Andreae MO, Annegarn H, Barrie L, Feichter J, Hegg D, Jayaraman A, Leaitch R, Murphy D, Nganga J, Pitari G. *Aerosols, their direct and indirect effects*. In Climate

Change 2001: The Scientific Basis. Contribution of Working Group I to the Third Assessment Report of the Intergovernmental Panel on Climate Change 2001 (pp. 289-348). Cambridge University Press.

[112] Charlson RJ, Schwartz SE. *Climate forcing by anthropogenic aerosols*. Science. 1992 Jan 24;255(5043):423.

[113] Bergin MH. *Aerosol Radiative Properties and Their Impacts*. From Weather Forecasting. 2000.

[114] Haywood, J.M. and Ramaswamy, V., 1998. *Global sensitivity studies of the direct radiative forcing due to anthropogenic sulfate and black carbon aerosols*. Journal of Geophysical Research: Atmospheres, 103(D6), pp.6043-6058.

[115] McClellan, Justin; Keith, David; Apt, Jay (30 August 2012). *Cost Analysis of Stratospheric Albedo Modification Delivery Systems*. Environmental Research Letters. 7 (3): 3 in 1âĂŞ8. doi:10.1088/1748-9326/7/3/034019.

[116] Robock, A.; Marquardt, A.; Kravitz, B.; Stenchikov, G. (2009). *Benefits, risks, and costs of stratospheric geoengineering*. Geophysical Research Letters. 36 (19): L19703. Bibcode:2009GeoRL..3619703R. doi:10.1029/2009GL039209.

[117] Wiesel, William E 1997, *Spaceflight dynamics*, 2nd ed, Irwin/McGraw-Hill, Boston, Mass.

[118] Wertz, J. R., & Larson, W. J. (1999). *Space Mission Analysis and Design, Space Technology Library*. Microcosm Press and Kluwer Academic Publishers, El Segundo, CA, USA,.

[119] Jagannatha, Bindu. *Solar radiation pressure, drag and gravitational effects on a dust particle in Earth orbit.*, University of Illinois at Urbana-Champaign, Department of Aerospace Eneigneering, M.S. Thesis (Dec 2012), URL: http://hdl.handle.net/2142/42385.

[120] Colombo C, Lücking C, McInnes CR. *Orbital dynamics of high area-to-mass ratio spacecraft with J2 and solar radiation pressure for novel Earth observation and communication services*. Acta Astronautica. 2012 Dec 31;81(1):pp.137-50. DOI:10.1016/j.actaastro.2012.07.009.

[121] Canady Jr JE, Allen Jr JL. *Illumination from space with orbiting solar-reflector spacecraft*. NASA Technical Paper 2065 19820025545.

[122] Hilton, W. F. *I. Theory of Flight of Artificial Earth Satellites. El'yasberg PE, II. Motion of an Artificial Satellite about its Center of Mass. Beletskii VV*. Israel Program for Scientific Translations, translated by Z. Lerman from Russian. The Aeronautical Journal 72, no. 690 (1968): 529-529.

[123] Born, G. H. *Motion of a Satellite under the influence of an Oblate Earth.* ASEN 3200 (2001).

[124] Anderson, Brian DO and Moore, John B *Optimal control: linear quadratic methods*. 2007. Courier Corporation.

[125] Lavretsky E, Wise KA. *Robust Adaptive Control*. In Robust and Adaptive Control 2013 (pp. 317-353). Springer London.

[126] Barkana I. *Simple adaptive control: a stable direct model reference adaptive control methodology—brief survey*. International Journal of Adaptive Control and Signal Processing. 2014 Jul 1;28(7-8):567-603.

[127] Nguyen NT. *Adaptive Control for linear uncertain systems with unmodeled dynamics revisited via optimal control modification*. InAIAA Guidance, Navigation, and Control (GNC) Conference 2013 (p. 4988).

[128] Gelfand, Izrail Moiseevitch, and Richard A. Silverman. *Calculus of variations*. Dover Publications 2000. ISBN 10: 0486414485 ISBN 13: 9780486414485.

[129] Cess RD. *Climate change: An appraisal of atmospheric feedback mechanisms employing zonal climatology*. Journal of the Atmospheric Sciences. 1976 Oct;33(10):1831–43.

[130] Kleidon A, Lorenz R. *1 Entropy Production by Earth System Processes. Non-equilibrium Thermodynamics and the Production of Entropy*. 2005:1–20.

[131] Warren SG, Schneider SH. *Seasonal simulation as a test for uncertainties in the parameterizations of a Budyko-Sellers zonal climate model*. Journal of the Atmospheric Sciences. 1979 Aug;36(8):1377–91.

[132] Knutti R, Sedláček J. *Robustness and uncertainties in the new CMIP5 climate model projections*. Nature Climate Change. 2013 Apr 1;3(4):369-73. DOI: 10.1038/NCLIMATE1716.

[133] Andrews, T., J. M. Gregory, M. J. Webb, and K. E. Taylor (2012), *Forcing, feedbacks and climate sensitivity in CMIP5 coupled atmosphere-ocean climate models*, Geophysical Research Letters, 39, L09712.

[134] Moore B. *Principal component analysis in linear systems: Controllability, observability, and model reduction*. IEEE transactions on automatic control. 1981 Feb;26(1):17-32.

[135] Moss RH, Edmonds JA, Hibbard KA, Manning MR, Rose SK, Van Vuuren DP, Carter TR, Emori S, Kainuma M, Kram T, Meehl GA. *The next generation of scenarios for climate change research and assessment*. Nature. 2010 Feb 11;463(7282):747-56.

[136] Seborg DE, Edgar TF, Shah SL. *Adaptive control strategies for process control: a survey*. AIChE Journal. 1986 Jun 1;32(6):881-913.

[137] Widiasih, E.R.: *Dynamics of the budyko energy balance model*. SIAM Journal on Applied Dynamical Systems 12(4), 2068-2092 (2013).

[138] Cole, K.D., Beck, J.V., Haji-Sheikh, A., Litkouhi, B., *Heat conduction using Greens functions*. Taylor and Francis (2010).

[139] Hahn David W Ozisik, M.N.: *Heat conduction*, 3 edn. John Wiley and Sons (2012).

[140] Schneider, S.H., Gal-Chen, T., *Numerical experiments in climate stability*. Journal of Geophysical Research 78(27), 6182-6194 (1973). DOI 10.1029/JC078i027p06182. URL http://dx.doi.org/10.1029/JC078i027p06182.

[141] La Salle, J.P.: *The stability of dynamical systems*. SIAM (1976).

[142] MacMynowski, D.G., Shin, H.J., Caldeira, K., *The frequency response of temperature and precipitation in a climate model*. Geophysical Research Letters 38(16) (2011). DOI 10.1029/2011GL048623.

[143] Rogelj, J., *Long-term climate change: projections, commitments and irreversibility* (2013).

[144] Gasser, T., Guivarch, C., Tachiiri, K., Jones, C., Ciais, P., *Negative emissions physically needed to keep global warming below 2°C*. Nature Communications 6 (2015). DOI 10.1038/ncomms8958. URL:http://dx.doi.org/10.1038/ncomms8958.

[145] Ban-Weiss, G.A., Caldeira, K., *Geoengineering as an optimization problem*, Environmental Research Letters 5(3), 034,009 (2010). DOI 10.1088/1748-9326/5/3/034009.

[146] Sarah M. Kang, Richard Seager, 2012, *Croll Revisited: Why Is the Northern Hemisphere Warmer Than the Southern Hemisphere?*, Columbia University Academic Commons, https://doi.org/10.7916/D80R9XNQ.

[147] Kravitz, B., Robock, A., Boucher, O., Schmidt, H., Taylor, K.E., Stenchikov, G., Schulz, M., *The geoengineering model intercomparison project (GeoMIP)*. Atmospheric Science Letters 12(2), 162-167 (2011).

[148] Caldeira, K., Kasting, J.F., *Susceptibility of the early earth to irreversible glaciation caused by carbon dioxide clouds*, Nature 359(6392), 226 (1992). DOI 10.1038/359226a0.

[149] Griffel, D., Drazin, P., *On diffusive climatological models*. Journal of the Atmospheric, Sciences 38(11), 2327-2332 (1981).

[150] Gates, W.L., *Modeling the ice-age climate*. Science 191(4232), 1138-1144 (1976). DOI 10.1126/science.191.4232.1138.

[151] Suresh, Rahul, and Andrew Meulenberg. *A LEO-based solar-shade system to mitigate global warming*. 60th International Astronautical Congress, Daejeon, 12-16 October 2009, IAC-09.D1.1.5. arXiv preprint arXiv:1504.05148 (2015).

[152] Govindasamy, B., & Caldeira, K. (2000). *Geoengineering Earth's radiation balance to mitigate CO2$\vee\bar{}$induced climate change*. Geophysical Research Letters, 27(14), 2141-2144.

[153] Polyanin, Andrei D., and Alexander V. Manzhirov. *Handbook of mathematics for engineers and scientists.* CRC Press, 2006.

[154] Omar, A. H., Won, J. G., Winker, D. M., Yoon, S. C., Dubovik, O., & McCormick, M. P. (2005). *Development of global aerosol models using cluster analysis of Aerosol*

Robotic Network (AERONET) measurements. Journal of Geophysical Research: Atmospheres, 110(D10).

[155] Carnevale, C., Decanini, E., & Volta, M. (2008). *Design and validation of a multiphase 3D model to simulate tropospheric pollution*. Science of the Total Environment, 390(1), 166-176.

[156] Borggräfe A, Heiligers J, Ceriotti M, McInnes CR. *Shape control of slack space reflectors using modulated solar pressure*. In Proceeding of Royal Society A, 2015 Jul 8. Vol. 471, No. 2179, p. 20150119. The Royal Society. doi:10.1098/rspa.2015.0119.

[157] Geoffroy, O., Saint-Martin, D., Olivié, D.J.L., Voldoire, A., Bellon, G., Tytéca, S.,*Transient Climate Response in a Two-Layer Energy-Balance Model. Part I: Analytical Solution and Parameter Calibration Using CMIP5 AOGCM Experiments*, Journal of Climate, 2013, Vol. 26, 1841-1857, DOI: 10.1175/JCLI-D-12-00195.1, http://adsabs.harvard.edu/abs/2013JCli...26.1841G.

[158] King, M. D., & Arking, A. (1984). *A model of the radiative properties of the El Chichon Stratospheric Aerosol layer*. Journal of Climate and Applied Meteorology, 23(7), 1121-1137.

[159] Brovkin V, Petoukhov V, Claussen M, Bauer E, Archer D, Jaeger C. *Geoengineering climate by stratospheric sulfur injections: Earth system vulnerability to technological failure*. Climatic Change. 2009 Feb 1;92(3):243-59.

[160] Niemeier U, Timmreck C. *What is the limit of climate engineering by stratospheric injection of SO_2?*. Atmospheric Chemistry and Physics. 2015 Aug 18;15(16):9129-41.

[161] Niemeier U, Schmidt H, Alterskjar K, Kristjánsson JE. *Solar irradiance reduction via climate engineering: Impact of different techniques on the energy balance and the hydrological cycle*. Journal of Geophysical Research: Atmospheres. 2013 Nov 16;118(21).

[162] Tilmes S, Mills MJ, Niemeier U, Schmidt H, Robock A, Kravitz B, Lamarque JF, Pitari G, English JM. *A new Geoengineering Model Intercomparison Project (GeoMIP) experiment designed for climate and chemistry models*. Geoscientific Model Development. 2015 Jan 15;8(1):43-9.

Appendix A

Analytical functions of $V(x_s(U,t))$

As seen in Chapter (7), the Lyapunov function depends on a number of analytical functions (Eq. (7.7)) depending on the model parameters, the stability eigenvalue and the slope of the ice line. Their complete description is given below.

In particular, function $F_1(x)$ is given by the combination of several functions as reported in Eq. (A.1):

$$F_1(x) = Q_0 \frac{\sqrt{f_{d1}}\ a_w F_w(x) + \frac{a_w^2 \Theta_\alpha F_{w_2}(x) + a_i^2 \Theta_\alpha F_i(x) + a_i \left(F_{i_2}(x) + a_w F_{w_3}(x) \Theta_\alpha \right)}{\left(B^2 + 62BD + 840D^2 \right)}}{f_{d_1}} \tag{A.1}$$

where the functions Θ_α, f_{d_1}, $F_w(x)$, $Fw_2(x)$, $Fw_3(x)$, $F_i(x)$ and $F_{i_2}(x)$ are given by the following expressions:

$$\Theta_\alpha = \frac{dx_s}{dQ}(x_{s0}) \frac{Q_0}{(S\alpha)_{x_{s0}}} \tag{A.2}$$

$$f_{d_1} = B(B+6D)(B+20D)(B+42D) \tag{A.3}$$

$$F_w(x) = B^3\left(0.027x^6 - 1.0x^4 + 0.25x^2 + 1.0\right) + B^2D\left(0.71x^6 - 49x^4 + 2.8x^2 + 68\right) + S_2(B^3\left(-1.3x^6 + 0.57x^4 + 1.5x^2 - 0.50\right) + B^2D\left(-34x^6 - 12x^4 + 98x^2 - 31\right) + BD^2\left(-160x^6 - 90x^4 + 1000x^2 - 410\right) - 420D^3) + BD^2(3.3x^6 - 260x^4 - 310x^2 + 1200) + 4400D^3 \quad \text{(A.4)}$$

$$F_{w_2}(x) = B^8\left(-6.3x^6 + 9.1x^4 - 1.8x^2 + 0.057\right) + B^7D\left(-1000x^6 + 1500x^4 - 250x^2 + 7.9\right) + B^6D^2\left(-66000x^6 + 98000x^4 - 12000x^2 + 490\right) + B^5D^3(-2.3\times10^6x^6 + 3.4\times10^6x^4 - 210000x^2 + 21000) + B^4D^4\left(-4.3\times10^7x^6 + 6.6\times10^7x^4 + 1.8\times10^6x^2 + 830000\right) + B^3D^5\left(-4.6\times10^8x^6 + 7.1\times10^8x^4 + 1.2\times10^8x^2 + 2.4\times10^7\right) + B^2D^6(-2.5\times10^9x^6 + 3.9\times10^9x^4 + 1.4\times10^9x^2 + 4.3\times10^8) + S_2(B^8\left(-6.1x^6 + 11x^4 - 2.5x^2 + 0.083\right) + B^7D\left(-920x^6 + 1700x^4 - 360x^2 + 11\right) + B^6D^2\left(-56000x^6 + 110000x^4 - 19000x^2 + 620\right) + B^5D^3\left(-1.7\times10^6x^6 + 3.5\times10^6x^4 - 420000x^2 + 21000\right) + B^4D^4(-2.8\times10^7x^6 + 6.2\times10^7x^4 - 2.1\times10^6x^2 + 670000) + B^3D^5(-2.4\times10^8x^6 + 6.0\times10^8x^4 + 6.3\times10^7x^2 + 1.9\times10^7) + B^2D^6(-8.6\times10^8x^6 + 2.7\times10^9x^4 + 8.8\times10^8x^2 + 3.2\times10^8) + S_2(B^8\left(-1.2x^6 + 2.9x^4 - 0.89x^2 + 0.030\right) + B^7D(-170x^6 + 460x^4 - 130x^2 + 3.9) + B^6D^2\left(-10000x^6 + 29000x^4 - 7100x^2 + 190\right) + B^5D^3(-290000x^6 + 910000x^4 - 170000.x^2 + 4500) + B^4D^4(-4.4\times10^6x^6 + 1.5\times10^7x^4 - 1.0\times10^6x^2 + 110000) + B^3D^5\left(-3.1\times10^7x^6 + 1.1\times10^8x^4 + 1.7\times10^7x^2 + 3.6\times10^6\right) + B^2D^6\left(-5.5\times10^7x^6 + 2.1\times10^8x^4 + 1.9\times10^8x^2 + 6.9\times10^7\right) + BD^7(1.3\times10^8x^6 - 5.0\times10^8x^4 - 2.8\times10^8x^2 + 4.5\times10^8) - 7.0\times10^8D^8) + BD^7(-8.7\times10^8x^6 + 4.4\times10^9x^4 + 2.3\times10^9x^2 + 2.6\times10^9) + 5.9\times10^9D^8) + BD^7(-5.3\times10^9x^6 + 8.3\times10^9x^4 + 5.8\times10^9x^2 + 3.9\times10^9) + 1.4\times10^{10}D^8 \quad \text{(A.5)}$$

$$F_{w_3}(x) = B^8(S_2(S_2\left(0.076x^6 - 0.19x^4 + 0.059x^2 - 0.0020\right) + 0.43x^6 - 0.76x^4 + 0.19x^2$$
$$-0.0061) + 0.51x^6 - 0.75x^4 + 0.15x^2 - 0.0047) + B^7D(S_2(S_2\left(8.4x^6 - 23x^4 + 6.3x^2 - 0.18\right)$$
$$+70x^6 - 150x^4 + 37x^2 - 1.2) + 150x^6 - 220x^4 + 39x^2 - 1.2) + B^6D^2(S_2(S_2(330x^6 - 980x^4$$
$$+210x^2 - 5.0) + 5100x^6 - 12000x^4 + 3000x^2 - 92) + 15000x^6 - 22000x^4 + 3200x^2 - 110) + B^5D^3$$
$$(S_2\left(S_2\left(2300x^6 - 10000x^4 - 730x^2 + 7.6\right) + 190000x^6 - 550000x^4 + 120000x^2 - 3600\right)$$
$$+710000x^6 - 1.1\times10^6x^4 + 110000x^2 - 5600) + B^4D^4(S_2(S_2(-220000x^6 + 590000x^4$$
$$-220000x^2 + 1800) + 3.9\times10^6x^6 - 1.4\times10^7x^4 + 2.2\times10^6x^2 - 83000) + 1.8\times10^7x^6 - 2.8\times10^7x^4$$
$$+640000x^2 - 230000) + B^3D^5(S_2(S_2\left(-7.1\times10^6x^6 + 2.3\times10^7x^4 - 4.3\times10^6x^2 - 7600\right)$$
$$+3.9\times10^7x^6 - 1.8\times10^8x^4 + 9.8\times10^6x^2 - 2.0\times10^6) + 2.5\times10^8x^6 - 3.9\times10^8x^4 - 3.8\times10^7x^2$$
$$-8.0\times10^6) + B^2D^6(S_2(S_2\left(-7.9\times10^7x^6 + 2.8\times10^8x^4 + 5.0\times10^6x^2 + 1.2\times10^6\right)$$
$$+1.5\times10^8x^6 - 1.2\times10^9x^4 - 1.6\times10^8x^2 - 5.1\times10^7) + 1.8\times10^9x^6 - 2.7\times10^9x^4 - 8.2\times10^8x^2$$
$$-1.9\times10^8) + BD^7(S_2(S_2\left(-2.7\times10^8x^6 + 9.9\times10^8x^4 + 5.5\times10^8x^2 + 1\times10^8\right)$$
$$+1.5\times10^8x^6 - 2.8\times10^9x^4 - 1.3\times10^9x^2 - 7.2\times10^8) + 4.5\times10^9x^6 - 7.0\times10^9x^4 - 4.9\times10^9x^2$$
$$-2.4\times10^9) + D^8\left(S_2\left(1.4\times10^9S_2 - 3.5\times10^9\right) - 1.2\times10^{10}\right) \tag{A.6}$$

$$
\begin{aligned}
F_i(x) = {} & B^8\left(5.8x^6 - 8.4x^4 + 1.7x^2 - 0.052\right) + B^7 D\left(860x^6 - 1300x^4 + 210x^2 - 6.7\right) \\
& + B^6 D^2\left(51000x^6 - 76000x^4 + 9000x^2 - 370\right) + B^5 D^3(1.5\times10^6 x^6 - 2.3\times10^6 x^4 \\
& + 110000x^2 - 16000) + B^4 D^4\left(2.5\times10^7 x^6 - 3.8\times10^7 x^4 - 2.5\times10^6 x^2 - 600000\right) \\
& + B^3 D^5\left(2.1\times10^8 x^6 - 3.2\times10^8 x^4 - 7.7\times10^7 x^2 - 1.6\times10^7\right) + B^2 D^6 \\
& \left(7.5\times10^8 x^6 - 1.2\times10^9 x^4 - 6.2\times10^8 x^2 - 2.4\times10^8\right) + S_2(B^8(5.6x^6 - 9.8x^4 \\
& + 2.4x^2 - 0.077) + B^7 D\left(850x^6 - 1500x^4 + 320x^2 - 10\right) + B^6 D^2(51000x^6 - 94000x^4 \\
& + 16000x^2 - 530) + B^5 D^3\left(1.5\times10^6 x^6 - 2.9\times10^6 x^4 + 300000x^2 - 18000\right) + B^4 D^4 \\
& \left(2.4\times10^7 x^6 - 4.9\times10^7 x^4 - 61000x^2 - 590000\right) + B^3 D^5(2.0\times10^8 x^6 - 4.1\times10^8 x^4 \\
& - 7.3\times10^7 x^2 - 1.7\times10^7) + B^2 D^6\left(7.1\times10^8 x^6 - 1.5\times10^9 x^4 - 7.2\times10^8 x^2 - 2.7\times10^8\right) \\
& + S_2(B^8\left(1.1x^6 - 2.7x^4 + 0.83x^2 - 0.028\right) + B^7 D\left(160x^6 - 430x^4 + 120x^2 - 3.8\right) \\
& + B^6 D^2\left(9700x^6 - 28000x^4 + 6900x^2 - 180\right) + B^5 D^3(290000x^6 - 900000x^4 \\
& + 170000x^2 - 4500) + B^4 D^4\left(4.7\times10^6 x^6 - 1.5\times10^7 x^4 + 1.3\times10^6 x^2 - 110000\right) \\
& + B^3 D^5\left(3.8\times10^7 x^6 - 1.3\times10^8 x^4 - 1.3\times10^7 x^2 - 3.6\times10^6\right) + B^2 D^6(1.3\times10^8 x^6 \\
& - 4.9\times10^8 x^4 - 2.0\times10^8 x^2 - 7.1\times10^7) + BD^7(1.3\times10^8 x^6 - 5.0\times10^8 x^4 - 2.8\times10^8 x^2 \\
& - 5.5\times10^8) - 7.0\times10^8 D^8) + BD^7\left(7.2\times10^8 x^6 - 1.6\times10^9 x^4 - 9.9\times10^8 x^2 - 1.9\times10^9\right) \\
& - 2.4\times10^9 D^8) + BD^7\left(8.0\times10^8 x^6 - 1.3\times10^9 x^4 - 8.7\times10^8 x^2 - 1.5\times10^9\right) - 2.0\times10^9 D^8
\end{aligned}
\tag{A.7}
$$

$$F_{i_2}(x) = B^9(S_2\left(1.3x^6 - 0.57x^4 + 0.035x^2 + 0.00018\right) - 0.027x^6 + 1.0x^4 - 0.25x^2 + 0.0091) + B^8D\left(S_2\left(200x^6 - 62x^4 - 0.071x^2 + 0.11\right) - 4.2x^6 + 180x^4 - 35x^2 + 1.3\right) + B^7D^2\left(S_2\left(13000x^6 - 1900x^4 - 170x^2 + 2.8\right) - 260x^6 + 13000x^4 - 1600x^2 + 78\right) + B^6D^3(S_2\left(410000x^6 + 7300x^4 + 3200x^2 - 210\right) - 8600x^6 + 490000x^4 - 12000x^2 + 3400) + B^5D^4(S_2\left(7.3\times10^6x^6 + 1.4\times10^6x^4 + 730000x^2 + 9700\right) - 150000x^6 + 9.8\times10^6x^4 + 1.2\times10^6x^2 + 150000) + B^4D^5(S_2(7.2\times10^7x^6 + 2.6\times10^7x^4 + 2.3\times10^7x^2 + 1.5\times10^6) - 1.5\times10^6x^6 + 1.1\times10^8x^4 + 3.7\times10^7x^2 + 5.1\times10^6) + B^3D^6(S_2(3.5\times10^8x^6 + 1.7\times10^8x^4 + 2.6\times10^8x^2 + 4.6\times10^7) - 7.3\times10^6x^6 + 5.5\times10^8x^4 + 4.0\times10^8x^2 + 9.8\times10^7) + B^2D^7(S_2\left(6.6\times10^8x^6 + 3.8\times10^8x^4 + 8.9\times10^8x^2 + 5.2\times10^8\right) - 1.4\times10^7x^6 + 1.1\times10^9x^4 + 1.3\times10^9x^2 + 9.0\times10^8) + BD^8\left(1.8\times10^9S_2 + 2.8\times10^9\right) \quad \text{(A.8)}$$

Finally, $f_5(\lambda)$ and $f_6(\lambda)$ depend on the stability eigenvalue and are given by the numerator and denominator of Eq. (3.20), respectively.

$$f_5(\lambda) = 1.6Q_0\left(a_i - a_w\right)(\lambda\left(\lambda\left(\lambda\left(S_2 + 1.5\right) - 44S_2 - 66\right) + 490S_2 + 750\right) - 1000S_2 - 1700) \quad \text{(A.9)}$$

$$f_6(\lambda) = (\lambda - 29)(\lambda - 15)(\lambda - 5.5)(\lambda - 1.6) \quad \text{(A.10)}$$

Appendix B

Analytical functions of $U_{ice}(x,t)$

The expression found in Eq. (7.8) for the family of control functions which would trigger the instability of the climate system depend on the functions f_{U1} and f_{U2}. These functions are given below:

$$f_{U1}(x) = \frac{f_5 x_{s0} F_1(x_{s0}) - f_5 x_{s0} F_1(x) - f_6 F_1(x_{s0}) T_0 + f_6 F_1(x) T_0}{1.30 \times 10^6} \tag{B.1}$$

$$f_{U2}(x) = \frac{\left(F_1^2(x_{s0}) - F_1^2(x)\right)^2}{76434.12} \tag{B.2}$$